Good Vibrations: A Microcavity-based Diamond Spin-Photon Interface for Quantum Networking

Herrmann, Y.S.

DOI
10.4233/uuid:8d6b9c4d-b926-462c-8640-fb917dd64b69

Publication date
2025

Document Version
Final published version

Citation (APA)
Herrmann, Y. S. (2025). *Good Vibrations: A Microcavity-based Diamond Spin-Photon Interface for Quantum Networking*. [Dissertation (TU Delft), Delft University of Technology]. https://doi.org/10.4233/uuid:8d6b9c4d-b926-462c-8640-fb917dd64b69

Important note
To cite this publication, please use the final published version (if applicable).
Please check the document version above.

Good Vibrations

A Microcavity-based Diamond Spin-Photon Interface for Quantum Networking

BY

YANIK HERRMANN

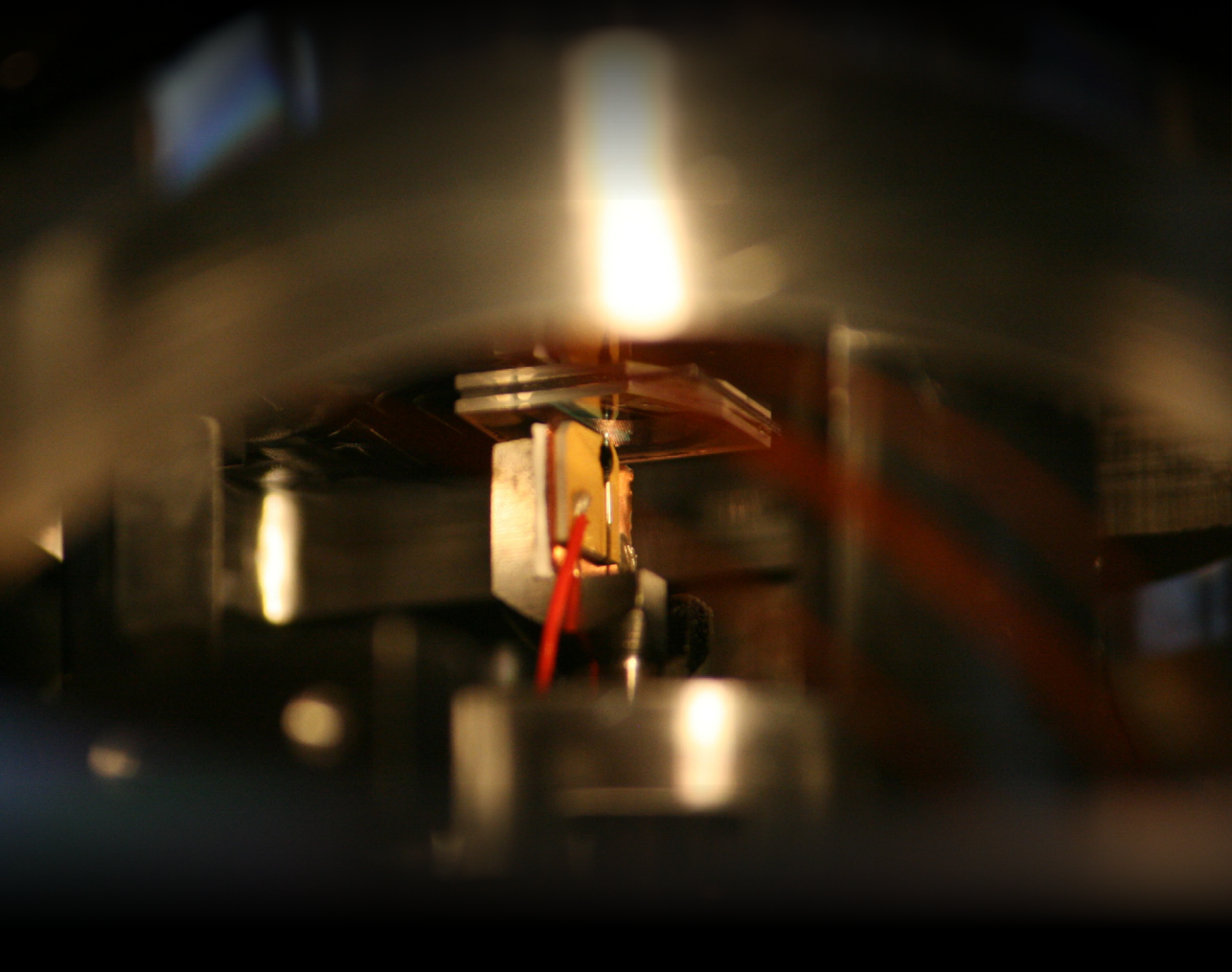

Good Vibrations

A Microcavity-based Diamond Spin-Photon Interface for Quantum Networking

Good Vibrations

A Microcavity-based Diamond Spin-Photon Interface for Quantum Networking

Proefschrift

ter verkrijging van de graad van doctor
aan de Technische Universiteit Delft,
op gezag van de Rector Magnificus Prof. dr. ir. T.H.J.J. van der Hagen,
voorzitter van het College voor Promoties,
in het openbaar te verdedigen op maandag 8 december 2025 om 15:00 uur.

door

Yanik Stefan Herrmann

Master of Science in Physics,
Johannes Gutenberg-Universität Mainz, Duitsland
geboren te Fulda, Duitsland.

Dit proefschrift is goedgekeurd door de promotoren.

Samenstelling promotiecommissie:

Rector Magnificus,	voorzitter
Prof. dr. ir. R. Hanson,	Technische Universiteit Delft, *promotor*
Prof. dr. S.D.C. Wehner,	Technische Universiteit Delft, *promotor*
Onafhankelijke leden:	
Prof. dr. D. Hunger,	Karlsruher Institut für Technologie, Duitsland
Prof. dr. M.P. van Exter,	Universiteit Leiden
Dr. E. Janitz,	University of Calgary, Canada
Dr. S. Rajabali,	Technische Universiteit Delft
Prof. dr. ir. T. van der Sar,	Technische Universiteit Delft
Prof. dr. A.F. Otte,	Technische Universiteit Delft, reservelid

Cover: Picture taken by Laurens Feije and confocal map measured by Colin Sauerzapf.

ISBN: 978-94-6518-180-6

Printed by: Gildeprint - Enschede

An electronic version of this dissertation is available at
`https://repository.tudelft.nl/`.

Dedicated to my grandparents.

Opgedragen aan mijn grootouders.

Meinen Großeltern gewidmet.

Contents

Summary

Quantum networks promise exciting applications that are not possible with their classical counterparts, such as distributed quantum computation or fundamentally secure quantum communication. Optically active spins in solid states are among the prime candidates for realizing quantum network nodes, while photons are used to distribute entanglement between nodes. The nitrogen-vacancy (NV) center in diamond is a pioneering system with the demonstrations of teleportation of quantum states within a three-node network and metropolitan-scale heralded entanglement. However, scaling to more nodes or longer distances is limited by the low extraction of resonant photons, creating a high interest in optical resonators (cavities) to improve the optical interface. Moreover, the diamond tin-vacancy (SnV) center with better optical properties emerged as a promising alternative candidate for quantum network nodes.

This dissertation presents the building blocks and the experimental realization of an open, fiber-based, cryogenic Fabry-Pérot microcavity enabling the Purcell enhancement of diamond NV and SnV centers, incorporated into the microcavity via a diamond membrane. The background on color centers in the context of quantum networking (Chapter 2) and optical cavities for diamond color centers is summarized (Chapter 3). A novel laser-cutting patterning method is introduced, which can be used to fabricate micrometer-thin diamond devices with arbitrary lateral shapes in the range of tens to hundreds of micrometers (Chapter 4). Microdevices fabricated by this method are characterized by scanning cavity microscopy, revealing a high cavity finesse. Furthermore, SnV and NV centers in the microdevices maintain bulk-like optical properties, which are required for quantum networking. Next to the sample fabrication, the detailed design, construction, and operation of a cryogenic microcavity system is presented, reaching a reproducible cavity length stability level of around 25 picometer with a sample temperature of about 8 kelvin on the cavity mirror (Chapter 5), a prerequisite for the following cavity experiments. Two cavity quantum optics experiments are conducted, exploring the regimes of coherent cavity coupling and efficient photon extraction with the cavity. In the first experiment, a single SnV center is coupled to the cavity, achieving a coherent cooperativity of 0.7. This enables the observation of nonlinear quantum effects, such as the modulation of the cavity resonance by an individual SnV center and the altered photon statistics of light transmitted through the cavity (Chapter 6). In the second experiment, a single NV center is coupled to the cavity, and the Purcell enhancement combined with a high cavity outcoupling leads to a resonant photon extraction (end-to-end) efficiency of 0.5 %. The NV center's electron spin qubit initialization, manipulation with an on-chip microwave stripline, and readout are utilized to generate spin-photon correlated states, a precondition for remote entanglement with a second color center (Chapter 7).

The presented platform combines an efficient optical interface with microwave control of the spin state and can be used for the exploration of optically active defects in solid states, as a bright source of single photons, and for cavity-enhanced quantum networking.

Samenvatting

Kwantumnetwerken beloven kansrijke toepassingen die niet mogelijk zijn met hun klassieke tegenhangers, zoals gedistribueerde kwantum berekeningen of fundamenteel veilige kwantum communicatie. Optisch actieve spins in vaste stoffen behoren tot de veelbelovende kandidaten voor het realiseren van kwantumnetwerkknooppunten, waarbij fotonen worden gebruikt om verstrengeling tussen deze knooppunten te distribueren. Het stikstof-holtecentrum (NV-centrum) in diamant is een pionier geweest die de teleportatie van kwantumtoestanden binnen een netwerk met drie knooppunten heeft gedemonstreerd. Daarnaast is verstrengeling met bevestigd succes tussen steden gerealiseerd. De opschaling naar meer knooppunten of langere afstanden wordt echter beperkt door de lage extractie van resonante fotonen. Dit zorgt voor grote interesse in optische resonatoren (trilholtes of caviteiten) om de optische interface te verbeteren. Daardoor is het diamant tin-holtecentrum (SnV-centrum) met betere optische eigenschappen naar voren gekomen als een veelbelovende alternatieve kandidaat voor kwantumnetwerkknooppunten.

Dit proefschrift presenteert de bouwstenen en de experimentele realisatie van een open, op fiber gebaseerde, cryogene Fabry-Pérot-microcaviteit die de Purcell-versterking van NV- en SnV-centra in diamant mogelijk maakt, die geïntegreerd zijn in een diamantmembraan in de microcaviteit. De achtergrondinformatie over kleurcentra in de context van kwantumnetwerken (Hoofdstuk 2) en optische caviteiten voor diamantkleurcentra wordt samengevat (Hoofdstuk 3). Er wordt een nieuwe lasersnijmethode voor structuren maken geïntroduceerd, die kan worden gebruikt om micrometer dunne diamantstructuren te realiseren met elke gewenste laterale vorm variërend van tientallen tot honderden micrometers (Hoofdstuk 4). Microstructuren die met deze methode zijn gerealiseerd, worden gekarakteriseerd door middel van scanning cavity microscopy, waarmee een hoge caviteitsfinesse wordt gemeten. Bovendien behouden SnV- en NV-centra in de microstructuren bulkachtige optische eigenschappen, die vereist zijn voor kwantumnetwerken. Naast de fabricage van deze microstructuren, worden het gedetailleerde ontwerp, de constructie en de werking van een cryogeen microcaviteitssysteem gepresenteerd. Met dit ontwerp wordt een reproduceerbare stabiliteit van de caviteitslengte van ongeveer 25 picometer bij een temperatuur van 8 kelvin op de caviteitsspiegel bereikt (Hoofdstuk 5). Dit is een voorwaarde voor de volgende caviteitsexperimenten. Er worden twee caviteitskwantumopticaexperimenten uitgevoerd. Hiermee worden de regimes van coherente caviteitskoppeling en efficiënte fotonenextractie van de caviteit onderzocht. In het eerste experiment wordt een enkel SnV-centrum gekoppeld aan de caviteit, waardoor een coherente coöperativiteit van 0.7 wordt bereikt. Dit maakt het mogelijk om niet-lineaire kwantumeffecten waar te nemen, zoals de modulatie van de caviteitsresonantie door een individueel SnV-centrum en de veranderde fotonstatistieken van licht dat door de caviteit wordt doorgelaten (Hoofdstuk 6). In het tweede experiment wordt een enkel NV-centrum gekoppeld aan de caviteit, waarbij de Purcell-versterking in combinatie met een hoge caviteitsuitkoppeling leidt tot

een resonante fotonenextractie-efficiëntie (end-to-end) van 0.5 %. De initialisatie van de elektronenspin-qubit van het NV-centrum, de manipulatie met een microgolfstriplijn op de chip en de uitlezing worden gebruikt om spin-foton gecorreleerde toestanden te genereren, een voorwaarde voor verstrengeling met een tweede kleurcentrum (Hoofdstuk 7). Het gepresenteerde platform combineert een efficiënte optische interface met microgolfcontrole van de spintoestand en kan worden gebruikt voor het ontdekken van optisch actieve defecten in vaste stoffen als een effectieve bron van enkele fotonen en voor caviteitsversterkte kwantumnetwerken.

Kurzfassung

Quantennetzwerke versprechen aussichtsreiche Anwendungen, die mit klassischen Netzwerken nicht möglich sind, wie etwa dezentrale Quantenberechnungen oder fundamental sichere Quantenkommunikation. Optisch aktive Spins in Festkörpern eignen sich ideal für die Realisierung von Knotenpunkten des Quantennetzwerks, wobei Photonen genutzt werden können, um Verschränkung zwischen den Knotenpunkten herzustellen. Das Stickstoff-Fehlstellen-Zentrum (NV-Zentrum) in Diamant ist ein Technologie-Vorreiter mit der Demonstration von Teleportation eines Quantenzustands innerhalb eines Quantennetzwerkes, bestehend aus drei Knotenpunkten und von angekündigter Verschränkung über städtische Distanzen. Jedoch ist die Skalierung auf mehr Netzwerkknoten oder längere Distanzen limitiert durch die niedrige Extrahierung resonanter Photonen. Dies führt zu einem hohen Interesse an optischen Hohlraumresonatoren (Kavitäten) zur Verbesserung der optische Schnittstelle. Zudem hat sich das Zinn-Fehlstellen-Zentrum (SnV-Zentrum) mit besseren optischen Eigenschaften für Quantennetzwerke etabliert.
Diese Dissertation präsentiert die einzelnen Komponenten und die experimentelle Realisierung einer offenen, faser-basierten, kryogenen Fabry-Pérot Mikrokavität. Diese ermöglicht die Purcell-Verstärkung von Diamant NV- und SnV-Zentren, die durch eine Diamantmembran in die Mikrokavität eingebracht werden. Die Grundlagen der Farbzentren im Kontext von Quantennetzwerken (Kapitel 2) und der optische Kavitäten für Diamant Farbzentren werden eingeführt (Kapitel 3). Eine neuartige Methode zum Strukturieren mittels Laserschneidens wird vorgestellt, welche sich zum Herstellen von Mikrometer-dünnen Diamantproben eignet, die beliebige laterale Formen im Bereich von mehreren zehn bis hunderten Mikrometern aufweisen (Kapitel 4). Diamantproben, welche mit dieser Methode hergestellt wurden, werden mit einem Rasterkavitätenmikroskop charakterisiert und weisen eine hohe Kavitäten Finesse auf. Weiterhin wird gezeigt, dass NV- und SnV-Zentren in den Diamantproben gute optische Eigenschaften behalten, die zum Quantennetzwerken benötigt werden. Neben der Diamantproben-Fabrikation werden das detaillierte Design sowie die Konstruktion und Operation eines kryogenen Mikrokavitäten-Systems präsentiert. Dieses erreicht reproduzierbar eine Kavitätenlängestabilität von etwa 25 Pikometern mit einer Probentemperatur von ungefähr 8 Kelvin auf dem Kavitätenspiegel (Kapitel 5), welches für die folgenden Experimente benötigt wird. Zwei Kavitäten-Quantenoptik Experimente werden durchgeführt, welche die Regime der kohärenten Kavitäten-Kopplung und der effizienten Photonen-Extrahierung durch die Kavität erproben. Im ersten Experiment wird ein einzelnes SnV-Zentrum an die Kavität gekoppelt und es wird eine kohärente Kooperativität von 0.7 erreicht. Dies ermöglicht die Beobachtung von nichtlinearen Quanteneffekten, wie die Modulation der Kavitäten-Resonanz durch ein individuelles SnV-Zentrum und die veränderte Photonenstatistik von transmittiertem Licht (Kapitel 6). Im zweiten Experiment wird ein einzelnes NV-Zentrum an die Kavität gekoppelt, und die Purcell-Verstärkung in Kombination mit einer hohen Kavitäten-Auskopplung führt zu einer resonanten Photonen-Extrahierungs-Effizienz (Ende-zu-Ende) von 0.5 %. Die Initiali-

sierung, die Manipulation mit Chip-basierten Mikrowellenleitern und das Auslesen des Elektronen-Spin-Qubits des NV-Zentrums werden genutzt, um Spin-Photon korrelierte Zustände zu erzeugen (Kapitel 7). Dies ist eine Voraussetzung für die Verschränkung mit einem zweiten, entfernten Farbzentrum.
Die vorgestellte Plattform kombiniert eine effiziente optische Schnittstelle mit Mikrowellenkontrolle des Spinzustands und kann für die Erforschung von optisch aktiven Defekten in Festkörpern, als helle Einzelphotonenquelle und zum Kavitäten-verstärkten Quantennetzwerken genutzt werden.

1 Introduction

"In this field [physics], almost everything is already discovered, and all that remains is to fill a few unimportant holes." - *Philipp von Jolly's advice on studying physics to Max Planck in 1878.*

1.1 Quantum Technologies

The United Nations declared 2025 to the International Year of Quantum Science and Technology, celebrating 100 years of quantum mechanics. This theory has fundamentally changed our worldview, and its implications remain under debate. After the development of quantum mechanics in places like Copenhagen, Brussels, or the German island Helgoland in the years around 1925 [1], technologies utilizing quantum mechanical phenomena, like transistors, lasers, or solar cells, were developed within the last century. Often summarized as the first quantum revolution, humans were passive observers of the microscopic quantum world, described by the theory. Now, one hundred years later, we are within the second quantum revolution [2], in which control over quantum systems, such as trapped atoms, is accomplished and can be engineered for scientific and practical applications, and quantum technologies are increasingly commercialized [3]. In this phase, humans turn into active creators and manipulators of peculiar quantum systems, which cannot be found in nature around us [2]. Technologies based on this can be grouped into quantum computation, quantum communication, quantum simulation, and quantum sensing.

At the core of many quantum applications lies entanglement, one of the most fascinating aspects of quantum mechanics [4]. Entangled quantum states can not be separated into individual states, even if they are distributed over vast distances. A quantum state can be represented by a quantum bit (qubit), which is, similar to its classical counterpart, the smallest possible unit for quantum information [5]. Next to qubits, higher-dimensional quantum states (qudits) are becoming increasingly relevant in quantum technologies [6].

1

1.2 Quantum Networking

Quantum networking refers to the tools, protocols, and systems that enable the transmission of quantum information between different devices or locations [3]. Quantum networks are at the intersection of quantum computing and communication, intending to connect separated quantum computers into a network. They provide the only way through which quantum computers can share quantum information [7]. Quantum computers form the nodes of the network and share entangled qubits as links between them. After its generation, an entangled link can be used as a resource [8] for applications like fundamentally secure communication [9], teleportation of a quantum state [10–12], distributed quantum computation [13, 14], blind quantum computation [15, 16], or quantum enhanced sensing [17–19]. Further applications might not be known yet, comparable to the early days of the classical internet. Initial demonstrations of quantum networks have been realized on the laboratory scale, and now several quantum systems have reached a level of maturity where they can be used over larger, metropolitan-scale distances [20–22]. At some point in the future, they might even turn into a quantum internet [23, 24].
Entanglement is at the heart of the quantum network, and to generate entanglement between different nodes, an interaction between a flying qubit as a mediator and a stationary qubit of the network node is required. There are multiple schemes and protocols available for entanglement generation [25]. For example, this can be the emission of a photon dependent on the quantum state of the stationary qubit. After two-photon interference at a middle station between the two nodes, a measurement of the photon entangles the stationary qubits and heralds the successful entanglement generation. Photons are a natural choice for serving as flying qubits, as they can be efficiently routed and transmitted with low losses in optical fibers or free space over larger distances. This capability is also part of DiVincenzo's criteria listing the physical requirements for quantum computation and communication: the ability to interconvert stationary and flying qubits [26].
Stationary qubits may be realized by physical systems consisting of ensembles [27] or single quantum emitters [28, 29]. Pioneering experiments have used atomic ensembles [30, 31], single trapped ions [32], and atoms [33, 34] to generate remote entanglement between two separated matter-based qubits. Diamond nitrogen-vacancy (NV) centers became the first solid-state emitters used to demonstrate entanglement of two remote emitters [35]. Furthermore, remote entanglement has also been shown with other systems such as superconducting circuits [36, 37], semiconductor quantum dots [38, 39], and rare-earth ion-doped crystals [40]. In recent years, other single optically-active solid-state spins such as silicon-vacancy (SiV) centers in diamond [21], T centers in silicon [41], and ytterbium rare earth ions [42], are successfully employed for remote entanglement generation. Due to its excellent optical properties [43–46], the tin-vacancy (SnV) center in diamond emerged over the last years into a promising candidate for the stationary qubit.

1.3 The Spin-Photon Interface

The optical properties of the stationary qubit determine how high the interaction probability with the flying qubit, the photon, is. For color centers in diamond, the stationary qubit is encoded in the ground states of the electron spin, which leads to the phrasing of a spin-photon interface. The ground states are connected with optical transitions to

short-lived excited states. The probability of interaction determines how successful an entanglement attempt is, which in turn sets the entanglement link generation rate. The spin-photon interface is therefore a key component for quantum networking. Note that the entanglement generation rate is also influenced by other parameters such as losses in the optical connections between the nodes or the length of the experimental sequence used to generate entanglement.

Due to the high index of refraction of diamond, emitted light from the color center is refracted at the diamond surface as shown in Fig. 1.1 (a), which limits the collection efficiency to a few percent [47]. This still enabled groundbreaking experiments such as the observation of room-temperature oscillations of the electron spin [48], the characterization of the carbon nuclear spin environment [49], room-temperature memory storage times exceeding one second [50], and the first demonstration of spin-photon entanglement [51]. To control the electron spin qubit of the color center, microwaves can be delivered through an antenna, which is typically realized by a bondwire or a stripline deposited on the diamond surface.

To improve the efficiency of the spin-photon interface, photonic structures around the color center can be used, and we can group approaches into non-resonant and resonant structures. Non-resonant structures improve the broadband fluorescence collection of photons from the color center, such as a solid immersion lens (SIL) [52]: a microscopic lens milled into the diamond surface shown in Fig. 1.1 (b), which circumvents total internal reflection and leads to an enhanced photon collection from an emitter placed in the focal point. SILs can provide a collection efficiency of about 10 % [53] and facilitated many quantum experiments, especially with NV centers. On the quantum computing side, this includes quantum error correction with a qubit register [54], the realization of a discrete time crystal [55], the fault-tolerant operation of a logical qubit [56], and the demonstration of high-fidelity qubit gates [57, 58]. Furthermore, a ten-qubit spin register with surrounding nuclear spins has been demonstrated [59] together with atomic-scale imaging of an up to 50-spin-qubit network around a NV center [60, 61]. In quantum networking, NV centers in SILs have been used for unconditional quantum teleportation [62], a loophole-free Bell test [63], entanglement distillation [64], deterministic delivery of remote entanglement [65], the entanglement of three remote NV centers in a multinode quantum network [66] with the teleportation of a quantum state across this network [67], metropolitan-scale, heralded entanglement [22], hybrid entanglement of photons and nuclear spins [68, 69] and the transfer of a quantum state by photon absorption [70]. The maturity of NV centers in SILs also made implementations of a quantum network operating system possible [71, 72]. Non-resonant structures are ultimately limited to the natural zero-phonon line (ZPL) emission rate: the direct transition from the optical excited state to the ground state without any phonons involved. Only indistinguishable ZPL photons can be used for entanglement generation; otherwise, quantum information would leak out through phonons. For the NV center, merely about 3 % of the total emission is via the ZPL [73]. In experimental realizations with SILs this leads to ZPL detection probabilities (resonant end-to-end efficiency) after pulsed excitation of about 5×10^{-4} [63, 65, 67, 74]. This is a major limitation for scaling quantum networks to larger distances or more nodes.

1

This limit can be overcome with a resonant photonic structure, which can be realized by an optical resonator, a cavity. In general, a cavity brings two advantages: First, the Purcell effect can be utilized to enhance the rate of photons emitted into the ZPL [75]. Second, by engineering the cavity mirror reflectivities and minimizing scattering losses, these photons can be channeled into a well-defined output mode, maximizing the collection efficiency. The cooperativity is the central figure of merit to quantify the coupling between a cavity and a quantum emitter; the higher the cooperativity, the more photons are emitted into the cavity mode (for a given cooperativity C, the fraction $C/(C+1)$ of photons is emitted into the cavity mode, see section 3.1.2 for more details).
There are two distinct approaches to combine diamond color centers and optical cavities (see also Table 3.1): in the first one, the cavity is fabricated around the color center by a monolithic resonator structure in diamond [76]. In the second, hybrid approach, the cavity is made into an external material, and the emitter is integrated with a suitable piece of diamond. In this thesis, we make use of the second, hybrid approach: the resonator is realized by an open fiber-based microcavity, sketched in Fig. 1.1 (c), and color centers are incorporated by a micrometer-thin diamond membrane. Open microcavities are detailed in the following, before we focus on the hybrid diamond integration.

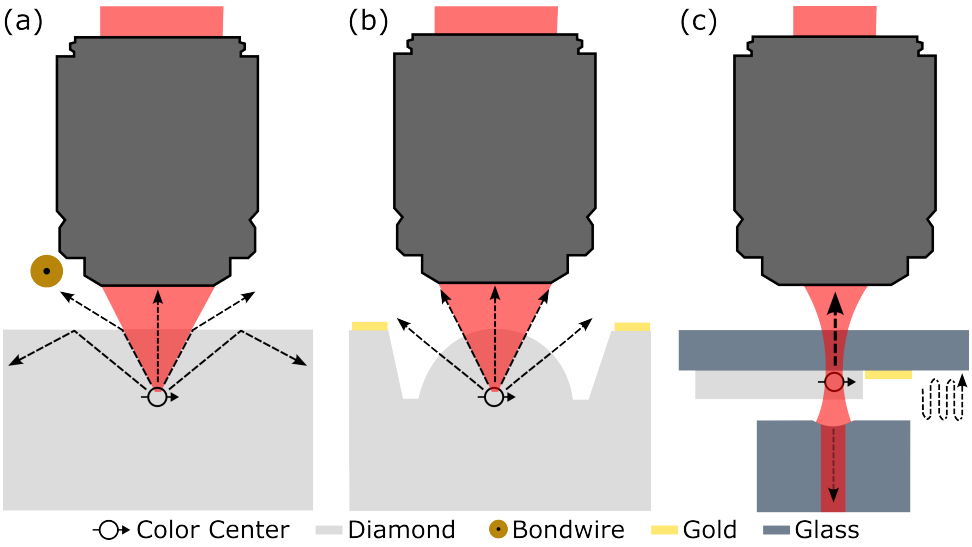

Figure 1.1: Three generations of diamond-based quantum optics experiments. Figures (a) and (b) are based on Bernien [77]. In each approach, an objective is used to collimate the emitted light to a free-space beam. (a) A planar bulk diamond sample with a bondwire delivering microwaves to control the spin qubit. Due to the high index of refraction of diamond, light is refracted at the surface for smaller angles, while total internal reflection occurs for larger angles. (b) A solid immersion lens (SIL) is milled into the diamond surface. The spherical dome-shaped structure mitigates total internal reflection. Microwaves are sent via a gold stripline deposited on the surface. (c) A fiber-based Fabry-Pérot microcavity with an incorporated diamond membrane. Light travels many times back and forth between the mirrors, effectively increasing the interaction probability with the color center. The cavity mirror coating is asymmetric, resulting in light predominantly exiting through the flat sample mirror on top. Microwaves are delivered with a gold stripline on that mirror. The figure is not to scale.

1.4 Open Microcavities: One Cavity to Enhance Them All

An optical cavity can be constructed by two highly reflective mirrors, facing each other to form a Fabry-Pérot cavity, which is the archetypal realization of an optical resonator. To ensure stable cavity operation, one of the mirrors or both have a spherical (curved) shape. An important figure of merit for cavities is the finesse, which, together with the beam waist inside the cavity (half of the beam diameter on the sample mirror), directly determines the cooperativity (see section 3.3). The finesse quantifies the average number of times a resonant photon bounces back and forth between the mirrors (average number of round trips), before being lost [78]. This loss can happen through absorption, scattering, or transmission through the mirrors out of the cavity. In a conventional optical cavity, often used for spectroscopy [79] or laser stabilization [80], the mirrors are spaced by a large distance compared to the light wavelength λ (cavity length $L \gg \lambda$). A high finesse can be accomplished with superpolished mirror substrates [81, 82]. Pioneering cavity-emitter experiments have been conducted with such macroscopic cavities and atoms [34, 83, 84] or ions [85]. For a microcavity [86] (a miniaturized cavity), the cavity length is much reduced and approaches values of multiple tens of the wavelength or less ($L \sim \lambda$). Due to the short cavity length, the radius of curvature of the spherical mirror can be reduced in order to confine light into a much smaller beam waist, especially required for solid-state emitters with typically more incoherent loss channels than atoms. A few methods are available to produce such micro-mirrors (see section 3.3.3). In the picture of the traveling photon inside the cavity, a photon is recycled many times, leading to a much higher probability of interaction with the quantum emitter (see also Fig. 1.1 (c)) [87].
To send and collect light from the cavity, direct fiber access is beneficial. This can be realized by fabricating one cavity mirror on the tip of an optical fiber [88, 89]. Solid-state emitters can be incorporated in the microcavity via the macroscopic, flat sample mirror and hosted inside membranes (see Fig. 1.1 (c)), atomically-thin layers, nanoparticles, or directly grown into the mirror material (see introduction of Chapter 5).
The sample integration makes open microcavities a versatile quantum optics platform compatible with many systems used in the context of quantum technologies, including:

- **Neutral atoms**: Microcavities have been used to reach the strong coupling regime (see section 3.1.2) with cooperativities exceeding 100 with ensembles of cold atoms forming a Bose-Einstein condensate [90] and with single rubidium atoms trapped inside the cavity [91–93]. A fiber-fiber microcavity has recently been utilized for ultrafast, high-fidelity state readout of single rubidium atoms, trapped by a two-dimensional optical lattice [94].

- **Semiconductor quantum dots**: The regime of strong coupling with cooperativities above 100 has been demonstrated with a single optical quantum dot and a cryogenic microcavity [95]. Moreover, a highly asymmetric (single-sided) cavity mirror design combined with low additional losses enabled the on-demand generation of fiber-coupled single photons with record efficiencies of 57 % [96] and 71 % [97]. The latter is higher than the efficiency threshold of 2/3 for scalable photonic quantum computing [98] and is used recently to demonstrate a secret key rate above the fundamental rate limit of a weak coherent pulse [99], a realization of an untrusted intermediate relay architecture [100], and for boosted fusion gates [101].

- **Organic molecules**: Microcavities at low temperatures have shown a high cooperativity above 10 of a single, optically-active organic molecule hosted by a solid-state matrix, turning it into a two-level quantum system [102].

- **Carbon nanotubes**: Microcavities have been used to collect 60 % of the emission of an individual single-wall carbon nanotube at room temperature [103]. Moreover, cavity-coupling could be extended to telecom band emitters at low temperatures [104] and room temperature [105]. In the latter work, the cavity enhanced the observation of photon indistinguishability from a single nanotube defect even under ambient conditions.

- **Rare-earth ions**: Erbium ions in a yttrium orthosilicate membrane have been coupled to a cryogenic microcavity, resulting in a 59-fold enhancement of the emission rate with a cavity outcoupling efficiency of 46 % [106]. This has recently been harnessed for the detection of individual nuclear spins [107].

- **Silicon carbide**: Single V2 color centers have been incorporated via a silicon carbide membrane into a microcavity at low temperatures, leading to a 13-fold Purcell enhancement of the ZPL [108].

- **Diamond**: Nanodiamonds or (sub) micrometer-thin diamond membranes enable the integration of color centers into microcavities. So far, individual nitrogen [109], as well as germanium- [110], silicon- [111], and tin-vacancy centers (Chapter 6) have been coupled to a microcavity at low temperatures, demonstrating Purcell enhancement. Furthermore, a zero-phonon line enhancement of a single NV center from about 3 % to 45 % has been accomplished [73, 112]. A detailed summary of diamond color centers in open microcavities is presented in section 3.3.2.

1.5 Open Microcavities with a Diamond Membrane

The open fiber-based microcavity approach utilized in this thesis is schematically shown in Fig. 1.2. One of the mirrors is coated on the tip of an optical fiber, allowing direct fiber-coupled optical access. The other sample mirror consists of a coated wafer of fused quartz glass, which is diced into an arbitrary, easy-to-handle size.
To ensure that a stable resonator is formed, the fiber tip mirror has a spherical shape. This is realized with a concave crater or dimple at the center of the fiber tip, which is fabricated with laser ablation before the mirror coating is applied [89]. This results in a hemispherical plano-concave cavity geometry. The cavity length is on the order of micrometers, and the beam waist in which the light is confined can be reduced by minimizing the radius of curvature of the spherical mirror (in this work, between 15 µm and 25 µm). Color centers are incorporated into the cavity by a micrometer-thin diamond membrane, bonded to the sample mirror by Van der Waals forces. The sample mirror is patterned with a gold stripline to deliver microwaves to manipulate the spin qubit state of the cavity-coupled color center.
A high cavity finesse can be achieved by using high-reflective mirror coatings and diamond samples with excellent surface quality (surface roughness below 1 nm). The sample mirror side of the cavity is optically interfaced with a high-numerical-aperture objective,

which is used to collimate the Gaussian beam leaving the cavity or to couple light from free space into the cavity. In this way, excitation and detection light can be sent and received from the cavity via the side of the fiber and via the objective.

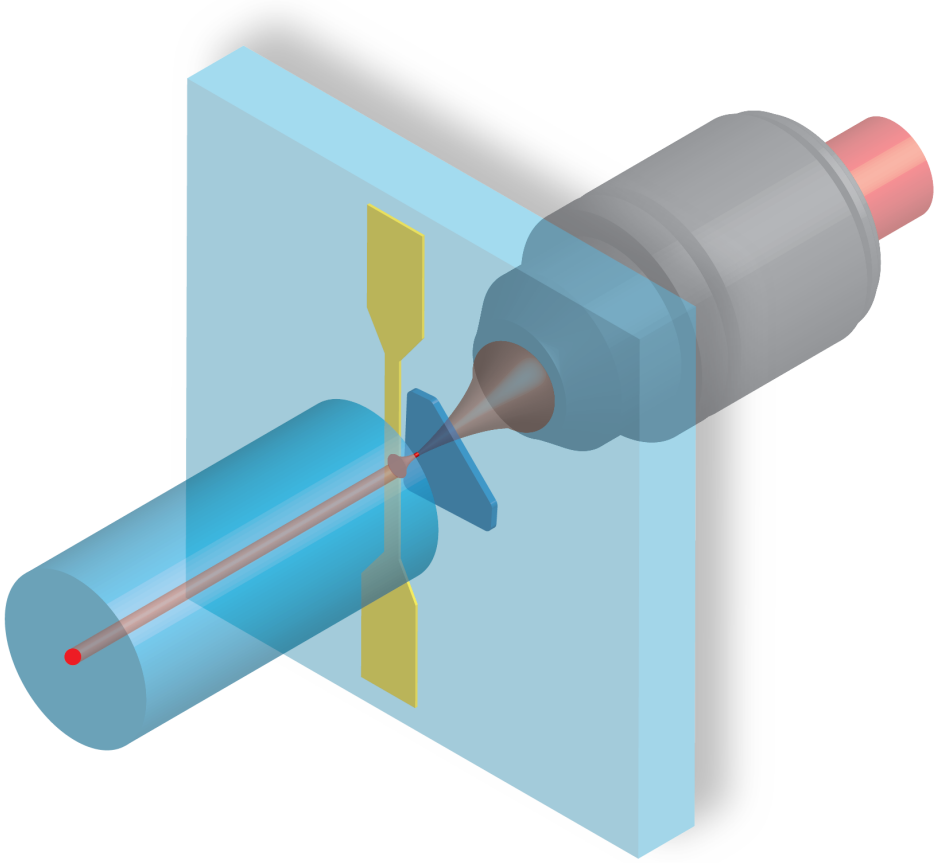

Figure 1.2: The open fiber-based microcavity approach: the spherical cavity fiber mirror (from the left side) can be moved to arbitrary lateral positions on the flat sample mirror. Micrometer-thin diamond membranes (dark blue) and gold striplines for microwave delivery are placed on the sample mirror. The cavity is optically interfaced with an objective through the sample mirror side (from the right side), which can also be freely positioned to match the cavity spot on the mirror.

1.6 Thesis Overview

This experimental thesis presents the individual building blocks and the realization of Purcell enhancement of single diamond SnV and NV centers with an open microcavity. The goal is to build a more efficient quantum network node. The thesis is structured as follows:

- **Chapter 2** summarizes the properties of diamond NV and SnV centers and how they can be utilized as stationary qubits of a quantum network node. The generation of remote entanglement is discussed together with the limitation by the collection of resonant ZPL photons.
- **Chapter 3** provides the background about optical cavities and how they can be used to enhance the ZPL emission of diamond color centers. After discussing several cavity approaches, we focus on open microcavities and particular aspects of this platform, such as the influence of diamond inside the cavity, the sensitivity to vibrations, and the integration of microwave delivery.
- **Chapter 4** introduces a novel method to fabricate micrometer-thin diamond devices with laser-cutting and reactive ion etching, which are required to incorporate diamond color centers into the microcavity. These microdevices are characterized by scanning cavity microscopy under ambient conditions to analyze the achievable cavity finesse. Furthermore, low-temperature confocal microscopy investigates the optical properties of NV centers created by electron irradiation and SnV centers created by ion implantation.
- **Chapter 5** presents in detail the technical aspects of the low-temperature microcavity setup used for the cavity experiments of the following chapters. This includes the design, construction, and operation of the cavity. Moreover, the integration of microwave delivery into the microcavity is shown.
- **Chapter 6** demonstrates the coherent coupling of an individual SnV center hosted inside a laser-cut diamond microdevice to the microcavity at cryogenic temperatures. Cavity coupling is quantified by the reduction of the excited state lifetime and the corresponding broadening of the emitter linewidth. The stable cavity, combined with the excellent optical emitter properties, allows reaching the regime of coherent coupling. The modulation of the cavity resonance by a single SnV center and the altered photon statistics in cavity transmission are studied.
- **Chapter 7** presents the coupling of a single NV center to the microcavity at cryogenic temperatures. A high finesse cavity combined with a large outcoupling efficiency leads to an enhanced ZPL photon detection from the NV center, outperforming solid immersion lens devices. Furthermore, the electron spin qubit is controlled with on-chip microwave lines, and resonant addressing of the optical transitions is used for qubit initialization and readout. This enables the cavity-enhanced generation of spin-photon correlated states, a precondition for generating remote entanglement with a second color center.
- **Chapter 8** concludes this thesis, including an outlook on follow-up experiments, cavity improvements, and how open microcavities can be utilized for quantum networking.

References

[1] E. P. Fischer, *Die Stunde der Physiker: Einstein, Bohr, Heisenberg und das Innerste der Welt*, 1st ed. (C.H. Beck, München, 2022).

[2] J. P. Dowling and G. J. Milburn, *Quantum technology: the second quantum revolution,* Philos. Trans. R. Soc. A **361**, 1655 (2003).

[3] J. Ruane, E. Kiesow, J. Galatsanos, C. Dukatz, E. Blomquist, and P. Shukla, *Quantum Index Report 2025,* MIT Initiative on the Digital Economy, Massachusetts Institute of Technology (2025), accessed via arXiv:2506.04259.

[4] A. Einstein, B. Podolsky, and N. Rosen, *Can Quantum-Mechanical Description of Physical Reality Be Considered Complete?* Phys. Rev. **47**, 777 (1935).

[5] M. A. Nielsen and I. L. Chuang, *Quantum Computation and Quantum Information: 10th Anniversary Edition*, 1st ed. (Cambridge University Press, 2012).

[6] R. Blume-Kohout, C. M. Caves, and I. H. Deutsch, *Climbing Mount Scalable: Physical Resource Requirements for a Scalable Quantum Computer,* Foundations of Physics **32**, 1641 (2002).

[7] K. van der Enden, *Metropolitan-scale quantum networks with diamond qubits: Applied quantum networks for business & society*, Ph.D. thesis, Delft University of Technology (2025).

[8] W. K. Wootters, *Quantum entanglement as a quantifiable resource,* Phil. Trans. R. Soc. A. **356**, 1717 (1998).

[9] A. Ekert and R. Renner, *The ultimate physical limits of privacy,* Nature **507**, 443 (2014).

[10] C. H. Bennett, G. Brassard, C. Crépeau, R. Jozsa, A. Peres, and W. K. Wootters, *Teleporting an unknown quantum state via dual classical and Einstein-Podolsky-Rosen channels,* Phys. Rev. Lett. **70**, 1895 (1993).

[11] D. Bouwmeester, J.-W. Pan, K. Mattle, M. Eibl, H. Weinfurter, and A. Zeilinger, *Experimental quantum teleportation,* Nature **390**, 575 (1997).

[12] A. Furusawa, J. L. Sørensen, S. L. Braunstein, C. A. Fuchs, H. J. Kimble, and E. S. Polzik, *Unconditional Quantum Teleportation,* Science **282**, 706 (1998).

[13] L. Jiang, J. M. Taylor, A. S. Sørensen, and M. D. Lukin, *Distributed quantum computation based on small quantum registers,* Phys. Rev. A **76**, 062323 (2007).

[14] M. Caleffi, M. Amoretti, D. Ferrari, J. Illiano, A. Manzalini, and A. S. Cacciapuoti, *Distributed quantum computing: A survey,* Comput. Netw. **254**, 110672 (2024).

[15] A. Broadbent, J. Fitzsimons, and E. Kashefi, *Universal Blind Quantum Computation,* in *2009 50th Annual IEEE Symposium on Foundations of Computer Science* (IEEE, Atlanta, GA, USA, 2009) pp. 517–526.

[16] J. F. Fitzsimons and E. Kashefi, *Unconditionally verifiable blind quantum computation,* Phys. Rev. A **96**, 012303 (2017).

[17] D. Gottesman, T. Jennewein, and S. Croke, *Longer-Baseline Telescopes Using Quantum Repeaters,* Phys. Rev. Lett. **109**, 070503 (2012).

[18] P. Kómár, E. M. Kessler, M. Bishof, L. Jiang, A. S. Sørensen, J. Ye, and M. D. Lukin, *A quantum network of clocks,* Nat. Phys. **10**, 582 (2014).

[19] T. J. Proctor, P. A. Knott, and J. A. Dunningham, *Multiparameter Estimation in Networked Quantum Sensors,* Phys. Rev. Lett. **120**, 080501 (2018).

[20] J.-L. Liu, X.-Y. Luo, Y. Yu, C.-Y. Wang, B. Wang, Y. Hu, J. Li, M.-Y. Zheng, B. Yao, Z. Yan, D. Teng, J.-W. Jiang, X.-B. Liu, X.-P. Xie, J. Zhang, Q.-H. Mao, X. Jiang, Q. Zhang, X.-H. Bao, and J.-W. Pan, *Creation of memory–memory entanglement in a metropolitan quantum network,* Nature **629**, 579 (2024).

[21] C. M. Knaut, A. Suleymanzade, Y.-C. Wei, D. R. Assumpcao, P.-J. Stas, Y. Q. Huan, B. Machielse, E. N. Knall, M. Sutula, G. Baranes, N. Sinclair, C. De-Eknamkul, D. S. Levonian, M. K. Bhaskar, H. Park, M. Lončar, and M. D. Lukin, *Entanglement of nanophotonic quantum memory nodes in a telecom network,* Nature **629**, 573 (2024).

[22] A. J. Stolk, K. L. Van Der Enden, M.-C. Slater, I. Te Raa-Derckx, P. Botma, J. Van Rantwijk, J. J. B. Biemond, R. A. J. Hagen, R. W. Herfst, W. D. Koek, A. J. H. Meskers, R. Vollmer, E. J. Van Zwet, M. Markham, A. M. Edmonds, J. F. Geus, F. Elsen, B. Jungbluth, C. Haefner, C. Tresp, J. Stuhler, S. Ritter, and R. Hanson, *Metropolitan-scale heralded entanglement of solid-state qubits,* Sci. Adv. **10**, eadp6442 (2024).

[23] H. J. Kimble, *The quantum internet,* Nature **453**, 1023 (2008).

[24] S. Wehner, D. Elkouss, and R. Hanson, *Quantum internet: A vision for the road ahead,* Science **362** (2018).

[25] H. K. Beukers, M. Pasini, H. Choi, D. Englund, R. Hanson, and J. Borregaard, *Remote-Entanglement Protocols for Stationary Qubits with Photonic Interfaces,* PRX Quantum **5**, 010202 (2024).

[26] D. P. DiVincenzo, *The Physical Implementation of Quantum Computation,* Fortschr. Phys. **48**, 771 (2000).

[27] L.-M. Duan, M. D. Lukin, J. I. Cirac, and P. Zoller, *Long-distance quantum communication with atomic ensembles and linear optics,* Nature **414**, 413 (2001).

[28] J. I. Cirac, P. Zoller, H. J. Kimble, and H. Mabuchi, *Quantum State Transfer and Entanglement Distribution among Distant Nodes in a Quantum Network,* Phys. Rev. Lett. **78**, 3221 (1997).

[29] L.-M. Duan and H. J. Kimble, *Scalable Photonic Quantum Computation through Cavity-Assisted Interactions,* Phys. Rev. Lett. **92**, 127902 (2004).

[30] C. W. Chou, H. De Riedmatten, D. Felinto, S. V. Polyakov, S. J. Van Enk, and H. J. Kimble, *Measurement-induced entanglement for excitation stored in remote atomic ensembles,* Nature **438**, 828 (2005).

[31] Z.-S. Yuan, Y.-A. Chen, B. Zhao, S. Chen, J. Schmiedmayer, and J.-W. Pan, *Experimental demonstration of a BDCZ quantum repeater node,* Nature **454**, 1098 (2008).

[32] D. L. Moehring, P. Maunz, S. Olmschenk, K. C. Younge, D. N. Matsukevich, L.-M. Duan, and C. Monroe, *Entanglement of single-atom quantum bits at a distance,* Nature **449**, 68 (2007).

[33] J. Hofmann, M. Krug, N. Ortegel, L. Gérard, M. Weber, W. Rosenfeld, and H. Weinfurter, *Heralded Entanglement Between Widely Separated Atoms,* Science **337**, 72 (2012).

[34] S. Ritter, C. Nölleke, C. Hahn, A. Reiserer, A. Neuzner, M. Uphoff, M. Mücke, E. Figueroa, J. Bochmann, and G. Rempe, *An elementary quantum network of single atoms in optical cavities,* Nature **484**, 195 (2012).

[35] H. Bernien, B. Hensen, W. Pfaff, G. Koolstra, M. S. Blok, L. Robledo, T. H. Taminiau, M. Markham, D. J. Twitchen, L. Childress, and R. Hanson, *Heralded entanglement between solid-state qubits separated by three metres,* Nature **497**, 86 (2013).

[36] P. Magnard, S. Storz, P. Kurpiers, J. Schär, F. Marxer, J. Lütolf, T. Walter, J.-C. Besse, M. Gabureac, K. Reuer, A. Akin, B. Royer, A. Blais, and A. Wallraff, *Microwave Quantum Link between Superconducting Circuits Housed in Spatially Separated Cryogenic Systems,* Phys. Rev. Lett. **125**, 260502 (2020).

[37] S. Storz, J. Schär, A. Kulikov, P. Magnard, P. Kurpiers, J. Lütolf, T. Walter, A. Copetudo, K. Reuer, A. Akin, J.-C. Besse, M. Gabureac, G. J. Norris, A. Rosario, F. Martin, J. Martinez, W. Amaya, M. W. Mitchell, C. Abellan, J.-D. Bancal, N. Sangouard, B. Royer, A. Blais, and A. Wallraff, *Loophole-free Bell inequality violation with superconducting circuits,* Nature **617**, 265 (2023).

[38] A. Delteil, Z. Sun, W.-b. Gao, E. Togan, S. Faelt, and A. Imamoğlu, *Generation of heralded entanglement between distant hole spins,* Nat. Phys. **12**, 218 (2016).

[39] R. Stockill, M. J. Stanley, L. Huthmacher, E. Clarke, M. Hugues, A. J. Miller, C. Matthiesen, C. Le Gall, and M. Atatüre, *Phase-Tuned Entangled State Generation between Distant Spin Qubits,* Phys. Rev. Lett. **119**, 010503 (2017).

[40] D. Lago-Rivera, S. Grandi, J. V. Rakonjac, A. Seri, and H. De Riedmatten, *Telecom-heralded entanglement between multimode solid-state quantum memories,* Nature **594**, 37 (2021).

[41] F. Afzal, S. J. Beale, O. Bedroya, K. Bell, L. Bergeron, K. Bonsma-Fisher, P. Bychkova, Z. M. E. Chaisson, C. Chartrand, C. Clear, A. Darcie, A. DeAbreu, C. DeLisle, L. A. Duncan, C. D. Smith, J. Dunn, A. Ebrahimi, N. Evetts, D. F. Pinheiro, P. Fuentes, T. Georgiou, B. Guha, R. Haenel, D. Higginbottom, D. M. Jackson, N. Jahed, A. Khorshidahmad, P. K. Shandilya, A. T. K. Kurkjian, N. Lauk, N. R. Lee-Hone, E. Lin,

R. Litynskyy, D. Lock, L. Ma, I. MacGilp, E. R. MacQuarrie, A. Mar, A. M. Khah, A. Matiash, E. Meyer-Scott, C. P. Michaels, J. Motira, N. K. Noori, E. Ospadov, E. Patel, A. Patscheider, D. Paulson, A. Petruk, A. L. Ravindranath, B. Reznychenko, M. Ruether, J. Ruscica, K. Saxena, Z. Schaller, A. Seidlitz, J. Senger, Y. S. Lee, O. Sevoyan, S. Simmons, O. Soykal, L. Stott, Q. Tran, S. Tserkis, A. Ulhaq, W. Vine, R. Weeks, G. Wolfowicz, and I. Yoneda, *Distributed Quantum Computing in Silicon,* arXiv:2406.01704 (2024).

[42] A. Ruskuc, C.-J. Wu, E. Green, S. L. N. Hermans, W. Pajak, J. Choi, and A. Faraon, *Multiplexed entanglement of multi-emitter quantum network nodes,* Nature **639**, 54 (2025).

[43] T. Iwasaki, Y. Miyamoto, T. Taniguchi, P. Siyushev, M. H. Metsch, F. Jelezko, and M. Hatano, *Tin-Vacancy Quantum Emitters in Diamond,* Phys. Rev. Lett. **119**, 253601 (2017).

[44] J. Görlitz, D. Herrmann, G. Thiering, P. Fuchs, M. Gandil, T. Iwasaki, T. Taniguchi, M. Kieschnick, J. Meijer, M. Hatano, A. Gali, and C. Becher, *Spectroscopic investigations of negatively charged tin-vacancy centres in diamond,* New J. Phys. **22**, 013048 (2020).

[45] A. E. Rugar, S. Aghaeimeibodi, D. Riedel, C. Dory, H. Lu, P. J. McQuade, Z.-X. Shen, N. A. Melosh, and J. Vučković, *Quantum Photonic Interface for Tin-Vacancy Centers in Diamond,* Phys. Rev. X **11**, 031021 (2021).

[46] J. Arjona Martínez, R. A. Parker, K. C. Chen, C. M. Purser, L. Li, C. P. Michaels, A. M. Stramma, R. Debroux, I. B. Harris, M. Hayhurst Appel, E. C. Nichols, M. E. Trusheim, D. A. Gangloff, D. Englund, and M. Atatüre, *Photonic Indistinguishability of the Tin-Vacancy Center in Nanostructured Diamond,* Phys. Rev. Lett. **129**, 173603 (2022).

[47] P. K. Shandilya, S. Flagan, N. C. Carvalho, E. Zohari, V. K. Kavatamane, J. E. Losby, and P. E. Barclay, *Diamond Integrated Quantum Nanophotonics: Spins, Photons and Phonons,* J. Lightwave Technol. **40**, 7538 (2022).

[48] F. Jelezko, T. Gaebel, I. Popa, A. Gruber, and J. Wrachtrup, *Observation of Coherent Oscillations in a Single Electron Spin,* Phys. Rev. Lett. **92**, 076401 (2004).

[49] L. Childress, M. V. Gurudev Dutt, J. M. Taylor, A. S. Zibrov, F. Jelezko, J. Wrachtrup, P. R. Hemmer, and M. D. Lukin, *Coherent Dynamics of Coupled Electron and Nuclear Spin Qubits in Diamond,* Science **314**, 281 (2006).

[50] P. C. Maurer, G. Kucsko, C. Latta, L. Jiang, N. Y. Yao, S. D. Bennett, F. Pastawski, D. Hunger, N. Chisholm, M. Markham, D. J. Twitchen, J. I. Cirac, and M. D. Lukin, *Room-Temperature Quantum Bit Memory Exceeding One Second,* Science **336**, 1283 (2012).

[51] E. Togan, Y. Chu, A. S. Trifonov, L. Jiang, J. Maze, L. Childress, M. V. G. Dutt, A. S. Sørensen, P. R. Hemmer, A. S. Zibrov, and M. D. Lukin, *Quantum entanglement between an optical photon and a solid-state spin qubit,* Nature **466**, 730 (2010).

[52] J. P. Hadden, J. P. Harrison, A. C. Stanley-Clarke, L. Marseglia, Y.-L. D. Ho, B. R. Patton, J. L. O'Brien, and J. G. Rarity, *Strongly enhanced photon collection from diamond defect centers under microfabricated integrated solid immersion lenses,* Appl. Phys. Lett. **97**, 241901 (2010).

[53] M. Ruf, N. H. Wan, H. Choi, D. Englund, and R. Hanson, *Quantum networks based on color centers in diamond,* J. Appl. Phys. **130**, 070901 (2021).

[54] G. Waldherr, Y. Wang, S. Zaiser, M. Jamali, T. Schulte-Herbrüggen, H. Abe, T. Ohshima, J. Isoya, J. F. Du, P. Neumann, and J. Wrachtrup, *Quantum error correction in a solid-state hybrid spin register,* Nature **506**, 204 (2014).

[55] J. Randall, C. E. Bradley, F. V. van der Gronden, A. Galicia, M. H. Abobeih, M. Markham, D. J. Twitchen, F. Machado, N. Y. Yao, and T. H. Taminiau, *Many-body–localized discrete time crystal with a programmable spin-based quantum simulator,* Science **374**, 1474 (2021).

[56] M. H. Abobeih, Y. Wang, J. Randall, S. J. H. Loenen, C. E. Bradley, M. Markham, D. J. Twitchen, B. M. Terhal, and T. H. Taminiau, *Fault-tolerant operation of a logical qubit in a diamond quantum processor,* Nature **606**, 884 (2022).

[57] X. Rong, J. Geng, F. Shi, Y. Liu, K. Xu, W. Ma, F. Kong, Z. Jiang, Y. Wu, and J. Du, *Experimental fault-tolerant universal quantum gates with solid-state spins under ambient conditions,* Nat. Commun. **6**, 8748 (2015).

[58] H. Bartling, J. Yun, K. Schymik, M. Van Riggelen, L. Enthoven, H. Van Ommen, M. Babaie, F. Sebastiano, M. Markham, D. Twitchen, and T. Taminiau, *Universal high-fidelity quantum gates for spin qubits in diamond,* Phys. Rev. Applied **23**, 034052 (2025).

[59] C. E. Bradley, J. Randall, M. H. Abobeih, R. C. Berrevoets, M. J. Degen, M. A. Bakker, M. Markham, D. J. Twitchen, and T. H. Taminiau, *A Ten-Qubit Solid-State Spin Register with Quantum Memory up to One Minute,* Phys. Rev. X **9**, 031045 (2019).

[60] M. H. Abobeih, J. Randall, C. E. Bradley, H. P. Bartling, M. A. Bakker, M. J. Degen, M. Markham, D. J. Twitchen, and T. H. Taminiau, *Atomic-scale imaging of a 27-nuclear-spin cluster using a quantum sensor,* Nature **576**, 411 (2019).

[61] G. L. Van De Stolpe, D. P. Kwiatkowski, C. E. Bradley, J. Randall, M. H. Abobeih, S. A. Breitweiser, L. C. Bassett, M. Markham, D. J. Twitchen, and T. H. Taminiau, *Mapping a 50-spin-qubit network through correlated sensing,* Nat. Commun. **15**, 2006 (2024).

[62] W. Pfaff, B. J. Hensen, H. Bernien, S. B. van Dam, M. S. Blok, T. H. Taminiau, M. J. Tiggelman, R. N. Schouten, M. Markham, D. J. Twitchen, and R. Hanson, *Unconditional quantum teleportation between distant solid-state quantum bits,* Science **345**, 532 (2014).

[63] B. Hensen, H. Bernien, A. E. Dréau, A. Reiserer, N. Kalb, M. S. Blok, J. Ruitenberg, R. F. L. Vermeulen, R. N. Schouten, C. Abellán, W. Amaya, V. Pruneri, M. W. Mitchell, M. Markham, D. J. Twitchen, D. Elkouss, S. Wehner, T. H. Taminiau, and R. Hanson, *Loophole-free Bell inequality violation using electron spins separated by 1.3 kilometres,* Nature **526**, 682 (2015).

[64] N. Kalb, A. A. Reiserer, P. C. Humphreys, J. J. W. Bakermans, S. J. Kamerling, N. H. Nickerson, S. C. Benjamin, D. J. Twitchen, M. Markham, and R. Hanson, *Entanglement distillation between solid-state quantum network nodes,* Science **356**, 928 (2017).

[65] P. C. Humphreys, N. Kalb, J. P. J. Morits, R. N. Schouten, R. F. L. Vermeulen, D. J. Twitchen, M. Markham, and R. Hanson, *Deterministic delivery of remote entanglement on a quantum network,* Nature **558**, 268 (2018).

[66] M. Pompili, *Multi-Node Quantum Networks with Diamond Qubits*, Ph.D. thesis, Delft University of Technology (2021).

[67] S. L. N. Hermans, M. Pompili, H. K. C. Beukers, S. Baier, J. Borregaard, and R. Hanson, *Qubit teleportation between non-neighbouring nodes in a quantum network,* Nature **605**, 663 (2022).

[68] J. Javadzade, M. Zahedian, F. Kaiser, V. Vorobyov, and J. Wrachtrup, *Efficient nuclear spin–photon entanglement with optical routing,* Phys. Rev. Applied **24**, 024059 (2025).

[69] X.-Y. Chang, P.-Y. Hou, W.-G. Zhang, X.-Q. Meng, Y.-F. Yu, Y.-N. Lu, Y.-Q. Liu, B.-X. Qi, D.-L. Deng, and L.-M. Duan, *Hybrid entanglement and bit-flip error correction in a scalable quantum network node,* Nat. Phys. **21**, 583 (2025).

[70] D. Ito, Y. Sekiguchi, R. Reyes, T. Fujiwara, T. Makino, H. Kato, and H. Kosaka, *Robust transfer of a quantum state from an absorbed photon into a diamond spin,* Opt. Lett. **50**, 5073 (2025).

[71] M. Pompili, C. Delle Donne, I. Te Raa, B. Van Der Vecht, M. Skrzypczyk, G. Ferreira, L. De Kluijver, A. J. Stolk, S. L. N. Hermans, P. Pawełczak, W. Kozlowski, R. Hanson, and S. Wehner, *Experimental demonstration of entanglement delivery using a quantum network stack,* npj Quantum Inf. **8**, 121 (2022).

[72] C. Delle Donne, M. Iuliano, B. Van Der Vecht, G. M. Ferreira, H. Jirovská, T. J. W. Van Der Steenhoven, A. Dahlberg, M. Skrzypczyk, D. Fioretto, M. Teller, P. Filippov, A. R.-P. Montblanch, J. Fischer, H. B. Van Ommen, N. Demetriou, D. Leichtle, L. Music, H. Ollivier, I. Te Raa, W. Kozlowski, T. H. Taminiau, P. Pawełczak, T. E. Northup, R. Hanson, and S. Wehner, *An operating system for executing applications on quantum network nodes,* Nature **639**, 321 (2025).

[73] D. Riedel, I. Söllner, B. J. Shields, S. Starosielec, P. Appel, E. Neu, P. Maletinsky, and R. J. Warburton, *Deterministic Enhancement of Coherent Photon Generation from a Nitrogen-Vacancy Center in Ultrapure Diamond,* Phys. Rev. X **7**, 031040 (2017).

[74] M. Pompili, S. L. N. Hermans, S. Baier, H. K. C. Beukers, P. C. Humphreys, R. N. Schouten, R. F. L. Vermeulen, M. J. Tiggelman, L. dos Santos Martins, B. Dirkse, S. Wehner, and R. Hanson, *Realization of a multinode quantum network of remote solid-state qubits,* Science **372**, 259 (2021).

[75] E. M. Purcell, *Spontaneous emission probabilities at radio frequencies,* Phys. Rev. **69**, 681 (1946).

[76] N. Codreanu, *Diamond Nanophotonic Devices for Quantum Networks Experiments*, Ph.D. thesis, Delft University of Technology (2025).

[77] H. Bernien, *Control, measurement and entanglement of remote quantum spin registers in diamond*, Ph.D. thesis, Technische Universtiteit Delft (2014).

[78] M. Bitarafan and R. DeCorby, *On-Chip High-Finesse Fabry-Perot Microcavities for Optical Sensing and Quantum Information,* Sensors **17**, 1748 (2017).

[79] W. Demtröder, *Laser Spectroscopy*, 4th ed. (Springer Berlin Heidelberg, Berlin, Heidelberg, 2008).

[80] T. Kessler, C. Hagemann, C. Grebing, T. Legero, U. Sterr, F. Riehle, M. J. Martin, L. Chen, and J. Ye, *A sub-40-mHz-linewidth laser based on a silicon single-crystal optical cavity,* Nat. Photonics **6**, 687 (2012).

[81] G. Rempe, R. Lalezari, R. J. Thompson, and H. J. Kimble, *Measurement of ultralow losses in an optical interferometer,* Opt. Lett. **17**, 363 (1992).

[82] C. J. Hood, H. J. Kimble, and J. Ye, *Characterization of high-finesse mirrors: Loss, phase shifts, and mode structure in an optical cavity,* Phys. Rev. A **64**, 033804 (2001).

[83] R. J. Thompson, G. Rempe, and H. J. Kimble, *Observation of normal-mode splitting for an atom in an optical cavity,* Phys. Rev. Lett. **68**, 1132 (1992).

[84] J. McKeever, A. Boca, A. D. Boozer, J. R. Buck, and H. J. Kimble, *Experimental realization of a one-atom laser in the regime of strong coupling,* Nature **425**, 268 (2003).

[85] A. Stute, B. Casabone, P. Schindler, T. Monz, P. O. Schmidt, B. Brandstätter, T. E. Northup, and R. Blatt, *Tunable ion–photon entanglement in an optical cavity,* Nature **485**, 482 (2012).

[86] K. J. Vahala, *Optical microcavities,* Nature **424**, 839 (2003).

[87] H. Pfeifer, L. Ratschbacher, J. Gallego, C. Saavedra, A. Faßbender, A. Von Haaren, W. Alt, S. Hofferberth, M. Köhl, S. Linden, and D. Meschede, *Achievements and perspectives of optical fiber Fabry–Perot cavities,* Appl. Phys. B **128**, 29 (2022).

[88] M. Trupke, E. A. Hinds, S. Eriksson, E. A. Curtis, Z. Moktadir, E. Kukharenka, and M. Kraft, *Microfabricated high-finesse optical cavity with open access and small volume,* Appl. Phys. Lett. **87**, 211106 (2005).

[89] D. Hunger, T. Steinmetz, Y. Colombe, C. Deutsch, T. W. Hänsch, and J. Reichel, *A fiber Fabry–Perot cavity with high finesse,* New J. Phys. **12**, 065038 (2010).

[90] Y. Colombe, T. Steinmetz, G. Dubois, F. Linke, D. Hunger, and J. Reichel, *Strong atom–field coupling for Bose–Einstein condensates in an optical cavity on a chip,* Nature **450**, 272 (2007).

[91] J. Volz, R. Gehr, G. Dubois, J. Estève, and J. Reichel, *Measurement of the internal state of a single atom without energy exchange,* Nature **475**, 210 (2011).

[92] J. Gallego, W. Alt, T. Macha, M. Martinez-Dorantes, D. Pandey, and D. Meschede, *Strong Purcell Effect on a Neutral Atom Trapped in an Open Fiber Cavity,* Phys. Rev. Lett. **121**, 173603 (2018).

[93] B. Grinkemeyer, E. Guardado-Sanchez, I. Dimitrova, D. Shchepanovich, G. E. Mandopoulou, J. Borregaard, V. Vuletić, and M. D. Lukin, *Error-detected quantum operations with neutral atoms mediated by an optical cavity,* Science **387**, 1301 (2025).

[94] J. Wang, D.-Y. Huang, X.-L. Zhou, Z.-M. Shen, S.-J. He, Q.-Y. Huang, Y.-J. Liu, C.-F. Li, and G.-C. Guo, *Ultrafast High-Fidelity State Readout of Single Neutral Atom,* Phys. Rev. Lett. **134**, 240802 (2025).

[95] D. Najer, I. Söllner, P. Sekatski, V. Dolique, M. C. Löbl, D. Riedel, R. Schott, S. Starosielec, S. R. Valentin, A. D. Wieck, N. Sangouard, A. Ludwig, and R. J. Warburton, *A gated quantum dot strongly coupled to an optical microcavity,* Nature **575**, 622 (2019).

[96] N. Tomm, A. Javadi, N. O. Antoniadis, D. Najer, M. C. Löbl, A. R. Korsch, R. Schott, S. R. Valentin, A. D. Wieck, A. Ludwig, and R. J. Warburton, *A bright and fast source of coherent single photons,* Nat. Nanotechnol. **16**, 399 (2021).

[97] X. Ding, Y.-P. Guo, M.-C. Xu, R.-Z. Liu, G.-Y. Zou, J.-Y. Zhao, Z.-X. Ge, Q.-H. Zhang, H.-L. Liu, L.-J. Wang, M.-C. Chen, H. Wang, Y.-M. He, Y.-H. Huo, C.-Y. Lu, and J.-W. Pan, *High-efficiency single-photon source above the loss-tolerant threshold for efficient linear optical quantum computing,* Nat. Photon. **19**, 387 (2025).

[98] D. Aharonov and M. Ben-Or, *Fault-Tolerant Quantum Computation With Constant Error Rate,* arXiv:quant-ph/9906129 (1999).

[99] Y. Zhang, X. Ding, Y. Li, L. Zhang, Y.-P. Guo, G.-Q. Wang, Z. Ning, M.-C. Xu, R.-Z. Liu, J.-Y. Zhao, G.-Y. Zou, H. Wang, Y. Cao, Y.-M. He, C.-Z. Peng, Y.-H. Huo, S.-K. Liao, C.-Y. Lu, F. Xu, and J.-W. Pan, *Experimental Single-Photon Quantum Key Distribution Surpassing the Fundamental Weak Coherent-State Rate Limit,* Phys. Rev. Lett. **134**, 210801 (2025).

[100] M. Zou, Y.-M. He, Y. Huang, J.-Y. Zhao, B.-C. Li, Y.-P. Guo, X. Ding, M.-C. Xu, R.-Z. Liu, G.-Y. Zou, Z. Ning, X. You, H. Wang, W.-X. Pan, H.-T. Zhu, M.-Y. Zheng, X.-P. Xie, D. Qin, X. Jiang, Y.-H. Huo, Q. Zhang, C.-Y. Lu, X. Ma, T.-Y. Chen, and J.-W. Pan, *Realization of an untrusted intermediate relay architecture using a quantum dot single-photon source,* Nat. Phys. **21**, 1670 (2025).

[101] Y.-P. Guo, G.-Y. Zou, X. Ding, Q.-H. Zhang, M.-C. Xu, R.-Z. Liu, J.-Y. Zhao, Z.-X. Ge, L.-C. Peng, K.-M. Xu, Y.-Y. Lou, Z. Ning, L.-J. Wang, H. Wang, Y.-H. Huo, Y.-M. He, C.-Y. Lu, and J.-W. Pan, *Boosted fusion gates above the percolation threshold for scalable graph-state generation,* arXiv:2412.18882 (2024).

[102] D. Wang, H. Kelkar, D. Martin-Cano, D. Rattenbacher, A. Shkarin, T. Utikal, S. Götzinger, and V. Sandoghdar, *Turning a molecule into a coherent two-level quantum system,* Nat. Phys. **15**, 483 (2019).

[103] T. Hümmer, J. Noe, M. S. Hofmann, T. W. Hänsch, A. Högele, and D. Hunger, *Cavity-enhanced Raman microscopy of individual carbon nanotubes,* Nat. Commun. **7**, 12155 (2016).

[104] A. Borel, T. Habrant-Claude, F. Rapisarda, J. Reichel, S. K. Doorn, C. Voisin, and Y. Chassagneux, *Telecom Band Single-Photon Source Using a Grafted Carbon Nanotube Coupled to a Fiber Fabry–Perot Cavity in the Purcell Regime,* ACS Photonics **10**, 2839 (2023).

[105] L. Husel, J. Trapp, J. Scherzer, X. Wu, P. Wang, J. Fortner, M. Nutz, T. Hümmer, B. Polovnikov, M. Förg, D. Hunger, Y. Wang, and A. Högele, *Cavity-enhanced photon indistinguishability at room temperature and telecom wavelengths,* Nat. Commun. **15**, 3989 (2024).

[106] B. Merkel, A. Ulanowski, and A. Reiserer, *Coherent and Purcell-Enhanced Emission from Erbium Dopants in a Cryogenic High- Q Resonator,* Phys. Rev. X **10**, 041025 (2020).

[107] A. Ulanowski, O. Kuijpers, B. Merkel, A. Holzäpfel, and A. Reiserer, *Cavity-Enhanced Spectroscopy of Individual Nuclear Spins in a Dense Bath,* PRX Quantum **6**, 020344 (2025).

[108] J. Hessenauer, J. Körber, M. Ghezellou, J. Ul-Hassan, G. V. Astakhov, W. Knolle, J. Wrachtrup, and D. Hunger, *Cavity enhancement of V2 centers in 4H-SiC with a fiber-based Fabry–Perot microcavity,* Opt. Quantum **3**, 175 (2025).

[109] M. Ruf, M. Weaver, S. van Dam, and R. Hanson, *Resonant Excitation and Purcell Enhancement of Coherent Nitrogen-Vacancy Centers Coupled to a Fabry-Perot Microcavity,* Phys. Rev. Applied **15**, 024049 (2021).

[110] R. Zifkin, C. D. Rodríguez Rosenblueth, E. Janitz, Y. Fontana, and L. Childress, *Lifetime Reduction of Single Germanium-Vacancy Centers in Diamond via a Tunable Open Microcavity,* PRX Quantum **5**, 030308 (2024).

[111] G. Bayer, R. Berghaus, S. Sachero, A. B. Filipovski, L. Antoniuk, N. Lettner, R. Waltrich, M. Klotz, P. Maier, V. Agafonov, and A. Kubanek, *Optical driving, spin initialization and readout of single SiV- centers in a Fabry-Perot resonator,* Commun. Phys. **6**, 300 (2023).

[112] V. Yurgens, Y. Fontana, A. Corazza, B. J. Shields, P. Maletinsky, and R. J. Warburton, *Cavity-assisted resonance fluorescence from a nitrogen-vacancy center in diamond,* npj Quantum Inf. **10**, 112 (2024).

2

Background: Nitrogen- and Tin-Vacancy Centers in Diamond

”God made the bulk; the surface was invented by the devil.”
- Wolfgang Pauli

This chapter is about the properties of diamond color centers relevant to this thesis. We focus on the nitrogen- and tin-vacancy (NV and SnV) centers, which are investigated in the presented microcavity experiments. The following sections summarize how diamond color centers can be used for quantum information processing (qubit initialization, manipulation, and readout) and how spin-photon and spin-spin entanglement can be created. The collection of a resonant photon from the color center into a single-mode fiber determines the efficiency of this process. Hence, we summarize the individual contributions and give an overview of state-of-the-art systems with NV and SnV centers. This chapter closes with an outline of the experimental methods used to obtain control of a single diamond color center inside a microcavity.

2.1 Diamond as Host Material for Quantum Emitters

Diamond is the hardest known bulk material with outstanding thermal and optical properties. It is a wide band gap semiconductor (5.5 eV at room temperature [1]) and has a large optical transparency window spanning from deep-ultraviolet to the infrared region, with a refractive index of $n_d = 2.41$ at 637 nm [2]. In addition, diamond is chemically inert and bio-compatible, making it an appealing platform for quantum sensing applications. Highly pure, single-crystal diamonds can be synthetically grown on a single-crystal substrate using chemical vapor deposition (CVD). CVD-grown diamonds are usually used in quantum information experiments.

Diamond can host more than 500 color centers [3] (sometimes also called point defects), of which some show an efficient single photon emission [4], and the nitrogen-vacancy center is best studied so far. Over the last two decades, the group IV color centers have been explored, which include the silicon-, germanium-, tin-, and lead-vacancy centers [5]. Other studied color centers are the nickel-vacancy (NiV) center [6] or a chromium-related defect [7]. Color centers behave like quantum emitters and can be hosted by bulk diamond samples or nanodiamonds with a size of a few 100 nm or less [8].

Furthermore, diamond has a low spin-orbit coupling and ^{12}C constitutes with 98.9 % the most abundant, nuclear spin-free isotope [9]. Together with the very high Debye temperature, diamond provides an electrically and magnetically clean environment, which is favorable to preserving good optical and spin properties of the incorporated quantum emitters [10]. Such an environment is also called the "semiconductor vacuum" [11]. More information about the material properties of diamond can be found in Zaitsev [2] and in the context of quantum technologies presented by Rogers et al. [12].

The diamond samples used in this thesis are obtained from commercially available, synthetic, single-crystal, type IIa bulk diamonds, grown by CVD with a very low (< 5 ppb) nitrogen concentration.

2.2 The Nitrogen-Vacancy (NV) Center

The nitrogen-vacancy (NV) center in a diamond is a color center with atom-like properties. To form a NV center, two neighboring carbon atoms from the diamond crystal lattice are removed. One is replaced with a nitrogen atom, while the other lattice site remains vacant, as shown in Fig. 2.1 (a).

The NV center can be found in a neutrally-charged state (NV^0), which is formed by five electrons, two stemming from the nitrogen atom, and three from the carbon atoms closest to the vacancy. For the negatively-charged state (NV^-), an additional electron is captured from the environment. For most applications in quantum communication and sensing, the negatively-charged state is used, which is also detailed in the following. The neutrally-charged state is less explored, with the fine structure revealed in the last years [13] and a recent demonstration of coherent control of the orbital states with microwaves [14]. Unless stated otherwise, the term NV center refers in this thesis to the negatively charged NV center.

NV centers can be created probabilistically by increasing the density of vacancies or/and nitrogen atoms in the diamond sample, leading to a higher probability of NV centers being formed. Vacancies can be created by laser writing [15, 16], non-nitrogen ion implantation (such as carbon [17]) or electron irradiation [18–20]. Nitrogen can be incorporated into the diamond by ion implantation [21–24] or delta-doping [25, 26]. In addition, nitrogen is incorporated during the CVD diamond growth due to the remaining nitrogen concentrations during the growth process. It is also possible to create NV centers by a combination of methods such as delta-doping and focused electron irradiation [27]. The diamond sample is subsequently annealed at temperatures of 800 °C to 1200 °C (at low pressures of about 1×10^{-6} mbar). At temperatures of around 800 °C, vacancies become mobile and can combine with nitrogen atoms to NV centers [23], while higher temperatures additionally repair the crystal lattice damage.

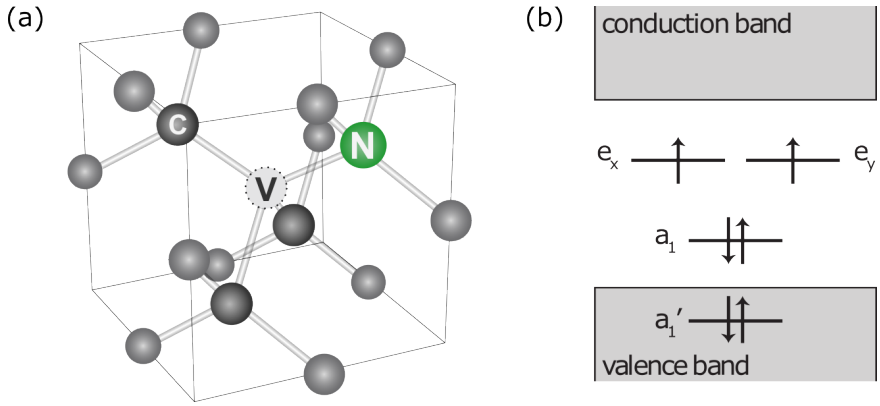

Figure 2.1: The nitrogen-vacancy (NV) center in diamond. (a) Diamond unit cell with the NV center, composed of a nitrogen (N) atom, substituting a carbon (C) atom, and a vacant (V) lattice site. The unit cell has a side length of 0.357 nm. The NV axis is aligned to the $\langle 111 \rangle$ crystallographic direction with a C_{3v} symmetry. Figure adapted from Ruf [28]. (b) Ground state molecular orbitals of the NV center. The lowest energy level is located inside the valence band, while the other levels lie within the diamond band gap. Figure adapted from Pfaff, Bernien [29, 30].

It is also demonstrated recently that high-pressure (order of Gigapascal), high-temperature (> 1200 °C) treated CVD-grown diamonds can contain optically-coherent NV centers, created from ingrown nitrogen impurities [31].
The NV centers in this thesis are created with electron irradiation and annealing, making use of the nitrogen naturally occurring in the CVD-grown diamond. This method leads to lower lattice damage and maintains good optical properties of the NV centers, compared to implantation [32, 33]. The optical coherence is retained in micrometer-thin diamond samples [34, 35].
Figure 2.1 (b) shows schematically the molecular orbitals of the ground state of the NV center. In the excited state, an electron from the a_1 orbital is promoted to the e_x or e_y. In both states, the unpaired electrons are placed within the diamond band gap, which isolates them from the solid-state environment and results in the atom-like spin coherence properties of the NV center [36, 37].
The NV center is a spin-1 system, and its electronic levels consist of a triplet and a short-lived (hundreds of nanoseconds) singlet state configuration (see Fig. 2.2 (a) and (b)). Upon excitation, the NV center can undergo a transition to the singlet state, which is referred to as intersystem crossing. The spin-triplet ground state splits due to spin-orbit interactions into two states ($m_s = 0$ and $m_s = \pm 1$) with a zero-field splitting of $D \approx 2.88\,\mathrm{GHz}$. An external magnetic field aligned to the axis of the NV center splits the degenerate $m_s = \pm 1$ levels through the Zeeman effect (Fig. 2.2 (e)). These electron spin levels can be used to encode a qubit.
The NV center couples to other spins in its proximity. The nitrogen atom of the NV center holds a nuclear spin with $I = 1$ (^{14}N with 99.6 % natural occurrence) or $I = 1/2$ (^{15}N with 0.4 % natural occurrence), resulting in additional splittings of the ground state levels in the range Megahertz. The NV center couples also to nearby nuclear spins of the stable ^{13}C isotope, occurring in the otherwise spinless ^{12}C diamond crystal lattice ($I = 1/2$, natural abundance of 1.1 %). The coupling via the hyperfine interaction depends on the distance and position of the ^{13}C spin to the NV center.
In the spin bath surrounding the NV center, other spins can be found, such as P1 centers [38, 39] (a dark defect formed by a nitrogen atom substituting a carbon atom) or pairs of ^{13}C nuclear spins [40].

2.2.1 Optical Properties of the NV Center

The cavity experiments in this thesis enhance the resonant optical emission of the NV center. We thus discuss in the following the optical properties in more detail.
The triplet ground and excited states of the NV center are connected by optical transitions, shown in Fig. 2.2 (b). A decay from the excited state can happen through the emission of a resonant photon at 637 nm in the zero-phonon line (ZPL). Next to this channel, the decay can also occur by the emission of a non-resonant photon at a longer wavelength, accompanied by the creation of a phonon. These photons are emitted into the so-called phonon sideband (PSB), which spans from 637 nm to about 800 nm (the emission spectrum of the NV center is shown in Fig. 2.3 (a)). Only resonant photons from the ZPL can be used to create entanglement, as the otherwise created phonon carries information about the spin state (in addition, ZPL photons are emitted at a well-defined wavelength, which is needed to make them indistinguishable from different emitters).

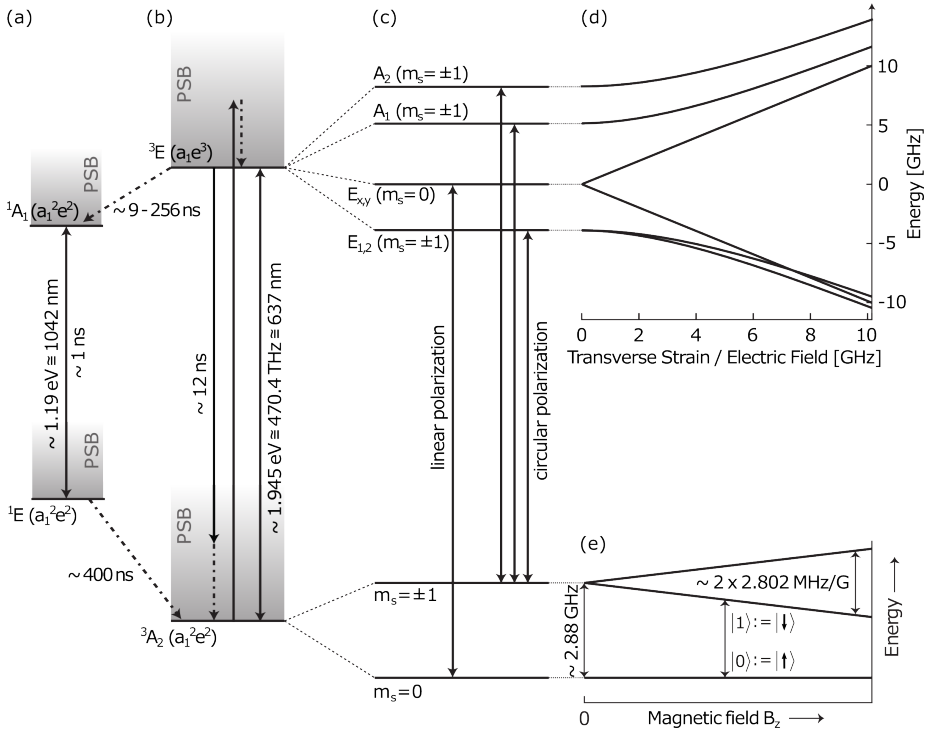

Figure 2.2: Electronic levels of the negatively charged NV center in diamond. Figure adapted from Pfaff, Bernien, Kalb, Ruf [28–30, 41]. (a) The NV centers ground and excited spin singlet states. (b) The ground and excited spin triplet states. The states of the singlet and the triplet are linked by optical transitions and can decay via emitting a resonant photon or off-resonantly via emitting a red-shifted photon and a phonon (shaded area indicating the phonon sideband, PSB). A spin-flip can occur via the intersystem crossing (triplet to singlet states), with a state-dependent decay rate of 9-256 ns [42]. The ground state of the singlet (^{1}E) decays to the degenerate triplet ground state ($^3A_2$) with a temperature-dependent rate, which is about 400 ns at cryogenic temperatures [42]. (c) Spin-orbit interactions split the triplet ground state ($^3A_2$) into two levels, while the excited state (^{3}E) is split into four levels by spin-spin and spin-orbit interactions, of which two are doubly degenerate. Selection rules define certain allowed transitions between the ground and excited states (linked by an arrow). The optical transitions are spin-selective for the $m_s = 0$ and $m_s = \pm 1$ states. (d) The excited state energy levels are shifted by transverse strain or electric fields, which do not affect the ground state energy levels to first order. (e) The $m_s = \pm 1$ states are split by an external magnetic field oriented along the NV axis (B_Z) due to the Zeeman effect. A qubit can be defined in the $m_s = 0$ ($|0\rangle$) and $m_s = -1$ ($|1\rangle$) spin states.

The Debye-Waller β_0 factor describes the ratio of resonant ZPL emission rate to the total radiative decay rate γ_{rad}:

$$\beta_0 = \frac{\gamma_{\text{ZPL}}}{\gamma_{\text{rad}}} = \frac{\gamma_{\text{ZPL}}}{\gamma_{\text{ZPL}} + \gamma_{\text{PSB}}}. \tag{2.1}$$

2

In this equation, γ_{ZPL} (γ_{PSB}) denotes the decay rate into the ZPL (PSB). The Debye-Waller factor of the NV center is $\beta_0 \approx 3\,\%$ [43, 44].
Most of the decay takes place through the ZPL and PSB, but the excited triplet state can also transition to the singlet state. The rate of this intersystem crossing is state-dependent, and the $m_s = \pm 1$ spin states decay with a higher probability to the singlet state, which further decays predominantly to the ground $m_s = 0$ spin state (Fig. 2.2 (a)). This effect can be used to polarize the spin population into the $m_s = 0$ ground state, as well as for optical readout, even with off-resonant excitation at room temperature [45].
Spin-spin and spin-orbit interactions splits the excited state ^{3}E into four levels [46] (see Fig. 2.2 (c)). Two of them are degenerate and lifted by external electric fields or with perpendicular strain to the NV center axis (Fig. 2.2 (d)). Electric fields along the NV center axis or axial strain overall shift the excited state energy. The optical transitions show a cyclic behavior with different cyclicities (number of optical excitation cycles until the NV center ends up in a different dark state), which depend on the strain of the NV center. For low strain, the E_x and E_y transitions connecting the $m_s = 0$ state have a high cyclicity, which can be used for optical readout and entanglement generation (see section 2.4). The excited state lifetime of the E_x and E_y states is around $\tau = 12\,\text{ns}$ for NV centers located more than tens of nanometers below the diamond surface [42, 44, 47]. This leads to an ideal Fourier transform-limited or "lifetime-limited" homogeneous linewidth of $\gamma = 13\,\text{MHz}$ [48], which can be calculated by $\gamma = 1/(2\pi\tau)$ [49]. Note that the lifetime is influenced by the local density of states (LDOS) and depends thereby on the depth of the NV center and the materials close to the surface. For example, shallow NV centers at a depth of 20 nm have shown lifetimes of 16.7 ns. Higher nitrogen concentrations (ppm level) can also influence the lifetime [50].
For remote entanglement generation (see section 2.5), optically coherent emitters are required, ideally with a transform-limited optical linewidth. Additional dephasing reduces the interference visibility in a Hong-Ou-Mandel experiment [51], which drastically diminishes entanglement rates and fidelities [49]. The additional dephasing of an emitter depends on the time scale of the noise τ_c, which can, for example, be created by magnetic or electric field fluctuations, compared to the optical lifetime τ. This can lead to a Gaussian broadened linewidth ($\tau_c < \tau$), discrete spectral jumps ($\tau_c \sim \tau$), or spectral wandering ($\tau_c > \tau$) [49]. Due to the lack of inversion symmetry, the NV center is first-order sensitive to electric field fluctuations, which can be caused by charge traps in the environment or occur at surfaces. The coherence of an optical linewidth can be quantified by optical Rabi oscillations [52].
The $E_{1,2}$ and $A_{1,2}$ levels of the NV center have a higher probability of decay through the singlet state [42, 47], which lowers their cyclicity. This can be used for optical spin-pumping to initialize the spin state into $m_s = 0$. A typical resonant laser scan at low temperatures resolving the different transition lines of an individual NV center is shown in Fig. 2.3 (b). The orbital states of the NV center mix with a T^5 dependence [53], which leads to a broad-

ening of the linewidth at higher temperatures (approximately above 10 K).
Next to the Debye-Waller factor, an important quantity influencing the brightness of the NV center (and quantum emitters in general) is the quantum efficiency η, which is defined as:

$$\eta = \frac{\gamma_{\text{rad}}}{\gamma} = \frac{\gamma_{\text{rad}}}{\gamma_{\text{rad}} + \gamma_{\text{nonrad}}}. \tag{2.2}$$

The quantum efficiency depends on the radiative decay rate γ_{rad} and the total decay rate γ, which is the sum of the radiative γ_{rad} and non-radiative decay rate γ_{nonrad}. It is a property of the NV center, but can also be influenced by the photonic environment, affected by the refractive index of the materials surrounding the NV center. For example, NV centers in nanodiamonds can show a quite different quantum efficiency [54, 55] than those hosted in bulk diamonds with larger distances (micrometers) to the next surface. A value of $\eta \gtrsim 0.86$ is estimated by measurements of shallow implanted NV centers [56], and usually a quantum efficiency of unity is assumed for NV centers in bulk diamonds. With the Debye-Waller factor and the quantum efficiency, the total resonant efficiency of the photonic interface of the NV center can be quantified to [43, 44]:

$$\xi_{\text{NV}} = \eta \times \beta_0 \approx 0.03. \tag{2.3}$$

For quantum networking applications, this number is an important figure of merit because only this fraction of light can be used for entanglement generation. Further details about the NV center can be found in Refs. [57–59].

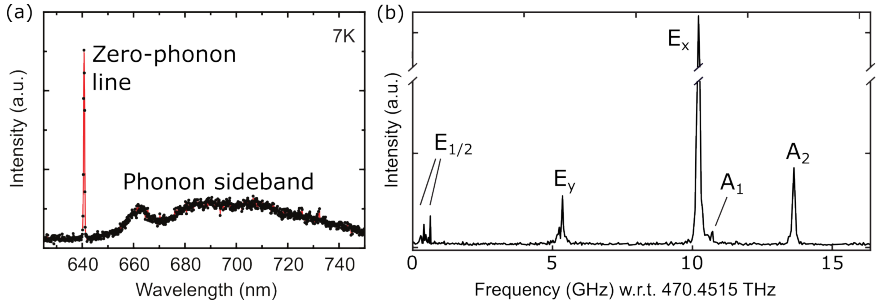

Figure 2.3: Optical properties of the NV center at cryogenic temperatures. (a) Spectrum of the NV photoluminescence under off-resonant excitation. The resonant zero-phonon line (ZPL) around 637 nm with the red-detuned PSB emission to longer wavelengths is visible. Figure adapted from Van der Sar [45]. (b) Typical photoluminescence laser excitation scan of a single NV center at cryogenic temperature, revealing the excited state fine structure. Light emitted from the NV center is detected in the PSB. The single ZPL line from (a) splits into a fine structure of multiple optical transitions connecting different electronic levels of the NV center, which are shown in Fig. 2.2 (c). The distance between the spin-conserving E_x and E_y lines can be used to determine the transversal strain. Figure adapted from Pfaff [29].

2.3 The Tin-Vacancy (SnV) Center

Similar to the NV center, the tin-vacancy (SnV) center is an atom-like color center in diamond. It is created by a single tin atom replacing two carbon atoms [60, 61]. The SnV center belongs to diamond color centers formed by group-IV elements of the periodic table (stable elements are silicon, germanium, tin, and lead). From these color centers, the silicon-vacancy (SiV) center is experimentally the most studied system with integration into nanophotonic cavities combined with qubit control of the electron and isotope nuclear spin [62] and remote entanglement between two SiV centers hosted in nanophotonic cavities [63]. For the germanium-vacancy (GeV) center, nanophotonic integration [64, 65] and control of the electron [66] and nuclear spin [67] have been demonstrated separately. In contrast, the lead-vacancy (PbV) center [68] is in an earlier stage, with a recent first demonstration of transform-limited photon emission [69].
The optically active, negatively-charged state of the SnV center is used for quantum applications and can be prepared in a heralded fashion[70]. Throughout this thesis, SnV center refers to the negatively-charged configuration, if not stated otherwise.
The tin atom is placed at an interstitial position between two missing carbon atoms of the diamond lattice. This split-vacancy configuration is shown in Fig. 2.4 (a), and results in D_{3d} symmetry [71], which makes the SnV center inversion symmetric (see Fig. 2.4 (a)). The inversion symmetry with no permanent electric dipole makes the SnV center insensitive to electric fields to first order. This is confirmed experimentally by the quadratic response of the SnV transition frequency to static electric fields due to the Stark effect [72–74]. In contrast to the NV center, the inversion symmetry makes the SnV center more robust against fluctuations in the charge environment and thereby more suitable for integration into nanophotonic structures [75, 76]. SnV centers can be created by tin ion implantation and subsequent high temperature annealing (≥ 1100 °C) under optionally high-pressure conditions [60, 77, 78].

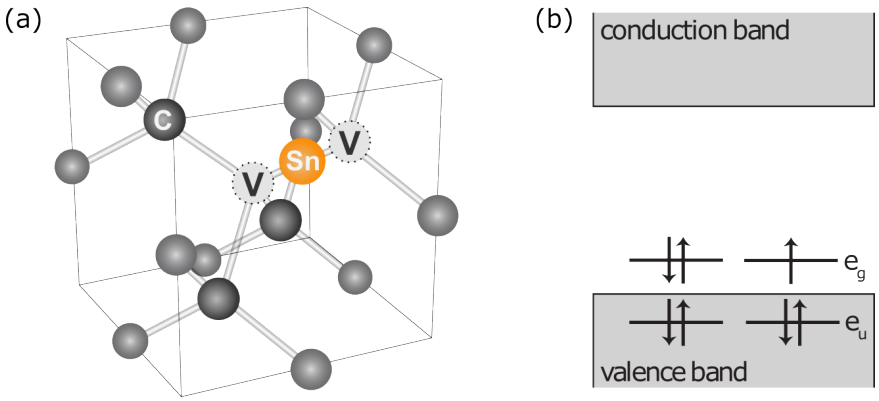

Figure 2.4: The tin-vacancy (SnV) center in diamond. (a) Structure of the SnV center inside the diamond unit cell, consisting of Carbon (C) atoms. The tin (Sn) atom is placed between two vacant (V) sides in a split-vacancy configuration. The figure is based on Ruf [28]. (b) Ground-state molecular orbitals of the SnV center within the band gap of diamond. The ground states are fully occupied, while one excited state is half-occupied. The diagram is based on Narita et al. [78].

The annealing step is used to repair the diamond crystal and leads to the migration of vacancies, forming the color center complex. Especially for larger impurity atoms, such as tin, shallow implantation followed by diamond overgrowth is favorable to reduce lattice damage [79]. In a recent study [80], site-selective creation and modification of single SnV centers have been demonstrated by laser activation with in-situ monitoring. More details about the creation of color centers in diamond can be found in Smith et al. [81].
The SnV ground state energy levels are placed within the diamond band gap (see Fig. 2.4 (b)). Under optical excitation, an electron is promoted from the ground state to the excited state, followed by back relaxation by emitting a photon [82]. The electronic level scheme of the SnV center is shown in Fig. 2.5. The SnV center is a spin-1/2 system. The ground and excited states have even (g) and odd (u) parity and are split by the Jahn-Teller effect and spin-orbit coupling into at least two spin-degenerate orbital branches [83]. Strain influences the splitting of the ground state (GS) and excited state (ES), with an unstrained GS splitting of 830 GHz and ES splitting of 2900 GHz [77]. Note that the exact electronic structure of the SnV center is still under investigation. In a magnetic field, the spin degeneracy is lifted by the Zeeman effect, which leads to eight spin-orbital energy levels with opposite spin. Each orbital branch has a different spin-orbit interaction strength, which results in a different spin quantization axis and an overlap between the spin states.
The Zeeman-split levels of the lower branch in the ground state can be used to define the electron qubit. Due to the opposite spin (denoted with plus and minus signs in the level scheme in Fig. 2.5) and orbital components, the direct qubit transition is forbidden. This can be overcome by mixing the orbital or spin component, which relaxes the selection rules. Crystal strain induces orbital mixing, which makes microwave spin control of the qubit transitions possible. This is demonstrated with moderately [84, 85] and highly strained [86, 87] SnV centers. In a recent theoretical study [88], the influence of strain and the direction of the static magnetic field for efficient microwave spin control of negatively charged group-IV color centers is discussed. Moreover, coherent control and entanglement of a ^{13}C nuclear spin qubit with the SnV center's electron spin have been demonstrated [89]. Alternatively, the qubit of the SnV center can also be controlled all-optically with two driving fields, via a stimulated Raman drive between the ground and excited states [90].
As indicated in the level scheme in Fig. 2.5, phonons couple between the orbital branches of the ground and excited states. Due to this effect, phonon transitions are the main source for optical and spin dephasing of the SnV center. The orbital branches have a certain energy splitting (Δ_{GS} and Δ_{GE}), so a direct way to reduce this effect is by lowering the population of phonons with enough energy. This can be achieved by cooling the diamond to low temperatures to freeze out these phonons. The most limiting factor is the ground state splitting Δ_{GS}, which sets an upper limit for the temperature. For the SnV center, the spin coherence is not limited by direct orbital transitions for temperatures less than ~ 1.5 K [91]. This is the maximum temperature allowed for operating the spin qubit with a reasonable coherence time.

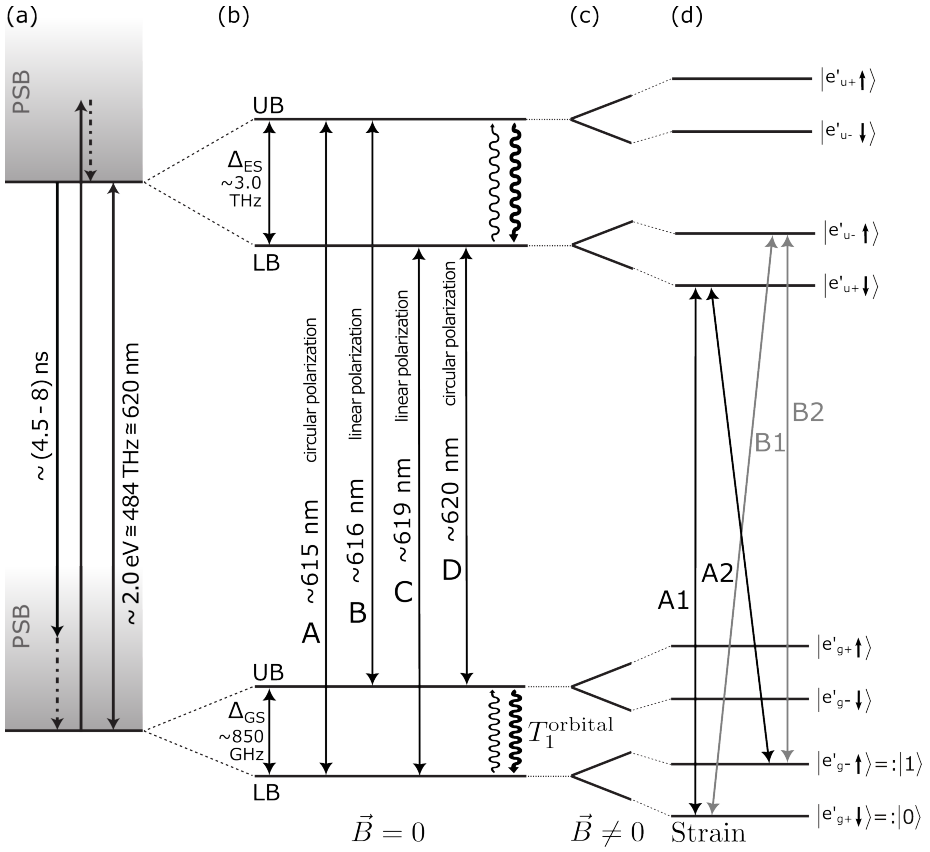

Figure 2.5: Electronic levels of the negatively charged SnV center in diamond. (a) At room temperature, the SnV center shows a pronounced ZPL around 620 nm accompanied by the PSB towards longer wavelengths up to ~ 700 nm. The excited state lifetime is influenced by the distance of the SnV center to the surface [77]. (b) The Jahn-Teller effect and spin-orbit coupling lead to a fine structure of four orbital states: the ground state and the excited state are each split into a lower branch (LB) and upper branch (UB) with splitting Δ_{GS} and Δ_{ES} for an unstrained emitter [92], respectively. Four ZPL transitions connect the different orbital states. In addition, temperature-dependent phonon processes with a relaxation time T_1^{orbital} can take place between the orbital levels. The electronic transition dipole of the C and B transitions is oriented along the $\langle 111 \rangle$ direction with the emission of linearly polarized light. The dipole of the A and D transitions is oriented in the perpendicular plane with the emission of circularly polarized light. (c) A magnetic field splits the orbital states into two states with opposite spin by the Zeeman effect. (d) Strain can further shift the levels. The qubit is defined in the two states of the ground state lower branch. Due to the magnetic field, the 619 nm C-transition is further split into two spin-conserving transitions A1 and B2, and two spin-flipping transitions A2 and B1.

As indicated on the right-most side of the level scheme in Fig. 2.5, strain alters the electronic states and thereby shifts the levels of the SnV center. Thus, strain can be used to tune the optical transition frequency of SnV centers, which is useful to make emitters indistinguishable in remote entanglement experiments. Micro-electro-mechanical strain tuning in integrated devices has been demonstrated with a range of up to 40 GHz [93–95]. Next to this, strain can also increase the ground state splitting Δ_{GS}, which allows for coherent spin control at elevated temperatures up to 4 K [86]. It has also been shown that static strain can be created deterministically in nanostructures by high-stress thin films deposited on the diamond surface [96].

Most commonly, SnV centers are created by implanting ^{120}Sn with zero nuclear spin [70, 95]. Next to this, spin-active tin isotopes can also be used, such as ^{117}Sn or ^{119}Sn, which gives access to a strongly-coupled spin-1/2 system [97, 98].

2.3.1 Optical Properties of the SnV Center

The SnV center has excellent optical properties due to the beneficial combination of high quantum efficiency and a large Debye-Waller factor. By comparing the fluorescence intensity of a single SnV center with other color centers, a quantum efficiency of $\eta \approx 0.8$ is estimated experimentally [60]. Similar to other group-IV color centers, the SnV center shows a large fraction of resonant photon emission. This is quantified by the Debye-Waller factor, which is experimentally determined to be $\beta_0 = 0.57$ [77], and is in agreement with theoretical calculations [71].

At room temperature, the SnV center shows a single ZPL with a nanometer-broad linewidth due to dephasing caused by temperature-induced phonon processes. The ZPL is centered around 620 nm (see, for example, off-resonant spectrum in Fig. 2.6 (b) inset). The fine structure of the ZPL into four peaks becomes resolvable by cooling to temperatures below about 100 K, where the ZPL also shifts to slightly lower wavelengths [77]. The population of the excited state in the upper branch is negligible at cryogenic temperatures, which leads to the suppression of the optical transitions A and B. At temperatures below 10 K, only the ZPL C and D transitions can be resolved [60, 77]. The spectral linewidth of the ZPL C transition narrows down with a T^3 power law [77] (shown in Fig. 2.6 (b)), and lifetime-limited linewidth values can be observed for temperatures below 6 K [92]. This temperature is low enough to make use of the SnV center for optical experiments, for example, as a source for single photons or to demonstrate coherent effects in a cavity, as presented in Chapter 6 of this thesis. The ZPL C transition can be further split by a magnetic field as shown in Fig. 2.6 (b).

Depending on the depth of the emitter inside the diamond, excited state lifetimes of the ZPL C transition between 4.5 to 8 ns can be found [77]. This corresponds to a transform-limited linewidth of 35 MHz to 20 MHz, which has been observed in bulk diamond [92] and in nanophotonic structures [75, 76, 99]. Simulations of the linewidth broadening of SnV centers depending on the distance to a planar surface and the density of charge traps can be found in Pieplow et al. [100].

The inhomogeneous broadening of the SnV center's ZPL transitions depends highly on the fabrication process. For SnV centers, generated by angled implantation and subsequent low-pressure ($\sim 1 \times 10^{-6}$ mbar) annealing up to 1100 °C, an inhomogeneous distribution of tens of Gigahertz is obtained [95] (see also SnV centers used in Chapter 6). In a recent

study [74], SnV ions are implanted along the crystal channels with a 0 ° angle. At the cost of a larger implantation straggle, this reduces the implantation-induced crystal damage and results in a narrower spectral distribution of about 4 GHz, which allowed the demonstration of two-photon quantum interference from two remote SnV centers [74]. It is also shown, that high temperature (2100 °C) annealing combined with high pressure (7.7 GPa) can lead to a highly reduced inhomogeneous distribution [77, 78].
The multiple ZPL transitions of the SnV center can be considered by an orbital branching ratio α of a specific ZPL decay versus the total ZPL decay. For the ZPL C transition, which is the relevant transition for quantum applications, this is:

$$\alpha = \frac{\gamma_C}{\gamma_{ZPL}}. \tag{2.4}$$

The exact value of the branching ratio is unclear and might also depend on the color centers' strain, but experimental values of $\alpha \approx 0.8$ have been determined by off-resonant photoluminescence spectra [101]. Taking the quantum efficiency η and the Debye-Waller factor β_0 from the beginning of this section also into account, we can calculate the total resonant efficiency for the photonic interface of the SnV center:

$$\xi_{SnV} = \eta \times \alpha \times \beta_0 \approx 0.8 \times 0.8 \times 0.57 = 0.36. \tag{2.5}$$

In Chapter 6 of this thesis, this value is also confirmed by optical measurements of a single SnV center inside an open microcavity. The SnV center is about one order of magnitude more efficient in resonant emission than the NV center. More details about the SnV center can be found in Refs. [91, 102].

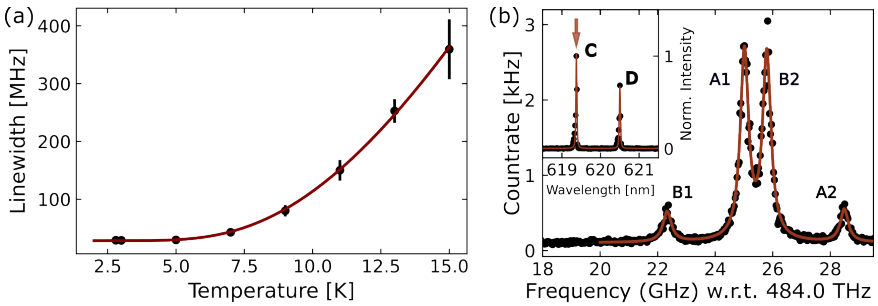

Figure 2.6: Optical properties of the SnV center at low temperatures in a magnetic field. Figure adapted from Pasini [91]. (a) Temperature dependence of the ZPL C transition linewidth. (b) Resonant laser scan over the ZPL C transition, split into the fine structure. The A1 and B2 transitions are spin-conserving, while the B1 and A2 transitions are spin-flipping (see also Fig. 2.5). To work with well-resolved, addressable optical transitions, A1 and B2 need to be separated by a distance much larger than their linewidth. Depending on the orientation, a magnetic field strength in the range of 10 mT to 100 mT is required. Inset: Spectrum of the C and D transitions of a single SnV center, measured with off-resonant excitation.

2.4 Quantum Control

This section summarizes the methods that are necessary to use the NV or SnV center for quantum information and quantum networking. We need a color center, which can be addressed by optical excitation, combined with a collection efficiency large enough to detect a reasonable number of photons for optical readout (depending on the cyclicity, see below). To make use of the spin-selective resonant excitation, it is further required to cool the color center to cryogenic temperatures. In addition, the proximity (typically a few tens of micrometers or less) to a microwave antenna is needed for high-fidelity control of the spin qubit of the color center. Furthermore, a magnetic field is required to encode the qubit states into the Zeeman-split levels, which is typically in the range of ten mT (hundred mT) for NV centers [103, 104] (SnV centers [84, 89]).

Charge-resonance (CR) checks can be employed in real-time before and after an experimental repetition to ensure that the color center is (and remains during the measurement) in the right charge state and on resonance with the resonant lasers used for initialization and readout. Further details are presented by Hermans [105] and the method is established for NV centers [106], SnV center [70] and V2 centers in silicon carbide [107].

The requirements to implement quantum computation and communication are summarized by the DiVincenzo criteria [108]. Most of the optical control methods have been developed for the manipulation of trapped ions [109], and are also used routinely for other solid-state systems such as color centers in silicon carbide [110] or silicon [111].

We focus here only on the electron spin qubit of the NV and SnV center, which, due to its coupling to optical transitions, is used as a central communication (or broker) qubit. A spin register can be formed by the nearby nitrogen [112, 113] or tin nuclear spin [98, 114] and surrounding carbon ^{13}C nuclear spins [89, 115, 116]. These qubits exhibit up to seconds-long coherence times and can work as memory qubits to store [40, 117, 118] and process [119–121] quantum states with high fidelities [104]. A recent review of coherent quantum control of spin qubits is also presented by Orphal-Kobin et al. [122].

Electron Spin Qubit

The electron spin of the NV and SnV center functions as a well-characterized qubit with spin dephasing times T_2^* (free induction decay) typically in the order of microseconds in diamond with a natural abundance of carbon isotopes [87, 123]. This can be prolonged by dynamical decoupling (repetitive application of driving pulses inverting the spin state) to a coherence time T_2 of around one second [37] (10 ms [87]) for the NV (SnV) center at cryogenic temperatures.

Qubit Initialization

The electron spin can be initialized into a certain state by optical pumping with a resonant laser on a transition, preferably with a low cyclicity (Fig. 2.7 (a)). For the NV center, these are typically the $E_{1/2}$ or $A_{1/2}$ transitions (see Fig. 2.2), while for the SnV center, the B1 or A2 transitions are used (Fig. 2.5). For the NV center, using the $E_{1/2}$ transitions is favorable, as the ground and excited states experience similar Zeeman shift, which requires most of the time only one light field [41]. Spin pumping times are on the order of microseconds for the NV center [124] ($\geq 100\,\mu$s for the SnV center [85, 86]), which leads to an initialization fidelity of 99% or higher [87, 125]. The fidelity of the state preparation can be estimated

by recording the time-trace of fluorescence decay during optical pumping [126]. The NV center can alternatively also be prepared in the $m_s = 0$ by applying a green laser pulse with a lower fidelity of around 90 % [125].

Qubit Manipulation

The electron qubit can be coherently manipulated by microwaves, which are delivered to the color center, for example, by a gold stripline deposited onto the diamond [125] or a bondwire close to the diamond surface [84]. The qubit frequency can be determined with an electron spin resonance measurement, in which the microwave frequency is swept and the electron spin qubit is readout [57]. When the resonance frequency is hit, part of the qubit population is transferred to a different spin state, which is dark for the readout (assuming a T_1 much longer than the measurement time). This measurement can be performed continuously, as shown in Fig. 2.7 (c) for a SnV center, or in a pulsed fashion, as shown in Fig. 2.7 (d) for a NV center. The latter method leads to a higher frequency resolution, which can be used to resolve the hyperfine nitrogen nuclear spin splitting of the NV center. Note that the microwave frequency is dependent on several factors, such as the magnetic field strength and direction. With the determined qubit frequency, the color center's spin can be coherently driven for a certain time, followed by a readout to observe Rabi oscillations as shown in Fig. 2.7 (e). Typical Rabi frequencies of up to tens of Megahertz [84, 123] are shown for both color centers, which leads to quantum gate operation times in the range of tens to hundreds of nanoseconds, much faster than the coherence times of the qubits. Note that the Rabi frequency is influenced by the distance of the color center to the microwave structure, the used microwave power, and for SnV centers also by the strain experienced by the color center [88]. Usually, a microwave amplifier with output powers in the range of watts is used for efficient driving. To address the three spin transitions independent of the nitrogen nuclear spin state (see Fig. 2.7 (d)), Hermite pulse envelopes can be used for the microwave pulses [127]. With a coplanar waveguide on the diamond surface, Rabi frequencies of up to 200 MHz have been observed for the NV center [128]. Single-qubit fidelities of above 99.99 % have been demonstrated for the NV center, which are among the most accurate quantum gates compared to other quantum information platforms [104, 129]. For the SnV center, π-pulse fidelities around 99 % have been shown [84, 86, 87].

Due to the typically higher achieved fidelities and easier experimental realization, microwave qubit control is most commonly used. However, for both the NV [130, 131] and the SnV center [90], the electron spin qubit can also be controlled all-optically. For NV centers, a combination of both via laser-activation and global microwave control has also been demonstrated [132].

Qubit Readout

Optical qubit readout can be achieved by resonantly driving one of the spin-selective, high-cycling transitions of the color center. These are the E_x or E_y transitions for the NV center (see Fig. 2.6 (b)) and the A1 or B2 transitions for SnV center (see Fig. 2.6 (a)). Typically, photons emitted from the color center into the PSB are collected for readout. A certain threshold is used to assign the detected counts to the binary qubit states [125], which leads to a dark state and a bright state. The readout fidelity of the dark state is typically limited

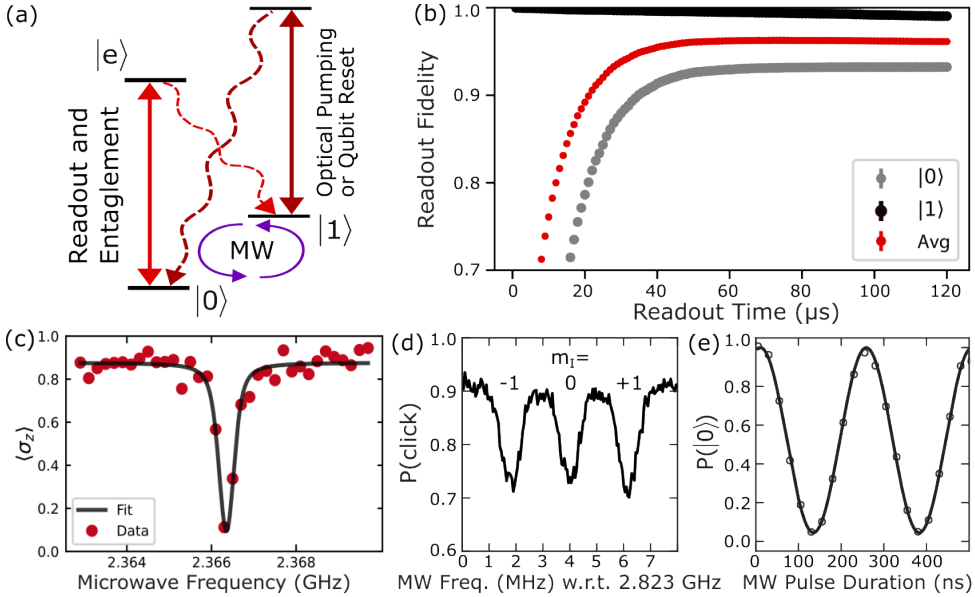

Figure 2.7: Quantum control of diamond color centers. (a) Simplified level scheme. The qubit is encoded in the ground state, which is split in a magnetic field by the Zeeman effect. The spin state can be coherently controlled by microwaves (MW). Qubit initialization is achieved by optical pumping the spin population to the ground state. A high-cyclicity transition of the spin ground state can be used for qubit readout and generating a photon entangled with the qubit state. (b) Readout of the qubit by exciting the highly cycling transition. The detection of a certain number of photons is assigned to a specific qubit state. Figure adapted from Hermans [105]. (c) Optically detected magnetic resonance (ODMR) of a SnV center, determining the microwave qubit frequency. Figure courtesy of Timo Dolné and Christopher Waas. (d) Electron spin resonance (ESR) measurement of a NV center to find the microwave qubit frequency (in this case, the transition between the $m_s = 0$ to $m_s = -1$ states). The state of the nitrogen nuclear spin is denoted by m_I. (e) Rabi spin oscillations of a NV center. The qubit is coherently driven between the ground and the excited state. A certain microwave pulse duration can be selected to drive the spin qubit by a π or $\pi/2$ rotation. Figures (d) and (e) adapted from Pfaff, Bernien [29, 30].

by dark counts of the detectors, while the readout fidelity of the bright state is limited by the cyclicity of the transition and the collection efficiency. For the case of the NV center, a transition into the (dark) metastable singlet state is also possible. When the qubit state can be read out with high fidelity in a single measurement repetition, the readout is referred to as being "single-shot" [133].

The cyclicity describes how many average optical excitations are needed until the color center decays to a different state. For low-strain NV centers, a cyclicity of ≈ 250 is found experimentally [125, 126, 134]. Note that the E_x and E_y transitions of the NV center have different cyclicity, and the E_x transition consistently has a higher cyclicity than the E_y transition [134]. For both the NV and the SnV center, the cyclicity depends on electric and magnetic fields, temperature, and strain. For the SnV center, a cyclicity of ≈ 1200 has been demonstrated for an aligned field, which allowed for readout of the qubit state by a single shot despite a low collection efficiency (in this work $\approx 0.2\,\%$) [89].

A typical qubit readout calibration, optimizing the individual readout fidelities of the dark and the bright qubit state, is shown in Fig. 2.7 (b). Typical readout times for both color

centers are on the order of tens of microseconds, with a single-shot readout fidelity of > 95 %[124] (> 87 %[85]) for the NV (SnV) center. The readout fidelity can also be enhanced by conditioning on multiple rounds of readouts[85, 103].
Next to resonant addressing of the optical transitions, qubit readout is also possible by applying a spin-to-charge conversion scheme. This enables single-shot readout even for a poor photon collection as demonstrated with NV centers [135, 136]. A review of spin readout techniques for NV centers is given by Hopper et al. [133].

Generating Spin-Photon Entanglement

Entanglement between the spins of two remote color centers can be created in two steps: first, each color center creates locally a photon entangled with the spin state. In the second step, these photons are interfered on a beam splitter, which erases the "which-path" information, and projects the total state into a spin-spin entangled state (see next section). An exemplary sequence to generate spin-photon entanglement [126], encoded in two different time bins, early $|E\rangle$ and late $|L\rangle$, is sketched in Fig. 2.8 (a) with the corresponding color center state shown in the level scheme in Fig. 2.8 (b). In the first step, the spin qubit is initialized in $|0\rangle_s$ by optical pumping, followed by a microwave $\pi/2$ pulse to generate an equal superposition state. In the following, s denotes the spin state and p the photon state with $|\text{vac}\rangle_p$ being the photonic vacuum state. We can write down the state as:

$$\frac{1}{\sqrt{2}}\left(|0\rangle_s + |1\rangle_s\right) \otimes |\text{vac}\rangle_p . \tag{2.6}$$

Next, an optical transition resonant with the $|0\rangle$ spin state is driven by a pulsed laser excitation. This only excites the color center to the state $|e\rangle$ if it is in the state $|0\rangle$. After spontaneous decay back to the ground state by emitting a photon, the following state is created:

$$\frac{1}{\sqrt{2}}\left(|0\rangle_s |1\rangle_p + |1\rangle_s |\text{vac}\rangle_p\right). \tag{2.7}$$

The photon number state is now entangled with the spin state of the color center. However, encoding into the photon number is not very robust, because losing a photon leads to an undetectable error. To avoid this, we can flip the spin state of the color center by a microwave π pulse, followed by a second resonant excitation round. This encodes the entanglement in the temporal mode (time bin) and leads to the spin-photon entangled state:

$$\frac{1}{\sqrt{2}}\left(|1\rangle_s |E\rangle_p + |0\rangle_s |L\rangle_p\right). \tag{2.8}$$

This state can be heralded by the detection of the photon in either the early $|E\rangle$ or the late $|L\rangle$ time bin. At the end of the sequence, an optional microwave $\pi/2$-pulse can be played to determine the readout basis, followed by optical readout with a resonant laser (can be the same laser as used to generate the single photon). An error in the protocol (an unsuccessful repetition) is detected by measuring no photon at all, and the efficiency of the protocol relies on the efficiency of collecting a single, resonant ZPL photon from the color center. The same sequences as shown in Fig. 2.8 is used for the spin-photon correlations

measurements in Chapter 7.
Spin-photon entanglement can be experimentally verified by measuring the different correlations between the photonic states and the spin state of the color center. For the time-bin encoding, this is achieved with an imbalanced Mach–Zehnder interferometer, whose path length difference is matched to the time difference between early and late photon emission.

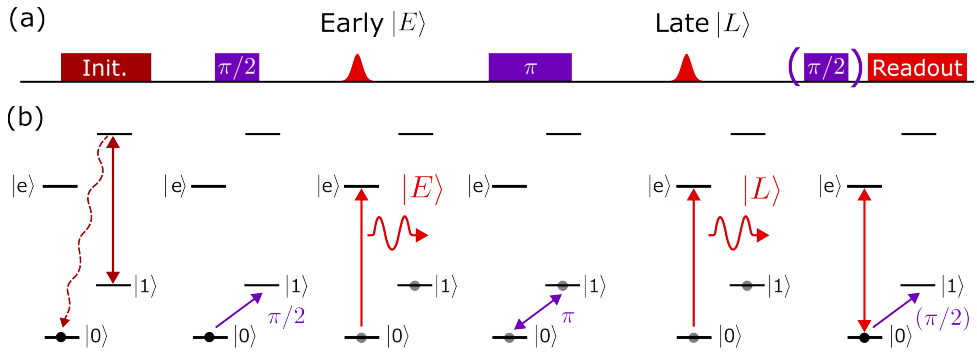

Figure 2.8: Protocol for generating time-bin encoded spin-photon entanglement. Figure based on Bernien et al. [126]. (a) Timing of optical (dark-red and red) and microwave (purple) signals. (b) Simplified level scheme with the qubit encoded into the two ground-state spin levels, connected by optical transitions. The state of equation (2.7) is generated after the first, bright red optical pulse (Early). After the second optical pulse, the spin-photon entangled state of equation (2.8) is created.

Entanglement with encoding in the photon polarization was first demonstrated with NV centers in a planar diamond sample [137]. Afterwards, experiments are realized with a NV center inside a solid-immersion lens (SIL) to enhance the photon collection efficiency. Time-bin encoded entanglement between a NV center and a telecom-band photon is demonstrated by down-converting the NV center ZPL photons [138]. Furthermore, the conversion of entanglement encoding from time-bin into polarization is shown [139], and high-speed electro-optical switching enabled the optimal routing of photons inside the interferometer for an improved success rate [140]. The same work demonstrated entanglement between the photon and the nitrogen nuclear spin of a NV center. Such hybrid entanglement is extended to carbon-13 nuclear spins by a recent work, combining it also with error correction [141]. Furthermore, the quantum teleportation-based state transfer from a photon to the electron spin qubit of the NV center is demonstrated by absorption recently [142].

2.5 Quantum Networking with Diamond Color Centers

We have discussed in the last section how spin-photon entanglement is created. Photons are a great mediator for entanglement, due to their flexible routing in an optical network and their simple transmission over longer distances at room temperature. The distance between the two color centers can be up to a few kilometers [106]. By down-converting [138, 143] the ZPL photons to telecom wavelengths (for example, the telecom L band at 1565 nm to 1625 nm), where much lower losses occur in optical fibers [144], a

distance of tens of kilometers can be covered [63, 145]. Frequency conversion can also be used to compensate for differences in the emission frequencies of the color centers [146]. We can use the spin-photon entanglement protocol, as introduced in the previous section, to also create spin-spin entanglement between two remote color centers. The protocol is applied to both color centers, and the ZPL photons are sent to a heralding station, where they are interfered on a beam splitter. Each output port of the beam splitter is connected to a single-photon detector. By heralding on a photon detection click pattern, where (exactly) one photon is detected in the early time bin and one in the late time bin, one of the following Bell states is generated with the electron spin states of the color centers:

$$\left|\Psi^{\pm}\right\rangle = \frac{1}{\sqrt{2}}\left(|01\rangle \pm |10\rangle\right). \tag{2.9}$$

The sign depends on the detector click pattern: when the same detectors click a photon $|\Psi^{+}\rangle$ is heralded, while different detector clicks herald $|\Psi^{-}\rangle$ [126]. This also gives the protocol the name *double-click protocol*, or sometimes also referred to as Barret-Kok protocol after the two inventors [147]. At the heralding station, the beam splitter erases the "which-path information". A strict requirement to succeed here is that both photons are indistinguishable. If photons are distinguishable (for example, by their frequency or polarization), it would be possible to discriminate between the two color centers [51], and entanglement would not be created. The indistinguishability of photons stemming from the two remote color centers can be characterized by the visibility in a two-photon quantum interference experiment, demonstrated with NV centers [148] and also recently with SnV centers [74].

After applying the protocol, the generation of the entangled state can be verified by measuring the correlations of the individual qubit quantum states in different bases or correlators. The double-click protocol has been used to successfully demonstrate the heralded spin-spin entanglement of two remote NV centers [126], which enabled the unconditional teleportation of a quantum state between two remote NV centers [149]. Furthermore, it unlocked the generation of remote entanglement between two NV centers spaced by 1.3 km and the first demonstration of a loophole-free Bell test [106].

After these initial demonstrations of spin-spin entanglement with NV centers, further works employed the single-click protocol, proposed by Cabrillo et al. [150] and Bose et al. [151]. This protocol requires only the interference of one photon from one of the two remote emitters, leading to higher entanglement rates and enabling the usage of quantum emitters with a relatively low resonant photon emission rate. However, the protocol requires phase-stabilization of the optical path between the nodes and comprises an inherent protocol error, limiting the fidelity. The single-click protocol is harnessed to demonstrate entanglement distillation between two remote NV centers [120] and the deterministic generation of entangled pairs within a certain time frame with a rate up to 39 Hz [124]. Furthermore, the protocol allowed the first realization of a NV center-based three-node quantum network [152], together with the demonstration of quantum teleportation between non-neighboring nodes of this network [103]. Recently, in combination with photon conversion to telecom wavelength, the heralded entanglement generation between two independently operated NV centers, separated by 10 km linked with 25 km of deployed fibers, is achieved [145].

The single- and double-click protocols belong to the class of emission-based entanglement protocols [153]. Another class of protocols uses a conditional gate between the spin of the color center and a photon. For example, this can be realized by the spin-state-dependent reflection from a photonic interface, such as an optical cavity. Recently, this protocol has been utilized to generate remote entanglement between two SiV centers inside nanophotonic cavities over a telecom network of 35 km of deployed fibers [63]. In this work, weak coherent states are used to encode time-bin qubits. For such reflection-based protocols, an optical cavity is essential to boost the cooperativity between the local color center spin and the photon mediating the entanglement.

2.6 Photon Detection

We have seen in the last section that the generation of entanglement critically depends on the measurement of a resonant ZPL photon emitted by the color center. Figure 2.9 summarizes the full chain of photon collection probabilities in color center-based optical setups. We assume here that the color center is prepared in the bright state and that the excitation laser is fully on resonance with the transition, which can be achieved by the already mentioned charge-resonance checks (section 2.4). The resonant photon detection chain can be broken down into:

- The first step is to excite the color center, which succeeds with a certain probability p_e. A straightforward way to do this is by excitation with a resonant, pulsed laser, whose pulse duration is sufficiently short compared to the excited state lifetime of the color center (nanoseconds). A short laser pulse is also required to avoid double excitations [48]. The color center decays by spontaneously emitting a photon, and it needs to be possible to discriminate between laser light and the emitted photons of the color center. The excitation pulse contains many photons, which leads to a highly demanding suppression of the laser pulse to avoid blinding the single-photon detector. This can be achieved by using a cross-polarization scheme, in which the linearly polarized emission of the color center is separated from the orthogonally polarized excitation laser [126]. Alternatively, the color center can also be excited in a different spatial mode. For example, this is demonstrated with a SnV center in a waveguide and orthogonal excitation from the top, leading to a suppression of over 60 dB of the excitation light [99]. Another method uses two detuned excitation pulses to ”swing up” the quantum emitters’ population (called SUPER scheme) [154]. Here, the excitation light can be filtered out spectrally. This scheme has been demonstrated with SnV centers [155]. The excitation probability p_e depends on several parameters, such as the laser power or pulse shape.

- The color center emits a resonant ZPL photon with a certain probability p_{zpl}, determined by its Debye-Waller factor, quantum efficiency, and eventual orbital branching ratio (see sections 2.2.1 and 2.3.1). This probability is ≈ 3 % (≈ 36 %) for the NV (SnV) center. The emission of a resonant photon can be enhanced with an optical cavity.

- The setup has a probability p_c to collect the emitted photon of the color center into an optical fiber (typically single-mode). In a planar diamond sample, collection ef-

ficiencies are usually in the percentage range [60, 156], due to the high index of refraction of diamond leading to total internal reflection. Non-resonant (such as a SILs) or resonant (such as a microcavity) photonic structures can be used to enhance the collection efficiency. For a SIL, the typical collection of photons with a high numerical aperture objective is around 15 % [106]. In practice, this number halves due to imperfections in the coupling of the ZPL photons from free space into the optical fiber.

- After collection, the photon is transmitted through the fiber with probability p_f. For 637 nm, the loss is about 8 dB/km (similar value for 620 nm) [106]. For efficient transmission over kilometer distances, conversion to telecom wavelengths is required [143]. For example, around 1560 nm (telecom C and L band), the fiber transmission losses reduce to below 0.2 dB/km [157]. Note that quantum frequency conversion adds additional losses, with state-of-the-art demonstrated external efficiencies of 43 % (28 %) for NV centers [158] (SnV centers [159]).

- Finally, a single photon detector will measure the photon with a probability p_{det}, determined by its efficiency and the coupling efficiency of the detector to the fiber. Typical values for silicon avalanche photodiodes in the red wavelength range are 70 % [160], while single-nanowire photon detectors (SNSPDs) can reach a detection efficiency of more than 95 % for 637 nm [152].

- Depending on the realized suppression of the excitation pulse, it might be necessary to employ additional time filtering to ensure that only photons emitted by the color center are detected. This can be achieved by using a fixed time window after the pulse, in which photon detection events are counted. This reduces the overall efficiency by another factor p_t.

For SIL-based NV center quantum network nodes [103, 106, 124, 152], the resonant ZPL photon detection efficiency p_p (ZPL detector click probability or "ZPL counts per shot") amounts to about 5×10^{-4} . Note that in these setups, the non-resonant PSB detection is still quite efficient, due to the emission of about 97 % of the light into the PSB (up to 10 % [152]), which enables single-shot readout of the qubit state with a high fidelity. SILs also enabled the quantum control of group-IV color centers such as silicon-vacancy [161, 162] or germanium-vacancy centers [66, 163].
For the SnV center, a resonant ZPL photon detection efficiency p_p of about 6×10^{-3} has been demonstrated with a packaged nanophotonic waveguide device, which is optically accessed by a tapered optical fiber [98]. An overview of resonant detection efficiencies of different solid-state quantum emitters can be found in Fig. 8.1 in the conclusion.
The collection of resonant ZPL photons directly determines the success of the entanglement generation protocols discussed in the last section. The success rate of the double-click protocol scales with the square of the probability of detecting a photon p_p^2, while the single-click protocol depends linearly on p_p with an inherent reduction of the entanglement fidelity. This limits entanglement generation rates to ~ 10 Hz (~ 10 mHz) for the single-click protocol [124] (double-click protocol [149]) with demonstrated fidelities of about 0.8 [103, 152] (0.9 [106, 149]).

An optical cavity can be used to increase the resonant photon detection of diamond color centers, which will be discussed in the next chapter.

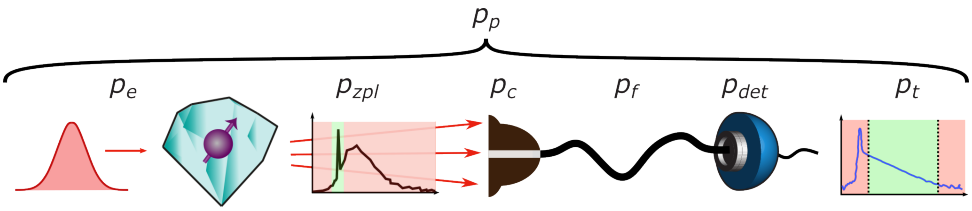

Figure 2.9: Efficiency of the photonic interface of a color center in diamond. Figure adapted from Ruf [28]. The overall detection efficiency of a resonant ZPL photon p_p (ZPL end-to-end efficiency) can be decomposed into multiple individual probabilities discussed in the text.

2.7 Experimental Methods for Quantum Control

This section summarizes the experimental control outside the cryostat needed to conduct the experiments in Chapters 5, 6, and 7. A detailed description of the low-vibration cryostat and the microcavity insert can be found in Chapter 5. In addition, each chapter lists the devices and components that are used. The results in Chapter 4 are conducted with different experimental setups, which are described or further referenced in this chapter.
To obtain quantum control over the SnV or NV center, a similar setup is used as in previous works [103, 152] with the microcavity replacing the SIL. This also makes the cavity setup compatible with the other SIL-based quantum nodes. The setup is summarized in Fig. 2.10, the key components are:

- Experiments are executed and saved by a central measurements computer and the Python 3 framework Quantum Measurement Infrastructure (QMI) [164]. QMI provides drivers for the different devices and enables the remote interfacing of devices connected to other computers in the network. Data is handled and processed with the Python package Quantify [165].
- The experimental logic is executed with a programmable microcontroller (MCU, Jäger Computergesteuerte Messtechnik Adwin Pro II) on a microsecond level. The MCU contains several modules for digital and analog output and input of voltage signals and it is used to record the counts of the single-photon detectors. This versatile approach can be used for simpler experiments, like resonant laser scans (for example, in Chapter 6), or more advanced experiments like the spin-photon correlations (Chapter 7), which also involve periodic checks of the cavity resonance frequency and polarization suppression of the excitation laser.
- The frequencies of the resonant lasers are stabilized with a wavemeter (HighFinesse WS-U) and feedback on a control voltage to the laser controllers.

- The intensities of the produced light fields are controlled by two cascaded acousto-optic modulators (AOMs, Gooch & Housego Fiber-Q 633 nm) with a rise/fall time of 25 ns. This ensures a high (> 100 dB) on-off laser ratio. The AOMs are operated by radio-frequency drivers (bkt Elektromechanik Zepto), which are controlled by the MCU. Due to the similar wavelength, the same modulators are used for the 620 nm and 637 nm lasers. To generate nanosecond-short optical pulses of the readout laser, an additional amplitude electro-optic modulator (EOM, Jenoptik AM635) is used with a rise time of 200 ps. The electric signal for the amplitude EOM is produced by a homebuilt, standalone pulse generator [166]. Details can be found in Wolfs [167].
- Experimental sequences with a nanosecond timing are executed by an arbitrary waveform generator (AWG, Tektronix AWG5014C), which produces the microwave signals by single-sideband modulation of a microwave source (Rohde & Schwarz SMBV100A). Sequences are orchestrated by the MCU on a microsecond level. The output of the microwave source is amplified (Mini-Circuits ZHL-50W-63+) and sent over a home-built microwave switch, controlled by the AWG, to the cryostat. The AWG can also control the acousto-optic modulators and trigger the standalone pulse generator. Details can be found in Wolfs [167].
- A timetagger (Picoquant Hydraharp 400) is used to record the signals of the single-photon detectors. This can optionally be triggered by the MCU or the AWG.
- The cavity fiber is placed on a nanometer level with a cryo positioning stage over a piezo controller (JPE Cryo Actuator Driver Module 2). For an even higher position accuracy, fine scanning piezo connected to a piezo amplifier (JPE Piezo Scanning Module) are used to set the cavity resonance frequency. The control signal is produced by the MCU, which allows integration with the conducted measurements.

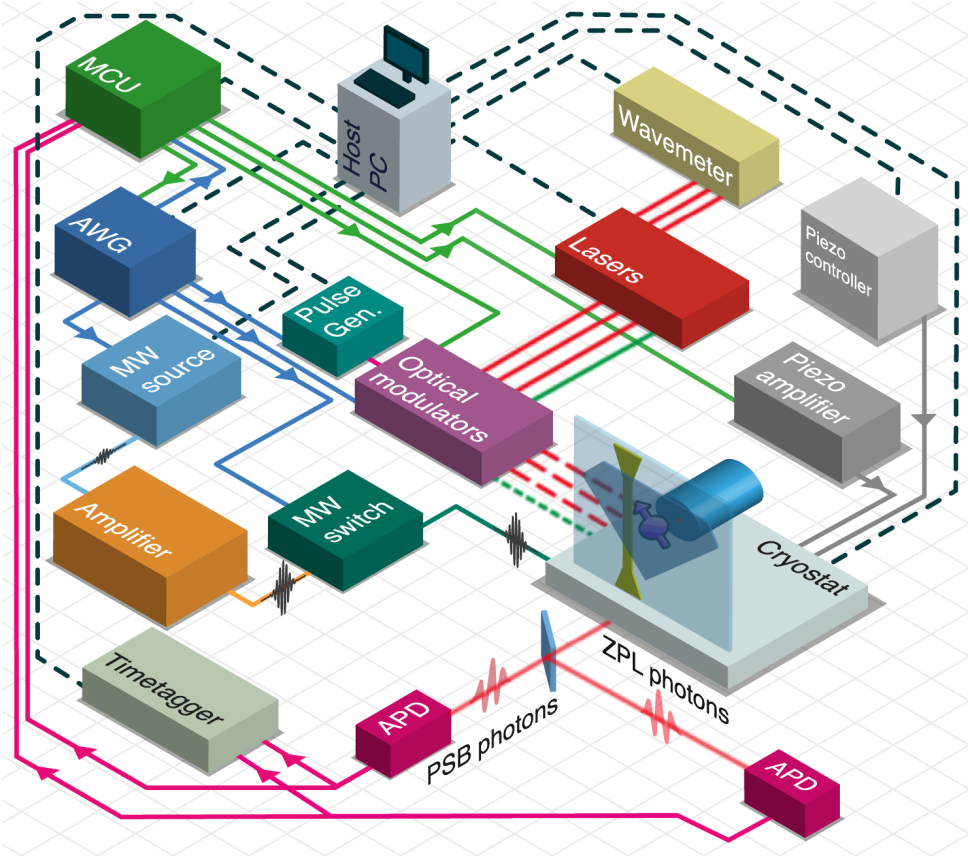

Figure 2.10: Orchestrating the quantum optics experiments. Figure based on Pompili [168]. The center of the setup is the diamond color center coupled to the open, fiber-based microcavity inside the cryostat. The color center is interfaced optically with different light fields for charge and spin initialization and readout. The spin is manipulated by microwave (MW) signals. Experiments take place by an interplay of devices on different time levels: milliseconds, controlled by the host PC; microseconds, controlled by the microcontroller (MCU); and nanoseconds, controlled by the arbitrary waveform generator (AWG). Fluorescence from the cavity-enhanced color center is separated into resonant, zero-phonon line (ZPL) and non-resonant, phonon-sidebands (PSB) photons, filtered, and detected by single-photon avalanche photodiode (APD) detectors. Readout of the detectors is achieved by the MCU (on the level of microseconds) or by the timetagger (sub-nanoseconds).

References

[1] I. Aharonovich, A. D. Greentree, and S. Prawer, *Diamond photonics,* Nat. Photonics **5**, 397 (2011).

[2] A. M. Zaitsev, *Optical Properties of Diamond* (Springer Berlin Heidelberg, Berlin, Heidelberg, 2001).

[3] A. M. Zaitsev, *Vibronic spectra of impurity-related optical centers in diamond,* Phys. Rev. B **61**, 12909 (2000).

[4] I. Aharonovich, S. Castelletto, D. A. Simpson, C.-H. Su, A. D. Greentree, and S. Prawer, *Diamond-based single-photon emitters,* Rep. Prog. Phys. **74**, 076501 (2011).

[5] C. Bradac, W. Gao, J. Forneris, M. E. Trusheim, and I. Aharonovich, *Quantum nanophotonics with group IV defects in diamond,* Nat. Commun. **10**, 5625 (2019).

[6] I. M. Morris, T. Lühmann, K. Klink, L. Crooks, D. Hardeman, D. J. Twitchen, S. Pezzagna, J. Meijer, S. S. Nicley, and J. N. Becker, *Lifetime-Limited and Tunable Emission from Single Charge-Stabilized Nickel Vacancy Centers in Diamond,* Phys. Rev. Lett. **135**, 043602 (2025).

[7] I. Aharonovich, S. Castelletto, B. C. Johnson, J. C. McCallum, D. A. Simpson, A. D. Greentree, and S. Prawer, *Chromium single-photon emitters in diamond fabricated by ion implantation,* Phys. Rev. B **81**, 121201 (2010).

[8] S. Sahoo, V. A. Davydov, V. N. Agafonov, and S. I. Bogdanov, *Hybrid quantum nanophotonic devices with color centers in nanodiamonds [Invited],* Opt. Mater. Express **13**, 191 (2023).

[9] G. Balasubramanian, P. Neumann, D. Twitchen, M. Markham, R. Kolesov, N. Mizuochi, J. Isoya, J. Achard, J. Beck, J. Tissler, V. Jacques, P. R. Hemmer, F. Jelezko, and J. Wrachtrup, *Ultralong spin coherence time in isotopically engineered diamond,* Nat. Mater. **8**, 383 (2009).

[10] D. D. Awschalom, R. Epstein, and R. Hanson, *The Diamond Age Diamond Age of Spintronics,* Sci. Am. **297**, 84 (2007).

[11] M. Steger, K. Saeedi, M. L. W. Thewalt, J. J. L. Morton, H. Riemann, N. V. Abrosimov, P. Becker, and H.-J. Pohl, *Quantum Information Storage for over 180 s Using Donor Spins in a ^{28}Si "Semiconductor Vacuum",* Science **336**, 1280 (2012).

[12] L. V. H. Rodgers, L. B. Hughes, M. Xie, P. C. Maurer, S. Kolkowitz, A. C. Bleszynski Jayich, and N. P. De Leon, *Materials challenges for quantum technologies based on color centers in diamond,* MRS Bull. **46**, 623 (2021).

[13] S. Baier, C. E. Bradley, T. Middelburg, V. V. Dobrovitski, T. H. Taminiau, and R. Hanson, *Orbital and Spin Dynamics of Single Neutrally-Charged Nitrogen-Vacancy Centers in Diamond,* Phys. Rev. Lett. **125**, 193601 (2020).

[14] H. Kurokawa, K. Wakamatsu, S. Nakazato, T. Makino, H. Kato, Y. Sekiguchi, and H. Kosaka, *Coherent electric field control of orbital state of a neutral nitrogen-vacancy center,* Nat. Commun. **15**, 4039 (2024).

[15] Y.-C. Chen, P. S. Salter, S. Knauer, L. Weng, A. C. Frangeskou, C. J. Stephen, S. N. Ishmael, P. R. Dolan, S. Johnson, B. L. Green, G. W. Morley, M. E. Newton, J. G. Rarity, M. J. Booth, and J. M. Smith, *Laser writing of coherent colour centres in diamond,* Nat. Photonics **11**, 77 (2017).

[16] V. Yurgens, J. A. Zuber, S. Flågan, M. De Luca, B. J. Shields, I. Zardo, P. Maletinsky, R. J. Warburton, and T. Jakubczyk, *Low-Charge-Noise Nitrogen-Vacancy Centers in Diamond Created Using Laser Writing with a Solid-Immersion Lens,* ACS Photonics **8**, 1726 (2021).

[17] T. Lühmann, R. John, R. Wunderlich, J. Meijer, and S. Pezzagna, *Coulomb-driven single defect engineering for scalable qubits and spin sensors in diamond,* Nat. Commun. **10**, 4956 (2019).

[18] G. Davies, S. C. Lawson, A. T. Collins, A. Mainwood, and S. J. Sharp, *Vacancy-related centers in diamond,* Phys. Rev. B **46**, 13157 (1992).

[19] E. Kim, V. M. Acosta, E. Bauch, D. Budker, and P. R. Hemmer, *Electron spin resonance shift and linewidth broadening of nitrogen-vacancy centers in diamond as a function of electron irradiation dose,* Appl. Phys. Lett. **101**, 082410 (2012).

[20] D. Farfurnik, N. Alfasi, S. Masis, Y. Kauffmann, E. Farchi, Y. Romach, Y. Hovav, E. Buks, and N. Bar-Gill, *Enhanced concentrations of nitrogen-vacancy centers in diamond through TEM irradiation,* Appl. Phys. Lett. **111**, 123101 (2017).

[21] J. Meijer, B. Burchard, M. Domhan, C. Wittmann, T. Gaebel, I. Popa, F. Jelezko, and J. Wrachtrup, *Generation of single color centers by focused nitrogen implantation,* Appl. Phys. Lett. **87**, 261909 (2005).

[22] J. R. Rabeau, P. Reichart, G. Tamanyan, D. N. Jamieson, S. Prawer, F. Jelezko, T. Gaebel, I. Popa, M. Domhan, and J. Wrachtrup, *Implantation of labelled single nitrogen vacancy centers in diamond using N15,* Appl. Phys. Lett. **88**, 023113 (2006).

[23] Y. Chu, N. De Leon, B. Shields, B. Hausmann, R. Evans, E. Togan, M. J. Burek, M. Markham, A. Stacey, A. Zibrov, A. Yacoby, D. Twitchen, M. Lončar, H. Park, P. Maletinsky, and M. Lukin, *Coherent Optical Transitions in Implanted Nitrogen Vacancy Centers,* Nano Lett. **14**, 1982 (2014).

[24] S. Chakravarthi, C. Pederson, Z. Kazi, A. Ivanov, and K.-M. C. Fu, *Impact of surface and laser-induced noise on the spectral stability of implanted nitrogen-vacancy centers in diamond,* Phys. Rev. B **104**, 085425 (2021).

[25] K. Ohno, F. Joseph Heremans, L. C. Bassett, B. A. Myers, D. M. Toyli, A. C. Bleszynski Jayich, C. J. Palmstrøm, and D. D. Awschalom, *Engineering shallow spins in diamond with nitrogen delta-doping,* Appl. Phys. Lett. **101**, 082413 (2012).

[26] J. C. Lee, D. O. Bracher, S. Cui, K. Ohno, C. A. McLellan, X. Zhang, P. Andrich, B. Alemán, K. J. Russell, A. P. Magyar, I. Aharonovich, A. Bleszynski Jayich, D. Awschalom, and E. L. Hu, *Deterministic coupling of delta-doped nitrogen vacancy centers to a nanobeam photonic crystal cavity,* Appl. Phys. Lett. **105**, 261101 (2014).

[27] C. A. McLellan, B. A. Myers, S. Kraemer, K. Ohno, D. D. Awschalom, and A. C. Bleszynski Jayich, *Patterned Formation of Highly Coherent Nitrogen-Vacancy Centers Using a Focused Electron Irradiation Technique,* Nano Lett. **16**, 2450 (2016).

[28] M. Ruf, *Cavity-enhanced quantum network nodes in diamond*, Ph.D. thesis, Delft University of Technology (2021).

[29] W. Pfaff, *Quantum measurement and entanglement of spin quantum bits in diamond*, Ph.D. thesis, Delft University of Technology (2013).

[30] H. Bernien, *Control, measurement and entanglement of remote quantum spin registers in diamond*, Ph.D. thesis, Technische Universtiteit Delft (2014).

[31] Y.-H. Tang, X. Zhang, K.-Y. Liu, F. Xia, H. Zheng, X. Liu, X.-Y. Pan, H. Fan, and G.-Q. Liu, *Optically coherent nitrogen-vacancy centers in high-pressure-high-temperature-treated diamonds,* Phys. Rev. Applied **23**, 054092 (2025).

[32] S. B. Van Dam, M. Walsh, M. J. Degen, E. Bersin, S. L. Mouradian, A. Galiullin, M. Ruf, M. IJspeert, T. H. Taminiau, R. Hanson, and D. R. Englund, *Optical coherence of diamond nitrogen-vacancy centers formed by ion implantation and annealing,* Phys. Rev. B **99**, 161203 (2019).

[33] M. Kasperczyk, J. A. Zuber, A. Barfuss, J. Kölbl, V. Yurgens, S. Flågan, T. Jakubczyk, B. Shields, R. J. Warburton, and P. Maletinsky, *Statistically modeling optical linewidths of nitrogen vacancy centers in microstructures,* Phys. Rev. B **102**, 075312 (2020).

[34] M. Ruf, M. IJspeert, S. van Dam, N. de Jong, H. van den Berg, G. Evers, and R. Hanson, *Optically Coherent Nitrogen-Vacancy Centers in Micrometer-Thin Etched Diamond Membranes,* Nano Lett. **19**, 3987 (2019).

[35] V. Yurgens, A. Corazza, J. A. Zuber, M. Gruet, M. Kasperczyk, B. J. Shields, R. J. Warburton, Y. Fontana, and P. Maletinsky, *Spectrally stable nitrogen-vacancy centers in diamond formed by carbon implantation into thin microstructures,* Appl. Phys. Lett. **121**, 234001 (2022).

[36] P. C. Maurer, G. Kucsko, C. Latta, L. Jiang, N. Y. Yao, S. D. Bennett, F. Pastawski, D. Hunger, N. Chisholm, M. Markham, D. J. Twitchen, J. I. Cirac, and M. D. Lukin, *Room-Temperature Quantum Bit Memory Exceeding One Second,* Science **336**, 1283 (2012).

[37] M. H. Abobeih, J. Cramer, M. A. Bakker, N. Kalb, M. Markham, D. J. Twitchen, and T. H. Taminiau, *One-second coherence for a single electron spin coupled to a multi-qubit nuclear-spin environment,* Nat. Commun. **9**, 2552 (2018).

[38] R. Hanson, F. M. Mendoza, R. J. Epstein, and D. D. Awschalom, *Polarization and Readout of Coupled Single Spins in Diamond,* Phys. Rev. Lett. **97**, 087601 (2006).

[39] M. J. Degen, S. J. H. Loenen, H. P. Bartling, C. E. Bradley, A. L. Meinsma, M. Markham, D. J. Twitchen, and T. H. Taminiau, *Entanglement of dark electron-nuclear spin defects in diamond,* Nat. Commun. **12**, 3470 (2021).

[40] H. P. Bartling, M. H. Abobeih, B. Pingault, M. J. Degen, S. J. H. Loenen, C. E. Bradley, J. Randall, M. Markham, D. J. Twitchen, and T. H. Taminiau, *Entanglement of Spin-Pair Qubits with Intrinsic Dephasing Times Exceeding a Minute,* Phys. Rev. X **12**, 011048 (2022).

[41] N. Kalb, *Diamond-based quantum networks with multi-qubit nodes*, Ph.D. thesis, Delft University of Technology (2018).

[42] M. L. Goldman, A. Sipahigil, M. W. Doherty, N. Y. Yao, S. D. Bennett, M. Markham, D. J. Twitchen, N. B. Manson, A. Kubanek, and M. D. Lukin, *Phonon-Induced Population Dynamics and Intersystem Crossing in Nitrogen-Vacancy Centers,* Phys. Rev. Lett. **114**, 145502 (2015).

[43] A. Faraon, C. Santori, Z. Huang, V. M. Acosta, and R. G. Beausoleil, *Coupling of Nitrogen-Vacancy Centers to Photonic Crystal Cavities in Monocrystalline Diamond,* Phys. Rev. Lett. **109**, 033604 (2012).

[44] D. Riedel, I. Söllner, B. J. Shields, S. Starosielec, P. Appel, E. Neu, P. Maletinsky, and R. J. Warburton, *Deterministic Enhancement of Coherent Photon Generation from a Nitrogen-Vacancy Center in Ultrapure Diamond,* Phys. Rev. X **7**, 031040 (2017).

[45] T. van der Sar, *Quantum control of single spins and single photons in diamond*, Ph.D. thesis, Delft University of Technology (2012).

[46] J. R. Maze, A. Gali, E. Togan, Y. Chu, A. Trifonov, E. Kaxiras, and M. D. Lukin, *Properties of nitrogen-vacancy centers in diamond: the group theoretic approach,* New J. Phys. **13**, 025025 (2011).

[47] N. Kalb, P. C. Humphreys, J. J. Slim, and R. Hanson, *Dephasing mechanisms of diamond-based nuclear-spin memories for quantum networks,* Phys. Rev. A **97**, 062330 (2018).

[48] S. L. N. Hermans, M. Pompili, L. D. Santos Martins, A. R-P Montblanch, H. K. C. Beukers, S. Baier, J. Borregaard, and R. Hanson, *Entangling remote qubits using the single-photon protocol: an in-depth theoretical and experimental study,* New J. Phys. **25**, 013011 (2023).

[49] G. Wolfowicz, F. J. Heremans, C. P. Anderson, S. Kanai, H. Seo, A. Gali, G. Galli, and D. D. Awschalom, *Quantum guidelines for solid-state spin defects,* Nat. Rev. Mater. **6**, 906 (2021).

[50] M. Capelli, L. Lindner, T. Luo, J. Jeske, H. Abe, S. Onoda, T. Ohshima, B. Johnson, D. A. Simpson, A. Stacey, P. Reineck, B. C. Gibson, and A. D. Greentree, *Proximal nitrogen reduces the fluorescence quantum yield of nitrogen-vacancy centres in diamond,* New J. Phys. **24**, 033053 (2022).

[51] C. K. Hong, Z. Y. Ou, and L. Mandel, *Measurement of subpicosecond time intervals between two photons by interference,* Phys. Rev. Lett. **59**, 2044 (1987).

[52] L. Robledo, H. Bernien, I. van Weperen, and R. Hanson, *Control and Coherence of the Optical Transition of Single Nitrogen Vacancy Centers in Diamond,* Phys. Rev. Lett. **105**, 177403 (2010).

[53] K.-M. C. Fu, C. Santori, P. E. Barclay, L. J. Rogers, N. B. Manson, and R. G. Beausoleil, *Observation of the Dynamic Jahn-Teller Effect in the Excited States of Nitrogen-Vacancy Centers in Diamond,* Phys. Rev. Lett. **103**, 256404 (2009).

[54] A. Mohtashami and A. Femius Koenderink, *Suitability of nanodiamond nitrogen–vacancy centers for spontaneous emission control experiments,* New J. Phys. **15**, 043017 (2013).

[55] M. Berthel, O. Mollet, G. Dantelle, T. Gacoin, S. Huant, and A. Drezet, *Photophysics of single nitrogen-vacancy centers in diamond nanocrystals,* Phys. Rev. B **91**, 035308 (2015).

[56] I. P. Radko, M. Boll, N. M. Israelsen, N. Raatz, J. Meijer, F. Jelezko, U. L. Andersen, and A. Huck, *Determining the internal quantum efficiency of shallow-implanted nitrogen-vacancy defects in bulk diamond,* Opt. Express **24**, 27715 (2016).

[57] F. Jelezko and J. Wrachtrup, *Single defect centres in diamond: A review,* phys. stat. sol. (a) **203**, 3207 (2006).

[58] M. W. Doherty, N. B. Manson, P. Delaney, F. Jelezko, J. Wrachtrup, and L. C. Hollenberg, *The nitrogen-vacancy colour centre in diamond,* Phys. Rep. **528**, 1 (2013).

[59] L. Childress and R. Hanson, *Diamond NV centers for quantum computing and quantum networks,* MRS Bull. **38**, 134 (2013).

[60] T. Iwasaki, Y. Miyamoto, T. Taniguchi, P. Siyushev, M. H. Metsch, F. Jelezko, and M. Hatano, *Tin-Vacancy Quantum Emitters in Diamond,* Phys. Rev. Lett. **119**, 253601 (2017).

[61] S. D. Tchernij, T. Herzig, J. Forneris, J. Küpper, S. Pezzagna, P. Traina, E. Moreva, I. P. Degiovanni, G. Brida, N. Skukan, M. Genovese, M. Jakšić, J. Meijer, and P. Olivero, *Single-Photon-Emitting Optical Centers in Diamond Fabricated upon Sn Implantation,* ACS Photonics **4**, 2580 (2017).

[62] P.-J. Stas, Y. Q. Huan, B. Machielse, E. N. Knall, A. Suleymanzade, B. Pingault, M. Sutula, S. W. Ding, C. M. Knaut, D. R. Assumpcao, Y.-C. Wei, M. K. Bhaskar, R. Riedinger, D. D. Sukachev, H. Park, M. Lončar, D. S. Levonian, and M. D. Lukin, *Robust multi-qubit quantum network node with integrated error detection,* Science **378**, 557 (2022).

[63] C. M. Knaut, A. Suleymanzade, Y.-C. Wei, D. R. Assumpcao, P.-J. Stas, Y. Q. Huan, B. Machielse, E. N. Knall, M. Sutula, G. Baranes, N. Sinclair, C. De-Eknamkul, D. S. Levonian, M. K. Bhaskar, H. Park, M. Lončar, and M. D. Lukin, *Entanglement of nanophotonic quantum memory nodes in a telecom network,* Nature **629**, 573 (2024).

[64] M. K. Bhaskar, D. D. Sukachev, A. Sipahigil, R. E. Evans, M. J. Burek, C. T. Nguyen, L. J. Rogers, P. Siyushev, M. H. Metsch, H. Park, F. Jelezko, M. Lončar, and M. D. Lukin, *Quantum Nonlinear Optics with a Germanium-Vacancy Color Center in a Nanoscale Diamond Waveguide,* Phys. Rev. Lett. **118**, 223603 (2017).

[65] N. H. Wan, T.-J. Lu, K. C. Chen, M. P. Walsh, M. E. Trusheim, L. De Santis, E. A. Bersin, I. B. Harris, S. L. Mouradian, I. R. Christen, E. S. Bielejec, and D. Englund, *Large-scale integration of artificial atoms in hybrid photonic circuits,* Nature **583**, 226 (2020).

[66] K. Senkalla, G. Genov, M. H. Metsch, P. Siyushev, and F. Jelezko, *Germanium Vacancy in Diamond Quantum Memory Exceeding 20 ms,* Phys. Rev. Lett. **132**, 026901 (2024).

[67] N. Grimm, K. Senkalla, P. J. Vetter, J. Frey, P. Gundlapalli, T. Calarco, G. Genov, M. M. Müller, and F. Jelezko, *Coherent Control of a Long-Lived Nuclear Memory Spin in a Germanium-Vacancy Multi-Qubit Node,* Phys. Rev. Lett. **134**, 043603 (2025).

[68] S. Ditalia Tchernij, T. Lühmann, T. Herzig, J. Küpper, A. Damin, S. Santonocito, M. Signorile, P. Traina, E. Moreva, F. Celegato, S. Pezzagna, I. P. Degiovanni, P. Olivero, M. Jakšić, J. Meijer, P. M. Genovese, and J. Forneris, *Single-Photon Emitters in Lead-Implanted Single-Crystal Diamond,* ACS Photonics **5**, 4864 (2018).

[69] P. Wang, L. Kazak, K. Senkalla, P. Siyushev, R. Abe, T. Taniguchi, S. Onoda, H. Kato, T. Makino, M. Hatano, F. Jelezko, and T. Iwasaki, *Transform-Limited Photon Emission from a Lead-Vacancy Center in Diamond above 10 K,* Phys. Rev. Lett. **132**, 073601 (2024).

[70] J. M. Brevoord, L. De Santis, T. Yamamoto, M. Pasini, N. Codreanu, T. Turan, H. K. Beukers, C. Waas, and R. Hanson, *Heralded initialization of charge state and optical-transition frequency of diamond tin-vacancy centers,* Phys. Rev. Applied **21**, 054047 (2024).

[71] G. Thiering and A. Gali, *Ab Initio Magneto-Optical Spectrum of Group-IV Vacancy Color Centers in Diamond,* Phys. Rev. X **8**, 021063 (2018).

[72] L. De Santis, M. Trusheim, K. Chen, and D. Englund, *Investigation of the Stark Effect on a Centrosymmetric Quantum Emitter in Diamond,* Phys. Rev. Lett. **127**, 147402 (2021).

[73] S. Aghaeimeibodi, D. Riedel, A. E. Rugar, C. Dory, and J. Vučković, *Electrical Tuning of Tin-Vacancy Centers in Diamond,* Phys. Rev. Appl. **15**, 064010 (2021).

[74] V. Bushmakin, O. v. Berg, C. Sauerzapf, S. Jayaram, A. Denisenko, V. Vorobyov, I. Gerhardt, D. Liu, and J. Wrachtrup, *Two-Photon Interference of Photons from Remote Tin-Vacancy Centers in Diamond,* arXiv:2412.17539 (2024).

[75] A. E. Rugar, C. Dory, S. Aghaeimeibodi, H. Lu, S. Sun, S. D. Mishra, Z.-X. Shen, N. A. Melosh, and J. Vučković, *Narrow-Linewidth Tin-Vacancy Centers in a Diamond Waveguide,* ACS Photonics **7**, 2356 (2020).

[76] M. Pasini, N. Codreanu, T. Turan, A. Riera Moral, C. F. Primavera, L. De Santis, H. K. C. Beukers, J. M. Brevoord, C. Waas, J. Borregaard, and R. Hanson, *Nonlinear Quantum Photonics with a Tin-Vacancy Center Coupled to a One-Dimensional Diamond Waveguide,* Phys. Rev. Lett. **133**, 023603 (2024).

[77] J. Görlitz, D. Herrmann, G. Thiering, P. Fuchs, M. Gandil, T. Iwasaki, T. Taniguchi, M. Kieschnick, J. Meijer, M. Hatano, A. Gali, and C. Becher, *Spectroscopic investigations of negatively charged tin-vacancy centres in diamond,* New J. Phys. **22**, 013048 (2020).

[78] Y. Narita, P. Wang, K. Ikeda, K. Oba, Y. Miyamoto, T. Taniguchi, S. Onoda, M. Hatano, and T. Iwasaki, *Multiple Tin-Vacancy Centers in Diamond with Nearly Identical Photon Frequency and Linewidth,* Phys. Rev. Applied **19**, 024061 (2023).

[79] A. E. Rugar, H. Lu, C. Dory, S. Sun, P. J. McQuade, Z.-X. Shen, N. A. Melosh, and J. Vučković, *Generation of Tin-Vacancy Centers in Diamond via Shallow Ion Implantation and Subsequent Diamond Overgrowth,* Nano Lett. **20**, 1614 (2020).

[80] X. Cheng, A. Thurn, G. Chen, G. S. Jones, J. E. Bennett, M. Coke, M. Adshead, C. P. Michaels, O. Balci, A. C. Ferrari, M. Atatüre, R. J. Curry, J. M. Smith, P. S. Salter, and D. A. Gangloff, *Laser activation of single group-IV colour centres in diamond,* Nat. Commun. **16**, 5124 (2025).

[81] J. M. Smith, S. A. Meynell, A. C. Bleszynski Jayich, and J. Meijer, *Colour centre generation in diamond for quantum technologies,* Nanophotonics **8**, 1889 (2019).

[82] J. Görlitz, D. Herrmann, P. Fuchs, T. Iwasaki, T. Taniguchi, D. Rogalla, D. Hardeman, P.-O. Colard, M. Markham, M. Hatano, and C. Becher, *Coherence of a charge stabilised tin-vacancy spin in diamond,* npj Quantum Inf. **8**, 45 (2022).

[83] C. Hepp, T. Müller, V. Waselowski, J. N. Becker, B. Pingault, H. Sternschulte, D. Steinmüller-Nethl, A. Gali, J. R. Maze, M. Atatüre, and C. Becher, *Electronic Structure of the Silicon Vacancy Color Center in Diamond,* Phys. Rev. Lett. **112**, 036405 (2014).

[84] E. I. Rosenthal, C. P. Anderson, H. C. Kleidermacher, A. J. Stein, H. Lee, J. Grzesik, G. Scuri, A. E. Rugar, D. Riedel, S. Aghaeimeibodi, G. H. Ahn, K. Van Gasse, and J. Vučković, *Microwave Spin Control of a Tin-Vacancy Qubit in Diamond,* Phys. Rev. X **13**, 031022 (2023).

[85] E. I. Rosenthal, S. Biswas, G. Scuri, H. Lee, A. J. Stein, H. C. Kleidermacher, J. Grzesik, A. E. Rugar, S. Aghaeimeibodi, D. Riedel, M. Titze, E. S. Bielejec, J. Choi, C. P. Anderson, and J. Vučković, *Single-Shot Readout and Weak Measurement of a Tin-Vacancy Qubit in Diamond,* Phys. Rev. X **14**, 041008 (2024).

[86] X. Guo, A. M. Stramma, Z. Li, W. G. Roth, B. Huang, Y. Jin, R. A. Parker, J. Arjona Martínez, N. Shofer, C. P. Michaels, C. P. Purser, M. H. Appel, E. M. Alexeev, T. Liu, A. C. Ferrari, D. D. Awschalom, N. Delegan, B. Pingault, G. Galli, F. J. Heremans, M. Atatüre, and A. A. High, *Microwave-Based Quantum Control and Coherence Protection of Tin-Vacancy Spin Qubits in a Strain-Tuned Diamond-Membrane Heterostructure,* Phys. Rev. X **13**, 041037 (2023).

[87] I. Karapatzakis, J. Resch, M. Schrodin, P. Fuchs, M. Kieschnick, J. Heupel, L. Kussi, C. Sürgers, C. Popov, J. Meijer, C. Becher, W. Wernsdorfer, and D. Hunger, *Microwave Control of the Tin-Vacancy Spin Qubit in Diamond with a Superconducting Waveguide,* Phys. Rev. X **14**, 031036 (2024).

[88] G. Pieplow, M. Belhassen, and T. Schröder, *Efficient microwave spin control of negatively charged group-IV color centers in diamond,* Phys. Rev. B **109**, 115409 (2024).

[89] H. K. C. Beukers, C. Waas, M. Pasini, H. B. Van Ommen, Z. Ademi, M. Iuliano, N. Codreanu, J. M. Brevoord, T. Turan, T. H. Taminiau, and R. Hanson, *Control of Solid-State Nuclear Spin Qubits Using an Electron Spin- 1 / 2,* Phys. Rev. X **15**, 021011 (2025).

[90] R. Debroux, C. P. Michaels, C. M. Purser, N. Wan, M. E. Trusheim, J. Arjona Martínez, R. A. Parker, A. M. Stramma, K. C. Chen, L. de Santis, E. M. Alexeev, A. C. Ferrari, D. Englund, D. A. Gangloff, and M. Atatüre, *Quantum Control of the Tin-Vacancy Spin Qubit in Diamond,* Phys. Rev. X **11**, 041041 (2021).

[91] M. Pasini, *Nanophotonics with Diamond Color Centers*, Ph.D. thesis, Delft University of Technology (2024).

[92] M. E. Trusheim, B. Pingault, N. H. Wan, M. Gündoğan, L. De Santis, R. Debroux, D. Gangloff, C. Purser, K. C. Chen, M. Walsh, J. J. Rose, J. N. Becker, B. Lienhard, E. Bersin, I. Paradeisanos, G. Wang, D. Lyzwa, A. R.-P. Montblanch, G. Malladi, H. Bakhru, A. C. Ferrari, I. A. Walmsley, M. Atatüre, and D. Englund, *Transform-Limited Photons From a Coherent Tin-Vacancy Spin in Diamond,* Phys. Rev. Lett. **124**, 023602 (2020).

[93] L. Li, L. D. Santis, I. B. W. Harris, K. C. Chen, Y. Gao, I. Christen, H. Choi, M. Trusheim, Y. Song, C. Errando-Herranz, J. Du, Y. Hu, G. Clark, M. I. Ibrahim, G. Gilbert, R. Han, and D. Englund, *Heterogeneous integration of spin–photon interfaces with a CMOS platform,* Nature **630**, 70 (2024).

[94] G. Clark, H. Raniwala, M. Koppa, K. Chen, A. Leenheer, M. Zimmermann, M. Dong, L. Li, Y. H. Wen, D. Dominguez, M. Trusheim, G. Gilbert, M. Eichenfield, and D. Englund, *Nanoelectromechanical Control of Spin–Photon Interfaces in a Hybrid Quantum System on Chip,* Nano Lett. **24**, 1316 (2024).

[95] J. M. Brevoord, L. G. C. Wienhoven, N. Codreanu, T. Ishiguro, E. van Leeuwen, M. Iuliano, L. De Santis, C. Waas, H. K. C. Beukers, T. Turan, C. Errando-Herranz, K. Kawaguchi, and R. Hanson, *Large-range tuning and stabilization of the optical transition of diamond tin-vacancy centers by in situ strain control,* Appl. Phys. Lett. **126** (2025).

[96] D. R. Assumpcao, C. Jin, M. Sutula, S. W. Ding, P. Pham, C. M. Knaut, M. K. Bhaskar, A. Panday, A. M. Day, D. Renaud, M. D. Lukin, E. Hu, B. Machielse, and M. Lončar, *Deterministic creation of strained color centers in nanostructures via high-stress thin films,* Appl. Phys. Lett. **123**, 244001 (2023).

[97] I. B. Harris, C. P. Michaels, K. C. Chen, R. A. Parker, M. Titze, J. Arjona Martínez, M. Sutula, I. R. Christen, A. M. Stramma, W. Roth, C. M. Purser, M. H. Appel, C. Li, M. E. Trusheim, N. L. Palmer, M. L. Markham, E. S. Bielejec, M. Atatüre, and D. Englund, *Hyperfine Spectroscopy of Isotopically Engineered Group-IV Color Centers in Diamond,* PRX Quantum **4**, 040301 (2023).

[98] R. A. Parker, J. Arjona Martínez, K. C. Chen, A. M. Stramma, I. B. Harris, C. P. Michaels, M. E. Trusheim, M. Hayhurst Appel, C. M. Purser, W. G. Roth, D. Englund, and M. Atatüre, *A diamond nanophotonic interface with an optically accessible deterministic electronuclear spin register,* Nat. Photon. **18**, 156 (2024).

[99] J. Arjona Martínez, R. A. Parker, K. C. Chen, C. M. Purser, L. Li, C. P. Michaels, A. M. Stramma, R. Debroux, I. B. Harris, M. Hayhurst Appel, E. C. Nichols, M. E. Trusheim, D. A. Gangloff, D. Englund, and M. Atatüre, *Photonic Indistinguishability of the Tin-Vacancy Center in Nanostructured Diamond,* Phys. Rev. Lett. **129**, 173603 (2022).

[100] G. Pieplow, C. G. Torun, C. Gurr, J. H. D. Munns, F. M. Herrmann, A. Thies, T. Pregnolato, and T. Schröder, *Quantum electrometer for time-resolved material science at the atomic lattice scale,* Nat. Commun. **16**, 6435 (2025).

[101] A. E. Rugar, S. Aghaeimeibodi, D. Riedel, C. Dory, H. Lu, P. J. McQuade, Z.-X. Shen, N. A. Melosh, and J. Vučković, *Quantum Photonic Interface for Tin-Vacancy Centers in Diamond,* Phys. Rev. X **11**, 031021 (2021).

[102] A. M. Stramma, *The tin-vacancy centre in diamond: a coherent spin-photon interface for quantum network nodes,* Ph.D. thesis, University of Cambridge (2024).

[103] S. L. N. Hermans, M. Pompili, H. K. C. Beukers, S. Baier, J. Borregaard, and R. Hanson, *Qubit teleportation between non-neighbouring nodes in a quantum network,* Nature **605**, 663 (2022).

[104] H. Bartling, J. Yun, K. Schymik, M. Van Riggelen, L. Enthoven, H. Van Ommen, M. Babaie, F. Sebastiano, M. Markham, D. Twitchen, and T. Taminiau, *Universal high-fidelity quantum gates for spin qubits in diamond,* Phys. Rev. Applied **23**, 034052 (2025).

[105] S. Hermans, *Quantum Networks using Spins in Diamond*, Ph.D. thesis, Delft University of Technology (2022).

[106] B. Hensen, H. Bernien, A. E. Dréau, A. Reiserer, N. Kalb, M. S. Blok, J. Ruitenberg, R. F. L. Vermeulen, R. N. Schouten, C. Abellán, W. Amaya, V. Pruneri, M. W. Mitchell, M. Markham, D. J. Twitchen, D. Elkouss, S. Wehner, T. H. Taminiau, and R. Hanson, *Loophole-free Bell inequality violation using electron spins separated by 1.3 kilometres,* Nature **526**, 682 (2015).

[107] G. L. Van De Stolpe, L. J. Feije, S. J. H. Loenen, A. Das, G. M. Timmer, T. W. De Jong, and T. H. Taminiau, *Check-probe spectroscopy of lifetime-limited emitters in bulk-grown silicon carbide,* npj Quantum Inf. **11**, 31 (2025).

[108] D. P. DiVincenzo, *The Physical Implementation of Quantum Computation,* Fortschr. Phys. **48**, 771 (2000).

[109] D. Leibfried, R. Blatt, C. Monroe, and D. Wineland, *Quantum dynamics of single trapped ions,* Rev. Mod. Phys. **75**, 281 (2003).

[110] C. P. Anderson, E. O. Glen, C. Zeledon, A. Bourassa, Y. Jin, Y. Zhu, C. Vorwerk, A. L. Crook, H. Abe, J. Ul-Hassan, T. Ohshima, N. T. Son, G. Galli, and D. D. Awschalom, *Five-second coherence of a single spin with single-shot readout in silicon carbide,* Sci. Adv. **8**, eabm5912 (2022).

[111] D. B. Higginbottom, A. T. K. Kurkjian, C. Chartrand, M. Kazemi, N. A. Brunelle, E. R. MacQuarrie, J. R. Klein, N. R. Lee-Hone, J. Stacho, M. Ruether, C. Bowness, L. Bergeron, A. DeAbreu, S. R. Harrigan, J. Kanaganayagam, D. W. Marsden, T. S. Richards, L. A. Stott, S. Roorda, K. J. Morse, M. L. W. Thewalt, and S. Simmons, *Optical observation of single spins in silicon,* Nature **607**, 266 (2022).

[112] T. Van Der Sar, Z. H. Wang, M. S. Blok, H. Bernien, T. H. Taminiau, D. M. Toyli, D. A. Lidar, D. D. Awschalom, R. Hanson, and V. V. Dobrovitski, *Decoherence-protected quantum gates for a hybrid solid-state spin register,* Nature **484**, 82 (2012).

[113] G. Waldherr, Y. Wang, S. Zaiser, M. Jamali, T. Schulte-Herbrüggen, H. Abe, T. Ohshima, J. Isoya, J. F. Du, P. Neumann, and J. Wrachtrup, *Quantum error correction in a solid-state hybrid spin register,* Nature **506**, 204 (2014).

[114] I. B. W. Harris, I. Christen, S. M. Patomäki, H. Raniwala, M. Sirotin, M. Colangelo, K. C. Chen, C. Errando-Herranz, D. J. Starling, R. Murphy, K. Shtyrkova, O. Medeiros, M. E. Trusheim, K. K. Berggren, P. B. Dixon, and D. Englund, *High-Fidelity Control of a Strongly Coupled Electro-Nuclear Spin-Photon Interface,* arXiv:2505.09267 (2025).

[115] C. E. Bradley, J. Randall, M. H. Abobeih, R. C. Berrevoets, M. J. Degen, M. A. Bakker, M. Markham, D. J. Twitchen, and T. H. Taminiau, *A Ten-Qubit Solid-State Spin Register with Quantum Memory up to One Minute,* Phys. Rev. X **9**, 031045 (2019).

[116] G. L. Van De Stolpe, D. P. Kwiatkowski, C. E. Bradley, J. Randall, M. H. Abobeih, S. A. Breitweiser, L. C. Bassett, M. Markham, D. J. Twitchen, and T. H. Taminiau,

Mapping a 50-spin-qubit network through correlated sensing, Nat. Commun. **15**, 2006 (2024).

[117] A. Reiserer, N. Kalb, M. S. Blok, K. J. M. Van Bemmelen, T. H. Taminiau, R. Hanson, D. J. Twitchen, and M. Markham, *Robust Quantum-Network Memory Using Decoherence-Protected Subspaces of Nuclear Spins,* Phys. Rev. X **6**, 021040 (2016).

[118] C. E. Bradley, S. W. De Bone, P. F. W. Möller, S. Baier, M. J. Degen, S. J. H. Loenen, H. P. Bartling, M. Markham, D. J. Twitchen, R. Hanson, D. Elkouss, and T. H. Taminiau, *Robust quantum-network memory based on spin qubits in isotopically engineered diamond,* npj Quantum Inf. **8**, 122 (2022).

[119] T. H. Taminiau, J. Cramer, T. van der Sar, V. V. Dobrovitski, and R. Hanson, *Universal control and error correction in multi-qubit spin registers in diamond,* Nat. Nanotechnol. **9**, 171 (2014).

[120] N. Kalb, A. A. Reiserer, P. C. Humphreys, J. J. W. Bakermans, S. J. Kamerling, N. H. Nickerson, S. C. Benjamin, D. J. Twitchen, M. Markham, and R. Hanson, *Entanglement distillation between solid-state quantum network nodes,* Science **356**, 928 (2017).

[121] M. H. Abobeih, Y. Wang, J. Randall, S. J. H. Loenen, C. E. Bradley, M. Markham, D. J. Twitchen, B. M. Terhal, and T. H. Taminiau, *Fault-tolerant operation of a logical qubit in a diamond quantum processor,* Nature **606**, 884 (2022).

[122] L. Orphal-Kobin, C. G. Torun, J. M. Bopp, G. Pieplow, and T. Schröder, *Coherent Microwave, Optical, and Mechanical Quantum Control of Spin Qubits in Diamond,* Adv. Quantum Tech. **8**, 2300432 (2024).

[123] G. De Lange, Z. H. Wang, D. Ristè, V. V. Dobrovitski, and R. Hanson, *Universal Dynamical Decoupling of a Single Solid-State Spin from a Spin Bath,* Science **330**, 60 (2010).

[124] P. C. Humphreys, N. Kalb, J. P. J. Morits, R. N. Schouten, R. F. L. Vermeulen, D. J. Twitchen, M. Markham, and R. Hanson, *Deterministic delivery of remote entanglement on a quantum network,* Nature **558**, 268 (2018).

[125] L. Robledo, L. Childress, H. Bernien, B. Hensen, P. F. A. Alkemade, and R. Hanson, *High-fidelity projective read-out of a solid-state spin quantum register,* Nature **477**, 574 (2011).

[126] H. Bernien, B. Hensen, W. Pfaff, G. Koolstra, M. S. Blok, L. Robledo, T. H. Taminiau, M. Markham, D. J. Twitchen, L. Childress, and R. Hanson, *Heralded entanglement between solid-state qubits separated by three metres,* Nature **497**, 86 (2013).

[127] H. K. C. Beukers, *Improving coherence of quantum memory during entanglement creation between nitrogen vacancy centres in diamond*, Master's thesis, University of Groningen (2019).

[128] G. D. Fuchs, V. V. Dobrovitski, D. M. Toyli, F. J. Heremans, and D. D. Awschalom, *Gigahertz Dynamics of a Strongly Driven Single Quantum Spin,* Science **326**, 1520 (2009).

[129] X. Rong, J. Geng, F. Shi, Y. Liu, K. Xu, W. Ma, F. Kong, Z. Jiang, Y. Wu, and J. Du, *Experimental fault-tolerant universal quantum gates with solid-state spins under ambient conditions,* Nat. Commun. **6**, 8748 (2015).

[130] C. G. Yale, B. B. Buckley, D. J. Christle, G. Burkard, F. J. Heremans, L. C. Bassett, and D. D. Awschalom, *All-optical control of a solid-state spin using coherent dark states,* Proc. Natl. Acad. Sci. U.S.A. **110**, 7595 (2013).

[131] Y. Chu, M. Markham, D. J. Twitchen, and M. D. Lukin, *All-optical control of a single electron spin in diamond,* Phys. Rev. A **91**, 021801 (2015).

[132] Y. Sekiguchi, K. Matsushita, Y. Kawasaki, and H. Kosaka, *Optically addressable universal holonomic quantum gates on diamond spins,* Nat. Photon. **16**, 662 (2022).

[133] D. Hopper, H. Shulevitz, and L. Bassett, *Spin Readout Techniques of the Nitrogen-Vacancy Center in Diamond,* Micromachines **9**, 437 (2018).

[134] O. S. M. Ubbens, *A Unified Model to Predict Excited State Cyclicity of Nitrogen Vacancy Centres in Diamond*, Master's thesis, Delft University of Technology (2022).

[135] D. M. Irber, F. Poggiali, F. Kong, M. Kieschnick, T. Lühmann, D. Kwiatkowski, J. Meijer, J. Du, F. Shi, and F. Reinhard, *Robust all-optical single-shot readout of nitrogen-vacancy centers in diamond,* Nat. Commun. **12**, 532 (2021).

[136] Q. Zhang, Y. Guo, W. Ji, M. Wang, J. Yin, F. Kong, Y. Lin, C. Yin, F. Shi, Y. Wang, and J. Du, *High-fidelity single-shot readout of single electron spin in diamond with spin-to-charge conversion,* Nat. Commun. **12**, 1529 (2021).

[137] E. Togan, Y. Chu, A. S. Trifonov, L. Jiang, J. Maze, L. Childress, M. V. G. Dutt, A. S. Sørensen, P. R. Hemmer, A. S. Zibrov, and M. D. Lukin, *Quantum entanglement between an optical photon and a solid-state spin qubit,* Nature **466**, 730 (2010).

[138] A. Tchebotareva, S. L. N. Hermans, P. C. Humphreys, D. Voigt, P. J. Harmsma, L. K. Cheng, A. L. Verlaan, N. Dijkhuizen, W. de Jong, A. Dréau, and R. Hanson, *Entanglement between a Diamond Spin Qubit and a Photonic Time-Bin Qubit at Telecom Wavelength,* Phys. Rev. Lett. **123**, 063601 (2019).

[139] R. Vasconcelos, S. Reisenbauer, C. Salter, G. Wachter, D. Wirtitsch, J. Schmiedmayer, P. Walther, and M. Trupke, *Scalable spin–photon entanglement by time-to-polarization conversion,* npj Quantum Inf. **6**, 9 (2020).

[140] J. Javadzade, M. Zahedian, F. Kaiser, V. Vorobyov, and J. Wrachtrup, *Efficient nuclear spin–photon entanglement with optical routing,* Phys. Rev. Applied **24**, 024059 (2025).

[141] X.-Y. Chang, P.-Y. Hou, W.-G. Zhang, X.-Q. Meng, Y.-F. Yu, Y.-N. Lu, Y.-Q. Liu, B.-X. Qi, D.-L. Deng, and L.-M. Duan, *Hybrid entanglement and bit-flip error correction in a scalable quantum network node,* Nat. Phys. **21**, 583 (2025).

[142] D. Ito, Y. Sekiguchi, R. Reyes, T. Fujiwara, T. Makino, H. Kato, and H. Kosaka, *Robust transfer of a quantum state from an absorbed photon into a diamond spin,* Opt. Lett. **50**, 5073 (2025).

[143] A. Dréau, A. Tchebotareva, A. E. Mahdaoui, C. Bonato, and R. Hanson, *Quantum Frequency Conversion of Single Photons from a Nitrogen-Vacancy Center in Diamond to Telecommunication Wavelengths,* Phys. Rev. Appl. **9**, 064031 (2018).

[144] A. Reiserer, *Colloquium : Cavity-enhanced quantum network nodes,* Rev. Mod. Phys. **94**, 041003 (2022).

[145] A. J. Stolk, K. L. Van Der Enden, M.-C. Slater, I. Te Raa-Derckx, P. Botma, J. Van Rantwijk, J. J. B. Biemond, R. A. J. Hagen, R. W. Herfst, W. D. Koek, A. J. H. Meskers, R. Vollmer, E. J. Van Zwet, M. Markham, A. M. Edmonds, J. F. Geus, F. Elsen, B. Jungbluth, C. Haefner, C. Tresp, J. Stuhler, S. Ritter, and R. Hanson, *Metropolitan-scale heralded entanglement of solid-state qubits,* Sci. Adv. **10**, eadp6442 (2024).

[146] A. Stolk, K. van der Enden, M.-C. Roehsner, A. Teepe, S. Faes, C. Bradley, S. Cadot, J. van Rantwijk, I. te Raa, R. Hagen, A. Verlaan, J. Biemond, A. Khorev, R. Vollmer, M. Markham, A. Edmonds, J. Morits, T. Taminiau, E. van Zwet, and R. Hanson, *Telecom-Band Quantum Interference of Frequency-Converted Photons from Remote Detuned NV Centers,* PRX Quantum **3**, 020359 (2022).

[147] S. D. Barrett and P. Kok, *Efficient high-fidelity quantum computation using matter qubits and linear optics,* Phys. Rev. A **71**, 060310 (2005).

[148] H. Bernien, L. Childress, L. Robledo, M. Markham, D. Twitchen, and R. Hanson, *Two-Photon Quantum Interference from Separate Nitrogen Vacancy Centers in Diamond,* Phys. Rev. Lett. **108**, 043604 (2012).

[149] W. Pfaff, B. J. Hensen, H. Bernien, S. B. van Dam, M. S. Blok, T. H. Taminiau, M. J. Tiggelman, R. N. Schouten, M. Markham, D. J. Twitchen, and R. Hanson, *Unconditional quantum teleportation between distant solid-state quantum bits,* Science **345**, 532 (2014).

[150] C. Cabrillo, J. I. Cirac, P. García-Fernández, and P. Zoller, *Creation of entangled states of distant atoms by interference,* Phys. Rev. A **59**, 1025 (1999).

[151] S. Bose, P. L. Knight, M. B. Plenio, and V. Vedral, *Proposal for Teleportation of an Atomic State via Cavity Decay,* Phys. Rev. Lett. **83**, 5158 (1999).

[152] M. Pompili, S. L. N. Hermans, S. Baier, H. K. C. Beukers, P. C. Humphreys, R. N. Schouten, R. F. L. Vermeulen, M. J. Tiggelman, L. dos Santos Martins, B. Dirkse, S. Wehner, and R. Hanson, *Realization of a multinode quantum network of remote solid-state qubits,* Science **372**, 259 (2021).

[153] H. K. Beukers, M. Pasini, H. Choi, D. Englund, R. Hanson, and J. Borregaard, *Remote-Entanglement Protocols for Stationary Qubits with Photonic Interfaces,* PRX Quantum **5**, 010202 (2024).

[154] T. K. Bracht, M. Cosacchi, T. Seidelmann, M. Cygorek, A. Vagov, V. M. Axt, T. Heindel, and D. E. Reiter, *Swing-Up of Quantum Emitter Population Using Detuned Pulses,* PRX Quantum **2**, 040354 (2021).

[155] C. G. Torun, M. Gökçe, T. K. Bracht, M. I. Monsalve, S. Benbouabdellah, Ö. O. Nacitarhan, M. E. Stucki, M. L. Markham, G. Pieplow, T. Pregnolato, J. H. D. Munns, D. E. Reiter, and T. Schröder, *SUPER and subpicosecond coherent control of an optical qubit in a tin-vacancy color center in diamond,* arXiv:2312.05246 (2023).

[156] J. P. Hadden, J. P. Harrison, A. C. Stanley-Clarke, L. Marseglia, Y.-L. D. Ho, B. R. Patton, J. L. O'Brien, and J. G. Rarity, *Strongly enhanced photon collection from diamond defect centers under microfabricated integrated solid immersion lenses,* Appl. Phys. Lett. **97**, 241901 (2010).

[157] K. Nagayama, M. Kakui, M. Matsui, T. Saitoh, and Y. Chigusa, *Ultra-low-loss (0.1484 dB/km) pure silica core fibre and extension of transmission distance,* Electron. Lett. **38**, 1168 (2002).

[158] J. F. Geus, F. Elsen, S. Nyga, A. J. Stolk, K. L. Van Der Enden, E. J. Van Zwet, C. Haefner, R. Hanson, and B. Jungbluth, *Low-noise short-wavelength pumped frequency downconversion for quantum frequency converters,* Opt. Quantum **2**, 189 (2024).

[159] J. M. Brevoord, J. F. Geus, T. Turan, M. G. Romero, D. B. Rodríguez, N. Codreanu, A. M. Stramma, R. Hanson, F. Elsen, and B. Jungbluth, *Quantum Frequency Conversion of Single Photons from a Tin-Vacancy Center in Diamond,* arXiv:2509.01661 (2025).

[160] M. D. Eisaman, J. Fan, A. Migdall, and S. V. Polyakov, *Invited Review Article: Single-photon sources and detectors,* Rev. Sci. Instrum. **82**, 071101 (2011).

[161] J. N. Becker and C. Becher, *Coherence Properties and Quantum Control of Silicon Vacancy Color Centers in Diamond,* Phys. Status Solidi A **214**, 1700586 (2017).

[162] M. H. Metsch, K. Senkalla, B. Tratzmiller, J. Scheuer, M. Kern, J. Achard, A. Tallaire, M. B. Plenio, P. Siyushev, and F. Jelezko, *Initialization and Readout of Nuclear Spins via a Negatively Charged Silicon-Vacancy Center in Diamond,* Phys. Rev. Lett. **122**, 190503 (2019).

[163] D. Chen, J. E. Fröch, S. Ru, H. Cai, N. Wang, G. Adamo, J. Scott, F. Li, N. Zheludev, I. Aharonovich, and W. Gao, *Quantum Interference of Resonance Fluorescence from Germanium-Vacancy Color Centers in Diamond,* Nano Lett. **22**, 6306 (2022).

[164] I. T. Raa, H. K. Ervasti, P. J. Botma, L. C. Visser, R. Budhrani, J. F. van Rantwijk, S. P. Cadot, J. Vermeltfoort, M. Pompili, A. J. Stolk, M. J. Weaver, K. L. van der Enden, D. de Leeuw Duarte, M. Teng, J. van Zwieten, and F. Grooteman, *QMI - Quantum Measurement Infrastructure, a Python 3 framework for controlling laboratory equipment,* 4TU.ResearchData, Software (2023).

[165] Qblox and Orange Quantum Systems, *Quantify Core,* Gitlab Web Page, available at `https://gitlab.com/quantify-os/quantify-core` (2025).

[166] R. F. L. Vermeulen, *Pulse generator and method for generating pulses,* Patent, IPC No. H03K, H04L, Priority date 23 Jun 2022, Priority No. WO2022/131924 (2020).

[167] C. F. J. Wolfs, *Towards a spin-photon interface based on nv centres in an open microcavity*, Master's thesis, Delft University of Technology (2024).

[168] M. Pompili, *Multi-Node Quantum Networks with Diamond Qubits*, Ph.D. thesis, Delft University of Technology (2021).

3

Background: Optical Cavities for Color Centers in Diamond

”Hohlraumresonatoren sind Gebilde, in denen sich durch Resonanz eine stehende Welle, meist mit verschiedenen Moden, bilden kann.”
- German Wikipedia[1]

This chapter contains the relevant background information on optical cavities in the context of this thesis. We briefly summarize how the Purcell effect can be utilized to obtain enhanced resonant emission of quantum emitters coupled to the cavity. Afterward, the coherent cooperativity is introduced as the central quantity that describes the photonic interface of a cavity-coupled emitter for quantum networking. We give a brief overview of how optical cavities can be realized with diamond color centers. Then, we focus on the open microcavity approach, give a literature overview, and discuss specific properties of this platform. This includes the effect of a diamond membrane hosting the color centers, which is incorporated into the cavity. Furthermore, we consider the vibration sensitivity and how microwave structures can be integrated. Finally, this chapter gives a summary of the micrometer-thin diamond samples used in this thesis and their fabrication.

[1] ”Cavities are structures in which resonance can cause a standing wave, usually forming different modes.”

3.1 Cavity Quantum Electrodynamics

Quantum electrodynamics describes the fundamental interaction between light and matter. When the light field is confined to an optical resonator (cavity), it is extended into cavity quantum electrodynamics (CQED) [1]. Pioneering experiments are achieved in the microwave domain, where the microwave cavity is probed with highly-excited Rydberg atoms, crossing the cavity [2]. This platform enables the first observation of Purcell-enhancement by measuring the cavity-enhanced spontaneous emission of a single atom [3]. By realizing an extremely high cavity quality factor, it is also possible to record the "birth, life and death of a single photon" [4].

Since these first experiments, the research has extended to light in the visible domain, and it has become possible to turn the experiments around: the cavity, containing a matter-based quantum system, is now probed with photons. This led to the observation of the Purcell effect at visible wavelengths by enhanced spontaneous emission [5] and a modified excited state lifetime [6]. Experiments, where (single) atoms modify the cavity modes [7], probed by a weak light field, have been realized. This culminated in the demonstration of a one-atom laser in the strong coupling regime [8], which could be used to deterministically generate single photons [9].

As demonstrated in the atom experiments, cavities can be used to generate photons from a single quantum emitter with a very high efficiency. The coupling of an optical transition to the cavity is characterized by the Purcell factor and depends for a perfect two-level system only on cavity properties. Taking the emitter properties into account leads to the cooperativity. These concepts are independent of the exact cavity geometry and are briefly summarized in the next section.

3.1.1 Transition Rates and Purcell Enhancement

The coupling of a quantum emitter to the cavity can be calculated by comparing the transition rates, appearing in a homogeneous medium (for example, into free space) and inside an optical cavity. We consider for this the dipole of a two-level quantum system with the excited state $|e\rangle$ and ground state $|g\rangle$. The transition frequency between the two levels is ν, with a corresponding angular frequency of $\omega = 2\pi\nu$. The spontaneous emission decay from the excited to ground state can be calculated by the electric dipole approximation and Fermi's golden rule [10]. By considering the photon density of states $D(\omega)$ and the emitter to vacuum field coupling g, the transition rate in a homogeneous medium with refractive index n is given by [11]:

$$\Gamma_{\text{hom}} = \Gamma_{\text{e}\rightarrow\text{g}}(\omega) = 2\pi g^2 |\hat{d}\cdot\hat{e}|^2 D(\omega) = \frac{\omega^3 n^3 \mu_{eg}^2}{3\hbar\pi\epsilon_0\epsilon_r c^3}. \tag{3.1}$$

In this equation, $\hat{e}$ is the electric field polarization, $\hat{d}$ is the dipole of the emitter with the dipole moment μ_{eg} and ϵ_0,ϵ_r are the vacuum and relative permittivity. For a randomly oriented dipole emitter, $|\hat{d}\cdot\hat{e}|^2$ averages to 1/3. Furthermore, c is the speed of light and $\hbar$ is the reduced Planck constant.

A cavity completely changes the photonic environment of a quantum emitter. This can be modeled by a modification of the density of states $D_{\text{cav}}(\omega)$, which is peaked around the normalized Lorentzian-shaped cavity resonances:

$$D_{\mathrm{cav}}(\omega) = \frac{1}{\pi}\frac{\delta\omega/2}{(\omega-\omega_c)^2+(\delta\omega/2)^2}. \tag{3.2}$$

In this formula, $\delta\omega$ denotes the full width at half maximum angular frequency of the cavity, while ω_c is the resonance angular frequency of the cavity. This is related to the exponential decay τ_{cav} of the light field out of the cavity with the rate $\kappa = \delta\omega = \tau_{\mathrm{cav}}^{-1}$ and the cavity quality factor:

$$Q = 2\pi\frac{\text{stored energy}}{\text{energy loss per cycle}} = \frac{\omega}{\delta\omega}. \tag{3.3}$$

The cavity quality factor describes the number of optical cycles inside the cavity until the field mode energy decays to $1/e$ of the initial value. For an emitter on resonance with the cavity, the density of states simplifies to:

$$D_{\mathrm{cav}}(\omega=\omega_c) = \frac{2}{\pi\delta\omega} = \frac{2Q}{\pi\omega}. \tag{3.4}$$

The cavity density of states leads to a spontaneous emission rate of the emitter into the cavity with mode volume V:

$$\Gamma_{\mathrm{cav}}(\omega_c) = \frac{2\mu_{eg}^2}{\hbar\epsilon_0\epsilon_r}|\hat{d}\cdot\hat{e}|^2\frac{Q}{V}. \tag{3.5}$$

With the spontaneous emission rates of a dipole emitter in a homogeneous medium Γ_{hom} and in a cavity Γ_{cav}, we can calculate the emission rate enhancement. This is quantified by the Purcell factor F_P, which compares the two rates:

$$F_P = \frac{\Gamma_{\mathrm{cav}}}{\Gamma_{\mathrm{hom}}} = \frac{|\hat{d}\cdot\hat{e}|^2}{1/3}\frac{D_{\mathrm{cav}}(\omega)}{D_{\mathrm{hom}}(\omega)} = \frac{3}{4\pi^2}\left(\frac{\lambda}{n}\right)^3\zeta^2\,\frac{Q}{V} \tag{3.6}$$

In the last step, $|\hat{d}\cdot\hat{e}|^2$ is summarized to ζ^2, describing the polarization overlap of the cavity and the emitter dipole. The cavity linewidth is $\delta\nu = \kappa/(2\pi) = \delta\omega/(2\pi)$. The original formula was derived in 1946 by Edward Mills Purcell for nuclear magnetic moment transitions at radio frequencies [12]. A more detailed derivation can be found in Refs. [11, 13]. Remarkably, the Purcell factor only depends on cavity properties, the cavity quality factor Q, and the mode volume V. Note that Purcell enhancement has a cubic dependence on the refractive index n of the material hosting the quantum emitter.

3.1.2 Cooperativity

The last section introduced the Purcell factor, which quantifies the emission enhancement of a cavity resonant with a two-level system. For diamond color centers, we are interested in enhancing the resonant, zero-phonon line (ZPL) emission. On resonance, the cavity opens another decay channel, which overlaps with the ZPL transition and whose enhancement is quantified by the Purcell factor F_P^{ZPL}. The spectral overlap function of the cavity has, due to the density of states from equation (3.2), a Lorentzian shape [14]. Next to the resonant emission, there is an off-resonant decay path, which is related to the Debye-Waller factor β_0, quantum efficiency η, and an eventual orbital branching ratio α

between different ZPL transitions (see Chapter 2 for more details). In addition, there could be a spatial mismatch ϵ between the emitter position and the maximum of the intracavity light field.
When the cavity is on resonance with the ZPL transitions, we can capture all of this by a single number, quantifying the photonic interface of a cavity-coupled diamond color center, which is known as the cooperativity:

$$\begin{aligned} C &= F_P^{\mathrm{ZPL}} \times \xi_{\mathrm{emitter}} \times (\zeta^2 \times \epsilon) \\ &= \underbrace{\frac{3}{4\pi^2}\left(\frac{\lambda}{n_d}\right)^3 \frac{Q}{V}}_{\text{Cavity properties}} \times \underbrace{(\beta_0 \times \eta \times \alpha)}_{\substack{\text{Emitter properties} \\ \text{NV centers: } \xi_{\mathrm{NV}} = 0.03 \\ \text{SnV centers: } \xi_{\mathrm{SnV}} = 0.36}} \times \underbrace{(\zeta^2 \times \epsilon)}_{\substack{\text{Emitter} \\ \text{orientation} \\ \text{and position}}} \end{aligned} \tag{3.7}$$

In this equation, n_d denotes the refractive index of diamond, which is about $n_d = 2.41$ for 620 nm and 637 nm [15]. For a given emitter, the cooperativity can be maximized by increasing the cavity quality factor Q and reducing the mode volume V by making the cavity very small (order of the cubic confined light wavelength). The cooperativity is a common quantity to compare the coupling of emitters to photonic structures and is also used, for example, with waveguides [16].
Note that due to the better optical properties of the SnV center, a cavity with the same Q/V ratio would lead to about ten times larger cooperativity as compared to the NV center.
Assuming that the cavity affects only the density of states along the direction of the cavity modes and that all other directions are mostly unaffected, we can compare the cavity-enhanced emission C with the total emission $C+1$ to calculate the spontaneous emission into the cavity mode β_{cav} (the branching ratio of photons into the ZPL and into the cavity mode) [11]:

$$\beta_{\mathrm{cav}} = \frac{C}{C+1}. \tag{3.8}$$

This quantifies the enhancement of the cavity on the ZPL transition. Thus, the cooperativity is the figure of merit for the optical interface, and for a large cooperativity, the emission into the cavity mode approaches unity.
It is also common to specify the photonic interface of a cavity-emitter system by the CQED parameters, consisting of the three following rates: cavity coupling or single photon Rabi frequency g, total cavity decay rate κ, and emitter decay rate or homogeneous dephasing linewidth γ (see Fig. 3.1). With these parameters, often specified as $\{g,\kappa,\gamma\}$, the cooperativity[2] is given by [18]:

$$C = \frac{4g^2}{\kappa\gamma}. \tag{3.9}$$

[2]Note that this equation is typically used in the context of solid state emitters. Depending on the definition of g, κ, γ, the equation $C = \frac{g^2}{2\kappa\gamma}$ with $\beta_{cav} = \frac{2C}{1+2C}$ is also used, for example with neutral atoms [17].

The three rates govern the interaction between the emitter and photons within the cavity [19]. The cooperativity gives insights about the balance of the different rates and becomes larger than one when the cavity coupling g compensates the decay rates $\{\kappa, \gamma\}$. These parameters quantify the cavity-emitter system, but they do not capture the optical coherence of the emitter. An optically broadened emitter, as can be encountered in solid-state hosts, features another source of an incoherent rate. To consider this, we can define the broadened emitter linewidth as $\gamma' = \gamma + \gamma_d$ with pure dephasing rate γ_d and the coherent cooperativity as [18]:

$$C_{\text{coh}} = \frac{4g^2}{\kappa(\gamma + \gamma_d)} = C\frac{\gamma}{\gamma'} \tag{3.10}$$

C_{coh} can be seen as the probability of a coherent interaction between a photon and the cavity-coupled emitter. Taking cavity losses and the dephasing rate into account, the dynamics of such an emitter-cavity system can be modeled by a Lindblad master equation approach [20].
Usually it is common to distinguish between weak ($g \ll \{\kappa, \gamma\}$) and strong coupling ($g \gg \{\kappa, \gamma\}$). However, for cavities with diamonds, the cavity decay rate κ is dominating so far in the experimental realizations ($\kappa \gg g \gg \gamma$). This case is also called the bad-cavity regime. We therefore distinguish experimental realizations of different coherent cooperativities in the following [13].

Low coherent cooperativity: $C_{\text{coh}} \lesssim 1$
In this regime, decay rates are larger than or equal to the coupling of the emitter to the cavity. This leads to a high probability that the photon leaks out of the cavity before it is reabsorbed by the emitter. The dynamics of the photon emission are quite different than those in free space, because the resonant cavity adds another decay channel, resulting in an enhanced decay rate into the cavity mode. This regime is mostly relevant for enhanced photon collection, as described in the following Section 3.1.3.
All cavity-enhanced NV center experiments so far have been operated in this regime, mostly limited due to inhomogeneously broadened optical transitions $\gamma' \gg \gamma$. This resulted in coherent cooperativities $C_{coh} \ll 1$ despite cooperativities being $C \gtrsim 1$ [21, 22]. Recently, a NV center with a narrow extrinsically broadened linewidth was coupled to a microcavity reaching a cooperativity of $C = 0.8$ [23]. Cooperativities around one have also been observed with diamond silicon-vacancy centers coupled to microcavities [24, 25] and evanescently coupled to photonic crystal cavities fabricated in silicon nitride [26, 27] and gallium phosphide [28].
As soon as the coherent cooperative approaches one, a single cavity-coupled emitter starts to modulate the cavity spectrum when probed with a weak excitation [29–31]. This regime enables nonlinear interactions at the single photon level [32], which can, for example, be utilized as a quantum-optical switch controlled by an individual cavity-coupled emitter [20]. The nonlinear behavior also manifests in an altered photon statistics of reflected or transmitted photons. The coherent coupling of a diamond tin-vacancy center to a microcavity is demonstrated in Chapter 6.

High coherent cooperativity: $C_{\text{coh}} \gg 1$
In this regime, the emitter-cavity coupling rate is larger than the decay rates. This results in a high probability that the photon interacts with the emitter again before it leaks out of the cavity. Therefore, the cavity completely alters the dynamics of the emission. For $g \gg \{\kappa, \gamma\}$, the reversible emitter-cavity coupling dominates over the irreversible processes, which makes it possible to observe vacuum-Rabi oscillations [17, 33]. For the case of an ideal two-level system with no losses, this can be described theoretically by the Jaynes-Cummings model [34].

The regime of high coherent cooperativity enables near-deterministic interactions between single photons and cavity-coupled emitters, which can be utilized for multiple building blocks of a quantum network, such as a nondestructive detection of a single photon [35]. The efficiency and fidelity of implemented protocols of quantum networking scale with the coherent cooperativity [18].
Due to their first-order insensitivity to electric fields, group-IV color centers in diamond can maintain transform-limited linewidth in nanophotonic structures [36, 37]. This enabled the demonstration of $C_{coh} > 100$ for silicon-vacancy centers in photonic crystal cavities [38]. Such a system can be used for spin-dependent cavity reflections [39, 40], which can be harnessed for remote entanglement generation [41].

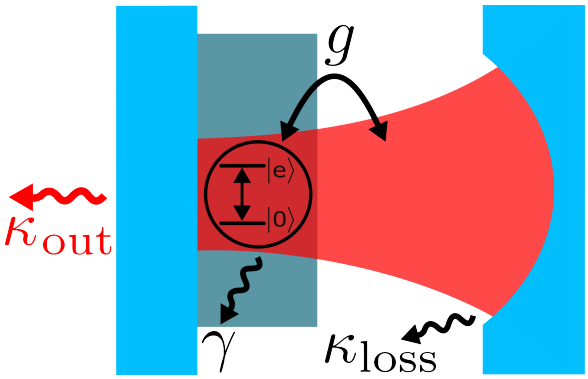

Figure 3.1: Cavity quantum electrodynamics parameters of a two-level quantum emitter hosted inside a membrane coupled to a cavity. The cavity frequency is on resonance with the transitions between the ground ($|g\rangle$) and excited state ($|e\rangle$). This transition decays with a free-space dephasing rate γ. The emitter-cavity coupling rate is captured by g. The light field leaks out of the cavity by a decay rate κ, which can be broken down into an outcoupled, useful photon extraction rate κ_{out} and a loss rate κ_{loss}.

3.1.3 Cavity Outcoupling

Next to cavity coupling as described above, an important property influencing the efficiency of the optical interface is the fraction of outcoupled light from a cavity. This can be captured by splitting the cavity decay rate κ into a useful cavity extraction channel κ_{out} and an inevitable loss rate κ_{loss}. The latter is composed of the decay rate through the other mirror(s) and additional losses such as scattering or absorption due to imperfect mirrors or an additional diamond interface inside the cavity. The total decay rate is then $\kappa = \kappa_{\text{out}} + \kappa_{\text{loss}}$.

Depending on the ratio of κ_{out} to the other loss channels κ_{loss}, we can distinguish between a critically- ($\kappa_{\text{out}} = \kappa_{\text{loss}}$ or symmetric), over- ($\kappa_{\text{out}} > \kappa_{\text{loss}}$) or undercoupled ($\kappa_{\text{out}} < \kappa_{\text{loss}}$) cavity. Here, the cavity is probed through the channel of κ_{out}.

An overcoupled cavity (also referred to as an asymmetric or single-sided cavity) is desired for an efficient photonic interface, as most of the enhanced emission leaves the cavity via the output mirror into a well-defined mode. For $\kappa \gg g$, we can express the cavity outcoupled resonant ZPL emission (after the cavity, before the first lens) to [17]:

$$\beta_{\text{out}} = \frac{\kappa_{\text{out}}}{\kappa} \times \beta_{cav} = \frac{\kappa_{\text{out}}}{\kappa_{\text{out}} + \kappa_{\text{loss}}} \times \frac{C}{1+C} \tag{3.11}$$

This is the central figure of merit for emission-based entanglement schemes [41]. Note that there is a tradeoff between high cooperativity (decreasing κ) and a balance between the different cavity decay rates determining the outcoupling efficiency of the cavity (increasing κ_{out}). Strategies for maximizing β_{out} are, for example, discussed in Van Dam et al. [14] for open microcavities and in Knall et al. [42] for photonic crystal cavities. The case of a critically- or overcoupled cavity is mostly relevant for maximizing the contrast of spin-dependent reflections [38, 42].

It is therefore possible to characterize the efficiency of the cavity-enhanced photonic interface by measuring the cooperativity (see next Section 3.1.4) and the cavity outcoupling rate. For the later discussed Fabry-Pérot microcavities, it is possible to determine the outcoupling rate via the cavity finesse and the design mirror coating of the outcoupling mirror (see Section 3.3.3).

3.1.4 Experimental Determination of the Cooperativity

The smoking gun for a cavity-coupled emitter is its reduced excited-state lifetime when the cavity is on resonance with the corresponding optical transitions. The cavity adds another decay channel on the transitions, quantified by the cooperativity, which leads to a higher decay rate and thereby reduced lifetime. The enhanced ZPL emission rate can be compared with the natural decay rate in a homogeneous medium such as free space (see Ruf et al. [43] for NV centers and Chapter 6 for the case of SnV centers). With this, the measured lifetime for the cavity on resonance with the emitter τ_P and the off-resonance lifetime τ directly yields the cooperativity:

$$C = \frac{\tau}{\tau_P} - 1. \tag{3.12}$$

Measuring the lifetimes for the two different cases (for example, with a pulsed laser as used in Chapter 6 for the SnV center and Chapter 7 for the NV center) can thus be used

to quantify the cooperativity. The natural lifetime of the emitter can also be measured independently with a confocal microscope, or literature values can be considered. However, the depth below the diamond surface [44] and the local strain might also influence the lifetime of an individual emitter. For example, in Chapter 7, the cavity off-resonance NV center lifetime is estimated to be around 9.5 ns due to higher strain, while in electron irradiated high purity diamonds with low strain, the natural NV center lifetime is typically around 12.4 ns [45, 46].

The excited state lifetime of an emitter is directly related to its linewidth ($\tau = 1/(2\pi\gamma)$). Therefore, the cooperativity can equivalently be characterized by a broadened emitter linewidth:

$$C = \frac{\gamma_P}{\gamma} - 1 = \frac{\gamma_P' - \gamma'}{\gamma}. \tag{3.13}$$

Here, γ_P denotes the Purcell-broadened emitter linewidth with the cavity fully on resonance, and γ denotes the off-resonance linewidth. Parameters with the additional prime consider additional dephasing of the emitter, which leads to a broader linewidth $\gamma' = \gamma + \gamma_d$ and a Purcell-broadened emitter linewidth with dephasing of $\gamma_P' = \gamma + \gamma_d + 4g^2/\kappa$ [13]. The transform-limited linewidth γ can be determined by measuring the cavity off-resonance excited-state lifetime. These measurements allow the direct determination of the coherent cooperativity [18]:

$$C_{\text{coh}} = \frac{\gamma_P'}{\gamma'} - 1. \tag{3.14}$$

Both equations are used to determine the (coherent) cooperativity of a cavity-enhanced SnV center in Chapter 6.

When the coherent cooperativity approaches one, a single emitter starts to significantly modulate the cavity transmission or reflection spectrum. When probed with a weak excitation, cavity QED parameters can be directly extracted from a resonant laser scan of the cavity mode with an analytic formula [17]. The cooperativity can then be calculated by equation (3.9). This has been used to characterize SiV centers in photonic crystal cavities [38, 47]. For this cavity design, the emission into the waveguide for a far-detuned cavity can be used to determine the off-resonance emitter linewidth.

So far, we have assumed that the emitter linewidth is much narrower than the cavity decay rate ($\gamma \ll \kappa$). When this is not the case (also referred to as bad-emitter regime), the cavity enhances only a fraction of transition, which can be modeled by a reduced, effective quality factor $Q_{\text{eff}} = (Q_{cav}^{-1} + Q_{em}^{-1})^{-1}$, where $Q_{em} = \nu_{em}/\gamma$ is the quality factor of the emitter with an emission frequency of ν_{em}, and Q_{cav} denotes the cavity quality factor [48, 49]. This might lead to a very small change in the emitter lifetime. In this case, the cooperativity can be estimated by comparing the saturated photon emission rates into free space and into the cavity. Combined with the collection and detection efficiencies, the total emission rate can be calculated, and the ratio determines the cooperativity [50]. Due to the cavity enhancement combined with the funneling into a spectrally narrow mode, this can be seen as a spectral density enhancement [51].

With the properties, placement, and orientation of the emitter, the cooperativity can be used to calculate the Purcell factor. When the cavity properties (quality factor and mode

volume) are known, this can also be turned around to estimate emitter properties (cavity properties such as the quality factor can be determined in independent measurements). This is used by Riedel et al. [22] to determine the Debye-Waller factor of the NV center with a microcavity. The cavity measurements presented in Chapter 6 allow for determining a lower bound on the product of branching ratio α and quantum efficiency η for the studied SnV center, confirming parameters measured independently before [52, 53].
Making a controlled change in the photonic environment of emitters has also been used to determine the quantum efficiency for implanted NV centers [54] (a method also known as Drexhage's scheme [55]).

3.2 Optical Cavities for Diamond Color Centers

We have discussed in the last section the basic properties of quantum emitters inside cavities. This section introduces some common cavity approaches used with color centers in diamond.
There is a lot of research focused on coupling diamond color centers to optical cavities. We can classify the different cavity approaches into two categories. In the monolithic approach, the cavity is fabricated directly into the diamond material. For example, this can be achieved by an all-diamond one- or two-dimensional photonic crystal cavity (PCC). Approaches of the second category fabricate the cavity in an external material, surrounded or near diamond hosting the color center ("emitter to structure" approach [56]). This hybrid approach contains, for example, photonic crystal cavities fabricated into silicon nitride, and a nanodiamond with color centers is placed onto or into the cavity [26, 57]. Historically, cavities in external materials [58] have been utilized first due to the challenging nanofabrication of diamond.
Table 3.1 provides an overview of cavities realized with diamond color centers. Note that the given cavity design overview is not complete and rather focuses on the most common structures, which have demonstrated the coupling of color centers. The following points should be taken into consideration when selecting an appropriate cavity design:

- **Emitter properties:** For integration into a cavity, color centers usually need to be within a sub-micrometer distance from the diamond surface. It is usually very challenging to incorporate NV centers into nanostructures while maintaining good optical properties [21, 59–62], which are required for quantum networking.
  In contrast, SnV centers [37, 63, 64] (as well as SiV centers [36] and GeV centers [16]) have shown good optical properties in diamond waveguides and in a 150 nm thin diamond membrane [65].

- **Cavity properties:** A high cavity quality factor and a low mode volume are desired to optimize the Purcell enhancement. For example, to achieve a Purcell factor larger than one, a quality factor of 2×10^4 for a cavity with a mode volume of 100 λ^3 is needed (assuming that the emitter is placed in diamond and perfectly coupled to the cavity). Two-dimensional and one-dimensional PCCs have been used to demonstrate Purcell factors of above 60 with the NV center [21, 66]. Furthermore, plasmonic nanocavities have enabled large lifetime reductions [67, 68]. However, the NV centers in the nanodiamonds or diamond posts usually show poor optical prop-

erties. For the SnV center, one-dimensional PCCs have been used to show Purcell factors above 25 [53, 69].

- **Diamond fabrication:** Nanofabrication of diamond is very challenging [70], which leads to a high variation of cavity quality factors of monolithic structures demonstrated in literature. However, recent breakthroughs with the smart cut approach to fabricate diamond on insulator (DOI) [65, 71] in combination with patterning by a silicon nitride hard mask showed record quality factor for one- and two-dimensional PCCs [72]. This method is expected to establish a new paradigm in diamond nanophotonics [73].
  Diamond membranes require much simpler fabrication (see Chapter 4), and can incorporate color centers into open microcavities or an evanescent light field of an external cavity fabricated in a different material like titanium dioxide (TiO_2) [74]. Alternatively, diamond nanofabrication can be avoided by using a hybrid approach with nanodiamonds, which have shown good optical properties with SiV centers [75, 76] or a PCC fabricated into a material like gallium phosphide (GaP) [28] transfer-stamped on bulk diamond.

- **Optical accessibility:** For an efficient emission-based photonic interface, it is particularly important that the extraction of photons is high, which can be achieved by engineering $k_{\text{out}} \gg \kappa_{\text{loss}}$. For some cavity designs, such as open microcavities, this is rather straightforward with commercially available design cavity mirror coatings (assuming that the additional losses due to the diamond membrane are known). For monolithic cavities, the asymmetric cavity design and nanofabrication become more challenging [42]. Furthermore, additional interfaces, such as a diamond waveguide to a tapered fiber, can reduce the extraction of photons. However, several works showed that these can be very efficient and even combined with photonic packaging [64, 77, 78]. Also, other cavity designs, such as the microdisks, rely on tapered fiber coupling [79].
  Plasmonic nanogap cavities can be engineered to feature a radiation pattern, which can be efficiently collected with a high numerical aperture objective [68, 80]. Moreover, some cavity designs allow for separating the excitation and detection into different spatial modes, which can be beneficial in obtaining a high signal-to-noise ratio of the emitter fluorescence (such as the hybrid approach of silicon nitride PCCs and nanodiamonds [57], see table 3.1 (e)).

- **Spectral and spatial tunability of the cavity:** Open microcavities feature direct fast tuning of their resonance frequency (bandwidth in the order of tens of kilohertz [81]). This can be harnessed for fast switching between multiple cavity-coupled emitters at different emission frequencies. PCCs can be tuned by gas deposition on a much slower timescale with a tuning range of several nanometers [28, 53].

- **Chances to find a well-coupled emitter:** The dipole orientation and a displacement from the cavity field maximum result in a lower cooperativity. It is usually required to characterize many different cavities (and tune their emission frequency over the inhomogeneously distributed quantum emitter wavelength range) until a well-coupled emitter is found. Open microcavities can benefit from a thicker diamond membrane with multiple intracavity field maxima, spaced by ≈ 130 nm inside the diamond. Next to the axial position, the lateral emitter placement is also less strict due to the micrometer-sized cavity beam waist (see Section 3.3.1). For PCCs, the cavity field is concentrated in a much smaller volume (see Tab. 3.1 (a)).
  For the hybrid approach with nanodiamonds, the coupling of emitters can be optimized by aligning the position and rotation of the emitter dipole with an atomic force microscope-based pick-and-place technique [27].

- **Sensitivity to the environment:** This includes vibrations, temperature or pressure changes. The large tunability of open microcavities comes with the cost that the resonance frequency is extremely sensitive to vibrations (picometer level, see Section 3.3.4), lowering the effective Purcell enhancement. This requires additional consideration in the cryostat and/or cavity insert design. In addition, it might be required to actively stabilize the resonance frequency, which can influence the experiments with color centers. Monolithic cavities are much more robust against these effects and are intrinsically not sensitive to vibrations from the environment.

- **Delivery of microwaves:** For quantum information applications, it is required to control the spin qubit state of cavity-coupled color centers. High-fidelity control is usually achieved with microwaves coherently driving their spin transitions. This typically requires a proximity (tens of micrometers or less) of the color centers to an electronic antenna, such as a stripline or bondwire.
  Microwave spin driving has been demonstrated for NV centers in nanocavities with a metallic on-chip stripline [66] and a gold wire loop antenna [62]. For SiV centers in nanocavities, microwave control has been established with on-chip microwave coplanar waveguides, which are also harnessed to control the nuclear spin [40, 82]. Efficient microwave control of SnV centers hosted in diamond membranes, compatible with open microcavities, has been demonstrated [83, 84]. Recently, this has also been achieved with an aluminium line running underneath diamond waveguides [85].

- **Compatibility with strain-tuning:** To overlap the emission frequency of a cavity-coupled emitter with a second emitter, strain tuning can be used, depending on the emitter and cavity properties. For SnV centers, strain-tuning has been demonstrated with diamond waveguide-based devices [86–88].
  Next to strain, the emission frequency of SnV centers can also be tuned by cavity-enhanced Raman emission, as demonstrated with SiV centers [89].

- **Large-scale integration:** For scalability, the cavity design needs to be compatible with the integration of a large number of color centers into a photonic architecture. Heterogeneous integration can be achieved in combination with a photonic integrated circuit fabricated by a second material (for example, aluminium or silicon nitride) featuring an already established nanofabrication. This can be directly achieved with one-dimensional photonic crystal cavities (for example, via transferring a diamond chiplet with a micromanipulator tip to a target photonic chip [90]). Integration of diamond microwaveguides into a silicon nitride photonic circuit has been demonstrated with NV centers [91].
  For the SnV center, waveguide microchiplets [87] and photonic crystal cavities [92] have been heterogeneously integrated into a silicon nitride photonic integrated circuit. Furthermore, large-scale integration of SnV centers into a commercially processed complementary metal–oxide–semiconductor (CMOS) chip is shown [86].
  The photonic integration of open microcavities is discussed in Section 8.3.4 in the conclusion.

In conclusion, several cavity approaches with different advantages and disadvantages are available to Purcell-enhance diamond color centers. Monolithic approaches, in particular PCCs, can enable high cooperativities ($C > 100$) due to the low mode volume. This is demonstrated with SiV centers [38], and should also be feasible with SnV centers. Open microcavities can reach the regime of low and medium cooperativity ($C \lesssim 50$), and can be especially suited for an efficient emission-based photonic interface, due to the straightforward design of the cavity outcoupling and a well-collectible mode from the cavity. Notably, SiV-based nanophotonic devices with cooperativities of $C = 1.5$ and $C = 12.4$ have facilitated quantum networking [93]. Other cavity designs require stable and optically coherent emitters in nanodiamonds or that the emitters maintain good properties, ideally in a few nanometers below the surface [28].
The field of diamond photonics, including diamond micro- and nanofabrication, is reviewed in Refs. [94, 95]. Reviews about cavity QED with diamond color centers are presented by Janitz et al. [96] and with an emphasis on quantum networks by Ruf et al. [13]. Furthermore, diamond integrated quantum nanophotonics is reviewed by Shandilya et al. [97].

Monolithic	**1d Photonic Crystal Cavities** 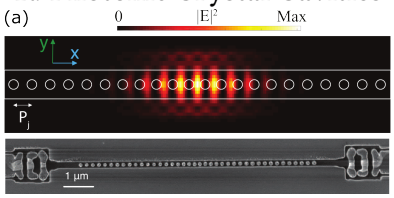 V: (0.5 to 2.5) $(\lambda/n_d)^3$ [20, 38] Q: 2000 [53] to 1.8×10^5 [72]	**2d Photonic Crystal Cavities** 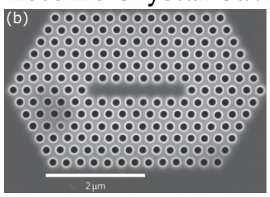 V: (0.35 to 1.5) $(\lambda/n_d)^3$ [62, 98] Q: 8000 [62] to 1.6×10^5 [72]
	Microring Resonators 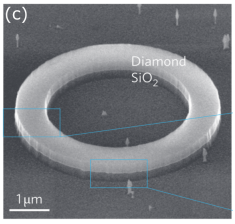 V: (17 to 32) $(\lambda/n_d)^3$ [99] Q: 5000 [99]	**Microdisk Resonators** 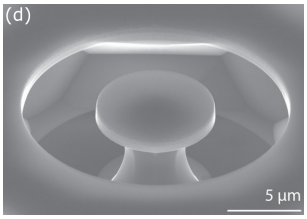 V: 11 $(\lambda/n_d)^3$ [100] Q: 1.1×10^5 [100] to 3.3×10^5 [101] (around 1550 nm)
Hybrid	**Ext. Material, Nanodiamonds** 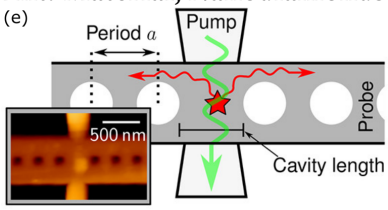 V: 6 $(\lambda/n)^3$ [27] Q: 2000 [27, 102] to 4.7×10^4 [57]	**Plasmonic Nanogap Cavities** 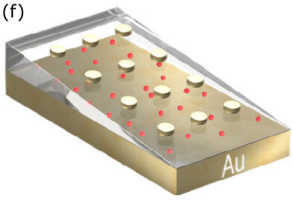 V: 2×10^{-4} λ^3 [103] Q: 13 [103] to 175 [104]
	Ext. Mat., Bulk/Membrane 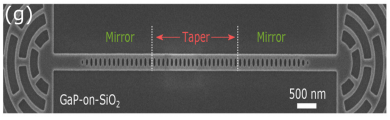 V: 2 $(\lambda/n)^3$ [74] Q: 4000 (TiO_2) [74] to 9000 (GaP) [28]	**Open Microcavities**  V: 4 λ^3 [50, 105] to 86 λ^3 (chapter 7) Q: 2×10^4 [24, 50] to 10^6 [106]

Table 3.1: Diamond cavity approaches. Figure sources: (a) Rugar et al. [53], reproduced under CC-BY 4.0 license terms. (b) Riedrich-Möller et al. [98], reproduced with permission from Springer Nature. (c) Faraon et al. [99], reproduced with permission from Springer Nature. (d) Adapted with permission from Khanaliloo et al. [100]. Copyright 2015 American Chemical Society. (e) Adapted with permission from Fehler et al. [57]. Copyright 2019 American Chemical Society. (f) Boyce et al. [103], reproduced under CC-BY-NC-ND 4.0 license terms. (g) Adapted with permission from Chakravarthi et al. [28]. Copyright 2023 American Chemical Society. (h) Ref. [107], used with permission of the author. Mode volumes V and quality factors Q are typical and based on realized devices. If not specified, quality factors are given for the wavelength range of 600 nm to 750 nm. Note that the quality factor of open microcavities is proportional to the cavity length (equation (3.20)), but also the mode volume increases with cavity length.

3.3 Fabry-Pérot Microcavities

We first consider an empty or bare cavity formed by two highly reflective mirrors facing each other. The two parallel mirrors of the cavity have the reflectivities R_1 and R_2 and are separated by the cavity length L. The cavity confines light of the resonance frequencies ν_a (assuming the cavity medium is air), which take discrete values depending on the fundamental mode number q_a and the corresponding wavelength λ:

$$L = q_a \frac{\lambda}{2} \iff \nu_a = q_a \frac{c}{2nL}. \tag{3.15}$$

In this equation, c is the speed of light, and n denotes the refractive index of the medium inside the cavity, which can be set to $n = 1$ for air. Note that L is the optical distance between the mirrors and includes also the penetration depth into the multilayer mirrors [108]. The boundary conditions defined by the cavity mirrors allow only the formation of standing waves with the resonance frequency ν_a. In the spectral domain, two consecutive resonance frequencies are spaced by the free spectral range ν_{FSR}, which can be calculated by:

$$\nu_{\mathrm{FSR}} = \nu_{q+1} - \nu_q = \frac{c}{2nL} \tag{3.16}$$

In the spatial domain along the cavity axis, consecutive resonance frequencies are separated by half of the wavelength $L_{q+1} - L_q = \lambda/2$.

The spectral resolution or frequency selectivity of a Fabry-Pérot cavity (sharpness of the resonances) is determined by the finesse $\mathscr{F}$, which depends on the reflectivities of the mirrors and characterizes the quality of the resonator [17]:

$$\mathscr{F} = \frac{\pi (R_1 R_2)^{1/4}}{1 - \sqrt{R_1 R_2}} \approx \frac{2\pi}{\mathscr{L}}. \tag{3.17}$$

In this equation, the total cavity losses per round-trip $\mathscr{L}$ are introduced. These are composed of the transmission through both mirrors $\mathscr{L}_{M,1/2}$ as well as additional losses $\mathscr{L}_{\mathrm{add}}$ due to scattering and absorption [109]:

$$\mathscr{L} = \mathscr{L}_{M,1} + \mathscr{L}_{M,2} + \mathscr{L}_{\mathrm{add}}. \tag{3.18}$$

The cavity resonances have a Lorentzian shape with a full width at half maximum of $\delta\nu$ (linewidth of the cavity). This can be connected with the losses and the cavity finesse to [14]:

$$\delta\nu = \frac{1}{2\pi} \frac{\text{losses per round-trip}}{\text{round-trip duration}} = \frac{1}{2\pi} \frac{\mathscr{L}}{2nL/c} = \frac{c/(2nL)}{2\pi/\mathscr{L}} = \frac{\nu_{\mathrm{FSR}}}{\mathscr{F}}. \tag{3.19}$$

The finesse can also be interpreted as the number of bounces between the two mirrors experienced by a photon before leaking out of the cavity. This corresponds to a lifetime $\tau_{\mathrm{cav}} = (2\pi\delta\nu)^{-1} = \kappa^{-1}$ of a photon trapped between the two mirrors and a decay rate κ out of the cavity. With these definitions and the cavity resonant condition of equation (3.15), we can relate the finesse with the cavity quality factor from equation (3.3):

$$\mathscr{F} = \frac{\nu_{\mathrm{FSR}}}{\delta\nu} = \frac{\pi c \tau_{cav}}{L} = \frac{\pi\nu\lambda}{L\kappa} = \frac{\lambda}{2L}\frac{\omega}{\kappa} = \frac{Q}{L/(\lambda/2)} = \frac{Q}{q}. \tag{3.20}$$

As long as clipping losses can be neglected (see below), the finesse is constant in length and determined by the losses $\mathscr{L}$ of the cavity. In contrast, the cavity quality factor increases for larger cavity lengths.
To determine the mode volume of the cavity, we consider the Gaussian beam inside the cavity. The microcavities used in this thesis have a hemispherical resonator design, where one mirror is flat and the other mirror has a spherical shape with a radius of curvature ROC (plano-concave microcavity). This approach has higher robustness against misalignment. The stability condition of the beam inside the cavity leads to the condition $L \leq ROC$ for the cavity length. For $L > ROC$, the beam waist (half of the beam diameter) on the spherical mirror becomes larger than the size of the spherical cavity mirror, which leads to clipping loss and a reduced cavity finesse [109].
The Gaussian beam fitting into such a cavity has a beam waist ω_0 on the flat mirror (see Fig. 3.3) of [110]:

$$\omega_0^2 = \frac{\lambda}{\pi}\sqrt{L(ROC-L)} \tag{3.21}$$

The beam waist is connected to the cavity mode volume by [109]:

$$V = \frac{\pi}{4} w_o^2 L = \frac{\lambda}{4}\sqrt{L^3(ROC-L)} \tag{3.22}$$

With the definitions of the cavity finesse of equation (3.20) and the cavity mode volume from equation (3.22) we can rewrite the equation of the Purcell enhancement (equation (3.6)) into a new form for open microcavities [13]:

$$\begin{aligned} \underbrace{F_P}_{\text{Purcell Factor}} &= \underbrace{\frac{3}{2\pi}\frac{\lambda^2}{n^2}}_{\substack{\text{Dipole absorption}\\ \text{cross section}}} \times \underbrace{\frac{\mathscr{F}}{\pi}}_{\substack{\text{Photon bounces}\\ \text{in cavity}}} \times \underbrace{\frac{4}{\omega_0^2\pi}}_{\substack{\text{Inverse cavity}\\ \text{beam area}}} \times \underbrace{\zeta^2}_{\substack{\text{Polarization overlap}\\ \text{cavity - dipole}}} \\ &\approx \frac{1}{74} \times \frac{\mathscr{F}}{(\omega_0[\mu\text{m}])^2} \end{aligned} \tag{3.23}$$

Note that this equation can be used for a quantum emitter, e.g., an atom, placed inside the bare cavity. The equation can be interpreted in a way that the traveling photon is recycled by the cavity $n_{\text{round}} = \mathscr{F}/\pi$ times [111]. In the approximation, we have assumed a wavelength of $\lambda = 637\,\text{nm}$, a refractive index of $n = 2.41$ for diamond, and a perfect polarization overlap $\zeta^2 = 1$ (the prefactor is 1/78 for $\lambda = 619\,\text{nm}$). Thus, a large Purcell enhancement can be realized by maximizing the cavity finesse and minimizing the cavity beam waist. With equation (3.21), the beam waist is lowered by a smaller radius of curvature and a short cavity length. The influence of a diamond membrane on the cavity is discussed in the next section.
More information about cavities, including the Gaussian intracavity beam and higher-order modes, can be found in reference [110]. Furthermore, details about fiber-based cavities are presented in reference [109].

3.3.1 Hybrid Cavity with a Diamond Membrane

A diamond membrane inside the cavity can be seen as two coupled cavities, one within the air gap with length t_a and one within the diamond part with thickness t_d. The cavity resonance frequency can still be tuned fully by changing the air gap length; however, the cavity dispersion relation is altered compared to the case of the bare cavity. For a given diamond thickness and diamond mode number q_d, we can calculate the corresponding resonance frequency of the pure diamond cavity by [14]:

$$\nu_d = (2q_d - 1)\frac{c}{(4n_d t_d)} \tag{3.24}$$

With the diamond membrane inside the cavity, the modes arising in the air part with mode number q_a (equation (3.15)) and modes arising in the diamond part with q_d hybridize [14]. This leads to a modified cavity resonance frequency given by [106]:

$$\nu_q = \frac{c}{2\pi(t_a + n_d t_d)}\left(q\pi - (-1)^q \arcsin\left(\left(\frac{n_d - 1}{n_d + 1}\right)\sin\left(\pi q \frac{t_a - n_d t_d}{t_a + n_d t_d}\right)\right)\right). \tag{3.25}$$

Where $q = q_a + q_d$ is the fundamental longitudinal mode number of the hybrid cavity. The dispersion of such a hybrid cavity is shown in Fig. 3.2 (b). Note that this formula is also used to extract the fundamental mode, air gap length, and diamond thickness from white light transmission spectra of the hybrid cavity (for example, in Fig. 4.10).
As mentioned above, the cavity resonance frequency is tuned by the air gap t_a. On a given cavity spot on the diamond membrane (lateral position), the thickness t_d fully determines the mode character (equation (4.3) in Chapter 4). For the hybrid cavity system, we can identify two special cases:

- **Diamond-like modes:** An antinode occurs at the diamond-air interface in the hybridized cavity modes. This leads to a stronger electric field inside the diamond part of the cavity. The corresponding hybrid cavity dispersion has a shallower slope compared to the modes of the bare cavity. In Fig. 3.2 (b), diamond-like modes are present at frequencies indicated with diamond modes q_d.

- **Air-like modes:** The hybridized cavity modes have a node at the diamond-air interface, which makes these modes less susceptible to surface losses [14]. A simulation of the intracavity electric field distribution for an air-like mode is shown in Fig. 6.8. The corresponding hybrid cavity dispersion has a steeper slope compared to the diamond-like modes, as shown in Fig. 3.2 (b) for an air-like mode at the SnV centers ZPL wavelength of 619 nm.

The electric field distribution inside the cavity can be simulated with a transfer matrix model [14, 113], which can then be used to determine the effective cavity length. We have seen how the diamond membrane influences the cavity resonance frequency. To determine the effect on the Purcell factor (equation (3.23)), we need to calculate the finesse and the beam waist of the hybrid cavity.
We can stay close to the case of a bare cavity by introducing an effective cavity length L_{eff} [14]:

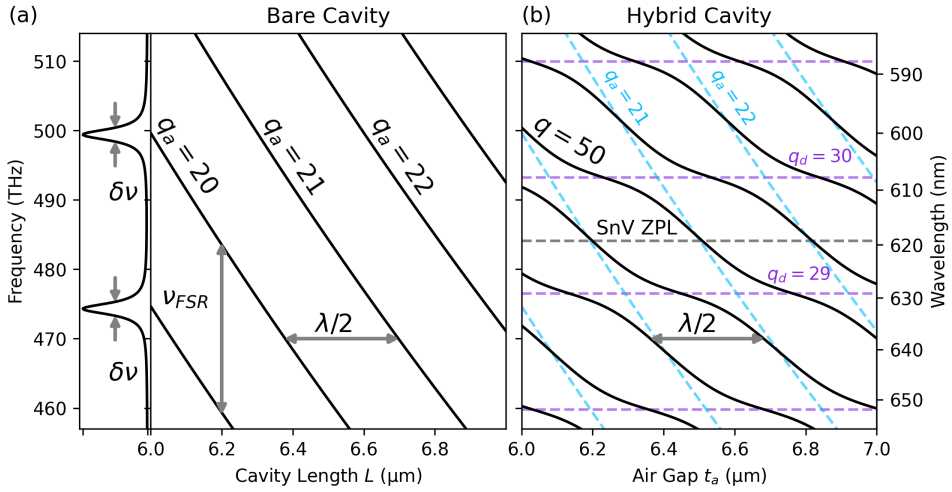

Figure 3.2: Resonance frequencies of the fundamental modes of a bare and hybrid cavity in dependence on the cavity (air gap) length. Figure based on Van Dam et al. [14]. In both cases, consecutive resonances along the cavity length are spaced by a distance of half of the wavelength ($\lambda/2$). (a) For the bare cavity, the resonance frequencies are calculated by equation (3.15) with the fundamental mode number q_a. The panel on the left side shows the Lorentzian peaks with a full width at half maximum cavity linewidth δ_ν. Consecutive modes are spaced by the free-spectral range ν_{FSR} in the spectral domain. (b) The resonance frequencies of modes appearing in a pure diamond cavity (purple) depend on the diamond thickness and the diamond mode number m_d and are calculated with equation (3.24). Air modes are the same as for the bare cavity (bright blue). For the hybrid diamond-air cavity, the resonance frequencies are calculated by equation (3.25) with $q = q_a + q_d$ for a diamond thickness of $t_d = 3.72\,\mu\mathrm{m}$. The SnV experiments in Chapter 6 are measured with the air-like $q = 50$ hybrid mode. The corresponding measurement of the resonance frequencies is shown in Fig. 6.1 (c). The plot script can be found under Ref. [112].

$$L_{\mathrm{eff}} = \frac{\int_{cav} \epsilon(z)|E(z)|^2 dz}{\epsilon_0 n_d^2 |E_{max,d}|^2/2}. \tag{3.26}$$

Here, $\epsilon = \epsilon_0 n^2$ is the permittivity of a medium with refractive index n, while $E(z)$ is the electric field in the cavity and $E_{\mathrm{max,d}}$ is the maximum electric field inside the diamond part. The effective length also includes the penetration depth into the layered dielectric cavity mirrors.

The effective length also leads to a modification of the losses encountered during the effective round trip, $\mathscr{L}_{\mathrm{eff}}$. For an emitter in diamond, we can model this by [14]:

$$\mathscr{L}_{\mathrm{eff}} = \frac{E_{\mathrm{max,a}}^2}{n_d E_{\mathrm{max,d}}^2} \mathscr{L}_{\mathscr{M},a} + \mathscr{L}_{\mathscr{M},d} + \mathscr{L}_{S,\mathrm{eff,d}}. \tag{3.27}$$

With $\mathscr{L}_{\mathscr{M},a}$ being the transmission losses through the air side and $\mathscr{L}_{\mathscr{M},d}$ through the diamond side mirror. Furthermore, $\mathscr{L}_{S,\mathrm{eff,d}}$ includes scattering losses at the air-diamond interface, which depend on the diamond surface roughness and the electric field amplitude at the interface [14] (equation (4.4) of Chapter 4). Absorption losses are excluded due

to their small contribution. The ratio of relative electric field intensities of air gap and diamond part $E^2_{\mathrm{max,a}}/(n_d E^2_{\mathrm{max,d}})$ fluctuates between a maximum of n_d in an air-like mode and a minimum of $1/n_d$ in the diamond-like mode (a formula to calculate this is given in Chapter 4, equation (4.3)).
We can take the equations of the bare cavity and replace the length L by L_{eff} and the losses $\mathscr{L}$ by $\mathscr{L}_{\mathrm{eff}}$. This leads to a cavity finesse and linewidth of the hybrid cavity [14]:

$$\mathscr{F} = \frac{2\pi}{\mathscr{L}_{\mathrm{eff}}} \qquad \delta\nu = \frac{c/(2n_d L_{\mathrm{eff}})}{2\pi/\mathscr{L}_{\mathrm{eff}}}. \tag{3.28}$$

By considering two coupled Gaussian beams in the air and diamond cavity, the beam waist of the hybrid cavity, located inside the diamond on the flat mirror, is given by [14]:

$$\omega_0 = \sqrt{\frac{\lambda}{\pi}}\left(\left(t_a + \frac{t_d}{n_d}\right)\left(ROC - \left(t_a + \frac{t_d}{n_d}\right)\right)\right)^{1/4} \tag{3.29}$$

Using this definition of the beam waist and the effective cavity length, equation (3.22) can be used to obtain the mode volume of the hybrid cavity. Note that the influence of the diamond membrane on the beam waist is small for the geometries explored in this thesis (percentage range).
With the beam waist and finesse of the hybrid cavity, we can calculate with equation (3.23) the Purcell factor of a color center hosted inside the diamond membrane.
More details on the hybrid microcavities can be found in Refs. [14, 106].

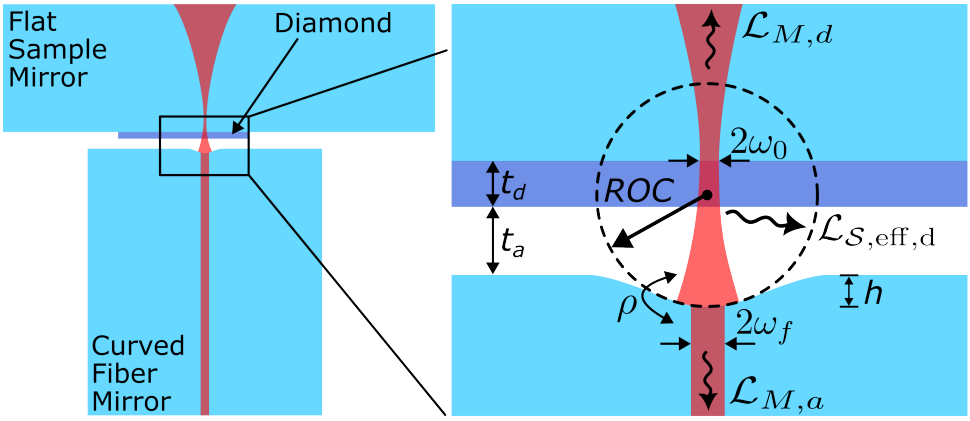

Figure 3.3: The hybrid diamond-air cavity. A diamond membrane of thickness t_d is bonded to the flat mirror, and a spherical fiber mirror with a radius of curvature ROC is placed at a distance of t_a from the diamond surface. The spherical feature on the fiber mirror has a depth of h. From the light guided by the optical fiber, a certain fraction ρ will couple into the cavity. This depends on the mode matching between the mode field radius ω_f of the fiber and the mode field radius of the cavity. An equation for ρ can be found in Hunger et al. [109]. The cavity beam waist is minimal on the flat mirror with ω_0. Light decays out of the cavity via the flat sample mirror (fiber mirror) with transmission loss $\mathscr{L}_{\mathrm{M,d}}$ ($\mathscr{L}_{\mathrm{M,a}}$) or is scattered from the diamond with $\mathscr{L}_{\mathrm{S,eff,d}}$.

3.3.2 A Brief History of Diamond Color Centers in Open Microcavities

For over a decade experiments with diamond color centers in open Fabry-Pérot microcavities have been conducted by more than ten research groups. Until now, NV centers, as well as many group-IV (GeV, SiV, and SnV), have been successfully coupled to a microcavity at cryogenic temperatures. Most of these works aim to enhance the resonant emission of the color centers for quantum applications. Furthermore, some of the realizations are enabled by fiber-based microcavities [109] (see next section).
The incorporation of a $\approx 10\,\mu m$ thin diamond membrane into a microcavity was demonstrated by Janitz et al. [106] in 2015. This work also introduced the modeling of the effects of the membrane on the cavity finesse and resonance frequency. The theory was extended by Van Dam et al. [14] with a cavity loss model to find the optimal design of diamond-air microcavities, including effects like cavity stability and efficient outcoupling.
On the experimental side, Bogdanović et al. [114] showed the design and characterization of a diamond membrane within a microcavity at low temperatures. A diamond microcavity with a high quality factor of a diamond-like mode ($Q = 1.2 \times 10^5$) combined with a small mode volume ($V = 3.9\ \lambda^3$) is demonstrated by Flågan et al. [105]. Further fabrication and characterization of smooth thinned-down diamond membranes and their incorporation into a microcavity are presented by Heupel et al. [115]. By performing scanning cavity microscopy, Körber et al. [116] systematically studied the influence of a diamond membrane on cavity properties such as finesse, transverse-mode mixing, and polarization-mode splitting. Chapter 4 of this thesis utilizes this technique to characterize microdevices obtained from a diamond membrane by laser-cutting and subsequent dry etching.
Ambient diamond microcavities have also been used in the context of lasing. The amplification by stimulated emission with NV centers as a gain medium in a diamond-loaded fiber cavity has been shown by Raman Nair et al. [117]. Furthermore, cavity-enhanced Raman scattering with a diamond membrane and a microcavity has been harnessed as a narrow-band high-intensity internal light source by Riedel et al. [118]. This is further developed by Flågan et al. [119], demonstrating that the in situ spectral and spatial tunability of the microcavity, combined with a diamond membrane exhibiting a small thickness gradient, can be used as a platform for tunable nonlinear optics.

NV centers: Pioneering cavity experiments have been realized under ambient conditions with nanodiamonds. In 2013, the cavity coupling of a single NV center was demonstrated by Albrecht et al. [120] and of a small NV center ensemble by Kaupp et al. [121]. The Purcell enhancement is determined by comparing the free space and cavity-enhanced emission rates. One year later, Albrecht et al. [122] coupled a single NV center to a fiber-fiber microcavity. By using a cavity fiber with a tapered end facet, Kaupp et al. [123] reached an ultrasmall mode volume of $1.0\ \lambda^3$ with nanodiamonds. As demonstrated by Dolan et al. [124], this platform can be used as a widely tunable, narrow-band source for single photons. At room temperature, the NV center shows a much broader linewidth (order of Terahertz). As described in Section 3.1.4, this can be considered in the calculation of the Purcell factor by a reduced, effective quality factor. Johnson et al. [125] demonstrated the first cavity-coupling at lower temperatures of 77 K, where the NV centers' ZPL is narrower. This work also showed the Purcell-reduced excited state lifetime of a NV center.
The following NV cavity experiments are realized with a diamond membrane. In 2017,

Riedel et al. [22] demonstrated Purcell-enhancement of individual NV centers for the first time at 4 K. The Purcell factor of 30 increased the resonant ZPL emission from 3 % to 46 %. Afterward, Ruf et al. [13] showed cavity-coupling of optically-coherent NV centers, which enabled the optical addressing of a single NV center with resonant excitation. This is further developed by Yurgens et al. [23], demonstrating cavity-assisted resonance fluorescence from a NV center combined with a high polarization suppression. This allowed, for the first time, the detection of resonant ZPL light without any temporal filtering. In Chapter 7 of this thesis, we combine such an efficient photonic interface for the NV center with coherent microwave control of the electron spin qubit to demonstrate cavity-enhanced spin-photon correlations.

All of these measurements are conducted with single NV centers. Recently, the collective emission of an ensemble of a few NV centers, mediated by a cryogenic microcavity, was demonstrated by Pallmann et al. [126]. Remarkably, for incoherent, inhomogeneous, and spatially separated NV centers, a superlinear power dependence of the emission is observed, which is a sign of superfluorescence.

SiV centers: In 2017, Benedikter et al. [50] coupled individual nanodiamond SiV centers to a fiber-based microcavity, with an excited state lifetime reduction at room temperatures. Bayer et al. [24] extended these measurements to low temperatures, including optical driving for spin initialization and readout. This work also demonstrated a SiV center linewidth close to the Fourier-transform limit for the used nanodiamonds. Häußler et al. [127] incorporated a $\approx 200\,\mathrm{nm}$ thin diamond membrane into a cavity-coupled fluorescence from an ensemble of SiV centers. This work also showed that the modification of the cavity mode dispersion is negligible for very thin diamond membranes. This is further developed by Salz et al. [128] to cryogenic temperatures, including optical spectroscopy of an ensemble of SiV centers. Recently, Berghaus et al. [25] demonstrated the lifetime reduction at low temperatures of SiV centers in a diamond membrane with selectable strain.

GeV centers: Cavity coupling of an individual GeV center hosted in a diamond membrane is demonstrated in 2020 by Jensen et al. [51] and 2023 with nanodiamonds by Feuchtmayr et al. [129]. These works observed the coupling with a spectral density enhancement of the ZPL emission.
With a GeV center in a diamond membrane, this is further developed by Zifkin et al. [130], demonstrating a large Purcell-reduced lifetime at low temperatures. This enabled the determination of a lower bound on the quantum efficiency of the GeV center of 0.34.

SnV centers: The first demonstration of SnV centers coupled to an open microcavity at low temperatures in the regime of coherent coupling is presented in Chapter 6. Recently, SnV centers in nanodiamond have been coupled to a microcavity at different temperatures, exploring the regimes of bad-emitter and bad-cavity coupling [131].

Note that there are also experiments conducted with diamonds in macroscopic Fabry-Pérot cavities (length of millimeters or more). The cavity enhancement can be used to boost the sensitivity of room temperature diamond magnetometers [132–134]. Moreover, a recent study presented the operation of a stable cavity at millikelvin temperatures in a cryogen-free dilution refrigerator in the context of quantum transduction [135].

3.3.3 Microcavity Mirrors

The spherical mirrors used in this thesis are fabricated on the tip of an optical fiber facet by laser ablation with a high-power, pulsed CO_2 laser. This method was introduced by Hunger, Reichel, and colleagues [109] and first utilized in cold atom experiments [136, 137]. Due to the high absorption of fused silica (SiO_2) in the range of 9-11 µm, the top part of the cleaved fiber end is heated up when irradiated with the ablation laser [111]. The laser is focused on the center of the fiber, matching the position of the fiber core. For appropriate irradiation parameters, glass is melted and evaporated, which leads to a Gaussian dimple (or crater) with a spherical structure at the bottom part. Such structures typically feature a low surface roughness [138]. After fabrication, the fiber end can be characterized with an interferometer to measure the height profile.

The cavity fibers used in this thesis are fabricated with a home-built CO_2 laser setup. The interferometer image and profile of an exemplary fiber after fabrication are shown in Fig. 3.4. The spherical part in the center can be fitted to extract the radius of curvature *ROC* of the dimple along an X- and Y-direction. This cavity fiber is later used for the SnV center measurements presented in Chapter 6.

After fabrication, the fiber is coated with a multilayer dielectric coating to obtain a highly reflective mirror. The coatings used in this thesis (for both, the fiber and the planar sample mirror) are composed of alternating layers of tantalum pentoxide Ta_2O_5 with an index of refraction of $n_{Ta_2O_5} = 2.13$ and silicon dioxide SiO_2 with an index of refraction of $n_{SiO_2} = 1.45$, both at 637 nm. The coating is produced with ion-beam sputtering by Laseroptik.

Before being used in the low-temperature setup, cavity fibers are characterized in a room temperature microcavity setup (details about the setup and the measurement methods can be found in the Appendix of Chapter 4). For fine positioning and active stabilization of the cavity length, the fiber can also be glued to a shear piezo (see also Section 5.2). The fiber mounting method is based on Janitz et al. [81], and further details about the gluing and active cavity length stabilization can be found in Feije [139]. The mirror coatings used in this thesis (except for the NV center measurements in Chapter 7) are specified with 50 ppm for the fiber mirror and 280 ppm for the sample mirror (air termination). This leads to a coating-limited finesse of around 2×10^4 (equations (3.17) and (3.18)). We typically observe finesse values limited to about 1×10^4 (corresponding to additional losses of about 280 ppm), which we attribute to the quality of the fiber dimple. To reduce the cavity beam waist, the fabrication of the cavity fibers aims for a minimal radius of curvature, with reached values in the range of 15 µm to 25 µm. With these fibers, the cavities usually show a constant finesse for length $L \leq 10\,\mu m$ (see Fig. 4.9 for an example measurement). More details and statistics of the fiber performances can be found in Scheijen [140].

The finesse of the cavity is an important quantity, as it determines the Purcell factor (equation (3.23)) and the cavity outcoupling efficiency. Especially for an optimization on outcou-

pled ZPL light, the additional losses from the fiber mirror need to be minimized. Assuming that the desired outcoupling mirror is the second mirror, the efficiency can be calculated by:

$$\frac{\kappa_{\text{out}}}{\kappa} = \frac{\mathscr{L}_{M,2}}{\mathscr{L}_{M,1} + \mathscr{L}_{M,2} + \mathscr{L}_{\text{add}}} = \frac{\mathscr{L}_{M,2}}{2\pi}\mathscr{F}. \tag{3.30}$$

Note that for the case of a hybrid cavity, the effective losses, the mode character, and a diamond mirror termination need to be considered. For the bare cavities of a finesse of 1×10^4 from above, the outcoupling efficiency through the planar sample mirror is about 46 %.

The coupling efficiency from the fiber into the cavity (ρ in Fig. 3.3) depends on the centering alignment between the fabricated dimple and the fiber core and the coupling between the two Gaussian modes in the fiber and in the cavity [109, 141]. The latter is also affected by the *ROC* of the fiber and decreases for smaller *ROC*s. This can be avoided by using an assembly of multiple fiber types for mode matching [142].

For the microdevices shown in Chapter 4, the additional fiber losses become a limitation for the used cavity fibers. However, it has been demonstrated that finesse values beyond 1×10^5 can be reached with fiber-based microcavities [138, 143–145]. Furthermore, it is also possible to taper the end of the fiber tip before fabricating the concave dimple, enabling submicron mirror separations [123].

Next to laser ablation, other methods have been employed to fabricate spherical mirrors with micrometer dimensions. For fiber tips, this includes top-down fabrication by focused ion beam milling [122] and bottom-up fabrication by three-dimensional direct laser writing [146, 147]. For substrates like silicon or borosilicate glass, methods for producing curved structures include chemical wet-etching [148, 149], thermal reflow [150, 151], or focused ion beam milling [152–155]. Moreover, a combination of different methods, such as focused ion beam milling and CO_2 laser smoothing [156] has shown promising results for fused silica substrates, which can also be used for fibers. A microcavity with a record finesse above one million could be reached by combining photoresist reflow and reactive ion etching [157]. This regime was previously limited to traditional polishing of glass substrates with much larger radii of curvature ($ROC \gg 1\,\text{mm}$) [158].

3.3.4 Vibration Sensitivity

The cavity resonance frequency can be tuned by changing the cavity length. However, this comes with the cost that every unwanted cavity length change influences the cavity resonance. This becomes especially challenging as the closed-cycle cryogenic system involves a moving cryostat cold head and pumps, introducing noise. To estimate the required stability level, we can calculate the spatial linewidth of an empty cavity (equation (3.20)) by:

$$\Delta L = \frac{\lambda}{2\mathscr{F}}. \tag{3.31}$$

The free spectral range is here replaced by $\lambda/2$ (the length distance between two fundamental resonances) and denotes the spatial cavity linewidth, only dependent on the cavity

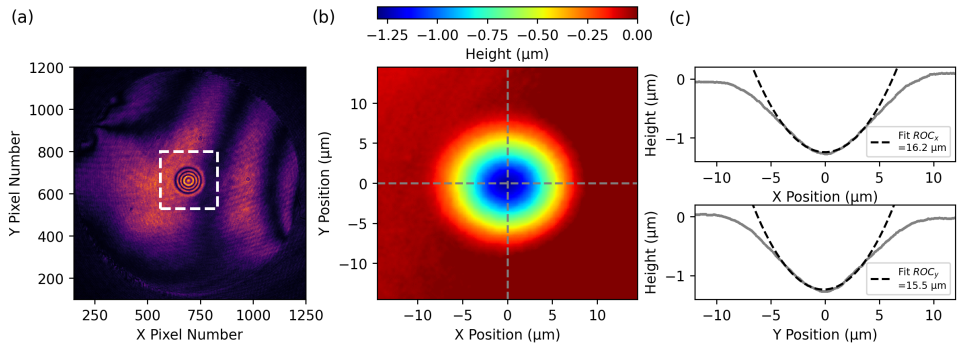

Figure 3.4: Fiber tip mirror used for the SnV center measurements presented in Chapter 6. The concave feature at the center of the fiber is produced by laser ablation. (a) Interference pattern of the cleaved fiber tip after fabrication of the concave dimple (without mirror coating). The white rectangle indicates the area of the height profile plotted in (b). The fiber has a diameter of 125 µm. (b) Height profile of the fiber tip extracted from the interferometer data. (c) Cross sections of the height profiles through the center of the dimple, indicated by the gray lines in (b). The black dashed line is a semicircle fit to extract the radius of curvature *ROC* along the different axes. The depth of the dimple is about 1.3 µm. The dataset and plot script can be found under Ref. [112].

finesse $\mathscr{F}$. For a finesse of 1×10^4 and a resonance frequency of 637 nm, the spatial cavity linewidth is about $\Delta L = 32\,\text{pm}$. Hence, the cavity length fluctuations need to be on a similar level, and such demanding requirements are comparable to cryogenic scanning probe microscopy experiments [159]. Note that the stability along the axial direction of the cavity is most critical, while the requirements on lateral vibrations are less stringent due to the micrometer-wide cavity beam waist.

For the hybrid diamond-air cavity system, the mode dispersion slope is altered and varies between a shallow slope in a diamond-like mode and a steeper slope in an air-like mode (see Fig. 3.2 (b)). This makes diamond-like modes less susceptible to vibrations. The cavity dispersion slope depends on the diamond thickness and air gap length and can be calculated by [14]:

$$s = \frac{\mathrm{d}\nu}{\mathrm{d}t_a} = \frac{-c}{(t_a + n_d t_d)\lambda}\left(1 \pm \frac{n_d - 1}{n_d + 1}\frac{2n_d t_d}{t_a + n_d t_d}\right) \tag{3.32}$$

The plus-sign (minus-sign) corresponds to an air-like (diamond-like) mode. Note that s can be experimentally determined by measuring the cavity resonance frequency in dependence on the length (see Fig. 6.1 (c) for example). With the mode dispersion slope, we can quantify the spatial linewidth of the hybrid cavity with $\Delta L = \delta\nu/s$).

The fluctuating cavity resonance frequency leads to detuning from the constant emitter frequency, which averages the Purcell factor. To quantify this, we can consider the spectral overlap of the emitter and cavity frequency [14] in dependence on the emitter-cavity detuning $\Delta\nu$:

$$\xi_s(\Delta\nu) = \frac{1}{1 + \frac{4Q^2}{\nu^2}\Delta\nu^2}. \tag{3.33}$$

Note that we assume here that the emitter linewidth is much smaller than the cavity linewidth. We can model the cavity frequency fluctuations by a Gaussian distribution with a probability density function [43]:

$$f(\Delta\nu) = \frac{1}{\sqrt{2\pi\sigma_\nu^2}} e^{-\Delta\nu^2/2\sigma_\nu^2}. \tag{3.34}$$

Here, σ_ν denotes the root mean square (RMS) cavity frequency fluctuations, which are related by the dispersion slope to the RMS cavity length fluctuations σ by $\sigma_\nu = s \cdot \sigma$.

Equation (3.23) can be used to calculate the maximum achievable Purcell factor F_P assuming no cavity length fluctuations. To include length fluctuations, we can calculate the vibration-averaged Purcell factor for an emitter on cavity resonance by [159]:

$$F_{\mathrm{P,avg}} = F_P \int_{-\infty}^{\infty} d(\Delta\nu)\xi_s(\Delta\nu)f(\Delta\nu) = F_P \sqrt{\frac{\pi}{8}} \frac{\delta\nu}{\sigma_\nu} e^{\frac{\delta\nu^2}{8\sigma_\nu^2}} \left(1 - \mathrm{erf}\left(\frac{\delta\nu}{2\sqrt{2}\sigma_\nu}\right)\right). \tag{3.35}$$

Where erf is the error function. Figure 3.5 shows this function plotted for the two different experimental scenarios of cavity-coupled SnV centers in Chapter 6 and NV centers in Chapter 7. In Chapter 5, we use this equation together with the Q/V dependence. Optimizing the quality factor leads to a maximum attainable Purcell factor, which can be reached for a given cavity geometry, which is defined by the mode volume V and the cavity dispersion slope s.

From Fig. 3.5 and equation (3.31), it becomes clear that for significant Purcell factors, a vibration level in the range of tens of picometers is required. Especially this is required when the cavity is operated in an air-like mode, which puts fewer requirements on the quality of diamond samples [14]. To reach these experimental conditions, a special low-vibration cryostat, together with a nanopositioning stage designed for stable cavity measurements, is used. This is described in detail in Chapter 5.

The experimentally demanding conditions to operate microcavities at low temperatures have first been achieved in a quite helium bath cryostats [160, 161] or with reduced spatial control in closed-cycle cryostats [162].

In recent years, several groups have demonstrated vibration levels down to tens of picometers in closed-cycle cryostats while still providing a large spatial tunability [159, 163–167]. Recently, cavity length fluctuations of 30 pm could also be achieved at 15 mK inside a cryogen-free dilution refrigerator system with a low finesse, millimeter-long cavity [135]. Furthermore, it is possible to improve the stability level by actively locking the cavity length. This can be achieved with electronic feedback on the fiber positioning system [81] or thermally by exploiting the self-stabilization mechanism of microcavities [168]. Utilizing both methods, a sub-picometer vibration level has been demonstrated at room temperature with a fiber-based microcavity [145]. Both methods have also been demonstrated at cryogenic temperatures [162, 166, 167, 169].

3.3.5 Microwave Delivery

Coherent qubit control over the electron spin of a cavity-coupled color center can be obtained by driving the spin state with microwaves. It is therefore required to bring a microwave antenna close to the cavity spot. The efficiency of the microwave driving determines the Rabi frequency and thereby the time needed for quantum gate operations. To

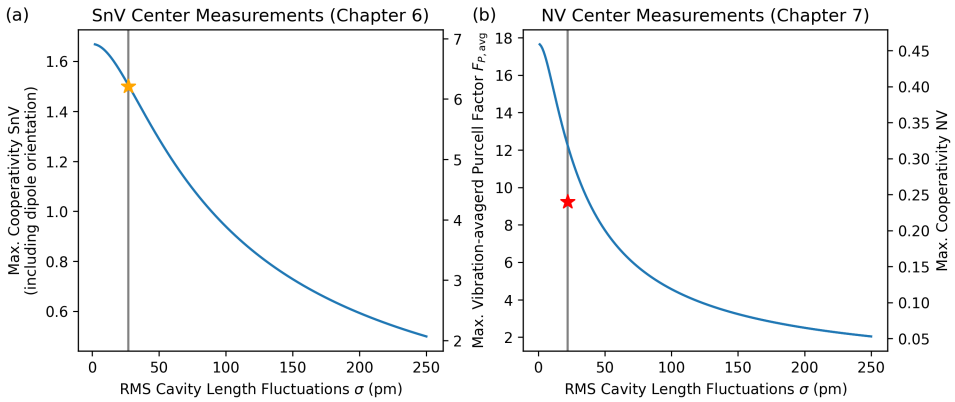

Figure 3.5: Influence of the root mean square (RMS) cavity length fluctuations on the maximum vibration-averaged Purcell factor and cooperativity assuming the parameters of the microcavity experiments presented in Chapter 6 and Chapter 7. The maximum vibration-averaged Purcell factor is calculated by equation (3.35), assuming that the cavity is on resonance with the emitter (no detuning) and that the emitter is ideally placed in the maximum of the intracavity electric field ($\epsilon = 1$). (a) The cavity properties of $Q = 7 \times 10^4$ and $V = 55\ \lambda^3$ result in a maximum Purcell factor of 6.9 without vibrations. This translates into a maximum cooperativity of $C = 1.7$ for a SnV center, assuming literature values of the optical properties ($\xi_{SnV} = 0.36$ [44, 52, 53]) and the dipole orientation of SnV centers in the used ⟨100⟩ diamond sample ($\zeta^2 = \cos^2(35^\circ)$). The star marks the measured cooperativity for the vibration level of 27 pm present during the measurements indicated by the gray line. (b) The cavity properties of $Q = 2.8 \times 10^5$ and $V = 86\ \lambda^3$ result in a maximum Purcell factor of about 17.5 without vibrations. This translates into a maximum cooperativity of $C = 0.52$ for a NV center, assuming literature values of the optical properties ($\xi_{NV} = 0.03$ [22, 99]) and perfect dipole orientation of the NV center $\zeta^2 = 1$. The star marks the measured cooperativity for the vibration level of 22 pm present during the measurements indicated by the gray line. The plot script can be found under Ref. [112].

obtain Rabi frequencies in the Megahertz regime, a high-power amplifier and an antenna at tens of micrometers distance from the color center are usually required. The antenna is often realized by a gold stripline or a bondwire.

In this work, we make use of a gold stripline deposited into or onto the cavity sample mirror. The fabrication of the microwave striplines is based on earlier work [170], which demonstrated that the achievable mirror finesse is not deterred by the fabrication process. This method is designed for a millimeter larger diameter membrane, which is bonded on the flat mirror (after stripline fabrication) and subsequently thinned down as detailed in Ruf et al. [171]. Due to the larger dimensions, the striplines are embedded into the sample mirror, which is used for microwave control in Chapter 7 of this thesis. The striplines can be connected with wirebonds to a custom printed circuit board inside the cryostat, which connects further to microwave cabling (shown in Chapter 5).

With the microdevices from Chapter 4, stripline can also be deposited onto the mirror without the prior etching of trenches. It is also possible to fabricate the stripline on the mirror after microdevices are bonded to it. An exemplary sample obtained in this way is shown in Fig. 3.6 (a). This method has the advantage that targeted microwave structures can be fabricated after well-bonded microdevices on the cavity mirror are obtained. Such devices can also be first characterized by scanning cavity microscopy [116, 172] to measure the finesse or a potential polarization splitting.

Due to the larger dimensions of a few tens of micrometers in diameter, it is challenging to bring a bondwire close to a microcavity mode. An alternative approach is therefore to attach a microwave antenna loop around the cavity fiber [111]. Despite being at a longer distance to the cavity-coupled color center (at least half of the fiber diameter, so 62.5 µm for typical single-mode fibers), this design brings the advantage that the produced microwave field is independent of the lateral position on the sample mirror, which allows for investigating larger sample areas. Another promising approach with the same advantage, but a reduced distance between electrodes and microcavity spot, is to equip the fiber end facet with additional electronic structures. This approach is demonstrated by Faßbender [173], and a schematic depiction with an omega-shaped antenna on a fiber end facet is shown in Fig. 3.6 (b). Arbitrary two-dimensional metallic structures are printed with a polymeric mask by three-dimensional laser lithography. Afterward, the fiber end is metalized by thermal evaporation in a deposition chamber. This process is conducted after laser ablating the spherical structure and subsequent mirror coating, and has shown that the cavity finesse does not deteriorate [111, 173].

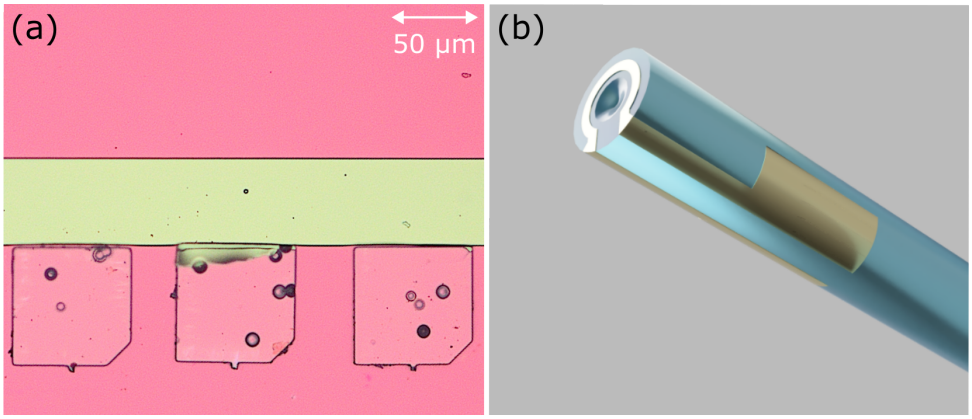

Figure 3.6: Methods for integrating microwave delivery into the microcavity. (a) A microwave stripline on the pink cavity mirror next to diamond microdevices. Note that the stripline is fabricated after bonding the devices to the mirror. This method of microwave delivery is used in Chapter 7 with a different diamond sample. Figure courtesy of Zahra Sadre Momtaz. (b) A cavity fiber tip with a concave dimple in the center is micro-structured with a metallic electrode forming an omega-shaped antenna. The antenna is fabricated with a polymeric mask and can be connected with contacting pads on the fiber tube. Figure adapted from Faßbender [173].

3.4 Micrometer-thin Diamond Samples

In this thesis, SnV centers created by tin implantation and NV centers created by electron irradiation are used. To fit between the two cavity mirrors, the diamond samples hosting the color centers need to have a thickness of up to a few micrometers. For the NV center, such samples have shown that good optical properties are maintained [171, 174]. In contrast, SnV centers have shown good optical properties even in nanostructures [37, 63], which would also allow using sub-micrometer thin diamond samples [83].
Table 3.2 provides an overview of the diamond samples used in this thesis, which are fabricated by three different methods, summarized in the following. All fabrication methods start with about 50 µm thick diamond membranes, which can be obtained from commercially available single-crystal, electronic-grade diamonds. These are laser-sliced into thinner pieces, followed by polishing, as detailed in the supplementary material of earlier work [171]. The three fabrication methods are:

- **Microdevices patterned by e-beam lithography:** A silicon nitride layer is deposited on the diamond membrane, followed by patterning with electron beam (e-beam) lithography. After transferring these structures into the diamond, the membrane is etched from the backside with a quartz mask until the target device thickness is reached. Suspended devices are held on the diamond membrane by a bridge and can be broken out with a micromanipulator above the mirror. This method is introduced in Ruf [13] and used in Chapter 4 to fabricate diamond microdevices. Further information is presented in Sauerzapf [175].
- **Microdevices patterned by laser-cutting:** The diamond membrane is patterned in one step by laser-cutting. Subsequently, devices are thinned down from the backside with a quartz mask and released with a micromanipulator. Further details can be found in Chapter 4 and Sauerzapf [175].
- **Thinned-down diamond membrane:** The $(2 \times 2)\,\mathrm{mm}^2$ membrane is bonded on the cavity mirror and subsequently thinned down to the required thickness by reactive ion etching with a quartz mask protecting the mirror. Details can be found in Ruf et al. [171].

Each sample is bonded to a highly reflective cavity sample mirror. In addition, some mirrors are equipped with gold striplines for microwave delivery (see previous section).

Sample Name	Color Center	Fabrication Method	Used in
Mr. Orange	NV Centers Electron Irradiation with $4 \times 10^{13}\,e^-/cm^2$	E-beam Lithography	Chapter 4
Ringo	NV Centers Electron Irradiation with $4 \times 10^{13}\,e^-/cm^2$	Laser-Cutting	Chapter 4 additional data (4.8.7)
Vincent Vega	SnV Centers Tin Ion Implantation with $3 \times 10^{10}\,ions/cm^2$	Laser-Cutting	Chapters 4 and 6
California Mountain Snake	SnV Centers Tin Ion Implantation with $5 \times 10^{10}\,ions/cm^2$	E-beam Lithography	Chapter 5
Pai Mei	Empty	E-beam Lithography	Chapter 4
THE Sample	NV Centers Electron Irradiation with $5 \times 10^{13}\,e^-/cm^2$	Bonded on mirror and thinned-down with quartz mask	Chapters 5 and 7 and Ruf et al. [43]

Table 3.2: Overview of diamond samples used in this thesis. The detailed fabrication process for the devices fabricated by e-beam lithography and laser-cutting can be found in Chapter 4. The parameters in the process of color center creation are the same; only the irradiation/implantation dose is varied to obtain different color center densities. The sample named *Pai Mei* is electron irradiated, but no NV centers could be found afterward. A possible explanation is that the membrane was accidentally interchanged with a different one, which is irradiated with a lower dose, leading to a lower color center density. The samples are listed in cinematographic order.

References

[1] S. Haroche and J.-M. Raimond, *Exploring the Quantum* (Oxford University Press, 2006).

[2] J. M. Raimond, M. Brune, S. Haroche, and L. K. Brossel, *Colloquium: Manipulating quantum entanglement with atoms and photons in a cavity,* Rev. Mod. Phys. **73**, 565 (2001).

[3] P. Goy, J. M. Raimond, M. Gross, and S. Haroche, *Observation of Cavity-Enhanced Single-Atom Spontaneous Emission,* Phys. Rev. Lett. **50**, 1903 (1983).

[4] S. Gleyzes, S. Kuhr, C. Guerlin, J. Bernu, S. Deléglise, U. Busk Hoff, M. Brune, J.-M. Raimond, and S. Haroche, *Quantum jumps of light recording the birth and death of a photon in a cavity,* Nature **446**, 297 (2007).

[5] D. J. Heinzen, J. J. Childs, J. E. Thomas, and M. S. Feld, *Enhanced and inhibited visible spontaneous emission by atoms in a confocal resonator,* Phys. Rev. Lett. **58**, 1320 (1987).

[6] F. D. Martini, G. Innocenti, G. R. Jacobovitz, and P. Mataloni, *Anomalous Spontaneous Emission Time in a Microscopic Optical Cavity,* Phys. Rev. Lett. **59**, 2955 (1987).

[7] R. J. Thompson, G. Rempe, and H. J. Kimble, *Observation of normal-mode splitting for an atom in an optical cavity,* Phys. Rev. Lett. **68**, 1132 (1992).

[8] J. McKeever, A. Boca, A. D. Boozer, J. R. Buck, and H. J. Kimble, *Experimental realization of a one-atom laser in the regime of strong coupling,* Nature **425**, 268 (2003).

[9] J. McKeever, A. Boca, A. D. Boozer, R. Miller, J. R. Buck, A. Kuzmich, and H. J. Kimble, *Deterministic Generation of Single Photons from One Atom Trapped in a Cavity,* Science **303**, 1992 (2004).

[10] E. Fermi, *Quantum Theory of Radiation,* Rev. Mod. Phys. **4**, 87 (1932).

[11] M. Fox, *Quantum Optics: An Introduction*, Oxford master series in physics No. 15 (Oxford University Press, Oxford; New York, 2006).

[12] E. M. Purcell, *Spontaneous emission probabilities at radio frequencies,* Phys. Rev. **69**, 681 (1946).

[13] M. Ruf, *Cavity-enhanced quantum network nodes in diamond*, Ph.D. thesis, Delft University of Technology (2021).

[14] S. B. van Dam, M. Ruf, and R. Hanson, *Optimal design of diamond-air microcavities for quantum networks using an analytical approach,* New J. Phys. **20**, 115004 (2018).

[15] A. M. Zaitsev, *Optical Properties of Diamond* (Springer Berlin Heidelberg, Berlin, Heidelberg, 2001).

[16] M. K. Bhaskar, D. D. Sukachev, A. Sipahigil, R. E. Evans, M. J. Burek, C. T. Nguyen, L. J. Rogers, P. Siyushev, M. H. Metsch, H. Park, F. Jelezko, M. Lončar, and M. D. Lukin, *Quantum Nonlinear Optics with a Germanium-Vacancy Color Center in a Nanoscale Diamond Waveguide,* Phys. Rev. Lett. **118**, 223603 (2017).

[17] A. Reiserer and G. Rempe, *Cavity-based quantum networks with single atoms and optical photons,* Rev. Mod. Phys. **87**, 1379 (2015).

[18] J. Borregaard, A. S. Sørensen, and P. Lodahl, *Quantum Networks with Deterministic Spin–Photon Interfaces,* Adv. Quantum Technol. **2**, 1800091 (2019).

[19] M. Bitarafan and R. DeCorby, *On-Chip High-Finesse Fabry-Perot Microcavities for Optical Sensing and Quantum Information,* Sensors **17**, 1748 (2017).

[20] A. Sipahigil, R. E. Evans, D. D. Sukachev, M. J. Burek, J. Borregaard, M. K. Bhaskar, C. T. Nguyen, J. L. Pacheco, H. A. Atikian, C. Meuwly, R. M. Camacho, F. Jelezko, E. Bielejec, H. Park, M. Lončar, and M. D. Lukin, *An integrated diamond nanophotonics platform for quantum-optical networks,* Science **354**, 847 (2016).

[21] A. Faraon, C. Santori, Z. Huang, V. M. Acosta, and R. G. Beausoleil, *Coupling of Nitrogen-Vacancy Centers to Photonic Crystal Cavities in Monocrystalline Diamond,* Phys. Rev. Lett. **109**, 033604 (2012).

[22] D. Riedel, I. Söllner, B. J. Shields, S. Starosielec, P. Appel, E. Neu, P. Maletinsky, and R. J. Warburton, *Deterministic Enhancement of Coherent Photon Generation from a Nitrogen-Vacancy Center in Ultrapure Diamond,* Phys. Rev. X **7**, 031040 (2017).

[23] V. Yurgens, Y. Fontana, A. Corazza, B. J. Shields, P. Maletinsky, and R. J. Warburton, *Cavity-assisted resonance fluorescence from a nitrogen-vacancy center in diamond,* npj Quantum Inf. **10**, 112 (2024).

[24] G. Bayer, R. Berghaus, S. Sachero, A. B. Filipovski, L. Antoniuk, N. Lettner, R. Waltrich, M. Klotz, P. Maier, V. Agafonov, and A. Kubanek, *Optical driving, spin initialization and readout of single SiV- centers in a Fabry-Perot resonator,* Commun. Phys. **6**, 300 (2023).

[25] R. Berghaus, S. Sachero, G. Bayer, J. Heupel, T. Herzig, F. Feuchtmayr, J. Meijer, C. Popov, and A. Kubanek, *Cavity-enhanced emission and absorption of color centers in a diamond membrane with selectable strain,* Phys. Rev. Applied **23**, 034050 (2025).

[26] K. G. Fehler, L. Antoniuk, N. Lettner, A. P. Ovvyan, R. Waltrich, N. Gruhler, V. A. Davydov, V. N. Agafonov, W. H. P. Pernice, and A. Kubanek, *Hybrid Quantum Photonics Based on Artificial Atoms Placed Inside One Hole of a Photonic Crystal Cavity,* ACS Photonics **8**, 2635 (2021).

[27] N. Lettner, L. Antoniuk, A. P. Ovvyan, H. Gehring, D. Wendland, V. N. Agafonov, W. H. P. Pernice, and A. Kubanek, *Controlling All Degrees of Freedom of the Optical Coupling in Hybrid Quantum Photonics,* ACS Photonics **11**, 696 (2024).

[28] S. Chakravarthi, N. S. Yama, A. Abulnaga, D. Huang, C. Pederson, K. Hestroffer, F. Hatami, N. P. De Leon, and K.-M. C. Fu, *Hybrid Integration of GaP Photonic Crystal Cavities with Silicon-Vacancy Centers in Diamond by Stamp-Transfer,* Nano Lett. **23**, 3708 (2023).

[29] J. Miguel-Sánchez, A. Reinhard, E. Togan, T. Volz, A. Imamoglu, B. Besga, J. Reichel, and J. Estève, *Cavity quantum electrodynamics with charge-controlled quantum dots coupled to a fiber Fabry–Perot cavity,* New J. Phys. **15**, 045002 (2013).

[30] D. Wang, H. Kelkar, D. Martin-Cano, T. Utikal, S. Götzinger, and V. Sandoghdar, *Coherent Coupling of a Single Molecule to a Scanning Fabry-Perot Microcavity,* Phys. Rev. X **7**, 021014 (2017).

[31] D. M. Lukin, M. A. Guidry, J. Yang, M. Ghezellou, S. Deb Mishra, H. Abe, T. Ohshima, J. Ul-Hassan, and J. Vučković, *Two-Emitter Multimode Cavity Quantum Electrodynamics in Thin-Film Silicon Carbide Photonics,* Phys. Rev. X **13**, 011005 (2023).

[32] D. E. Chang, V. Vuletić, and M. D. Lukin, *Quantum nonlinear optics — photon by photon,* Nat. Photonics **8**, 685 (2014).

[33] J. Bochmann, M. Mücke, G. Langfahl-Klabes, C. Erbel, B. Weber, H. P. Specht, D. L. Moehring, and G. Rempe, *Fast Excitation and Photon Emission of a Single-Atom-Cavity System,* Phys. Rev. Lett. **101**, 223601 (2008).

[34] E. Jaynes and F. Cummings, *Comparison of quantum and semiclassical radiation theories with application to the beam maser,* Proc. IEEE **51**, 89 (1963).

[35] A. Reiserer, S. Ritter, and G. Rempe, *Nondestructive Detection of an Optical Photon,* Science **342**, 1349 (2013).

[36] R. E. Evans, A. Sipahigil, D. D. Sukachev, A. S. Zibrov, and M. D. Lukin, *Narrow-Linewidth Homogeneous Optical Emitters in Diamond Nanostructures via Silicon Ion Implantation,* Phys. Rev. Applied **5**, 044010 (2016).

[37] A. E. Rugar, C. Dory, S. Aghaeimeibodi, H. Lu, S. Sun, S. D. Mishra, Z.-X. Shen, N. A. Melosh, and J. Vučković, *Narrow-Linewidth Tin-Vacancy Centers in a Diamond Waveguide,* ACS Photonics **7**, 2356 (2020).

[38] M. K. Bhaskar, R. Riedinger, B. Machielse, D. S. Levonian, C. T. Nguyen, E. N. Knall, H. Park, D. Englund, M. Lončar, D. D. Sukachev, and M. D. Lukin, *Experimental demonstration of memory-enhanced quantum communication,* Nature **580**, 60 (2020).

[39] C. T. Nguyen, D. D. Sukachev, M. K. Bhaskar, B. Machielse, D. S. Levonian, E. N. Knall, P. Stroganov, R. Riedinger, H. Park, M. Lončar, and M. D. Lukin, *Quantum Network Nodes Based on Diamond Qubits with an Efficient Nanophotonic Interface,* Phys. Rev. Lett. **123**, 183602 (2019).

[40] P.-J. Stas, Y. Q. Huan, B. Machielse, E. N. Knall, A. Suleymanzade, B. Pingault, M. Sutula, S. W. Ding, C. M. Knaut, D. R. Assumpcao, Y.-C. Wei, M. K. Bhaskar, R. Riedinger, D. D. Sukachev, H. Park, M. Lončar, D. S. Levonian, and M. D. Lukin,

Robust multi-qubit quantum network node with integrated error detection, Science **378**, 557 (2022).

[41] H. K. Beukers, M. Pasini, H. Choi, D. Englund, R. Hanson, and J. Borregaard, *Remote-Entanglement Protocols for Stationary Qubits with Photonic Interfaces,* PRX Quantum **5**, 010202 (2024).

[42] E. N. Knall, C. M. Knaut, R. Bekenstein, D. R. Assumpcao, P. L. Stroganov, W. Gong, Y. Q. Huan, P.-J. Stas, B. Machielse, M. Chalupnik, D. Levonian, A. Suleymanzade, R. Riedinger, H. Park, M. Lončar, M. K. Bhaskar, and M. D. Lukin, *Efficient Source of Shaped Single Photons Based on an Integrated Diamond Nanophotonic System,* Phys. Rev. Lett. **129**, 053603 (2022).

[43] M. Ruf, M. Weaver, S. van Dam, and R. Hanson, *Resonant Excitation and Purcell Enhancement of Coherent Nitrogen-Vacancy Centers Coupled to a Fabry-Perot Microcavity,* Phys. Rev. Applied **15**, 024049 (2021).

[44] J. Görlitz, D. Herrmann, G. Thiering, P. Fuchs, M. Gandil, T. Iwasaki, T. Taniguchi, M. Kieschnick, J. Meijer, M. Hatano, A. Gali, and C. Becher, *Spectroscopic investigations of negatively charged tin-vacancy centres in diamond,* New J. Phys. **22**, 013048 (2020).

[45] N. Kalb, P. C. Humphreys, J. J. Slim, and R. Hanson, *Dephasing mechanisms of diamond-based nuclear-spin memories for quantum networks,* Phys. Rev. A **97**, 062330 (2018).

[46] S. L. N. Hermans, M. Pompili, L. D. Santos Martins, A. R-P Montblanch, H. K. C. Beukers, S. Baier, J. Borregaard, and R. Hanson, *Entangling remote qubits using the single-photon protocol: an in-depth theoretical and experimental study,* New J. Phys. **25**, 013011 (2023).

[47] R. E. Evans, M. K. Bhaskar, D. D. Sukachev, C. T. Nguyen, A. Sipahigil, M. J. Burek, B. Machielse, G. H. Zhang, A. S. Zibrov, E. Bielejec, H. Park, M. Lončar, and M. D. Lukin, *Photon-mediated interactions between quantum emitters in a diamond nanocavity,* Science **362**, 662 (2018).

[48] A. Auffèves, D. Gerace, J.-M. Gérard, M. F. Santos, L. C. Andreani, and J.-P. Poizat, *Controlling the dynamics of a coupled atom-cavity system by pure dephasing,* Phys. Rev. B **81**, 245419 (2010).

[49] A. Meldrum, P. Bianucci, and F. Marsiglio, *Modification of ensemble emission rates and luminescence spectra for inhomogeneously broadened distributions of quantum dots coupled to optical microcavities,* Opt. Express **18**, 10230 (2010).

[50] J. Benedikter, H. Kaupp, T. Hümmer, Y. Liang, A. Bommer, C. Becher, A. Krueger, J. M. Smith, T. W. Hänsch, and D. Hunger, *Cavity-Enhanced Single-Photon Source Based on the Silicon-Vacancy Center in Diamond,* Phys. Rev. Applied **7**, 024031 (2017).

[51] R. Høy Jensen, E. Janitz, Y. Fontana, Y. He, O. Gobron, I. P. Radko, M. Bhaskar, R. Evans, C. D. Rodríguez Rosenblueth, L. Childress, A. Huck, and U. Lund Andersen, *Cavity-Enhanced Photon Emission from a Single Germanium-Vacancy Center in a Diamond Membrane,* Phys. Rev. Applied **13**, 064016 (2020).

[52] T. Iwasaki, Y. Miyamoto, T. Taniguchi, P. Siyushev, M. H. Metsch, F. Jelezko, and M. Hatano, *Tin-Vacancy Quantum Emitters in Diamond,* Phys. Rev. Lett. **119**, 253601 (2017).

[53] A. E. Rugar, S. Aghaeimeibodi, D. Riedel, C. Dory, H. Lu, P. J. McQuade, Z.-X. Shen, N. A. Melosh, and J. Vučković, *Quantum Photonic Interface for Tin-Vacancy Centers in Diamond,* Phys. Rev. X **11**, 031021 (2021).

[54] I. P. Radko, M. Boll, N. M. Israelsen, N. Raatz, J. Meijer, F. Jelezko, U. L. Andersen, and A. Huck, *Determining the internal quantum efficiency of shallow-implanted nitrogen-vacancy defects in bulk diamond,* Opt. Express **24**, 27715 (2016).

[55] K. Drexhage, *Influence of a dielectric interface on fluorescence decay time,* J. Lumin. **1-2**, 693 (1970).

[56] A. Kubanek, A. P. Ovvyan, L. Antoniuk, N. Lettner, and W. H. P. Pernice, *Hybrid Quantum Nanophotonics - Interfacing Color Center in Nanodiamonds with Si_3N_4 - Photonics,* in *Progress in Nanophotonics 7*, edited by T. Yatsui (Springer International Publishing, Cham, 2022) pp. 123–174.

[57] K. G. Fehler, A. P. Ovvyan, N. Gruhler, W. H. P. Pernice, and A. Kubanek, *Efficient Coupling of an Ensemble of Nitrogen Vacancy Center to the Mode of a High-Q, Si_3N_4 Photonic Crystal Cavity,* ACS Nano **13**, 6891 (2019).

[58] D. Englund, B. Shields, K. Rivoire, F. Hatami, J. Vučković, H. Park, and M. D. Lukin, *Deterministic Coupling of a Single Nitrogen Vacancy Center to a Photonic Crystal Cavity,* Nano Lett. **10**, 3922 (2010).

[59] T. Ishikawa, K.-M. C. Fu, C. Santori, V. M. Acosta, R. G. Beausoleil, H. Watanabe, S. Shikata, and K. M. Itoh, *Optical and Spin Coherence Properties of Nitrogen-Vacancy Centers Placed in a 100 nm Thick Isotopically Purified Diamond Layer,* Nano Lett. **12**, 2083 (2012).

[60] K. W. Lee, D. Lee, P. Ovartchaiyapong, J. Minguzzi, J. R. Maze, and A. C. Bleszynski Jayich, *Strain Coupling of a Mechanical Resonator to a Single Quantum Emitter in Diamond,* Phys. Rev. Applied **6**, 034005 (2016).

[61] I. Lekavicius, T. Oo, and H. Wang, *Diamond Lamb wave spin-mechanical resonators with optically coherent nitrogen vacancy centers,* J. Appl. Phys. **126**, 214301 (2019).

[62] T. Jung, J. Görlitz, B. Kambs, C. Pauly, N. Raatz, R. Nelz, E. Neu, A. M. Edmonds, M. Markham, F. Mücklich, J. Meijer, and C. Becher, *Spin measurements of NV centers coupled to a photonic crystal cavity,* APL Photonics **4**, 120803 (2019).

[63] M. Pasini, N. Codreanu, T. Turan, A. Riera Moral, C. F. Primavera, L. De Santis, H. K. C. Beukers, J. M. Brevoord, C. Waas, J. Borregaard, and R. Hanson, *Nonlinear Quantum Photonics with a Tin-Vacancy Center Coupled to a One-Dimensional Diamond Waveguide,* Phys. Rev. Lett. **133**, 023603 (2024).

[64] R. A. Parker, J. Arjona Martínez, K. C. Chen, A. M. Stramma, I. B. Harris, C. P. Michaels, M. E. Trusheim, M. Hayhurst Appel, C. M. Purser, W. G. Roth, D. Englund, and M. Atatüre, *A diamond nanophotonic interface with an optically accessible deterministic electronuclear spin register,* Nat. Photon. **18**, 156 (2024).

[65] X. Guo, M. Xie, A. Addhya, A. Linder, U. Zvi, S. Wang, X. Yu, T. D. Deshmukh, Y. Liu, I. N. Hammock, Z. Li, C. T. DeVault, A. Butcher, A. P. Esser-Kahn, D. D. Awschalom, N. Delegan, P. C. Maurer, F. J. Heremans, and A. A. High, *Direct-bonded diamond membranes for heterogeneous quantum and electronic technologies,* Nat. Commun. **15**, 8788 (2024).

[66] L. Li, T. Schröder, E. H. Chen, M. Walsh, I. Bayn, J. Goldstein, O. Gaathon, M. E. Trusheim, M. Lu, J. Mower, M. Cotlet, M. L. Markham, D. J. Twitchen, and D. Englund, *Coherent spin control of a nanocavity-enhanced qubit in diamond,* Nat. Commun. **6**, 6173 (2015).

[67] J. T. Choy, B. J. M. Hausmann, T. M. Babinec, I. Bulu, M. Khan, P. Maletinsky, A. Yacoby, and M. Lončar, *Enhanced single-photon emission from a diamond–silver aperture,* Nat. Photonics **5**, 738 (2011).

[68] S. I. Bogdanov, M. Y. Shalaginov, A. S. Lagutchev, C.-C. Chiang, D. Shah, A. S. Baburin, I. A. Ryzhikov, I. A. Rodionov, A. V. Kildishev, A. Boltasseva, and V. M. Shalaev, *Ultrabright Room-Temperature Sub-Nanosecond Emission from Single Nitrogen-Vacancy Centers Coupled to Nanopatch Antennas,* Nano Lett. **18**, 4837 (2018).

[69] K. Kuruma, B. Pingault, C. Chia, D. Renaud, P. Hoffmann, S. Iwamoto, C. Ronning, and M. Lončar, *Coupling of a single tin-vacancy center to a photonic crystal cavity in diamond,* Appl. Phys. Lett. **118**, 230601 (2021).

[70] N. Codreanu, *Diamond Nanophotonic Devices for Quantum Networks Experiments*, Ph.D. thesis, Delft University of Technology (2025).

[71] X. Guo, N. Delegan, J. C. Karsch, Z. Li, T. Liu, R. Shreiner, A. Butcher, D. D. Awschalom, F. J. Heremans, and A. A. High, *Tunable and Transferable Diamond Membranes for Integrated Quantum Technologies,* Nano Lett. **21**, 10392 (2021).

[72] S. W. Ding, M. Haas, X. Guo, K. Kuruma, C. Jin, Z. Li, D. D. Awschalom, N. Delegan, F. J. Heremans, A. A. High, and M. Lončar, *High-Q cavity interface for color centers in thin film diamond,* Nat. Commun. **15**, 6358 (2024).

[73] R. Katsumi, K. Takada, F. Jelezko, and T. Yatsui, *Recent progress in hybrid diamond photonics for quantum information processing and sensing,* Commun. Eng. **4**, 85 (2025).

[74] A. Butcher, X. Guo, R. Shreiner, N. Delegan, K. Hao, P. J. I. Duda, D. D. Awschalom, F. J. Heremans, and A. A. High, *High-Q Nanophotonic Resonators on Diamond Membranes using Templated Atomic Layer Deposition of TiO2,* Nano Lett. **20**, 4603 (2020).

[75] L. J. Rogers, O. Wang, Y. Liu, L. Antoniuk, C. Osterkamp, V. A. Davydov, V. N. Agafonov, A. B. Filipovski, F. Jelezko, and A. Kubanek, *Single Si - V - Centers in Low-Strain Nanodiamonds with Bulklike Spectral Properties and Nanomanipulation Capabilities,* Phys. Rev. Applied **11**, 024073 (2019).

[76] R. Waltrich, M. Klotz, V. N. Agafonov, and A. Kubanek, *Two-photon interference from silicon-vacancy centers in remote nanodiamonds,* Nanophotonics **12**, 3663 (2023).

[77] M. J. Burek, C. Meuwly, R. E. Evans, M. K. Bhaskar, A. Sipahigil, S. Meesala, B. Machielse, D. D. Sukachev, C. T. Nguyen, J. L. Pacheco, E. Bielejec, M. D. Lukin, and M. Lončar, *Fiber-Coupled Diamond Quantum Nanophotonic Interface,* Phys. Rev. Appl. **8**, 024026 (2017).

[78] B. Zeng, C. De-Eknamkul, D. Assumpcao, D. Renaud, Z. Wang, D. Riedel, J. Ha, C. Robens, D. Levonian, M. Lukin, R. Riedinger, M. Bhaskar, D. Sukachev, M. Lončar, and B. Machielse, *Cryogenic packaging of nanophotonic devices with a low coupling loss <1 dB,* Appl. Phys. Lett. **123**, 161106 (2023).

[79] T. Masuda, J. P. E. Hadden, D. P. Lake, M. Mitchell, S. Flågan, and P. E. Barclay, *Fiber-taper collected emission from NV centers in high-Q/V diamond microdisks,* Opt. Express **32**, 8172 (2024).

[80] H. Li, D. Acil, A. M. Boyce, N. S. Yama, C. Pederson, S. Chakravarthi, K.-M. C. Fu, and M. H. Mikkelsen, *Room-Temperature Picosecond Single-Photon Emission from a Silicon Vacancy Center in Diamond,* ACS Nano **19**, 19310 (2025).

[81] E. Janitz, M. Ruf, Y. Fontana, J. Sankey, and L. Childress, *High mechanical bandwidth fiber-coupled Fabry-Perot cavity,* Opt. Express **25**, 20932 (2017).

[82] C. T. Nguyen, D. D. Sukachev, M. K. Bhaskar, B. Machielse, D. S. Levonian, E. N. Knall, P. Stroganov, C. Chia, M. J. Burek, R. Riedinger, H. Park, M. Lončar, and M. D. Lukin, *An integrated nanophotonic quantum register based on silicon-vacancy spins in diamond,* Phys. Rev. B **100**, 165428 (2019).

[83] X. Guo, A. M. Stramma, Z. Li, W. G. Roth, B. Huang, Y. Jin, R. A. Parker, J. Arjona Martínez, N. Shofer, C. P. Michaels, C. P. Purser, M. H. Appel, E. M. Alexeev, T. Liu, A. C. Ferrari, D. D. Awschalom, N. Delegan, B. Pingault, G. Galli, F. J. Heremans, M. Atatüre, and A. A. High, *Microwave-Based Quantum Control and Coherence Protection of Tin-Vacancy Spin Qubits in a Strain-Tuned Diamond-Membrane Heterostructure,* Phys. Rev. X **13**, 041037 (2023).

[84] I. Karapatzakis, J. Resch, M. Schrodin, P. Fuchs, M. Kieschnick, J. Heupel, L. Kussi, C. Sürgers, C. Popov, J. Meijer, C. Becher, W. Wernsdorfer, and D. Hunger, *Microwave Control of the Tin-Vacancy Spin Qubit in Diamond with a Superconducting Waveguide,* Phys. Rev. X **14**, 031036 (2024).

[85] I. B. W. Harris, I. Christen, S. M. Patomäki, H. Raniwala, M. Sirotin, M. Colangelo, K. C. Chen, C. Errando-Herranz, D. J. Starling, R. Murphy, K. Shtyrkova, O. Medeiros, M. E. Trusheim, K. K. Berggren, P. B. Dixon, and D. Englund, *High-Fidelity Control of a Strongly Coupled Electro-Nuclear Spin-Photon Interface,* arXiv:2505.09267 (2025).

[86] L. Li, L. D. Santis, I. B. W. Harris, K. C. Chen, Y. Gao, I. Christen, H. Choi, M. Trusheim, Y. Song, C. Errando-Herranz, J. Du, Y. Hu, G. Clark, M. I. Ibrahim, G. Gilbert, R. Han, and D. Englund, *Heterogeneous integration of spin–photon interfaces with a CMOS platform,* Nature **630**, 70 (2024).

[87] G. Clark, H. Raniwala, M. Koppa, K. Chen, A. Leenheer, M. Zimmermann, M. Dong, L. Li, Y. H. Wen, D. Dominguez, M. Trusheim, G. Gilbert, M. Eichenfield, and D. Englund, *Nanoelectromechanical Control of Spin–Photon Interfaces in a Hybrid Quantum System on Chip,* Nano Lett. **24**, 1316 (2024).

[88] J. M. Brevoord, L. G. C. Wienhoven, N. Codreanu, T. Ishiguro, E. van Leeuwen, M. Iuliano, L. De Santis, C. Waas, H. K. C. Beukers, T. Turan, C. Errando-Herranz, K. Kawaguchi, and R. Hanson, *Large-range tuning and stabilization of the optical transition of diamond tin-vacancy centers by in situ strain control,* Appl. Phys. Lett. **126** (2025).

[89] S. Sun, J. L. Zhang, K. A. Fischer, M. J. Burek, C. Dory, K. G. Lagoudakis, Y.-K. Tzeng, M. Radulaski, Y. Kelaita, A. Safavi-Naeini, Z.-X. Shen, N. A. Melosh, S. Chu, M. Lončar, and J. Vučković, *Cavity-Enhanced Raman Emission from a Single Color Center in a Solid,* Phys. Rev. Lett. **121**, 083601 (2018).

[90] N. H. Wan, T.-J. Lu, K. C. Chen, M. P. Walsh, M. E. Trusheim, L. De Santis, E. A. Bersin, I. B. Harris, S. L. Mouradian, I. R. Christen, E. S. Bielejec, and D. Englund, *Large-scale integration of artificial atoms in hybrid photonic circuits,* Nature **583**, 226 (2020).

[91] S. L. Mouradian, T. Schröder, C. B. Poitras, L. Li, J. Goldstein, E. H. Chen, M. Walsh, J. Cardenas, M. L. Markham, D. J. Twitchen, M. Lipson, and D. Englund, *Scalable Integration of Long-Lived Quantum Memories into a Photonic Circuit,* Phys. Rev. X **5**, 031009 (2015).

[92] K. C. Chen, I. Christen, H. Raniwala, M. Colangelo, L. De Santis, K. Shtyrkova, D. Starling, R. Murphy, L. Li, K. Berggren, P. B. Dixon, M. Trusheim, and D. Englund, *A scalable cavity-based spin–photon interface in a photonic integrated circuit,* Opt. Quantum **2**, 124 (2024).

[93] C. M. Knaut, A. Suleymanzade, Y.-C. Wei, D. R. Assumpcao, P.-J. Stas, Y. Q. Huan, B. Machielse, E. N. Knall, M. Sutula, G. Baranes, N. Sinclair, C. De-Eknamkul, D. S. Levonian, M. K. Bhaskar, H. Park, M. Lončar, and M. D. Lukin, *Entanglement of nanophotonic quantum memory nodes in a telecom network,* Nature **629**, 573 (2024).

[94] T. Schröder, S. L. Mouradian, J. Zheng, M. E. Trusheim, M. Walsh, E. H. Chen, L. Li, I. Bayn, and D. Englund, *Quantum nanophotonics in diamond [Invited],* J. Opt. Soc. Am. B **33**, B65 (2016).

[95] S. Mi, M. Kiss, T. Graziosi, and N. Quack, *Integrated photonic devices in single crystal diamond,* J. Phys. Photonics **2**, 042001 (2020).

[96] E. Janitz, M. K. Bhaskar, and L. Childress, *Cavity quantum electrodynamics with color centers in diamond,* Optica **7**, 1232 (2020).

[97] P. K. Shandilya, S. Flagan, N. C. Carvalho, E. Zohari, V. K. Kavatamane, J. E. Losby, and P. E. Barclay, *Diamond Integrated Quantum Nanophotonics: Spins, Photons and Phonons,* J. Lightwave Technol. **40**, 7538 (2022).

[98] J. Riedrich-Möller, L. Kipfstuhl, C. Hepp, E. Neu, C. Pauly, F. Mücklich, A. Baur, M. Wandt, S. Wolff, M. Fischer, S. Gsell, M. Schreck, and C. Becher, *One- and two-dimensional photonic crystal microcavities in single crystal diamond,* Nat. Nanotechnol. **7**, 69 (2012).

[99] A. Faraon, P. E. Barclay, C. Santori, K.-M. C. Fu, and R. G. Beausoleil, *Resonant enhancement of the zero-phonon emission from a colour centre in a diamond cavity,* Nat. Photonics **5**, 301 (2011).

[100] B. Khanaliloo, M. Mitchell, A. C. Hryciw, and P. E. Barclay, *High-Q/V Monolithic Diamond Microdisks Fabricated with Quasi-isotropic Etching,* Nano Lett. **15**, 5131 (2015).

[101] M. Mitchell, D. P. Lake, and P. E. Barclay, *Realizing Q > 300 000 in diamond microdisks for optomechanics via etch optimization,* APL Photonics **4** (2019).

[102] K. G. Fehler, A. P. Ovvyan, L. Antoniuk, N. Lettner, N. Gruhler, V. A. Davydov, V. N. Agafonov, W. H. Pernice, and A. Kubanek, *Purcell-enhanced emission from individual SiV $^-$ center in nanodiamonds coupled to a Si_3N_4 -based, photonic crystal cavity,* Nanophotonics **9**, 3655 (2020).

[103] A. M. Boyce, H. Li, N. C. Wilson, D. Acil, A. Shams-Ansari, S. Chakravarthi, C. Pederson, Q. Shen, N. Yama, K.-M. C. Fu, M. Lončar, and M. H. Mikkelsen, *Plasmonic Diamond Membranes for Ultrafast Silicon Vacancy Emission,* Nano Lett. **24**, 3575 (2024).

[104] I. Bulu, T. Babinec, B. Hausmann, J. T. Choy, and M. Lončar, *Plasmonic resonators for enhanced diamond NV- center single photon sources,* Opt. Express **19**, 5268 (2011).

[105] S. Flågan, D. Riedel, A. Javadi, T. Jakubczyk, P. Maletinsky, and R. J. Warburton, *A diamond-confined open microcavity featuring a high quality-factor and a small mode-volume,* J. Appl. Phys. **131**, 113102 (2022).

[106] E. Janitz, M. Ruf, M. Dimock, A. Bourassa, J. Sankey, and L. Childress, *Fabry-Perot microcavity for diamond-based photonics,* Phys. Rev. A **92**, 043844 (2015).

[107] Y. Herrmann, *Silicon Vacancy Centers in Diamond Coupled to a Fiber-based Microcavity at Cryogenic Temperatures*, Master's thesis, Johannes Gutenberg-Universität Mainz (2019).

[108] C. Koks and M. P. Van Exter, *Microcavity resonance condition, quality factor, and mode volume are determined by different penetration depths,* Opt. Express **29**, 6879 (2021).

[109] D. Hunger, T. Steinmetz, Y. Colombe, C. Deutsch, T. W. Hänsch, and J. Reichel, *A fiber Fabry–Perot cavity with high finesse,* New J. Phys. **12**, 065038 (2010).

[110] H. Kogelnik and T. Li, *Laser beams and resonators,* Proc. IEEE **54**, 1312 (1966).

[111] H. Pfeifer, L. Ratschbacher, J. Gallego, C. Saavedra, A. Faßbender, A. Von Haaren, W. Alt, S. Hofferberth, M. Köhl, S. Linden, and D. Meschede, *Achievements and perspectives of optical fiber Fabry–Perot cavities,* Appl. Phys. B **128**, 29 (2022).

[112] Y. Herrmann, *Data underlying the dissertation "Good Vibrations: A Microcavity-based Diamond Spin-Photon Interface for Quantum Networking",* 4TU.ResearchData, Dataset (2025).

[113] S. van Dam, *Optical cavities, coherent emitters, and protocols for diamond-based quantum networks*, Ph.D. thesis, Delft University of Technology (2019).

[114] S. Bogdanović, S. B. van Dam, C. Bonato, L. C. Coenen, A.-M. J. Zwerver, B. Hensen, M. S. Z. Liddy, T. Fink, A. Reiserer, M. Lončar, and R. Hanson, *Design and low-temperature characterization of a tunable microcavity for diamond-based quantum networks,* Appl. Phys. Lett. **110**, 171103 (2017).

[115] J. Heupel, M. Pallmann, J. Körber, R. Merz, M. Kopnarski, R. Stöhr, J. P. Reithmaier, D. Hunger, and C. Popov, *Fabrication and Characterization of Single-Crystal Diamond Membranes for Quantum Photonics with Tunable Microcavities,* Micromachines **11**, 1080 (2020).

[116] J. Körber, M. Pallmann, J. Heupel, R. Stöhr, E. Vasilenko, T. Hümmer, L. Kohler, C. Popov, and D. Hunger, *Scanning Cavity Microscopy of a Single-Crystal Diamond Membrane,* Phys. Rev. Applied **19**, 064057 (2023).

[117] S. Raman Nair, L. J. Rogers, X. Vidal, R. P. Roberts, H. Abe, T. Ohshima, T. Yatsui, A. D. Greentree, J. Jeske, and T. Volz, *Amplification by stimulated emission of nitrogen-vacancy centres in a diamond-loaded fibre cavity,* Nanophotonics **9**, 4505 (2020).

[118] D. Riedel, S. Flågan, P. Maletinsky, and R. J. Warburton, *Cavity-Enhanced Raman Scattering for In Situ Alignment and Characterization of Solid-State Microcavities,* Phys. Rev. Applied **13**, 014036 (2020).

[119] S. Flågan, P. Maletinsky, R. J. Warburton, and D. Riedel, *Microcavity platform for widely tunable optical double resonance,* Optica **9**, 1197 (2022).

[120] R. Albrecht, A. Bommer, C. Deutsch, J. Reichel, and C. Becher, *Coupling of a Single Nitrogen-Vacancy Center in Diamond to a Fiber-Based Microcavity,* Phys. Rev. Lett. **110**, 243602 (2013).

[121] H. Kaupp, C. Deutsch, H.-C. Chang, J. Reichel, T. W. Hänsch, and D. Hunger, *Scaling laws of the cavity enhancement for nitrogen-vacancy centers in diamond,* Phys. Rev. A **88**, 053812 (2013).

[122] R. Albrecht, A. Bommer, C. Pauly, F. Mücklich, A. W. Schell, P. Engel, T. Schröder, O. Benson, J. Reichel, and C. Becher, *Narrow-band single photon emission at room temperature based on a single nitrogen-vacancy center coupled to an all-fiber-cavity,* Appl. Phys. Lett. **105**, 073113 (2014).

[123] H. Kaupp, T. Hümmer, M. Mader, B. Schlederer, J. Benedikter, P. Haeusser, H.-C. Chang, H. Fedder, T. W. Hänsch, and D. Hunger, *Purcell-Enhanced Single-Photon Emission from Nitrogen-Vacancy Centers Coupled to a Tunable Microcavity,* Phys. Rev. Applied **6**, 054010 (2016).

[124] P. R. Dolan, S. Adekanye, A. A. P. Trichet, S. Johnson, L. C. Flatten, Y. C. Chen, L. Weng, D. Hunger, H.-C. Chang, S. Castelletto, and J. M. Smith., *Robust, tunable, and high purity triggered single photon source at room temperature using a nitrogen-vacancy defect in diamond in an open microcavity,* Opt. Express **26**, 7056 (2018).

[125] S. Johnson, P. R. Dolan, T. Grange, A. A. P. Trichet, G. Hornecker, Y. C. Chen, L. Weng, G. M. Hughes, A. A. R. Watt, A. Auffèves, and J. M. Smith, *Tunable cavity coupling of the zero phonon line of a nitrogen-vacancy defect in diamond,* New J. Phys. **17**, 122003 (2015).

[126] M. Pallmann, K. Köster, Y. Zhang, J. Heupel, T. Eichhorn, C. Popov, K. Mølmer, and D. Hunger, *Cavity-Mediated Collective Emission from Few Emitters in a Diamond Membrane,* Phys. Rev. X **14**, 041055 (2024).

[127] S. Häußler, J. Benedikter, K. Bray, B. Regan, A. Dietrich, J. Twamley, I. Aharonovich, D. Hunger, and A. Kubanek, *Diamond photonics platform based on silicon vacancy centers in a single-crystal diamond membrane and a fiber cavity,* Phys. Rev. B **99**, 165310 (2019).

[128] M. Salz, Y. Herrmann, A. Nadarajah, A. Stahl, M. Hettrich, A. Stacey, S. Prawer, D. Hunger, and F. Schmidt-Kaler, *Cryogenic platform for coupling color centers in diamond membranes to a fiber-based microcavity,* Appl. Phys. B **126**, 131 (2020).

[129] F. Feuchtmayr, R. Berghaus, S. Sachero, G. Bayer, N. Lettner, R. Waltrich, P. Maier, V. Agafonov, and A. Kubanek, *Enhanced spectral density of a single germanium vacancy center in a nanodiamond by cavity integration,* Appl. Phys. Lett. **123**, 024001 (2023).

[130] R. Zifkin, C. D. Rodríguez Rosenblueth, E. Janitz, Y. Fontana, and L. Childress, *Lifetime Reduction of Single Germanium-Vacancy Centers in Diamond via a Tunable Open Microcavity,* PRX Quantum **5**, 030308 (2024).

[131] S. Sachero, R. Berghaus, E. N. Hernandez, F. Feuchtmayr, N. Lettner, P. Maier, S. D. Tchernij, and A. Kubanek, *Tunable cavity coupling of a single SnV- center in nanodiamond across bad-emitter and bad-cavity regimes,* arXiv:2507.06553 (2025).

[132] K. Jensen, N. Leefer, A. Jarmola, Y. Dumeige, V. M. Acosta, P. Kehayias, B. Patton, and D. Budker, *Cavity-Enhanced Room-Temperature Magnetometry Using Absorption by Nitrogen-Vacancy Centers in Diamond,* Phys. Rev. Lett. **112**, 160802 (2014).

[133] G. Chatzidrosos, A. Wickenbrock, L. Bougas, N. Leefer, T. Wu, K. Jensen, Y. Dumeige, and D. Budker, *Miniature Cavity-Enhanced Diamond Magnetometer,* Phys. Rev. Applied **8**, 044019 (2017).

[134] F. A. Hahl, L. Lindner, X. Vidal, T. Luo, T. Ohshima, S. Onoda, S. Ishii, A. M. Zaitsev, M. Capelli, B. C. Gibson, A. D. Greentree, and J. Jeske, *Magnetic-field-dependent stimulated emission from nitrogen-vacancy centers in diamond,* Sci. Adv. **8**, eabn7192 (2022).

[135] T. Hamamoto, A. Bhunia, H. Takahashi, and Y. Kubo, *Stabilizing an optical cavity containing a bulk diamond crystal at millikelvin temperatures in a cryogen-free dilution refrigerator,* Rev. Sci. Instrum. **96**, 085201 (2025).

[136] Y. Colombe, T. Steinmetz, G. Dubois, F. Linke, D. Hunger, and J. Reichel, *Strong atom–field coupling for Bose–Einstein condensates in an optical cavity on a chip,* Nature **450**, 272 (2007).

[137] J. Volz, R. Gehr, G. Dubois, J. Estève, and J. Reichel, *Measurement of the internal state of a single atom without energy exchange,* Nature **475**, 210 (2011).

[138] D. Hunger, C. Deutsch, R. J. Barbour, R. J. Warburton, and J. Reichel, *Laser microfabrication of concave, low-roughness features in silica,* AIP Advances **2**, 012119 (2012).

[139] L. J. Feije, *Active Length Stabilisation of an Open Fabry-Pérot Microcavity for Colour Centres in Diamond*, Master's thesis, Delft University of Technology (2021).

[140] S. Scheijen, *Cavity-Enhanced Coherent Emission of Nitrogen-Vacancy Centers in Diamond*, Master's thesis, Delft University of Technology (2024).

[141] J. Gallego, S. Ghosh, S. K. Alavi, W. Alt, M. Martinez-Dorantes, D. Meschede, and L. Ratschbacher, *High-finesse fiber Fabry–Perot cavities: stabilization and mode matching analysis,* Appl. Phys. B **122**, 47 (2016).

[142] G. K. Gulati, H. Takahashi, N. Podoliak, P. Horak, and M. Keller, *Fiber cavities with integrated mode matching optics,* Sci. Rep. **7**, 5556 (2017).

[143] A. Muller, E. B. Flagg, J. R. Lawall, and G. S. Solomon, *Ultrahigh-finesse, low-mode-volume Fabry Perot microcavity,* Opt. Lett. **35**, 2293 (2010).

[144] M. Uphoff, M. Brekenfeld, G. Rempe, and S. Ritter, *Frequency splitting of polarization eigenmodes in microscopic Fabry–Perot cavities,* New J. Phys. **17**, 013053 (2015).

[145] J. F. S. Brachmann, H. Kaupp, T. W. Hänsch, and D. Hunger, *Photothermal effects in ultra-precisely stabilized tunable microcavities,* Opt. Express **24**, 21205 (2016).

[146] J. Hessenauer, K. Weber, J. Benedikter, T. Gissibl, J. Höfer, H. Giessen, and D. Hunger, *Laser written mirror profiles for open-access fiber Fabry-Perot microcavities,* Opt. Express **31**, 17380 (2023).

[147] J. W. Smith, J. C. Williams, J. S. Suelzer, N. G. Usechak, and H. Chandrahalim, *Three-dimensional Fabry–Pérot cavities sculpted on fiber tips using a multiphoton polymerization process,* J. Micromech. Microeng. **30**, 125007 (2020).

[148] M. Trupke, E. A. Hinds, S. Eriksson, E. A. Curtis, Z. Moktadir, E. Kukharenka, and M. Kraft, *Microfabricated high-finesse optical cavity with open access and small volume,* Appl. Phys. Lett. **87**, 211106 (2005).

[149] G. Wachter, S. Kuhn, S. Minniberger, C. Salter, P. Asenbaum, J. Millen, M. Schneider, J. Schalko, U. Schmid, A. Felgner, D. Hüser, M. Arndt, and M. Trupke, *Silicon microcavity arrays with open access and a finesse of half a million,* Light. Sci. Appl. **8**, 37 (2019).

[150] G. Cui, J. M. Hannigan, R. Loeckenhoff, F. M. Matinaga, M. G. Raymer, S. Bhongale, M. Holland, S. Mosor, S. Chatterjee, H. M. Gibbs, and G. Khitrova, *A hemispherical, high-solid-angle optical micro-cavity for cavity-QED studies,* Opt. Express **14**, 2289 (2006).

[151] A. Roy and M. D. Barrett, *Fabrication of glass micro-cavities for cavity quantum electrodynamics experiments,* Appl. Phys. Lett. **99**, 171112 (2011).

[152] P. R. Dolan, G. M. Hughes, F. Grazioso, B. R. Patton, and J. M. Smith, *Femtoliter tunable optical cavity arrays,* Opt. Lett. **35**, 3556 (2010).

[153] Z. Di, H. V. Jones, P. R. Dolan, S. M. Fairclough, M. B. Wincott, J. Fill, G. M. Hughes, and J. M. Smith, *Controlling the emission from semiconductor quantum dots using ultra-small tunable optical microcavities,* New J. Phys. **14**, 103048 (2012).

[154] H. Kelkar, D. Wang, D. Martín-Cano, B. Hoffmann, S. Christiansen, S. Götzinger, and V. Sandoghdar, *Sensing Nanoparticles with a Cantilever-Based Scannable Optical Cavity of Low Finesse and Sub- λ 3 Volume,* Phys. Rev. Applied **4**, 054010 (2015).

[155] B. T. Walker, B. J. Ash, A. A. P. Trichet, J. M. Smith, and R. A. Nyman, *Bespoke mirror fabrication for quantum simulation with light in open-access microcavities,* Opt. Express **29**, 10800 (2021).

[156] P. Maier, S. Rupp, N. Lettner, J. H. Denschlag, and A. Kubanek, *Fabrication of customized low-loss optical resonators by combination of FIB-milling and CO_2 laser smoothing,* Opt. Express **33**, 19205 (2025).

[157] N. Jin, C. A. McLemore, D. Mason, J. P. Hendrie, Y. Luo, M. L. Kelleher, P. Kharel, F. Quinlan, S. A. Diddams, and P. T. Rakich, *Micro-fabricated mirrors with finesse exceeding one million,* Optica **9**, 965 (2022).

[158] G. Rempe, R. Lalezari, R. J. Thompson, and H. J. Kimble, *Measurement of ultralow losses in an optical interferometer,* Opt. Lett. **17**, 363 (1992).

[159] Y. Fontana, R. Zifkin, E. Janitz, C. D. Rodríguez Rosenblueth, and L. Childress, *A mechanically stable and tunable cryogenic Fabry–Pérot microcavity,* Rev. Sci. Instrum. **92**, 053906 (2021).

[160] L. Greuter, S. Starosielec, D. Najer, A. Ludwig, L. Duempelmann, D. Rohner, and R. J. Warburton, *A small mode volume tunable microcavity: Development and characterization,* Appl. Phys. Lett. **105**, 121105 (2014).

[161] D. Najer, I. Söllner, P. Sekatski, V. Dolique, M. C. Löbl, D. Riedel, R. Schott, S. Starosielec, S. R. Valentin, A. D. Wieck, N. Sangouard, A. Ludwig, and R. J. Warburton, *A gated quantum dot strongly coupled to an optical microcavity,* Nature **575**, 622 (2019).

[162] B. Merkel, A. Ulanowski, and A. Reiserer, *Coherent and Purcell-Enhanced Emission from Erbium Dopants in a Cryogenic High- Q Resonator,* Phys. Rev. X **10**, 041025 (2020).

[163] B. Casabone, C. Deshmukh, S. Liu, D. Serrano, A. Ferrier, T. Hümmer, P. Goldner, D. Hunger, and H. De Riedmatten, *Dynamic control of Purcell enhanced emission of erbium ions in nanoparticles,* Nat. Commun. **12**, 3570 (2021).

[164] S. Vadia, J. Scherzer, H. Thierschmann, C. Schäfermeier, C. Dal Savio, T. Taniguchi, K. Watanabe, D. Hunger, K. Karraï, and A. Högele, *Open-Cavity in Closed-Cycle Cryostat as a Quantum Optics Platform,* PRX Quantum **2**, 040318 (2021).

[165] T. Ruelle, D. Jaeger, F. Fogliano, F. Braakman, and M. Poggio, *A tunable fiber Fabry–Perot cavity for hybrid optomechanics stabilized at 4 K,* Rev. Sci. Instrum. **93**, 095003 (2022).

[166] M. Pallmann, T. Eichhorn, J. Benedikter, B. Casabone, T. Hümmer, and D. Hunger, *A highly stable and fully tunable open microcavity platform at cryogenic temperatures,* APL Photonics **8**, 046107 (2023).

[167] M. Fisicaro, M. Witlox, H. Van Der Meer, and W. Löffler, *Active stabilization of an open-access optical microcavity for low-noise operation in a standard closed-cycle cryostat,* Rev. Sci. Instrum. **95**, 033101 (2024).

[168] T. Carmon, L. Yang, and K. J. Vahala, *Dynamical thermal behavior and thermal self-stability of microcavities,* Opt. Express **12**, 4742 (2004).

[169] A. Farsi, M. Siciliani De Cumis, F. Marino, and F. Marin, *Photothermal and thermo-refractive effects in high reflectivity mirrors at room and cryogenic temperature,* J. Appl. Phys. **111**, 043101 (2012).

[170] S. Bogdanović, M. S. Z. Liddy, S. B. van Dam, L. C. Coenen, T. Fink, M. Lončar, and R. Hanson, *Robust nano-fabrication of an integrated platform for spin control in a tunable microcavity,* APL Photonics **2**, 126101 (2017).

[171] M. Ruf, M. IJspeert, S. van Dam, N. de Jong, H. van den Berg, G. Evers, and R. Hanson, *Optically Coherent Nitrogen-Vacancy Centers in Micrometer-Thin Etched Diamond Membranes,* Nano Lett. **19**, 3987 (2019).

[172] M. Mader, J. Reichel, T. W. Hänsch, and D. Hunger, *A scanning cavity microscope,* Nat. Commun. **6**, 7249 (2015).

[173] A. Faßbender, *Adding New Functionalities to Optical Fiber Cavities by Direct Laser Writing*, Ph.D. thesis, Rheinische Friedrich-Wilhelms-Universität Bonn (2023).

[174] V. Yurgens, A. Corazza, J. A. Zuber, M. Gruet, M. Kasperczyk, B. J. Shields, R. J. Warburton, Y. Fontana, and P. Maletinsky, *Spectrally stable nitrogen-vacancy centers in diamond formed by carbon implantation into thin microstructures,* Appl. Phys. Lett. **121**, 234001 (2022).

[175] C. Sauerzapf, *Fabrication and characterization of micrometerthin, color center-enriched diamonds for open microcavity quantum network nodes*, Master's thesis, Delft University of Technology (2023).

4

Laser-cut Patterned, Micrometer-thin Diamond Membranes with Coherent Color Centers for Open Microcavities

"It is the wood that should fear your hand, not the other way around."
- Pai Mei in Kill Bill: Vol. 2

Y. Herrmann*, J. M. Brevoord*, J. Fischer*, S. Scheijen, N. Codreanu, L .G. C. Wienhoven, Y. M. Q. van der Graaf, C. F. J. Wolfs, R. Méjard, M. Ruf, N. de Jong and R. Hanson

Micrometer-scale thin diamond devices are key components for various quantum sensing and networking experiments, including the integration of color centers into optical microcavities. In this work, we introduce a laser-cutting method for patterning microdevices from millimeter-sized diamond membranes. The method can be used to fabricate devices with micrometer thicknesses and edge lengths of typically 10 µm to 100 µm. We compare this method with an established nanofabrication process based on electron-beam lithography, a two-step transfer pattern utilizing a silicon nitride hard mask material, and reactive ion etching. Microdevices fabricated using both methods are bonded to a cavity Bragg mirror and characterized using scanning cavity microscopy. We record two-dimensional cavity finesse maps over the devices, revealing insights about the variation in diamond thickness, surface quality, and strain. The scans demonstrate that devices fabricated by laser-cutting exhibit similar properties to devices obtained by the conventional method. Finally, we show that the devices host optically coherent tin- and nitrogen-vacancy centers suitable for applications in quantum networking.

*These authors contributed equally to this work.

This chapter, excluding Section 4.8, has been published in Materials for Quantum Technology **5**, 035001 (2025) under Ref. [1]. The authors Y. H., J. M. B., J. F., C. S., M. R., N. d. J., and R. H. filed a patent for the method of laser-cutting device fabrication used in this chapter.

4.1 Introduction

Single-crystal (sub) micrometer-thin diamond samples hosting coherent color centers are relevant for several quantum technology applications spanning from quantum networking to sensing. In quantum networking, such platforms can be used to engineer the photonic environment of color centers for enhanced photon collection [2–5]. This includes photonic crystal cavities, fabricated directly into the diamond [6–9] and thinned-down membranes, coated from both sides with a dielectric layer, which can function as an optical antenna [10]. Furthermore, such platforms can be incorporated into open microcavities [11–13] and they facilitate the manufacturing of heterogeneous photonic structures such as solid immersion lenses [14], nanophotonic resonators [15, 16] or plasmonic nanogap cavities [17].

In quantum sensing, chemically inert and biocompatible, thin diamond samples can bring color centers near other materials, while still providing optical access. This can be used in sensing of living cells [16], wide-field microscopy of electrical currents [18], or magnetic fields [19–23].

In this work, our main focus is on the fabrication of diamond microdevices for open microcavities to Purcell-enhance color centers hosted inside the device. While pioneering work made use of color centers in nanodiamonds [24–26], a micrometer-thin diamond sample is beneficial to maintain good optical coherence, especially in the case of nitrogen-vacancy centers [27, 28]. Such diamond samples have been used to couple nitrogen-vacancy and group-IV vacancy centers to open microcavities [29–32]. The coupling of color centers to the cavity is quantified by the Purcell factor, which is proportional to Q/V, where Q denotes the cavity quality factor and V is the cavity mode volume. To demonstrate significant Purcell enhancement of color centers, the following microdevice properties must be taken into consideration: (1) A thickness of a few micrometers (or less) is desired to minimize the cavity mode volume. (2) A smooth surface (roughness R_q ⊠ 1 nm) is needed to maintain a high cavity quality factor (finesse). (3) Large lateral dimensions (tens of micrometers) with a small wedge are beneficial to provide an area to probe several cavity spots (cavity beam waist is on the order of a micrometer). (4) Bonding to a cavity Bragg mirror at a micrometer distance to a stripline for delivering microwaves [33] or static electric fields [34] is necessary. (5) The sample should contain color centers with good optical properties for quantum science and technology applications. While these criteria are relevant for the microcavity platform, they are also relevant to most of the applications mentioned.

Several fabrication methods have been developed to realize (sub) micrometer-thin diamond samples. These include the fabrication methods listed in the following: smart cut makes use of the implantation of light ions (like carbon [35] or helium [36]) to produce a sacrificial layer of amorphous carbon, which can be removed electrochemically [7, 37]. Additional overgrowth is necessary for a high crystalline quality thin film diamond released from the sacrificial layer [38]. In a diamond-on-insulator approach, a thin diamond membrane is bonded to a host (e.g. silicon) substrate and subsequently thinned down to the required thickness [6, 8, 39–41]. Furthermore, ~ 50 µm diamond microdevices can be patterned in a one-step (e.g. with a hydrogen silsesquioxane (HSQ) mask [42]) or two-step pattern transfer process (e.g. with a silicon nitride (Si_xN_y) hard mask [43]) and thinned down by dry etching and a heterogeneously integrated mask (e.g. a fused

quartz mask [44]). Alternatively, such diamond membranes can be first bonded to the cavity mirror and then thinned down with a fused quartz [27] or diamond [45] mask. Other methods start from bulk diamond and use an undercutting process (via angled plasma etching [46] or quasi-isotropic plasma etching [47]). Moreover, the production of free-standing diamond nanoslabs with a Chromium protection mask and dry etching has been demonstrated [48]. These fabrication methods are typically complex, labor-intensive, and necessitate additional equipment for the pattern transfer, lithography tools, and deposition tools to define microstructures in lateral dimensions.
In this work, we present a fabrication method for patterning microdevices of different sizes and shapes using laser-cutting to engrave ~ 50 µm thick diamond membranes. This approach utilizes only two fabrication tools (a femtosecond pulsed laser writer and a reactive ion etcher), significantly simplifying the process, reducing its duration, and increasing accessibility. The method allows to achieve feature sizes of approximately 3 µm, limited by the laser spot size. We compare this new fabrication method with an already established method of patterning the diamond membrane with electron-beam lithography (EBL) based on two-step patterning: the desired design is EBL patterned into a resist, followed by a reactive ion etch (RIE) to transfer the pattern into a hard mask material. Next, the hard mask pattern is transferred into the diamond membrane via RIE [43]. Diamond microdevices obtained from both fabrication methods are then subsequently bonded to a cavity Bragg sample mirror, equipped with striplines for microwave delivery, see Fig. 4.1 (a) and (b). To demonstrate that the laser-cut microdevices are suitable for microcavity applications, we characterize the microdevices by scanning cavity microscopy (SCM) [49–51], see Fig. 4.1 (d). This demonstrates that both methods lead to microdevices with comparable cavity quality factors (cavity finesses). Furthermore, we study the optical properties of negatively charged tin-vacancy (SnV) and negatively charged nitrogen-vacancy (NV) centers embedded in diamond microdevices at low temperatures. Both methods result in devices suitable for microcavity applications in quantum networking.

4.2 Fabrication of Diamond Microdevices

The two fabrication methods are compared and described in detail in the following. The process flow of both methods can be divided into five steps: sample preparation, patterning, color center creation, device release etch, and bonding. Specifically, the two methods majorly differ in the patterning fabrication step, where the method presented here foresees a design pattern transfer via laser-cutting. In contrast, the conventional fabrication method foresees a two-step transfer pattern based on EBL. The laser-cut method with SnV center creation is schematically summarized in Fig. 4.1 (c). The conventional EBL-based fabrication method is detailed in [43]. Detailed fabrication steps and parameters can be found in the Appendix Tab. 4.1.

4.2.1 Sample Preparation

For both methods, we follow the sample preparation step outlined in Ref. [27]. We start with commercially available single-crystal, electronic-grade bulk diamonds, measuring $(2 \times 2)\,\mathrm{mm}^2$ and 0.5 mm in thickness with a face-orientation of $\langle 100 \rangle$, grown by chemical vapor deposition. The diamonds are laser-sliced into three ~ 50 µm thick membranes and polished on both sides (Almax Easylab). The roughness of the polished surface is typically $R_q < 1\,\mathrm{nm}$. Before patterning, the membranes are cleaned by fuming nitric acid (65 %) at room temperature (step (1) in Fig. 4.1 (c)).

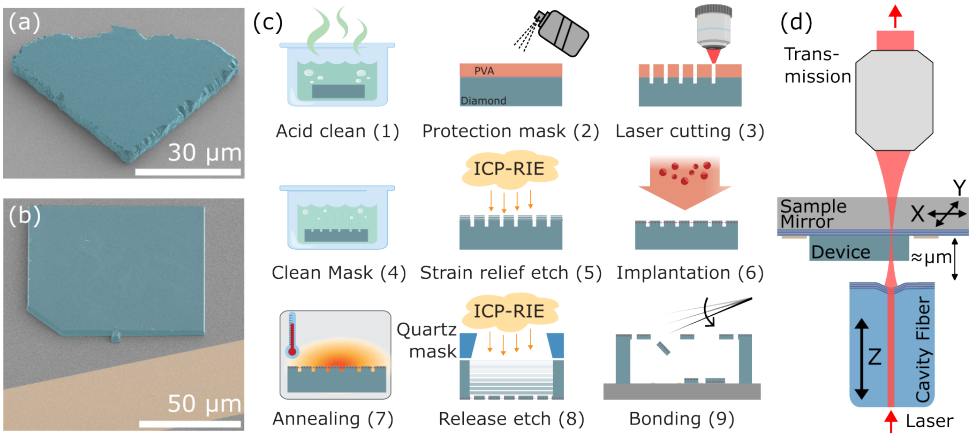

Figure 4.1: False-colored (cyan) scanning electron microscope (SEM) images of diamond microdevices obtained by laser-cutting (device originated from a parent diamond membrane named: *Vincent Vega*) in (a) and electron-beam lithography, and dry etching with a silicon nitride hard mask (*Pai Mei*) in (b). The devices are bonded to the cavity mirror. A gold stripline (yellow false-colored) can be used for microwave delivery. (c) Process flow to fabricate laser-cut diamond microdevices with tin-vacancy centers bonded to the cavity mirror. PVA: polyvinyl alcohol, ICP-RIE: inductively coupled plasma reactive ion etching. (d) Schematic of the scanning cavity microscope. The cavity is optically probed from the fiber side, and the transmission is detected. The sample mirror with the bonded diamond microdevices is scanned laterally in front of the fiber.

4.2.2 Patterning

Patterns of arbitrary microdevice designs are transferred into the ~ 50 µm thick diamond membrane via the two methods by selectively removing diamond material. In the case of the laser-cutting method, the diamond membrane is coated with a polyvinyl alcohol (PVA) mask using standard PVA-based hairspray (step (2)). Next, approximately 10 µm to 15 µm deep trenches are created with a femtosecond-pulsed laser (Lasertec), transferring an arbitrary design into the diamond membrane (step (3)) [52]. After patterning, the PVA mask is removed via an ultrasonic bath in de-ionized (DI) water (H_2O) and acetone for 10 min each at room temperature (step (4)), followed by inorganic wet cleaning in a Piranha mixture (ratio 3:1 of H_2SO_4 (95 %) : H_2O_2 (31 %)) at 80 °C for 20 min. In the next step, the surface is treated with a strain relief etch for cleaning and to remove the residual polishing-induced strain from the membrane surface (step (5)) [42]. The membrane is mounted with PMMA495 A4 on a fused quartz carrier wafer and etched with inductively coupled plasma reactive ion etching (ICP/RIE) for 35 min in Ar/Cl_2 plasma chemistry, fol-

lowed by 7 min etch in O_2 plasma chemistry (Oxford Instruments, Plasmalab System 100). This removes ~ 1.4 µm and ~ 2.1 µm, respectively, of diamond material from the surface. Alternatively, the strain relief etch can also be performed with a cyclic Ar/Cl_2 and O_2 recipe to improve surface roughness, as demonstrated in Ref. [45].
The EBL method starts with processing the diamond membrane with a strain relief etch as described above (with different etching times). After the color center creation (described below), a ~ 320 nm thin Si_xN_y layer hard mask material is deposited on the top diamond surface by plasma-enhanced chemical vapor deposition (PECVD, Oxford Instruments Plasmalab 80 Plus). Next, CSAR-13 (AR-P 6200.13) positive tone resist is spin-coated, followed by the spin coating of Electra 92 (AR-PC 5090) conductive polymer to prevent charging effects during EBL exposure (Raith EPBG-5200). Before the development step, the Electra 92 is removed in deionized water and blow-dried with nitrogen. The resist is then developed by immersing the sample for 1 min in pentyl acetate, 5 s in ortho-xylene, 1 min in isopropyl alcohol (IPA), and blow-drying with nitrogen. The pattern is transferred into the Si_xN_y hard mask layer via ICP/RIE (Adixen AMS 100 I-speeder) in a CHF_3/O_2 based plasma chemistry [53]. The resist is removed in a two-fold step: first, a coarse resist removal is executed by immersing the sample in a PRS 3000 positive resist stripper solution, followed by a second fine resist removal in a Piranha mixture clean, which is executed two times. Next, the pattern is transferred from the Si_xN_y hard mask into the diamond membrane by ICP/RIE with an O_2 plasma (Oxford Instruments, Plasmalab System 100), resulting in a trench depth of around 6 µm to 10 µm. The Si_xN_y hard mask is then removed by wet inorganic etch in hydrofluoric (HF) acid (40 %) for 15 min at room temperature.
The patterning step in the EBL method accounts for at least half of the total processing time, which can be saved with the laser-cutting method, especially when outsourced.

4.2.3 Color Center Creation

SnV centers are created in the diamond membrane by ion implantation of tin (^{120}Sn) at an implantation energy of 350 keV and a dose of 3×10^{10} ions/cm^2 under an implantation angle of 7° (step (6)). The desired implantation energy is determined using Stopping Range of Ions in Matter (SRIM) simulations [54], resulting in an implantation depth of ~ 90 nm (straggle of ~ 17 nm), and the implantation angle is adopted to prevent ion channeling effects. For laser-cut samples, ion implantation is performed after patterning and strain relief etch. For EBL samples, the ion implantation is performed after the strain relief etch, but before the patterning step.
For the generation of NV centers with high optical coherence, we employ electron irradiation with minimal crystal damage to generate NV centers from the native nitrogen concentration [27, 34, 55]. We irradiate and anneal the bulk diamonds before laser-slicing into membranes, but this step can also be performed later in the process. Irradiation is realized at the Reactor Institute in Delft with an electron-beam acceleration energy of 2 MeV and a dose of 4×10^{13} e$^-$/cm^2. The energy leads to penetration of electrons through the full diamond (for both substrates used in this study, the 0.5 mm thick bulk and ~ 50 µm membranes). This results in lattice vacancies formed over the full thickness extent of the diamond substrates.
After the implantation and the irradiation steps, the diamond substrates are processed with a tri-acid clean (mixture of 1:1:1 ratio of H_2SO_4(97 %):HNO_3(65 %):$HClO_4$(60 %)) at

120 °C for one hour. To enable vacancy migration and to activate color centers, as well as to remove defects (such as divacancies from the lattice), the samples are high-temperature annealed (at a pressure of ~ 1×10^{-6} mbar) with a temperature of up to 1100 °C (step (7)), followed by a tri-acid clean to remove any created graphite during the annealing step. We use the same annealing recipe as presented in former work [27]. Both ways to create color centers (implantation and electron irradiation) are compatible with the two demonstrated fabrication methods.

4.2.4 Device Release Etch

To release the structures, the membrane with the patterned side facing down is placed on a fused quartz wafer. A 0.5 mm thick fused quartz mask with a 1.4 mm rectangular central opening and angled sidewalls (30°) is positioned and aligned on top of the back surface of the diamond membrane [27]. The mask allows the etching plasma to access the back surface of the diamond membrane over the entire opening area, whereas areas of the membrane covered yield a supporting diamond frame. The center part of the membrane is etched with an ICP/RIE process (Oxford Instruments, Plasmalab System 100) composed of Ar/Cl_2 for 45 min for cleaning and smoothening the surface, followed by consecutive multiple rounds of O_2 plasma deep etching (step (8), depending on the diamond membrane thickness). Between etching rounds, the membrane is inspected under an optical light microscope to assess the progressing thickness and verify the release of the microdevices, connected to the parent membrane by a small tether by design. The device release etch step is concluded when the target thickness is reached.

4.2.5 Bonding

Prior to the diamond microdevice bonding to the cavity sample mirrors [13], microwave striplines can be fabricated on top of the mirrors. These are produced by an EBL and lift-off fabrication process, resulting in 5 nm titanium and 75 nm thick, 50 µm wide gold striplines. A wet inorganic Piranha clean concludes the microwave stripline fabrication, improving the bonding quality of the diamond microdevices. The stripline fabrication process does not reduce the cavity mirror reflectivity, as demonstrated in Ref. [33].

The bonding is performed by a four-degrees-of-freedom, piezo micromanipulator (Imina Technologies SA, miBots), used to controllably break the tether and release the diamond microdevices from the parent membrane (shown in Appendix Fig. 4.7 (a), see also Supplementary Video 1, which can be found on Ref. [56]). As a result, the microdevices land on the cavity mirror, aligned and positioned under the parent diamond membrane such that proximity to the microwave striplines is ensured (step (9)). The micromanipulator is equipped with a 0.6 µm fine tungsten needle (Ted Pella, Ultrafine Tungsten Manipulator Probe). To increase the probability of obtaining well-bonded devices, the surface of the cavity mirror can be activated for 30 min inside an Ozone chamber (BioForce Nanosciences UV/Ozone ProCleaner), which removes organic contamination on the molecular level. In addition, the overall parent diamond membrane with the released microdevices can be cleaned in HF (40 %) at room temperature. A well-bonded device exhibits a color matching with the mirror surface and does not show any interference patterns. Furthermore, these devices do not move when a lateral force with the micromanipulator tip is applied. Bonded microdevices from both fabrication methods are shown in Fig. 4.1 (a) and (b), mea-

sured with an SEM, and in Fig. 4.2 (a) and (c) with a light microscope.
In contrast, devices that are not fully bonded are typically identified by wave-like interference patterns (Newton's rings) or an opaque appearance (see Appendix Fig. 4.7 (b) and (c)). Unbonded devices can be repositioned on the mirror surface for alignment, such as placement near the stripline. For some devices, gentle force or tapping with the micromanipulator has resulted in bonding. Both fabrication methods, laser-cutting (Fig. 4.2 (a)) and EBL (Fig. 4.2 (c)), produce well-bonded devices.

4.2.6 Fabrication Results

Representative examples of bonded microdevices fabricated with the two methods presented in the previous sections are shown in Fig. 4.2. A laser-cut $(70 \times 70)\,\mu m^2$, ~ 2.5 µm thin microdevice shown in Fig. 4.2 (a) hosts SnV centers. The corresponding height map in Fig. 4.2 (b) is measured by a white light interferometer (Bruker ContourX-500) and yields a wedge with a slope of ~ 0.7 µm/100µm. The second microdevice, fabricated by EBL is $(90 \times 90)\,\mu m^2$ in size and around 3.5 µm thin, shown in Fig. 4.2 (c) and contains NV centers. The height maps (Fig.4.2 (d)) shows a wedge of ~ 1.4 µm/100µm. The higher gradient wedge indicates that this device originated from the outer region of the parent diamond membrane, where the etched profile is less homogeneous, because of the proximity effect due to the fused quartz mask. The determined wedge of both microdevices enables the investigation of the two different mode types, which are formed in the diamond-microcavity system (air-like and diamond-like, see next section).
The laser-cutting method yields devices with a significantly higher surface roughness for an extent of ~ 10 µm from the edges when compared to the EBL method obtained devices (compare Fig. 4.2 (a) to (c)). Beyond the high surface roughness extent of ~ 10 µm, the inner area of the laser-cut microdevice shows a comparable surface quality to the devices fabricated by EBL.
Both methods lead to the successful fabrication of microdevices with high-quality surfaces in the center, suitable for microcavity experiments (next section).

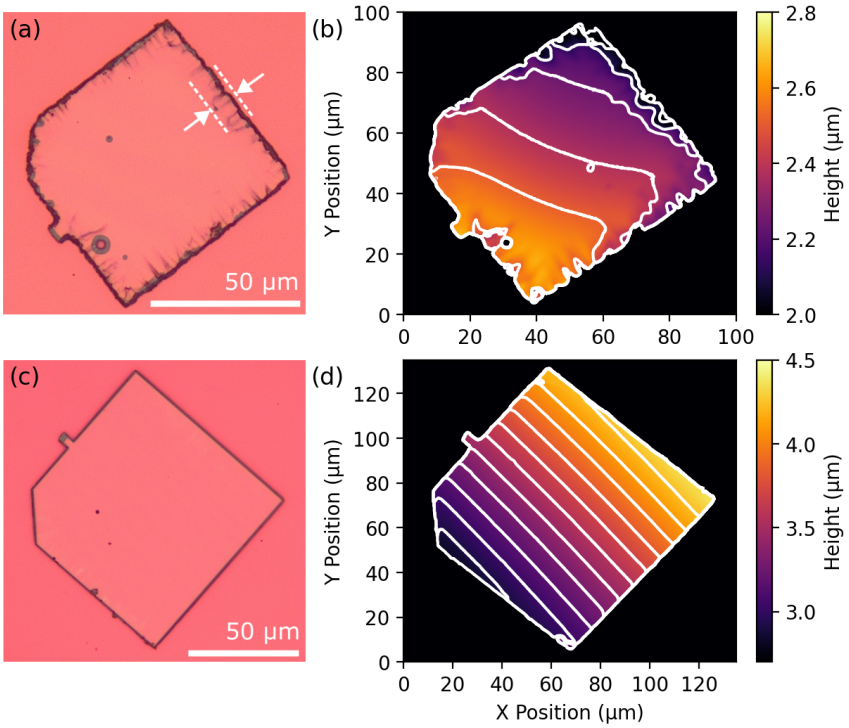

Figure 4.2: Comparison of diamond microdevices fabricated by laser-cutting and EBL. (a) Optical light microscope picture of the laser-cut microdevice (*Vincent Vega*). The rougher edge (indicated by the 10 µm spaced, dashed lines) of the laser-cut microdevice is visible. (b) The corresponding height map is measured with a white light interferometer. The white lines are overlayed and indicate a microdevice thickness matching air-like modes with $q = 16$ to $q = 19$, calculated by equation (4.1). (c) Optical light microscope picture of the EBL microdevice (*Pai Mei*). (d) Corresponding height map with diamond thicknesses leading to an air-like mode of $q = 22$ to $q = 32$, calculated by equation (4.1). Both devices are well-bonded to the underlying (pink) cavity mirror. The height data of the white light interferometer is stated with respect to the mirror surface.

4.3 Scanning Cavity Microscopy

In this section, we use SCM (see Supplementary Video 2, which can be found on Ref. [56]) to study the quality of the bonded diamond microdevices. The experiments involve finesse measurements of the microcavity that give insights into cavity losses and allow us to conclude the diamond device surface wedge and quality. For this, we first introduce a cavity loss model to describe the finesse determined in length, as done in our cavity finesse measurements.

4.3.1 Cavity Loss Model

We consider a hemispherical plano–concave microcavity, where both Bragg mirrors are terminated with a high refractive index material and the diamond microdevices are bonded to the (flat) sample mirror (see Fig. 4.1 (d)). The cavity finesse $\mathcal{F} = 2\pi/\mathcal{L}_{\text{eff}}$ is inversely

proportional to the sum of the effective losses $\mathscr{L}_{\text{eff}}$. Together with the known mirror transmission loss values, this results in a complete understanding of the system. Most fundamentally, the diamond devices change the sample mirror transmission loss for a given probe laser wavelength depending on their thickness. Hereby so-called air-like and diamond-like mode [11, 57] thicknesses can be defined:

$$t_d = q\frac{\lambda}{2n_d} \quad (\text{air}-\text{like}), \qquad t_d = (2q+1)\frac{\lambda}{4n_d} \quad (\text{diamond}-\text{like}), \tag{4.1}$$

with a corresponding fundamental mode number q and the refractive index of diamond $n_d = 2.41$ [58] (for our laser wavelength of $\lambda = 637\,\text{nm}$). For the air-like (diamond-like) modes, the mirror transmission loss is minimal (maximal). This phenomenon is associated with the electric field intensity ratio of the air and the diamond part of the cavity. A consecutive air-like and diamond-like mode is separated by a diamond thickness of $\lambda/(4n_d) \approx 66\,\text{nm}$ and hence can indicate a device thickness wedge.
To include further diamond-related loss mechanisms, we can model the effective losses for the here conducted finesse measurements with:

$$\mathscr{L}_{\text{eff}} = \mathscr{L}_{M,a} + \frac{n_d E^2_{\text{max,d}}}{E^2_{\text{max,a}}}\left(\mathscr{L}_{M,d} + \mathscr{L}_{A,d} + \mathscr{L}_{S,\text{eff,d}}\right) + \mathscr{L}_{\text{add}}. \tag{4.2}$$

In this equation, $\mathscr{L}_{M,a}$ accounts for the loss through the air-side mirror and $\mathscr{L}_{\text{add}}$ considers any additional losses. The fraction $n_d E^2_{\text{max,d}}/E^2_{\text{max,a}}$ describes the electric field intensity ratio between the air and diamond part, and can be calculated by [57]:

$$\left(\frac{n_d E^2_{\text{max,d}}}{E^2_{\text{max,a}}}\right)^{-1} = \frac{1}{n_d}\sin^2\left(\frac{2\pi n_d t_d}{\lambda}\right) + n_d\cos^2\left(\frac{2\pi n_d t_d}{\lambda}\right). \tag{4.3}$$

The ratio depends on the diamond thickness and leads to the modulation of the finesse values between air-like ($n_d E^2_{\text{max,d}}/E^2_{\text{max,a}} = 1/n_d$) and diamond-like modes ($n_d E^2_{\text{max,d}}/E^2_{\text{max,a}} = n_d$). The modulated losses are: the diamond-side sample mirror loss $\mathscr{L}_{M,d}$, the absorption losses $\mathscr{L}_{A,d}$, and the scattering losses at the air-diamond interface $\mathscr{L}_{S,\text{eff,d}}$. The absorption losses can be calculated with the diamond absorption coefficient α to $\mathscr{L}_{A,d} \approx 2\alpha t_d$, while the scattering losses can be calculated by [57]:

$$\mathscr{L}_{S,\text{eff,d}} \approx \sin^2\left(\frac{2\pi n_d t_d}{\lambda}\right)\frac{(n_d+1)(n_d-1)^2}{n_d}\left(\frac{4\pi\sigma_{DA}}{\lambda}\right)^2. \tag{4.4}$$

Here, σ_{DA} includes the device surface roughness at the air-diamond interface. For an air-like mode, the scattering losses are zero, while they become maximal in a diamond-like mode. The cavity finesse on the diamond is thus also a measure of the surface roughness.

4.3.2 Cavity Finesse Measurements

We characterize the diamond microdevices by two-dimensional scans, in which the cavity finesse is measured on each lateral spot with a room temperature fiber-based Fabry-Pérot microcavity, schematically depicted in Fig. 4.1(d) (scanning cavity microscopy [59]). The $(1 \times 1)\,\text{cm}^2$ sample mirror, on which the diamond devices are bonded, is scanned laterally

with a piezo nanopositioning stage in steps of 0.2 µm. Technical details about the microcavity setup can be found in 4.7.3. An individual finesse measurement is performed by scanning the cavity length over two fundamental modes while probing the cavity transmission with a resonant laser, shown in Appendix Fig. 4.9 (a). We record all measurements with cavity lengths below 15 µm, to ensure that the cavity finesse is not limited by clipping losses (see Appendix Fig. 4.9 (b) for characterization of the cavity fiber). A scan of the two devices fabricated by laser-cutting and EBL is presented in Fig. 4.3 (a) and (c).
The mirror coatings (Laseroptik) are designed to be maximally reflective for 637 nm light with $\mathscr{L}_{M,a}$ = 50 ppm ($\mathscr{L}_{M,d}$ = 670 ppm for diamond termination) losses for the fiber tip (sample) mirror. As follows from equation (4.2), in a bare cavity (t_d = 0 µm), scattering and absorption losses vanish and the sample mirror transmission losses translate to the air-terminated value of $1/n_d \times \mathscr{L}_{M,d}$ = 280 ppm. The measured finesse around 8000 (see green distributions in Fig. 4.3 (b) and (d)) indicates additional losses around $\mathscr{L}_{\text{add}}$ = 470 ppm. We attribute these additional losses to the quality of the concave fiber tip.

On both diamond microdevices in Fig. 4.3 (a) and (c), the finesse shows a clear modulation with the same pattern as in the diamond thickness variation from Fig. 4.2 (b) and (d). We associate the variation in finesse values with the alternation between air-like modes (higher finesse) and diamond-like modes (lower finesse). In the air-like modes, only a slight reduction of the cavity finesse compared to the bare cavity is observed. For the diamond-like modes, the finesse is much reduced. The cavity transmission on the EBL device (*Pai Mei*) is reduced around diamond-like mode regions so much that no finesse can be determined. Some thin lines with reduced finesse are visible in the scan in Fig. 4.3 (c), which are attributed to transverse-mode mixing [59].

To study the effect of the diamond microdevices more quantitatively, we investigate the finesse depending on the device thickness. This data is obtained by overlaying the white light interferometer data from Fig. 4.2 (b) and (d) with the finesse scans from Fig. 4.3 (a) and (c). The interferometer data has a sufficient lateral resolution of about 0.13 µm per step. For every measured finesse value, within the white rectangle in the scan, we take the corresponding diamond thickness from the interferometer data. This is shown in Fig. 4.4 for both diamond devices.
We notice that the absolute thickness values from the white light interferometer do not directly match the expected positions of the air-like and diamond-like modes according to equation (4.1). The measured values might be distorted due to the multilayer Bragg mirror on which the devices are bonded. We compensate for this by measuring the diamond thickness using the cavity mode dispersion (Appendix Fig. 4.10) on an air-like mode on the diamond (indicated in Fig. 4.3) to determine an offset for the diamond thickness values. The absolute thickness from the white light interferometer and the thickness determined by the cavity dispersion differ by 0.16 µm to 0.32 µm.
We fit the measured finesse values depending on the diamond thickness in Fig. 4.4 with the effective losses from equation (4.2). In the fit, we use the known mirror losses from the coating design as stated above, and a small diamond thickness translation of < 20 nm is allowed. Furthermore, for the used high-purity, electronic-grade diamonds grown by chemical vapor deposition, no absorption losses are expected [60]. This leaves the additional losses $\mathscr{L}_{\text{add}}$ and the diamond surface roughness σ_{DA} as free parameters in the fit.

For the laser-cut microdevice, the fit yields a diamond surface roughness value of 0.9 nm

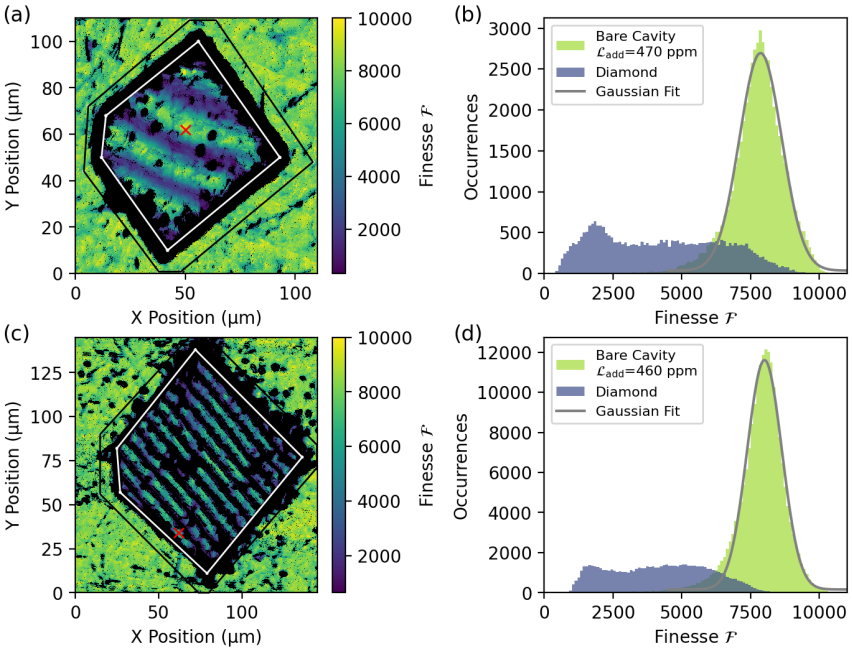

Figure 4.3: Scanning cavity microscopy of the diamond microdevices. Both devices show a clear modulation of the finesse due to the alternation between air-like and diamond-like modes. (a) Measured two-dimensional finesse scan on a laser-cut diamond microdevice (*Vincent Vega*). (b) Histogram of the finesse values measured in (a). Values on the diamond (bare cavity) are taken from inside the white rectangle (outside the black rectangle). (c) Measured two-dimensional finesse scan on an EBL diamond microdevice (*Pai Mei*). (d) Histogram of finesse values measured in (c). Finesse values on the diamond (bare cavity) are taken from inside the white rectangle (outside the black rectangle). For the bare cavity, a finesse centered around 8000 is determined by the Gaussian fits in (b) and (d). The red crosses in (a) and (c) indicate the positions where the cavity length measurements presented in 4.7.5 are taken. The histograms are plotted in bins of 100.

and additional losses of 610 ppm. The EBL device fit yields values of 1.2 nm surface roughness and 820 ppm additional losses. For both devices, a distribution of finesse values for a fixed diamond thickness is observed, leading to the band-like structure in Fig. 4.4. This means that for a specific diamond thickness, lateral cavity positions with varying surface quality are found. To quantify the spread in surface roughness of the data presented in Fig. 4.4, we use the following procedure: the finesse values for a thickness segment of 10 nm are binned into a histogram, which is fitted with a Gaussian function. This fit determines for every thickness segment a mean value and a standard deviation. We fit the mean plus (minus) the standard deviation values of all segments with the model losses of equation (4.2), to determine the upper yellow (lower bright green) curves in Fig. 4.4. With that, we find that our laser-cut (EBL) device exhibits areas with surface roughness values as low as 0.6 nm (1.1 nm), which are common values for these fabrication methods. For both samples finesse values similar to the bare cavity are reached in the air-like modes, whereas in the diamond-like modes scattering losses of $\mathscr{L}_{S,\mathrm{eff,d}}$ = 390 ppm (1330 ppm) limit the achievable finesse in the laser-cut (EBL) device.

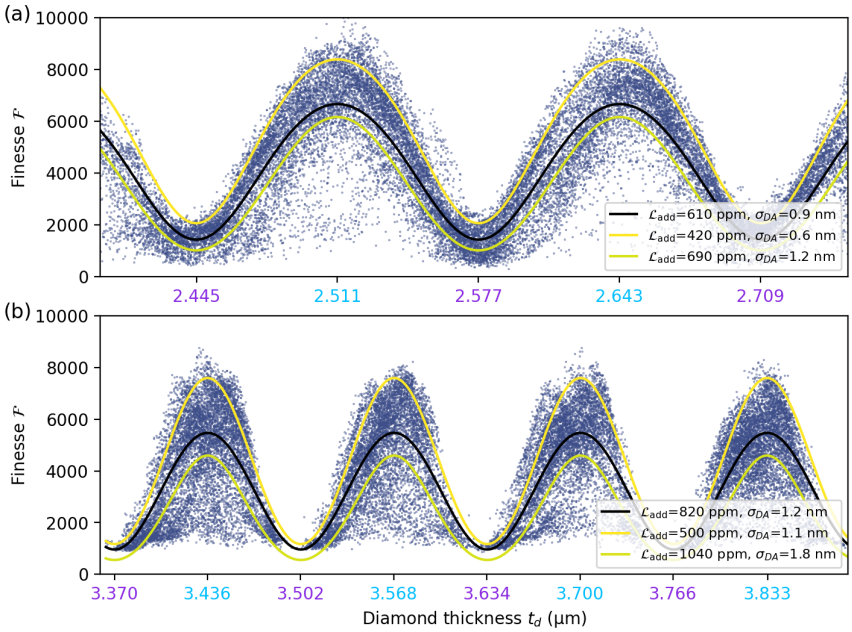

Figure 4.4: Diamond thickness dependent finesse values observed by SCM. Finesse values are taken from inside the white rectangle in Fig. 4.3. The black line is a fit of the finesse values with losses from equation (4.2). The modulation of the finesse values between high-finesse air-like modes and low-finesse diamond-like modes is visible. The diamond thickness values that correspond to an air-like (diamond-like) mode are indicated by the bright blue (purple) axis ticks, determined by equation (4.1). By determining the mean and standard deviation of the finesse values in 10 nm segments (see text), we also give an upper (yellow) and lower finesse curve (bright green) for both devices. More than 60 % of the finesse values lie between the two curves. The diamond thickness measurement by the cavity dispersion is performed for the displayed first air-like mode for both samples (see Appendix Fig. 4.10). (a) Finesse measured on the laser-cut diamond microdevice (*Vincent Vega*). (b) Finesse measured on the EBL diamond microdevice (*Pai Mei*). Note that the black fit is lowered due to the higher spread in finesse values.

4.3.3 Frequency Splitting of the Polarization Cavity Modes

In addition to the finesse, the frequency splitting of the two orthogonal polarization modes of the microcavity is studied. Strain-induced birefringence in the diamond microdevice can cause a splitting of the horizontal and vertical polarization cavity mode [61]. In general, diamond color centers couple differently to these modes depending on their electric dipole overlap with the electric field of the cavity. These polarization modes are used in cross-polarization resonant excitation and detection schemes, and the magnitude of polarization splitting becomes relevant for excitation laser power considerations [29].

We investigate the polarization splitting of the fundamental modes within the same scan used for the finesse measurements. To measure the splitting, the cavity is resonantly probed using laser light with frequency-modulated sidebands, generated by a phase electro-optic modulator. The cavity length is scanned around the fundamental mode, and a typical measurement is shown in 4.7.6. The spacing of the sidebands is set by the modulator driving frequency and is used to determine the frequency splitting of the polarization modes.

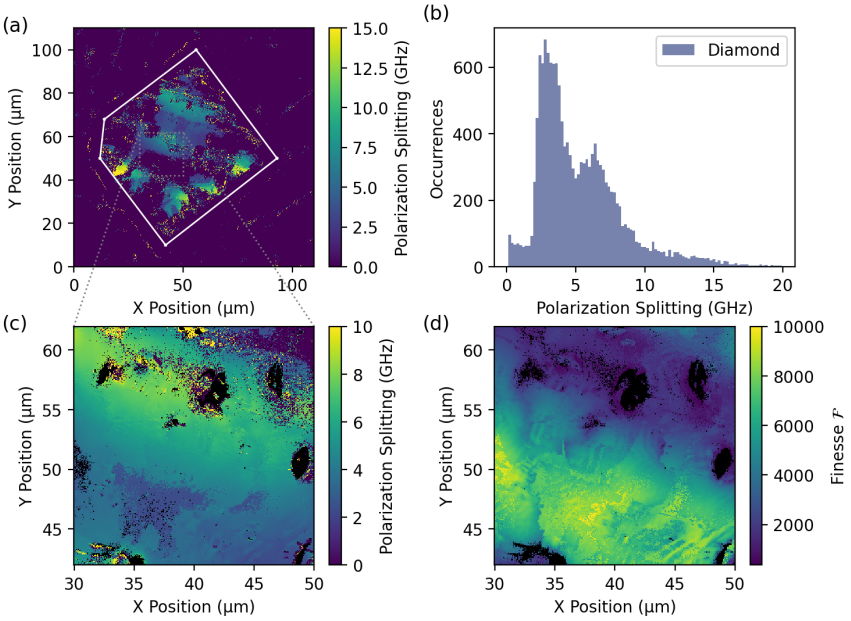

Figure 4.5: Polarization splitting on the laser-cut diamond microdevice (*Vincent Vega*). (a) Polarization splitting is measured on the bare mirror and the diamond device. Data is taken within the same scan as shown in Fig. 4.3 (a). (b) Histogram of the polarization splitting measured on the diamond device inside the white rectangle in (a). Around half of the measured lateral points do not show a polarization splitting (zero bin not included in the histogram). The bin size is 0.2 GHz. (c) Polarization splitting, seperately measured with a 70 nm resolution in the $(20 \times 20)\,\mu m^2$ area indicated in (a). (d) Corresponding finesse values of the same area as shown in (c). The air-like modes with a higher finesse show a smaller polarization splitting compared to the diamond-like modes.

Figure 4.5 (a) shows the polarization splitting measured on and around the laser-cut microdevice. On the bare mirror, no polarization splitting is measured, while on the diamond device, polarization splittings up to 15 GHz can be observed (histogram shown in Fig. 4.5 (b)). It seems that regions with higher polarization splitting in Fig. 4.5 (a) are closer to the device edges, which can be explained by higher strain, possibly induced by the damage of the laser-cutting. Figure 4.5 (c) shows a selected part of the device with the corresponding finesse scan in Fig. 4.5 (d). It is observed that the polarization splitting is higher in the low-finesse, diamond-like mode part (upper area in the scan). This can be explained by the higher electric field intensity inside the diamond for diamond-like modes, leading to a more pronounced effect of the birefringence [59].
For the EBL microdevices presented here, we do not observe significant polarization splitting beyond the cavity linewidth. However, we have also seen polarization splittings up to 10 GHz on other EBL-fabricated devices. To understand the origin of the different strain values, further investigations are needed.

4.4 Optically Coherent Color Centers

For quantum network applications, the color centers in the diamond microdevices must show a (close to) transform-limited optical emitter linewidth. Noise in the environment of the color center (such as fluctuating charges) broadens the emitter linewidth. We can decompose the linewidth broadening into a slow noise contribution, spectral diffusion, and a fast noise contribution, pure dephasing [62]. The former leads to a Gaussian broadening and can be mitigated by active tracking and feedback on the emitter transition frequency [63–66]. Whereas pure dephasing leads to a Lorentzian broadening with a more fundamental influence, as it directly determines the indistinguishability in a two-photon quantum interference experiment of color centers [67, 68] and limits the achievable remote entanglement fidelity in emission-based entanglement protocols [62, 69]. Moreover, the pure dephasing linewidth enters the coherent cooperativity determining fidelities of quantum information protocols [70].

We study the optical emitter linewidth of the color centers in our diamond microdevices with photoluminescence excitation (PLE) measurements. These measurements are performed in a home-built confocal microscope setup, where the samples are mounted in a closed-cycle helium cryostat. In the PLE measurements, a resonant laser is scanned over the zero-phonon line (ZPL) of the color center, and the fluorescence is detected in the phonon sideband.

Figure 4.6 (a) shows a confocal scan of the laser-cut diamond microdevice hosting SnV centers. Note that this device is a different microdevice than shown before, but it originated from the same fabrication run and parent membrane (*Vincent Vega*). For the PLE measurements, an off-resonant, 515 nm laser is used before each resonant laser scan to initialize the SnV center in its negatively charged state. The application of a green laser pulse is known to change the charge environment of the color center, resulting in spectral diffusion. We acquire 100 of these scans on three different SnV centers (Fig. 4.6 (b)) and average all scans to get a measure of the spectral diffusion linewidth. In some of these measurements, a bistability of the SnV center transition frequency is observed. These discrete jumps between two spectral positions separated by about 100 MHz might be caused by a charge trap near the SnV center [71, 72].

To quantify the pure dephasing linewidth, scans that show a complete Lorentzian fluorescence peak are manually selected (more than 50 %), fitted, and centered before averaging. The SnV centers of Fig. 4.6 (b) show good optical coherence with pure dephasing linewidths close to the transform limit around 32 MHz. The corresponding excited state lifetime was determined in previous work [32], which also demonstrated the coherent cavity coupling of a single SnV center in a device obtained from the same diamond membrane. These results demonstrate that coherent SnV centers are created in the laser-cut microdevices.

Figure 4.6 (c) shows the confocal scan of an EBL diamond microdevice hosting NV centers. Note that this device is fabricated in a second run with the EBL method (device originated from parent membrane named *Mr. Orange*). For NV centers, we probe the spin-conserving E_x or E_y emitter transition of the ZPL, which involves the application of intermediate off-resonant, 515 nm, laser pulses at every resonant laser scan frequency to mitigate spin state pumping. These off-resonant laser pulses initialize the NV center predominantly in the negatively charged and spin ground state [73]. Because of the intermediate applica-

tion of green laser pulses, we can experimentally not measure spectral diffusion and pure dephasing linewidth separately. We thus analyze the emitter fluorescence peaks by fitting a Voigt profile, which is a convolution of a Gaussian and a Lorentzian function. In the fit routine, the Lorentzian linewidth is lower bound to the transform-limited linewidth of 13 MHz of the NV center [74]. Typical scan results with their corresponding Voigt fits are shown in Fig. 4.6 (d).
We analyze 20 different NV centers at several lateral diamond microdevice positions and find linewidths between 38 MHz and 130 MHz with a median linewidth of 62 MHz (statistics shown in Appendix Fig. 4.12). These results are in line with former work with larger $(2 \times 2)\,\mathrm{mm}^2$ thinned-down diamond membranes [27], indicating that the much tighter lateral dimensions do not induce additional optical decoherence.

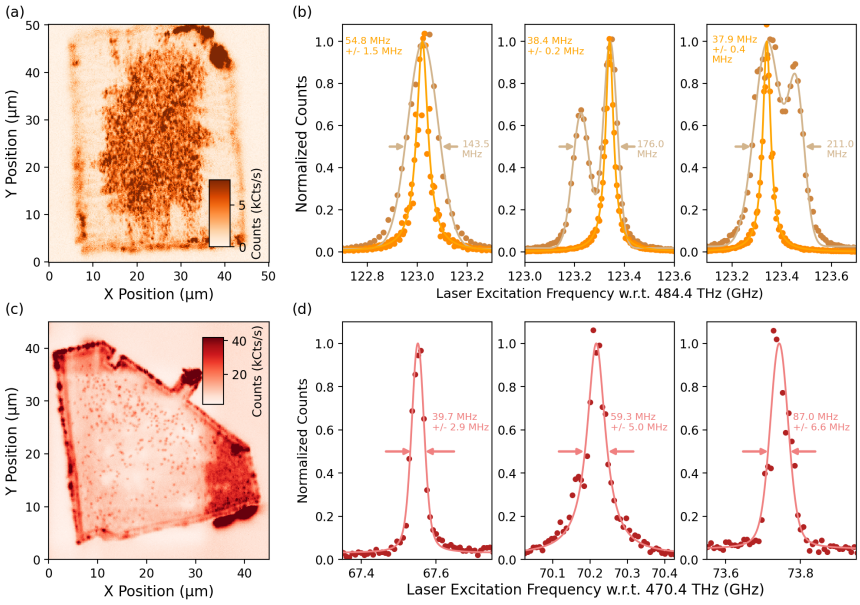

Figure 4.6: Optical properties of SnV centers inside a laser-cut diamond microdevice (*Vincent Vega*) and NV centers inside an EBL patterned diamond device (*Mr. Orange*). The emitter linewidth measurements are performed at ~ 4 K with a confocal microscope. (a) A map of the SnV device with off-resonant, 515 nm excitation. The fluorescence is filtered with a 620 nm bandpass filter (full-width half maximum of 10 nm) to detect predominantly fluorescence of SnV centers. A high SnV center density is observed in the center of the device, while the SnV center layer is removed at the wedged edges. Note that this map is measured in a room-temperature scanning confocal microscope. (b) Typical PLE laser scans of SnV centers, fitted with a Gaussian (ocher) and Lorentzian (orange) function to obtain the spectral diffusion and dephasing linewidth, respectively. (c) Confocal map of the electron-beam patterned device, showing individual, spatially separated NV centers. (d) Typical PLE laser scans of NV centers, fitted with a Voigt function to extract the linewidth. To initialize the NV center into the bright state, a green laser pulse is applied in every repetition. The relevant measurement parameters for the scans in (b) and (d) can be found in 4.7.7.

4.5 Conclusion

We present a method for patterning high-quality micrometer-thin diamond devices utilizing laser-cutting. This method significantly simplifies the fabrication process compared to previously reported methods. Also, the process step of laser-cutting can be readily outsourced. We show that these microdevices can be successfully bonded to a dielectric cavity Bragg sample mirror using a micromanipulator. SCM scans reveal a high surface quality of the fabricated devices, reflected by high cavity finesse values. In addition, we demonstrate that the devices host coherent color centers, which are suitable for quantum optical experiments and applications.

For quantum spin-photon interfaces, the expected microdevice performance in microcavities can be estimated with the measured finesse of 9000 (2000) in the air-like (diamond-like) mode. With the 17.3 µm radius of curvature of the used fiber mirror, these values translate to a maximum Purcell factor of about 30 (39) for a NV center and, with adjusted mirror coatings, also for a SnV center. The Purcell enhancement would be combined with a high outcoupling efficiency through the sample mirror of 40 % (51 %) for the air-like (diamond-like) modes and the used mirror coatings. The performance values could be further improved by using a fiber tip mirror that shows lower additional losses [75–77].

Combined with the integrated gold striplines on the sample mirror for microwave control of the spin qubits [33, 78, 79], the presented approach can enable the realization of an efficient spin-photon interface with diamond color centers.

4.6 Acknowledgment

The authors thank Alexander Stramma for proofreading the manuscript. Furthermore, the authors thank the Quentin Tarantino movie universe for providing the sample names.

The authors acknowledge financial support from the Dutch Research Council (NWO) by the Spinoza prize 2019 (project number SPI 63-264) and from the Dutch Ministry of Economic Affairs and Climate Policy (EZK), as part of the Quantum Delta NL programme. The authors gratefully acknowledge that this work was partially supported by the joint research program “Modular quantum computers” by Fujitsu Limited and Delft University of Technology, co-funded by the Netherlands Enterprise Agency under project number PPS2007. This research was supported by the Early Research Program of the Netherlands Organisation for Applied Scientific Research (TNO) and by the Top Sector High Tech Systems and Materials.

4.6.1 Author Contributions

Y. H., J. M. B., and J. F. contributed equally to this work. M. R. and N. C. developed the EBL fabrication process used in this work. N. d. J. contributed to developing the laser-cutting method. J. M. B., C. S., and Y. H. fabricated the diamond devices. C. S. and L. G. C. W. characterized the devices with the white light interferometer. J. F., Y. vd. G., C. F. J. W., and S. S. built the cavity characterization setup. S. S. measured the two-dimensional cavity scans and characterized the cavity fiber. C. S., Y. H., J. M. B., and J. F. characterized the color centers. R. M. fabricated the cavity fiber. J. F. derived the used cavity loss model. Y. H., J. F., and S. S. analyzed the data. Y. H., J. M. B., J. F., S. S., and R. H. wrote the

manuscript with input from all authors. R. H. supervised the experiments.

4.6.2 Data Availability

The datasets of this study and the Python software for analysis and plotting are publicly available on 4TU.ResearchData under Ref. [56].

4.7 Appendix

4.7.1 Outline of Fabrication

The detailed steps of both fabrication methods are summarized in table 4.1.

Fab. Step	Electron-Beam Lithography (EBL)	Laser-Cutting
I. Cleaning	Fuming nitric acid (1): 10 min in HNO_3 (65 %) at room temperature	
(II. Strain Relief Etch, Implantation, Annealing)	Strain relief etch as described in Section 4.2.2, followed by tri-acid clean, implantation, annealing, and a post-anneal tri-acid clean as detailed in Subsection 4.2.3	-
III. Application of Protection Mask	PECVD ~ 320 nm silicon nitride Si_xN_y	Application of PVA layer (2)
IV. Spin Coating	Sample mounted with PMMA495 A4 on silicon piece, resist CSAR-13 (AR-P 6200.13), 3500 rpm (thickness of ~ 430 nm), bake 3 min at 150 °C Spin coat Electra 92 (AR-PC 5090), 4000 rpm (thickness of ~ 30 nm), bake 2 min at 90 °C	-
V. Exposure	Electron-beam: Dose of 400 uC/cm^2 with 3 nm spot size	-
VI. Development	Remove Electra 92 with 1 min deionized water, blow dry with nitrogen. CSAR-13 development: 1 min in pentyl-acetate, 5 s in ortho-xylene, 1 min in IPA, blow dry with nitrogen	-
VII. Patterning Hard Mask	Si_xN_y etch with plasma composed of CHF_3/O_2 [80]	-
VIII. Resist Removal	PRS 3000 for 2 h at 80 °C, followed by overnight PRS 3000 at room temperature	-
IX. Cleaning	Double Piranha clean: Mixture with ratio 3:1 of H_2SO_4 (95 %) : H_2O_2 (31 %) at 80 °C for 20 min	-
X. Transfer Pattern into Diamond	Anisotropic ICP/RIE: Sample mounted with PMMA495 A4 on fused quartz carrier wafer, 30 min O_2 plasma chemistry	Laser-cutting (3) with a femtosecond pulsed laser
XI. Cleaning	Removal of the Si_xN_y hard mask: Hydrofluoric (HF) acid (40 %) clean 15 min at room temperature	Removal of PVA: Ultrasonic bath in de-ionized water and acetone for 10 min, each at room temperature (4), followed by Piranha clean
(XII. Strain Relief Etch, Implantation, Annealing)	-	Strain relief etch (5) as described in Section 4.2.2, followed by tri-acid clean, implantation (6), annealing (7), and post-anneal tri-acid clean as detailed in Section 4.2.3
XIII. Release Etch	ICP/RIE (8): Membrane protected by fused quartz mask with central opening, 45 min Ar/Cl_2. Multiple rounds of O_2 etch until individual microdevices are released. Etch rates can be found in Ruf et al. [27].	
XIV. Cleaning	HF clean	
XV. Bonding	Micromanipulator (9)	

Table 4.1: Detailed fabrication steps and process parameters of the two fabrication methods to obtain diamond microdevices, starting with ~ 50 µm membranes. All wet processing steps are followed by a dip in acetone and IPA and blow-drying with a nitrogen gun. The numbers in brackets for the laser-cutting refer to Fig. 4.1 (c) of the main text. Fabrication step II. (XII.) of the EBL (laser-cutting) method is used to create SnV centers. In the case of NV centers, the color centers are created in the bulk diamond, before slicing into membranes, as described in Section 4.2.3.

4.7.2 Bonding of Microdevices to Cavity Mirror

Figure 4.7 (a) shows the breaking out of individual microdevices by a micromanipulator. Supplementary Video 1 (Ref. [56]) shows the process with devices from a second laser-cut membrane. We observe that up to 30 % of the devices bond fully to the cavity mirror. Figure 4.7 (b) and (c) show diamond devices that are not fully bonded to the mirror. When approached by the cavity fiber, such devices can be moved or picked up accidentally.

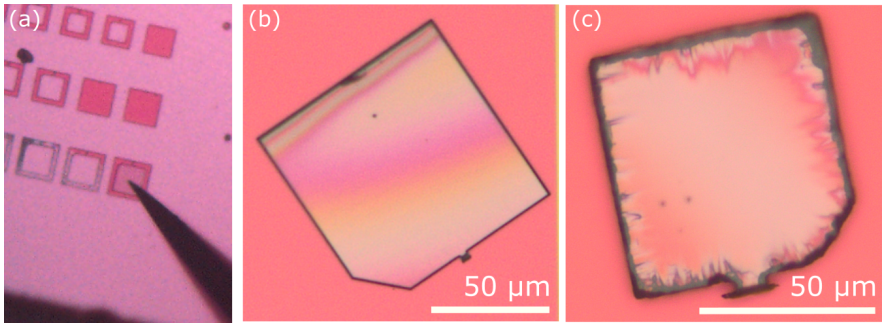

Figure 4.7: Bonding of diamond microdevices to the cavity mirror. (a) Released, thinned-down diamond devices above the cavity mirror. Individual devices can be broken out with the tip of a micromanipulator. An ill-bonded device fabricated by EBL (*Pai Mei*) in (b) and by laser-cutting (*Vincent Vega*) in (c). Both devices show interference fringes and an opaque color.

4.7.3 Experimental Setup: Room Temperature Microcavity

The cavity sample mirror with the microdevices (Fig. 4.8 (a)) is mounted on a piezo nanopositioning stage (Physik Instrumente P-542.2SL) with a range of 200 µm in both the X- and Y-direction. The other cavity mirror is a coated, laser-ablated fiber tip [75], which can be moved in the axial direction by a high-precision objective scanner (Physik Instrumente P-721) to change the cavity length along the Z-direction.

Figure 4.8 (b) shows a sketch of the optical setup and the microcavity. The cavity can be probed with resonant 637 nm light (Newport New Focus Velocity TLB-6300-LN) or with a white light supercontinuum source (NKT Photonics SC-450-2), spectrally filtered for 600 nm to 700 nm. The excitation light is combined in fiber and sent via the fiber side into the cavity. The transmitted light is collimated with an objective (100X Mitutoyo Plan Apochromat Objective) and collected on a photodiode (Thorlabs APD130A2) or sent via fiber to a spectrometer (Princeton Instruments SP-2500i). In addition, the microcavity can be imaged from the sample mirror side by a lamp and a camera for lateral alignment. Supplementary Video 2 (Ref. [56]) shows a two-dimensional cavity finesse scan over an exemplary device recorded with the camera.

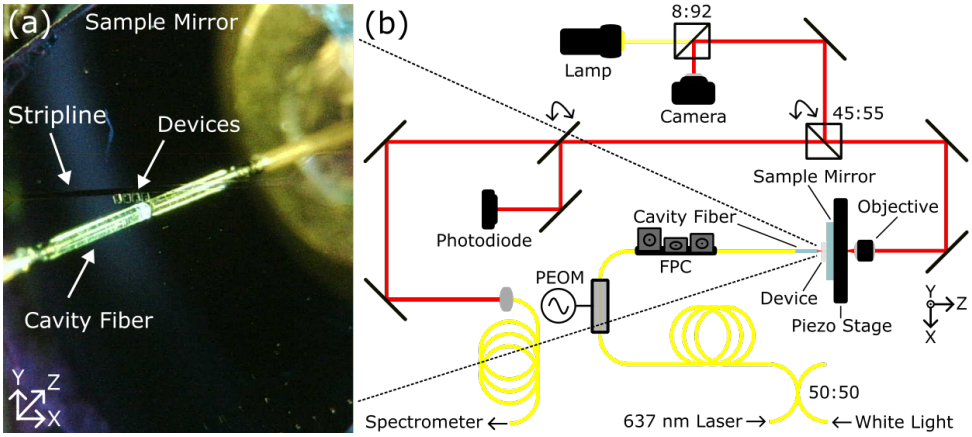

Figure 4.8: (a) Microscope picture of the microcavity with exemplary microdevices on the sample mirror next to a gold stripline. The cavity fiber can be seen on the left side, while the reflection in the mirror is on the right side. (b) Sketch of the home-built SCM setup. Excitation light (resonant laser or white light) is sent into the cavity via the fiber. The light can be modulated with a phase electro-optic modulator (PEOM), and the polarization is set manually with a 3-paddle fiber polarization controller (FPC). The outcoupled detection beam is collimated with an objective and sent either to a photodiode or coupled into a single-mode fiber for the spectrometer.

4.7.4 Experimental Methods: Finesse Measurements and Cavity Fiber Properties

To measure the finesse, the cavity is probed with a resonant 637 nm laser, and the transmission signal is recorded on the photodiode. We record the time trace of the photodiode voltage with an oscilloscope (Picotech Picoscope 3403). The cavity length is scanned by a triangular voltage with a frequency of 300 Hz over approximately five fundamental modes to ensure that the middle of these modes is not affected by nonlinearities occurring at the edges of the scanning range. The middle modes are fitted with Lorentzian functions, resulting in a measured cavity finesse defined as the ratio of the mode distance to the linewidth in time. An exemplary trace with two fundamental modes is shown in Fig. 4.9 (a). The resonance peak with the higher coefficient of determination (R^2) is used to determine the finesse. The data is filtered by requiring the mode distance to be within an acceptance range to ensure that only the fundamental modes are fitted.

As discussed in the main text, birefringence in diamond microdevices can cause polarization splitting, which is observed as a frequency splitting of the fundamental cavity mode. To correctly fit these modes in the finesse measurements, two Lorentzian functions are fitted (see Fig. 4.11 (a)).

The same cavity fiber is used for all the presented measurements. From an interferometric measurement of the concave fiber tip, we extract a spherical radius of curvature ROC of 17.3 µm with an asymmetry of 7.8 %. To determine the range in which the fiber exhibits a stable finesse, we measure the cavity length-dependent finesse in Fig. 4.9 (b) on the bare mirror. The cavity length is determined by taking white light transmission spectra, which directly yield the cavity free spectral range and thereby the cavity length. For longer cavity lengths L_{cav} clipping losses $\mathscr{L}_{clip}$ emerge which dependent on the diameter of the

concave feature D_d and the ROC of the fiber mirror and can be calculated by [57]:

$$\mathscr{L}_{clip} = e^{\left(-2\left(\frac{D_d}{2\omega_m}\right)^2\right)}. \tag{4.5}$$

In this formula, ω_m denotes the cavity beam width on the fiber mirror and can be calculated by the beam waist on the sample cavity mirror ω_0 [81]:

$$\omega_m = \omega_o \sqrt{1 + \left(\frac{L_{cav}\lambda}{\pi n \omega_0^2}\right)^2}, \qquad \omega_0 = \sqrt{\frac{\lambda}{\pi}} \left(L_{cav}(ROC - L_{cav})\right)^{1/4}. \tag{4.6}$$

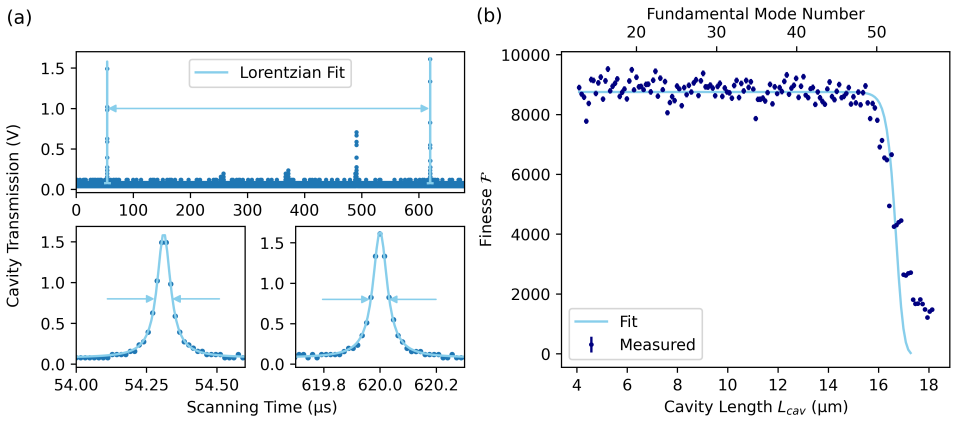

Figure 4.9: (a) Typical cavity finesse measurement recorded with an oscilloscope. The cavity length is scanned with a triangular voltage, and two fundamental modes with a few higher-order modes are visible in the upper panel. The peaks of the fundamental modes are fitted with a Lorentzian function, yielding the cavity linewidth in time. The free spectral range in time is given by the spacing of the fundamental modes. From the shown measurement, a finesse of 9500 is determined. (b) Cavity length-dependent measured finesse of the fiber used to characterize the diamond microdevices. The coating limited finesse is 19000 with 330 ppm losses. A clear plateau of finesse values of ~ 8700 is reached for a cavity length smaller than 15 µm.

We fit the measured finesse values in Fig. 4.9 (b), with the losses determined by equation (4.2) plus the clipping losses $\mathscr{L}_{clip}$. Like in Section 4.3.2 of the main text, we set $t_d = 0\,\mu m$ and leave the additional losses and the diameter of the concave feature as free parameters. The radius of curvature is set to the measured value as stated above.
Note that the finesse values measured on the plateau in Fig. 4.9 (b) are a bit higher than the average bare cavity finesse values due to a local optimization on the lateral spot and reveal additional losses of 390 ppm determined by the fit.

4.7.5 Experimental Methods: Hybrid Cavity Modes

To determine the cavity length and the thickness of incorporated devices, we probe the cavity with broadband white light and send the transmitted light to a spectrometer. The cavity length is changed by applying a voltage to the objective scanner, which holds the cavity fiber.

For the broadband white light, the cavity acts as a spectral filter, and fundamental modes appear as bright lines. We fit the fundamental modes with an analytic formula [11], yielding the length of the air gap and the device thickness. The measurements are shown in Fig. 4.10.

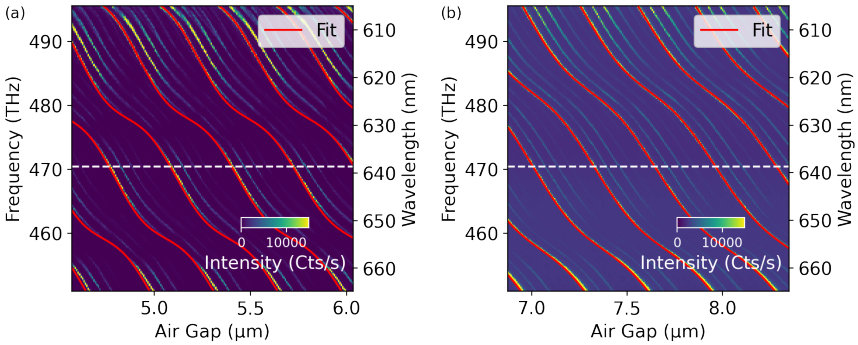

Figure 4.10: Cavity dispersion measured by transmission spectra of a broadband light source. (a) On the EBL microdevice (*Pai Mei*), we measure a device thickness of 3.31 µm. (b) On the laser-cut microdevice (*Vincent Vega*), the fit determines a thickness of 2.51 µm. Both devices are probed in the air-like mode (steeper slope) at 637 nm, indicated by the white, dashed line. The positions on the devices of these measurements are indicated in Fig. 4.3 (a) and (c) with a red cross.

4.7.6 Experimental Methods: Polarization Splitting

To measure the cavity polarization splitting, a second trace of the resonance peaks is measured at each lateral scan point with the resonant 637 nm laser, modulated by sidebands. The sidebands are imprinted by a phase electro-optic modulator (Jenoptik PM635) with a microwave source (Rohde & Schwarz SGS100A) at a frequency of 6 GHz. The obtained modes are fitted with three (or six) Lorentzian peaks, and the sidebands are used to convert the polarization splitting from scanning time to frequency. The data are filtered by requiring $R^2 > 0.95$ to ensure the fit succeeded. An example measurement is shown in Fig. 4.11.

4.7.7 Experimental Methods: PLE Scans

Measurements are performed in a home-built, cryogenic confocal microscope, whose excitation and detection path can be adapted for the measurements of SnV and NV centers. Details about the low-temperature setup and the measurement methods are described in the Supplementary Information of Brevoord et al. [64] and Ruf et al. [27].

The parameters for the SnV center measurements shown in Fig. 4.6 (b) are: 1 µW green repump for 100 ms and 0.5 nW to 1 nW resonant laser excitation power for 10 ms integration. The resonant laser is detuned in steps between 10 MHz to 20 MHz with a speed of ~ 2 GHz/s.

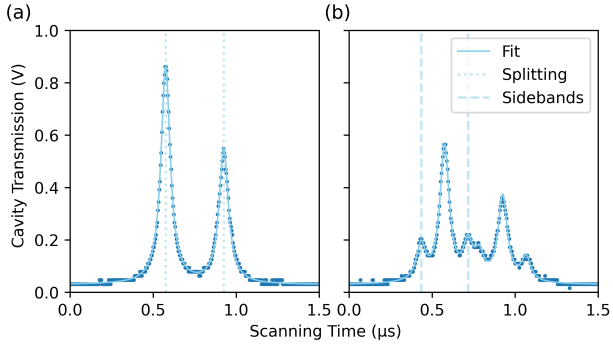

Figure 4.11: Exemplary measurement of the polarization splitting of the two orthogonal cavity modes on the diamond device. The cavity length is scanned with a triangular voltage over the fundamental mode, and the transmission is measured on a photodiode. (a) The length-dependent polarization splitting of the fundamental mode. (b) The same measurement with the sideband modulation. The fixed distance of the sidebands (indicated by the dashed lines) is used to determine the cavity linewidth and polarization splitting in frequency. In this measurement, a linewidth of 2.9 GHz and polarization splitting of 14.9 GHz (dotted lines in (a)) is extracted.

The parameters of the NV center measurements in Fig. 4.6 (d) are: 40 µW green repump for 10 µs and 40 nW resonant laser excitation power for 20 µs integration. At each frequency step between 8 MHz to 20 MHz, a sequence of repump, waiting of 10 µs, and readout is repeated for a total time of 200 ms. The statistics of the NV center measurements can be found in Fig. 4.12.

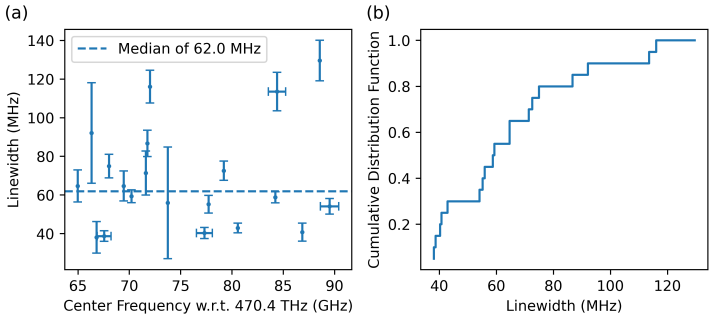

Figure 4.12: Statistics of the optical coherence of 20 different NV centers in an EBL patterned diamond microdevice (*Mr. Orange*), measured at ~ 4 K with a confocal microscope. (a) ZPL center frequencies and linewidth values, obtained by a Voigt fit to the individual NV center resonances (see Fig. 4.6 for exemplary data and fit). The errors are also obtained by the fit. (b) The linewidth values are plotted as a cumulative distribution function (CDF). The measurement parameters can be found in 4.7.7.

4.7.8 Measurements on the Laser-cut Microdevice

An overview of all measurements performed on the laser-cut microdevice (*Vincent Vega*) is shown in Fig. 4.13.

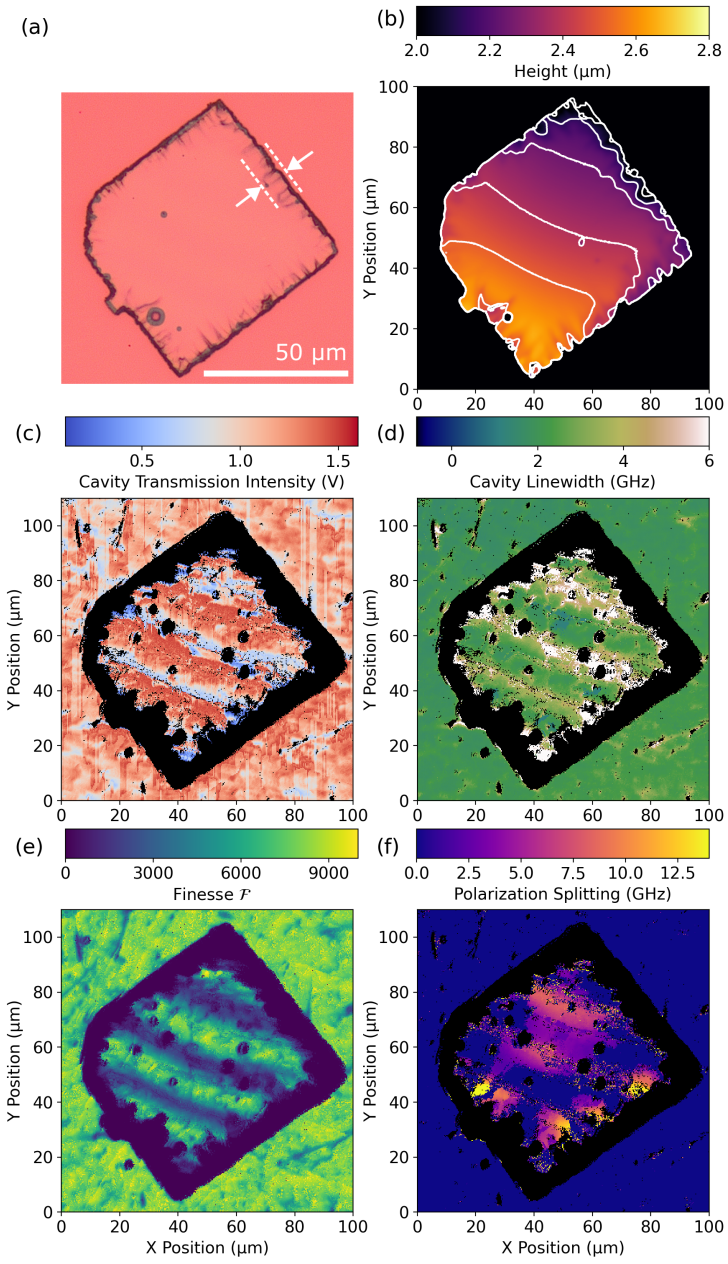

Figure 4.13: Summary of different measurements of the laser-cut diamond microdevice (*Vincent Vega*). (a) Light microscope image. (b) Height map measured by a white light interferometer. (c)-(f) Scanning cavity microscopy. All data is measured within one scan and by probing the cavity with a resonant laser. (c) Cavity transmission intensity is measured on a photodiode. Note that the laser power is varied during the measurement. (d) Cavity linewidth. (e) Cavity finesse. (f) Cavity polarization splitting.

4.8 Additional Data

This section presents additional figures on the fabrication process and data of the laser-cut and EBL microdevices shown in this chapter. The underlying data can be found in the repository accompanying this thesis [82].

4.8.1 Measurements on the EBL Microdevice

An overview of all measurements performed on the EBL microdevice (*Pai Mei*) is shown in Fig. 4.14.

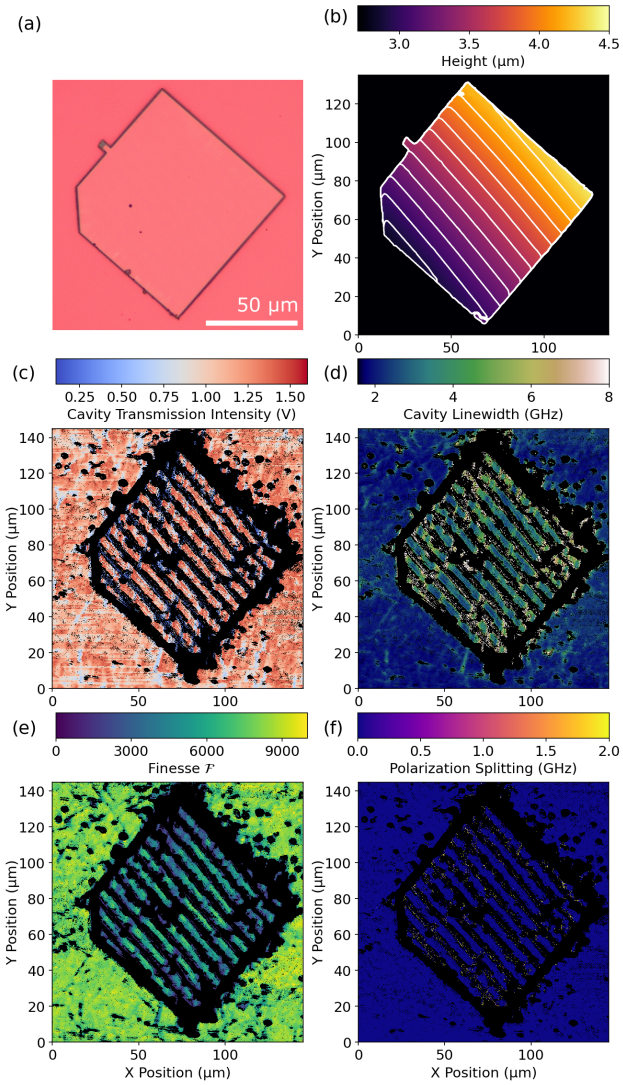

Figure 4.14: Summary of different measurements of the EBL diamond microdevice (*Pai Mei*).

4.8.2 Creation of NV Centers

Systematic studies have shown that NV centers formed from nitrogen naturally occurring in the diamond lattice show much narrower optical linewidth than NV centers created by ion implantation [55, 83].

We therefore employ electron irradiation with minimal crystal damage to generate NV centers from the native nitrogen concentration to obtain NV centers with high optical coherence [27]. As described in Section 4.2.3, the bulk diamond is irradiated with electrons at the Reactor Institute in Delft. A Van de Graaff electron accelerator produces a 2 MeV electron beam, in which the diamonds are placed for a certain time, determining the irradiation dose. The energy is large enough that electrons fully penetrate the sample and vacancies are formed throughout the diamond. The sample is afterward processed with a tri-acid clean and annealed under vacuum (see Section 4.2.3).

To assess the NV center density, confocal microscopy scans are conducted of the bulk samples after annealing. Typical confocal scans are shown in Fig. 4.15 with different electron irradiation doses. Irradiation with a higher electron dose with subsequent annealing can be repeated until a sufficient NV density is reached. Afterwards, the 0.5 mm thick bulk diamonds are sliced and polished into three membranes as described in Section 4.2.1.

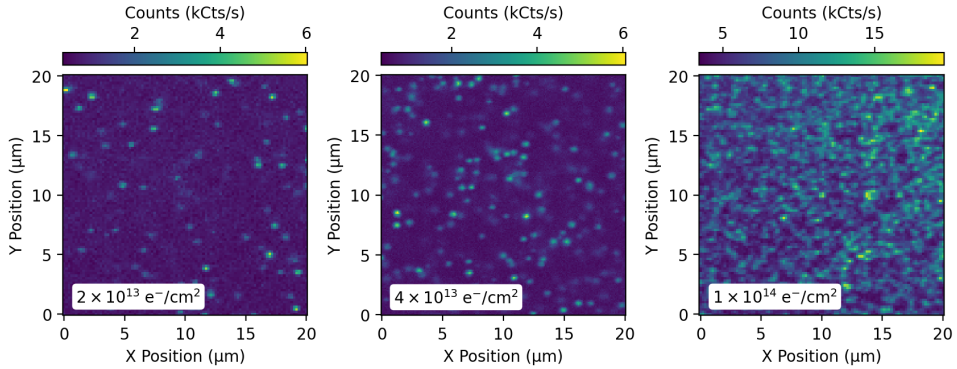

Figure 4.15: Confocal microscopy scans of three bulk diamond samples, after electron irradiation and annealing. An energy of 2 MeV is used, and the respective electron irradiation doses are indicated in the inset box. Confocal scans are performed under ambient conditions with 400 µW off-resonant, green excitation at a focal depth of about 5 µm below the diamond surface. A higher electron dose leads to the creation of more vacancies and subsequently more NV centers in the sample, despite the unknown starting nitrogen density of the commercial samples, which is specified to be below 5 ppb. The native NV center density in these samples is even smaller, with typical numbers below 0.03 ppb.

4.8.3 Fabrication of EBL Microdevices

Parts of the EBL fabrication process are shown in Fig. 4.16. The membrane after transferring the pattern from the silicon nitride hard mask into the diamond surface with the anisotropic inductively coupled plasma reactive ion etching is shown in Fig. 4.16 (a) (fabrication step X. in Tab. 4.1). Figure 4.16 (b) shows the membrane during the device release etch with the quartz mask from the backside (fabrication step XIII. in Tab. 4.1). Note that the release etch is used for both fabrication methods, laser-cutting and EBL.

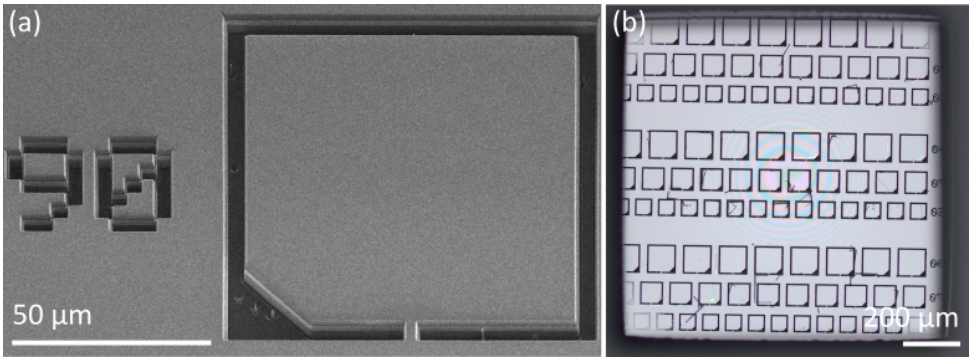

Figure 4.16: Diamond microdevices patterned by electron beam lithography (EBL) during the fabrication process (*Pai Mei*). (a) Scanning electron microscope image of the sample after etching the trenches with the silicon nitride hard mask. (b) Light microscope image from the backside of the sample after multiple rounds of the release etch. The quartz mask protecting the outer frame of the membrane is visible on the edges. Most of the trenches have opened, and the interference pattern in the center of the sample indicates a thickness of up to a few micrometers or less. Figure adapted from Sauerzapf [84].

4.8.4 Fabrication of Laser-cut Microdevices

For the laser-cutting method, the diamond membranes are protected with a polyvinyl alcohol (PVA) layer. Figure 4.17 (a) shows a diamond membrane after laser-cutting (fabrication step X. in Tab. 4.1). The protection layer is removed by de-ionized water and acetone, and the sample is subsequently cleaned in a Piranha mixture (Fig. 4.17 (b)). Finally, to obtain a smooth and clean surface, a strain-relief etch is conducted as shown in Fig. 4.17 (c) (fabrication step XII. in Tab. 4.1). For SnV centers, the membranes are, after this step, implanted with tin ions, followed by annealing (see Section 4.2.3).

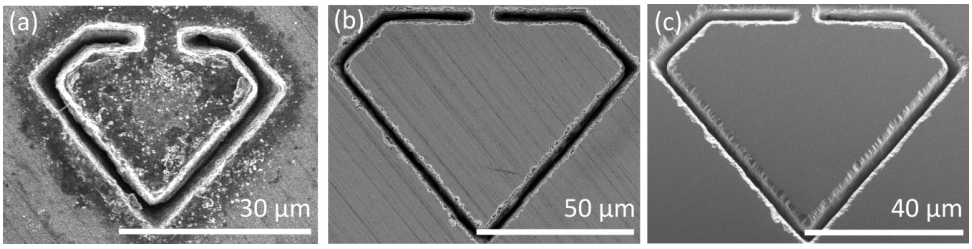

Figure 4.17: Diamond microdevices patterned by laser-cutting during the fabrication process (*Vincent Vega*), investigated by scanning electron microscopy. The membrane is protected with a PVA mask. (a) The membrane is shown directly after laser cutting, with debris created by the irradiation. (b) The protection layer and debris are removed by a Piranha clean. The membrane still exhibits marks from the polishing process. (c) A strain relief etch (see Section 4.2.2) leads to a smooth and clean diamond surface. The laser-cutting results in wedged edges with a higher surface roughness. However, the center of the devices maintains a high quality. Figure adapted from Sauerzapf [84].

4.8.5 SnV Centers in Laser-cut Microdevices

Confocal microscopy scans are performed under ambient conditions to assess the SnV center density in the microdevices after bonding to the cavity mirror. A confocal scan is shown in Fig. 4.18 (b) together with a spectrum recorded at the center of the device, shown in Fig. 4.18 (c). A clear peak in the spectrum around 620 nm confirms the ZPL emission of SnV centers, accompanied by the phonon sideband emission towards longer wavelengths.

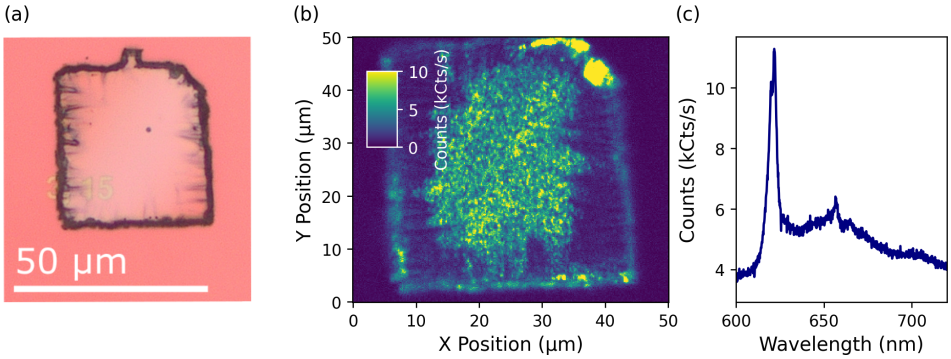

Figure 4.18: SnV centers in a laser-cut diamond microdevice ((*Vincent Vega*) bonded to the cavity mirror. (a) Light microscope image of the device. (b) Scanning confocal microscopy of the device. Off-resonant, green excitation is used, and the fluorescence is filtered with a 620 nm bandpass filter (full-width half maximum of 10 nm) to select only the light of SnV centers. A high SnV density is observed in the center of the platelet, while the SnV layer is removed at the wedged edges. Note that this scan is also shown in Fig. 4.6 (a). (c) A spectrum is recorded in the center of the device, showing a peak around 620 nm of the SnV centers emission (detection light only filtered with a long pass filter at 600 nm). The measurements are performed at room temperature.

The optical properties of SnV centers are further investigated at low temperatures in Fig. 4.19. A series of PLE laser scans is conducted at low temperatures for three different SnV centers. The spectral wandering of the SnV centers can be observed, as well as the bistability as mentioned in Section 4.4.

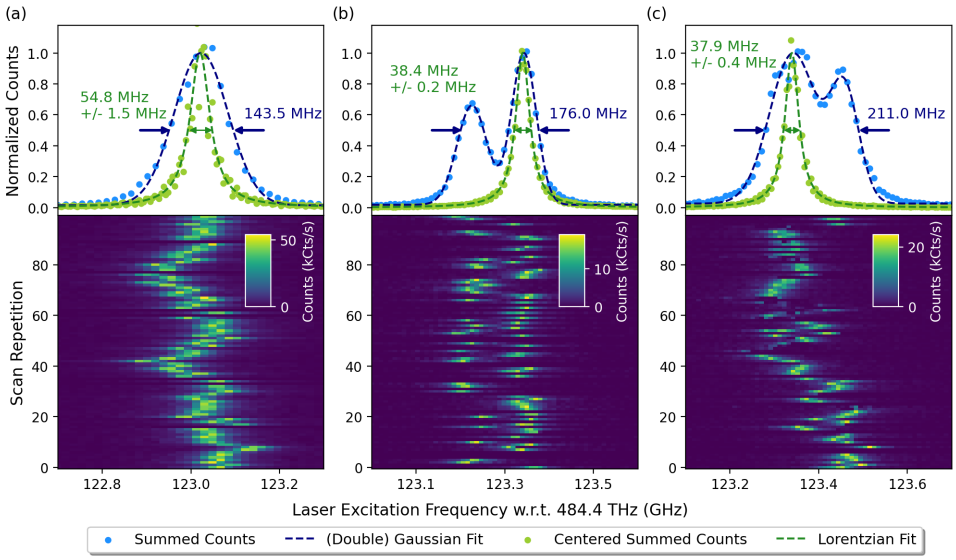

Figure 4.19: Lower panel: hundred consecutive PLE laser scans of three different SnV centers hosted in a laser-cut diamond microdevice (*Vincent Vega*) at a temperature of 4K. To initialize the charge state, the off-resonant green repump laser is applied at the beginning of each scan. Upper panel: Integrated counts (in blue) fit with a Gaussian function to determine the spectral diffusion. An individual scan is fit with a Lorentzian function and centered to sum (in green), yielding the SnV center's dephasing linewidth. Scans with a full Lorentzian lineshape peak are manually selected. The data of the upper panel is shown in Fig. 4.6 (b). Measurement parameters can be found in Section 4.7.7.

4.8.6 NV Centers in EBL Microdevices

The light microscope image and a two-dimensional confocal microscopy scan of the EBL-fabricated microdevice are shown in Fig. 4.20. The scan reveals the NV center density. A thickness of 5 µm to 6 µm of the microdevice is measured with a white light interferometer.

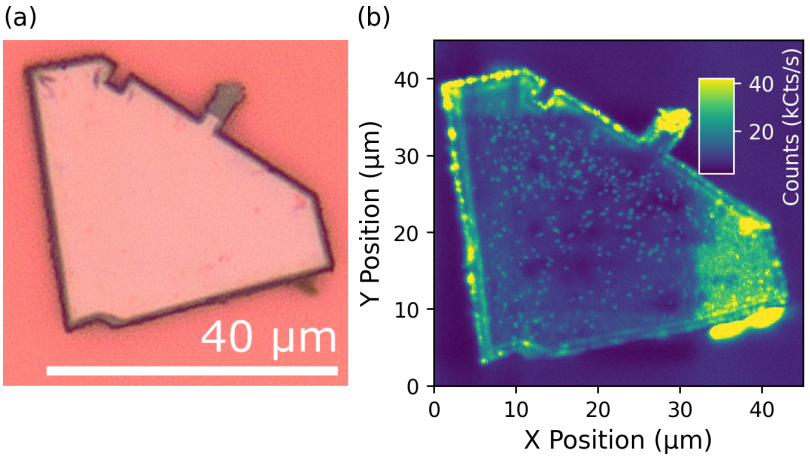

Figure 4.20: NV centers in an EBL-fabricated diamond microdevice (*Mr. Orange*) bonded to the cavity mirror. (a) Light microscope image of the device. (b) Scanning confocal microscopy. Off-resonant, green excitation is used, and the fluorescence at longer wavelengths is detected. A moderate NV center density is observed. Note that this scan is also shown in Fig. 4.6 (c).

Figure 4.21 (a) shows a broad PLE laser scan with several NV center transitions. The spectrum is relatively clean, confirming the low density of NV centers as expected from the two-dimensional confocal scan shown in Fig. 4.20 (b).

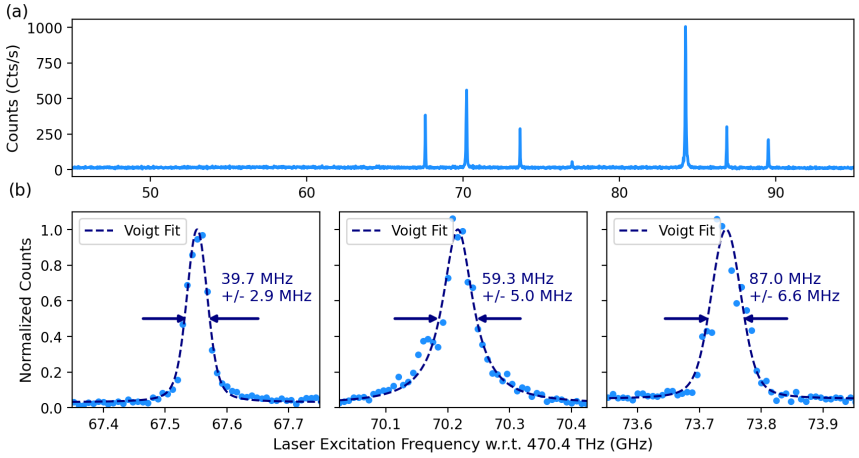

Figure 4.21: Optical properties of NV centers inside the EBL patterned diamond microdevice (*Mr. Orange*) measured by PLE laser scan at low temperatures with a confocal microscope. At each frequency step, the NV center is initialized with a green laser pulse into the negative charge state and predominantly in the spin ground state. (a) Wide frequency scan in steps of 20 MHz showing the optical resonances of several NV centers. (b) Narrower scans in steps of 8 MHz over the three peaks on the left side of (a). Each peak is fit with a Voigt profile, and the extracted linewidth is displayed next to it. The same data is shown in Fig. 4.6 (d). Measurement parameters can be found in Section 4.7.7.

4.8.7 NV Centers in Laser-cut Microdevices

This section presents preliminary data on NV centers in laser-cut microdevices. Note that this device has not been included in the measurements so far. NV centers are created by electron irradiation with a dose of $4 \times 10^{13}\,e^{-}/cm^{2}$. A thickness of 6 µm to 7 µm of the microdevice is measured with a white light interferometer. The device is placed on the mirror at a distance of about 50 µm to a gold stripline, which can be used for microwave delivery.

Figure 4.22 shows measurements under ambient conditions, confirming that the device contains NV centers and that they can be addressed by microwaves applied through the stripline. The spin-excited states of the NV center have a higher probability of decaying through the intersystem crossing, which leads to reduced fluorescence in the optical signal. When the driving frequency of the microwaves becomes resonant with the spin transition around 2.88 GHz, a reduced fluorescence due to the intersystem crossing can be observed.

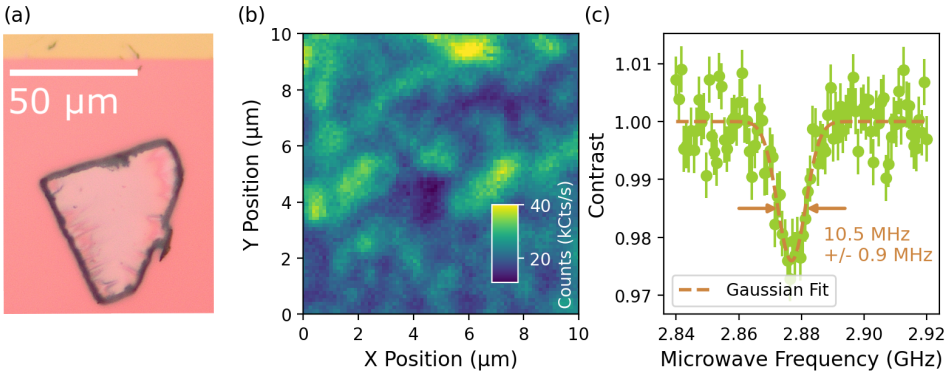

Figure 4.22: NV centers in a diamond microdevice, fabricated by laser cutting (*Ringo*). (a) Light microscope image of the device bonded to the cavity mirror. Before bonding, a gold stripline is deposited on the mirror for microwave control. (b) A confocal microscopy scan of the center of the device shows a high NV center density under off-resonant, 515 nm excitation. (c) Optically detected magnetic resonance measurement of NV centers under off-resonant, continuous wave excitation without a magnetic field. The microwave frequency is changed in steps of 0.8 MHz with an integration time of 100 ms per step. A microwave power of 25 dBm is used, integrated over ten repetitions. The measurements are conducted at room temperature.

Figure 4.23 (a) presents PLE laser scan conducted at low temperatures over a frequency range covering around 65 GHz. The optical transitions of multiple NV centers are visible. This confirms the high density of the device as indicated by the confocal scan.

The stability of one NV center's transition is further investigated by repetitive scans in Fig. 4.23 (b). We use constant microwave driving at the NV center's resonance frequency during the measurement to mix the spin state. Without the microwave driving, the resonant laser would optically pump the NV center to a different spin state, which appears dark during the resonant scan. The stable count trace in the lower panel of Fig. 4.23 (a) indicates that the NV centers are not spin pumped into the dark state.

To conclude about the NV center quality in laser-cut devices, further investigation is required to gather more statistics.

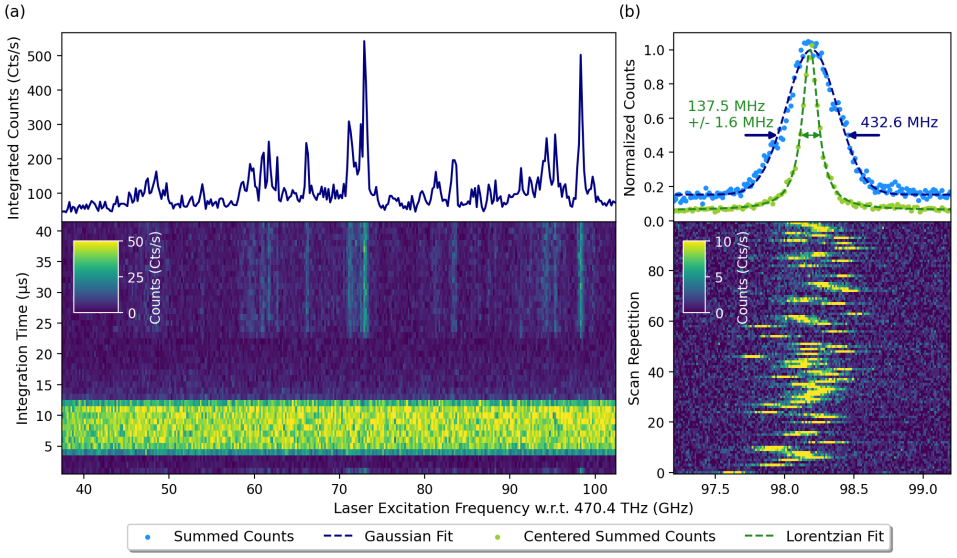

Figure 4.23: Optical properties of NV centers in a laser-cut diamond microdevice (*Ringo*). (a) PLE scan at low temperatures. The lower panel shows the obtained counts during the measurement sequences: at each frequency point, an off-resonant, green laser is used to repump with 5 µW for 10 µs. After a wait time of 10 µs, the resonant laser is applied with 30 nW for 20 µs. 10000 repetitions are averaged over time per frequency step of 0.2 MHz. The upper panel shows the integrated counts during the time of the application of the resonant laser pulse. (b) Consecutive PLE scans around the dominant peak on the right side of the spectrum of (a). Scans with a full Lorentzian peak are manually selected and summed up in blue, which is fit by a Gaussian function. In green: each scan is separately fit with a Lorentzian function and centered before summation. The obtained spectrum is fitted with a Lorentzian function. Measurement parameters: before each scan, an off-resonant, green laser pulse is applied with 10 µW for 200 ms. The resonant laser is detuned in steps of ~ 12 MHz with a speed of ~ 0.3 GHz/s. Per frequency step, the counts are integrated for 40 ms with 1 nW resonant laser power. In both measurements of (a) and (b), microwaves at 2.877 GHz with 25 dBm are constantly applied.

References

[1] Y. Herrmann, J. M. Brevoord, J. Fischer, S. Scheijen, C. Sauerzapf, N. Codreanu, L. G. C. Wienhoven, Y. M. Q. Van Der Graaf, C. F. J. Wolfs, R. Méjard, M. Ruf, N. De Jong, and R. Hanson, *Laser-cut patterned, micrometer-thin diamond membranes with coherent color centers for open microcavities,* Mater. Quantum. Technol. **5**, 035001 (2025).

[2] E. Janitz, M. K. Bhaskar, and L. Childress, *Cavity quantum electrodynamics with color centers in diamond,* Optica **7**, 1232 (2020).

[3] S. Mi, M. Kiss, T. Graziosi, and N. Quack, *Integrated photonic devices in single crystal diamond,* J. Phys. Photonics **2**, 042001 (2020).

[4] M. Ruf, N. H. Wan, H. Choi, D. Englund, and R. Hanson, *Quantum networks based on color centers in diamond,* J. Appl. Phys. **130**, 070901 (2021).

[5] P. K. Shandilya, S. Flagan, N. C. Carvalho, E. Zohari, V. K. Kavatamane, J. E. Losby, and P. E. Barclay, *Diamond Integrated Quantum Nanophotonics: Spins, Photons and Phonons,* J. Lightwave Technol. **40**, 7538 (2022).

[6] J. Riedrich-Möller, L. Kipfstuhl, C. Hepp, E. Neu, C. Pauly, F. Mücklich, A. Baur, M. Wandt, S. Wolff, M. Fischer, S. Gsell, M. Schreck, and C. Becher, *One- and two-dimensional photonic crystal microcavities in single crystal diamond,* Nat. Nanotechnol. **7**, 69 (2012).

[7] J. C. Lee, A. P. Magyar, D. O. Bracher, I. Aharonovich, and E. L. Hu, *Fabrication of thin diamond membranes for photonic applications,* Diam. Relat. Mater. **33**, 45 (2013).

[8] A. Faraon, C. Santori, Z. Huang, K.-M. C. Fu, V. M. Acosta, D. Fattal, and R. G. Beausoleil, *Quantum photonic devices in single-crystal diamond,* New J. Phys. **15**, 025010 (2013).

[9] S. W. Ding, M. Haas, X. Guo, K. Kuruma, C. Jin, Z. Li, D. D. Awschalom, N. Delegan, F. J. Heremans, A. A. High, and M. Lončar, *High-Q cavity interface for color centers in thin film diamond,* Nat. Commun. **15**, 6358 (2024).

[10] P. Fuchs, T. Jung, M. Kieschnick, J. Meijer, and C. Becher, *A cavity-based optical antenna for color centers in diamond,* APL Photonics **6**, 086102 (2021).

[11] E. Janitz, M. Ruf, M. Dimock, A. Bourassa, J. Sankey, and L. Childress, *Fabry-Perot microcavity for diamond-based photonics,* Phys. Rev. A **92**, 043844 (2015).

[12] S. Bogdanović, S. B. van Dam, C. Bonato, L. C. Coenen, A.-M. J. Zwerver, B. Hensen, M. S. Z. Liddy, T. Fink, A. Reiserer, M. Lončar, and R. Hanson, *Design and low-temperature characterization of a tunable microcavity for diamond-based quantum networks,* Appl. Phys. Lett. **110**, 171103 (2017).

[13] D. Riedel, I. Söllner, B. J. Shields, S. Starosielec, P. Appel, E. Neu, P. Maletinsky, and R. J. Warburton, *Deterministic Enhancement of Coherent Photon Generation from a Nitrogen-Vacancy Center in Ultrapure Diamond,* Phys. Rev. X **7**, 031040 (2017).

[14] D. Riedel, D. Rohner, M. Ganzhorn, T. Kaldewey, P. Appel, E. Neu, R. J. Warburton, and P. Maletinsky, *Low-Loss Broadband Antenna for Efficient Photon Collection from a Coherent Spin in Diamond,* Phys. Rev. Applied **2**, 064011 (2014).

[15] A. Butcher, X. Guo, R. Shreiner, N. Delegan, K. Hao, P. J. I. Duda, D. D. Awschalom, F. J. Heremans, and A. A. High, *High-Q Nanophotonic Resonators on Diamond Membranes using Templated Atomic Layer Deposition of TiO2,* Nano Lett. **20**, 4603 (2020).

[16] X. Guo, M. Xie, A. Addhya, A. Linder, U. Zvi, S. Wang, X. Yu, T. D. Deshmukh, Y. Liu, I. N. Hammock, Z. Li, C. T. DeVault, A. Butcher, A. P. Esser-Kahn, D. D. Awschalom, N. Delegan, P. C. Maurer, F. J. Heremans, and A. A. High, *Direct-bonded diamond membranes for heterogeneous quantum and electronic technologies,* Nat. Commun. **15**, 8788 (2024).

[17] A. M. Boyce, H. Li, N. C. Wilson, D. Acil, A. Shams-Ansari, S. Chakravarthi, C. Pederson, Q. Shen, N. Yama, K.-M. C. Fu, M. Lončar, and M. H. Mikkelsen, *Plasmonic Diamond Membranes for Ultrafast Silicon Vacancy Emission,* Nano Lett. **24**, 3575 (2024).

[18] S. Asif, H. Chen, J. Cremer, S. Ravan, J. Támara-Isaza, S. Lamsal, R. Ebadi, Y. Li, L.-J. Zhou, C.-Z. Chang, J. Q. Xiao, A. Yacoby, R. L. Walsworth, and M. J. H. Ku, *Diamond micro-chip for quantum microscopy,* AVS Quantum Sci. **6**, 044405 (2024).

[19] Y. Schlussel, T. Lenz, D. Rohner, Y. Bar-Haim, L. Bougas, D. Groswasser, M. Kieschnick, E. Rozenberg, L. Thiel, A. Waxman, J. Meijer, P. Maletinsky, D. Budker, and R. Folman, *Wide-Field Imaging of Superconductor Vortices with Electron Spins in Diamond,* Phys. Rev. Applied **10**, 034032 (2018).

[20] J. J. Carmiggelt, I. Bertelli, R. W. Mulder, A. Teepe, M. Elyasi, B. G. Simon, G. E. W. Bauer, Y. M. Blanter, and T. Van Der Sar, *Broadband microwave detection using electron spins in a hybrid diamond-magnet sensor chip,* Nat. Commun. **14**, 490 (2023).

[21] T. S. Ghiasi, M. Borst, S. Kurdi, B. G. Simon, I. Bertelli, C. Boix-Constant, S. Mañas-Valero, H. S. J. Van Der Zant, and T. Van Der Sar, *Nitrogen-vacancy magnetometry of CrSBr by diamond membrane transfer,* npj 2D Mater. Appl. **7**, 62 (2023).

[22] M. Borst, P. H. Vree, A. Lowther, A. Teepe, S. Kurdi, I. Bertelli, B. G. Simon, Y. M. Blanter, and T. Van Der Sar, *Observation and control of hybrid spin-wave–Meissner-current transport modes,* Science **382**, 430 (2023).

[23] J. Zhou, G. Q. Yan, M. Huang, N. J. McLaughlin, C. R. Du, and H. Wang, *Quantum sensing of local stray field environment of micron-scale magnetic disks,* Appl. Phys. Lett. **123**, 024003 (2023).

[24] R. Albrecht, A. Bommer, C. Deutsch, J. Reichel, and C. Becher, *Coupling of a Single Nitrogen-Vacancy Center in Diamond to a Fiber-Based Microcavity,* Phys. Rev. Lett. **110**, 243602 (2013).

[25] H. Kaupp, C. Deutsch, H.-C. Chang, J. Reichel, T. W. Hänsch, and D. Hunger, *Scaling laws of the cavity enhancement for nitrogen-vacancy centers in diamond,* Phys. Rev. A **88**, 053812 (2013).

[26] S. Johnson, P. R. Dolan, T. Grange, A. A. P. Trichet, G. Hornecker, Y. C. Chen, L. Weng, G. M. Hughes, A. A. R. Watt, A. Auffèves, and J. M. Smith, *Tunable cavity coupling of the zero phonon line of a nitrogen-vacancy defect in diamond,* New J. Phys. **17**, 122003 (2015).

[27] M. Ruf, M. IJspeert, S. van Dam, N. de Jong, H. van den Berg, G. Evers, and R. Hanson, *Optically Coherent Nitrogen-Vacancy Centers in Micrometer-Thin Etched Diamond Membranes,* Nano Lett. **19**, 3987 (2019).

[28] V. Yurgens, A. Corazza, J. A. Zuber, M. Gruet, M. Kasperczyk, B. J. Shields, R. J. Warburton, Y. Fontana, and P. Maletinsky, *Spectrally stable nitrogen-vacancy centers in diamond formed by carbon implantation into thin microstructures,* Appl. Phys. Lett. **121**, 234001 (2022).

[29] V. Yurgens, Y. Fontana, A. Corazza, B. J. Shields, P. Maletinsky, and R. J. Warburton, *Cavity-assisted resonance fluorescence from a nitrogen-vacancy center in diamond,* npj Quantum Inf. **10**, 112 (2024).

[30] R. Zifkin, C. D. Rodríguez Rosenblueth, E. Janitz, Y. Fontana, and L. Childress, *Lifetime Reduction of Single Germanium-Vacancy Centers in Diamond via a Tunable Open Microcavity,* PRX Quantum **5**, 030308 (2024).

[31] R. Berghaus, S. Sachero, G. Bayer, J. Heupel, T. Herzig, F. Feuchtmayr, J. Meijer, C. Popov, and A. Kubanek, *Cavity-enhanced emission and absorption of color centers in a diamond membrane with selectable strain,* Phys. Rev. Applied **23**, 034050 (2025).

[32] Y. Herrmann, J. Fischer, J. M. Brevoord, C. Sauerzapf, L. G. C. Wienhoven, L. J. Feije, M. Pasini, M. Eschen, M. Ruf, M. J. Weaver, and R. Hanson, *Coherent Coupling of a Diamond Tin-Vacancy Center to a Tunable Open Microcavity,* Phys. Rev. X **14**, 041013 (2024).

[33] S. Bogdanović, M. S. Z. Liddy, S. B. van Dam, L. C. Coenen, T. Fink, M. Lončar, and R. Hanson, *Robust nano-fabrication of an integrated platform for spin control in a tunable microcavity,* APL Photonics **2**, 126101 (2017).

[34] P. Tamarat, T. Gaebel, J. R. Rabeau, M. Khan, A. D. Greentree, H. Wilson, L. C. L. Hollenberg, S. Prawer, P. Hemmer, F. Jelezko, and J. Wrachtrup, *Stark Shift Control of Single Optical Centers in Diamond,* Phys. Rev. Lett. **97**, 083002 (2006).

[35] N. R. Parikh, J. D. Hunn, E. McGucken, M. L. Swanson, C. W. White, R. A. Rudder, D. P. Malta, J. B. Posthill, and R. J. Markunas, *Single-crystal diamond plate liftoff achieved by ion implantation and subsequent annealing,* Appl. Phys. Lett. **61**, 3124 (1992).

[36] A. H. Piracha, P. Rath, K. Ganesan, S. Kühn, W. H. P. Pernice, and S. Prawer, *Scalable Fabrication of Integrated Nanophotonic Circuits on Arrays of Thin Single Crystal Diamond Membrane Windows,* Nano Lett. **16**, 3341 (2016).

[37] B. A. Fairchild, P. Olivero, S. Rubanov, A. D. Greentree, F. Waldermann, R. A. Taylor, I. Walmsley, J. M. Smith, S. Huntington, B. C. Gibson, D. N. Jamieson, and

S. Prawer, *Fabrication of Ultrathin Single-Crystal Diamond Membranes,* Adv. Mater. **20**, 4793 (2008).

[38] X. Guo, N. Delegan, J. C. Karsch, Z. Li, T. Liu, R. Shreiner, A. Butcher, D. D. Awschalom, F. J. Heremans, and A. A. High, *Tunable and Transferable Diamond Membranes for Integrated Quantum Technologies,* Nano Lett. **21**, 10392 (2021).

[39] A. Faraon, P. E. Barclay, C. Santori, K.-M. C. Fu, and R. G. Beausoleil, *Resonant enhancement of the zero-phonon emission from a colour centre in a diamond cavity,* Nat. Photonics **5**, 301 (2011).

[40] B. J. M. Hausmann, B. Shields, Q. Quan, P. Maletinsky, M. McCutcheon, J. T. Choy, T. M. Babinec, A. Kubanek, A. Yacoby, M. D. Lukin, and M. Lončar, *Integrated Diamond Networks for Quantum Nanophotonics,* Nano Lett. **12**, 1578 (2012).

[41] P. Ovartchaiyapong, L. M. A. Pascal, B. A. Myers, P. Lauria, and A. C. Bleszynski Jayich, *High quality factor single-crystal diamond mechanical resonators,* Appl. Phys. Lett. **101**, 163505 (2012).

[42] P. Appel, E. Neu, M. Ganzhorn, A. Barfuss, M. Batzer, M. Gratz, A. Tschöpe, and P. Maletinsky, *Fabrication of all diamond scanning probes for nanoscale magnetometry,* Rev. Sci. Instrum. **87**, 063703 (2016).

[43] M. Ruf, *Cavity-enhanced quantum network nodes in diamond*, Ph.D. thesis, Delft University of Technology (2021).

[44] Y. Tao, J. M. Boss, B. A. Moores, and C. L. Degen, *Single-crystal diamond nanomechanical resonators with quality factors exceeding one million,* Nat. Commun. **5**, 3638 (2014).

[45] J. Heupel, M. Pallmann, J. Körber, D. Hunger, J. P. Reithmaier, and C. Popov, *Fabrication of High-Quality Thin Single-Crystal Diamond Membranes with Low Surface Roughness,* Phys. Status Solidi (a) **220**, 2200465 (2023).

[46] M. J. Burek, N. P. de Leon, B. J. Shields, B. J. M. Hausmann, Y. Chu, Q. Quan, A. S. Zibrov, H. Park, M. D. Lukin, and M. Lončar, *Free-Standing Mechanical and Photonic Nanostructures in Single-Crystal Diamond,* Nano Lett. **12**, 6084 (2012).

[47] B. Khanaliloo, M. Mitchell, A. C. Hryciw, and P. E. Barclay, *High-Q/V Monolithic Diamond Microdisks Fabricated with Quasi-isotropic Etching,* Nano Lett. **15**, 5131 (2015).

[48] J. S. Hodges, L. Li, M. Lu, E. H. Chen, M. E. Trusheim, S. Allegri, X. Yao, O. Gaathon, H. Bakhru, and D. Englund, *Long-lived NV ¯ spin coherence in high-purity diamond membranes,* New J. Phys. **14**, 093004 (2012).

[49] C. Toninelli, Y. Delley, T. Stöferle, A. Renn, S. Götzinger, and V. Sandoghdar, *A scanning microcavity for in situ control of single-molecule emission,* Appl. Phys. Lett. **97**, 021107 (2010).

[50] M. Mader, J. Reichel, T. W. Hänsch, and D. Hunger, *A scanning cavity microscope,* Nat. Commun. **6**, 7249 (2015).

[51] J. Benedikter, T. Moosmayer, M. Mader, T. Hümmer, and D. Hunger, *Transverse-mode coupling effects in scanning cavity microscopy,* New J. Phys. **21**, 103029 (2019).

[52] S. M. Eaton, J. P. Hadden, V. Bharadwaj, J. Forneris, F. Picollo, F. Bosia, B. Sotillo, A. N. Giakoumaki, O. Jedrkiewicz, A. Chiappini, M. Ferrari, R. Osellame, P. E. Barclay, P. Olivero, and R. Ramponi, *Quantum Micro–Nano Devices Fabricated in Diamond by Femtosecond Laser and Ion Irradiation,* Adv. Quantum Tech. **2**, 1900006 (2019).

[53] R. A. Norte, J. P. Moura, and S. Gröblacher, *Mechanical Resonators for Quantum Optomechanics Experiments at Room Temperature,* Phys. Rev. Lett. **116**, 147202 (2016).

[54] J. F. Ziegler, M. Ziegler, and J. Biersack, *SRIM – The stopping and range of ions in matter (2010),* Nucl. Instrum. Methods Phys. Res. B **268**, 1818 (2010).

[55] S. B. Van Dam, M. Walsh, M. J. Degen, E. Bersin, S. L. Mouradian, A. Galiullin, M. Ruf, M. IJspeert, T. H. Taminiau, R. Hanson, and D. R. Englund, *Optical coherence of diamond nitrogen-vacancy centers formed by ion implantation and annealing,* Phys. Rev. B **99**, 161203 (2019).

[56] Y. Herrmann, J. M. Brevoord, J. Fischer, S. Scheijen, C. Sauerzapf, N. Codreanu, L. G. C. Wienhoven, Y. M. Q. van der Graaf, C. F. J. Wolfs, R. Méjard, M. Ruf, N. de Jong, and R. Hanson, *Data and software underlying the publication "Laser-cut Patterned, Micrometer-thin Diamond Membranes with Coherent Color Centers for Open Microcavities",* 4TU.ResearchData, Dataset (2025).

[57] S. B. van Dam, M. Ruf, and R. Hanson, *Optimal design of diamond-air microcavities for quantum networks using an analytical approach,* New J. Phys. **20**, 115004 (2018).

[58] A. M. Zaitsev, *Optical Properties of Diamond* (Springer Berlin Heidelberg, Berlin, Heidelberg, 2001).

[59] J. Körber, M. Pallmann, J. Heupel, R. Stöhr, E. Vasilenko, T. Hümmer, L. Kohler, C. Popov, and D. Hunger, *Scanning Cavity Microscopy of a Single-Crystal Diamond Membrane,* Phys. Rev. Applied **19**, 064057 (2023).

[60] I. Friel, S. L. Geoghegan, D. J. Twitchen, and G. A. Scarsbrook, *Development of high quality single crystal diamond for novel laser applications,* in *Optics and Photonics for Counterterrorism and Crime Fighting VI and Optical Materials in Defence Systems Technology VII*, edited by C. Lewis, D. Burgess, R. Zamboni, F. Kajzar, and E. M. Heckman (Toulouse, France, 2010) p. 783819.

[61] D. Howell, *Strain-induced birefringence in natural diamond: a review,* Eur. J. Mineral. **24**, 575 (2012).

[62] H. K. Beukers, M. Pasini, H. Choi, D. Englund, R. Hanson, and J. Borregaard, *Remote-Entanglement Protocols for Stationary Qubits with Photonic Interfaces,* PRX Quantum **5**, 010202 (2024).

[63] B. Hensen, H. Bernien, A. E. Dréau, A. Reiserer, N. Kalb, M. S. Blok, J. Ruitenberg, R. F. L. Vermeulen, R. N. Schouten, C. Abellán, W. Amaya, V. Pruneri, M. W. Mitchell, M. Markham, D. J. Twitchen, D. Elkouss, S. Wehner, T. H. Taminiau, and R. Hanson, *Loophole-free Bell inequality violation using electron spins separated by 1.3 kilometres,* Nature **526**, 682 (2015).

[64] J. M. Brevoord, L. De Santis, T. Yamamoto, M. Pasini, N. Codreanu, T. Turan, H. K. Beukers, C. Waas, and R. Hanson, *Heralded initialization of charge state and optical-transition frequency of diamond tin-vacancy centers,* Phys. Rev. Applied **21**, 054047 (2024).

[65] J. M. Brevoord, L. G. C. Wienhoven, N. Codreanu, T. Ishiguro, E. van Leeuwen, M. Iuliano, L. De Santis, C. Waas, H. K. C. Beukers, T. Turan, C. Errando-Herranz, K. Kawaguchi, and R. Hanson, *Large-range tuning and stabilization of the optical transition of diamond tin-vacancy centers by in situ strain control,* Appl. Phys. Lett. **126** (2025).

[66] G. L. Van De Stolpe, L. J. Feije, S. J. H. Loenen, A. Das, G. M. Timmer, T. W. De Jong, and T. H. Taminiau, *Check-probe spectroscopy of lifetime-limited emitters in bulk-grown silicon carbide,* npj Quantum Inf. **11**, 31 (2025).

[67] H. Bernien, L. Childress, L. Robledo, M. Markham, D. Twitchen, and R. Hanson, *Two-Photon Quantum Interference from Separate Nitrogen Vacancy Centers in Diamond,* Phys. Rev. Lett. **108**, 043604 (2012).

[68] A. Sipahigil, K. D. Jahnke, L. J. Rogers, T. Teraji, J. Isoya, A. S. Zibrov, F. Jelezko, and M. D. Lukin, *Indistinguishable Photons from Separated Silicon-Vacancy Centers in Diamond,* Phys. Rev. Lett. **113**, 113602 (2014).

[69] H. Bernien, B. Hensen, W. Pfaff, G. Koolstra, M. S. Blok, L. Robledo, T. H. Taminiau, M. Markham, D. J. Twitchen, L. Childress, and R. Hanson, *Heralded entanglement between solid-state qubits separated by three metres,* Nature **497**, 86 (2013).

[70] J. Borregaard, A. S. Sørensen, and P. Lodahl, *Quantum Networks with Deterministic Spin–Photon Interfaces,* Adv. Quantum Technol. **2**, 1800091 (2019).

[71] Z. Li, X. Guo, Y. Jin, F. Andreoli, A. Bilgin, D. D. Awschalom, N. Delegan, F. J. Heremans, D. Chang, G. Galli, and A. A. High, *Atomic optical antennas in solids,* Nat. Photon. **18**, 1113– (2024).

[72] G. Pieplow, C. G. Torun, C. Gurr, J. H. D. Munns, F. M. Herrmann, A. Thies, T. Pregnolato, and T. Schröder, *Quantum electrometer for time-resolved material science at the atomic lattice scale,* Nat. Commun. **16**, 6435 (2025).

[73] D. M. Irber, F. Poggiali, F. Kong, M. Kieschnick, T. Lühmann, D. Kwiatkowski, J. Meijer, J. Du, F. Shi, and F. Reinhard, *Robust all-optical single-shot readout of nitrogen-vacancy centers in diamond,* Nat. Commun. **12**, 532 (2021).

[74] S. L. N. Hermans, M. Pompili, L. D. Santos Martins, A. R-P Montblanch, H. K. C. Beukers, S. Baier, J. Borregaard, and R. Hanson, *Entangling remote qubits using the single-photon protocol: an in-depth theoretical and experimental study,* New J. Phys. **25**, 013011 (2023).

[75] D. Hunger, T. Steinmetz, Y. Colombe, C. Deutsch, T. W. Hänsch, and J. Reichel, *A fiber Fabry–Perot cavity with high finesse,* New J. Phys. **12**, 065038 (2010).

[76] M. Uphoff, M. Brekenfeld, G. Rempe, and S. Ritter, *Frequency splitting of polarization eigenmodes in microscopic Fabry–Perot cavities,* New J. Phys. **17**, 013053 (2015).

[77] P. Maier, S. Rupp, N. Lettner, J. H. Denschlag, and A. Kubanek, *Fabrication of customized low-loss optical resonators by combination of FIB-milling and CO_2 laser smoothing,* Opt. Express **33**, 19205 (2025).

[78] X. Guo, A. M. Stramma, Z. Li, W. G. Roth, B. Huang, Y. Jin, R. A. Parker, J. Arjona Martínez, N. Shofer, C. P. Michaels, C. P. Purser, M. H. Appel, E. M. Alexeev, T. Liu, A. C. Ferrari, D. D. Awschalom, N. Delegan, B. Pingault, G. Galli, F. J. Heremans, M. Atatüre, and A. A. High, *Microwave-Based Quantum Control and Coherence Protection of Tin-Vacancy Spin Qubits in a Strain-Tuned Diamond-Membrane Heterostructure,* Phys. Rev. X **13**, 041037 (2023).

[79] Y. Herrmann, J. Fischer, S. Scheijen, C. F. J. Wolfs, J. M. Brevoord, C. Sauerzapf, L. G. C. Wienhoven, L. J. Feije, M. Eschen, M. Ruf, M. J. Weaver, and R. Hanson, *A low-temperature tunable microcavity featuring high passive stability and microwave integration,* AVS Quantum Sci. **6**, 041401 (2024).

[80] M. Ruf, M. Weaver, S. van Dam, and R. Hanson, *Resonant Excitation and Purcell Enhancement of Coherent Nitrogen-Vacancy Centers Coupled to a Fabry-Perot Microcavity,* Phys. Rev. Applied **15**, 024049 (2021).

[81] S. van Dam, *Optical cavities, coherent emitters, and protocols for diamond-based quantum networks*, Ph.D. thesis, Delft University of Technology (2019).

[82] Y. Herrmann, *Data underlying the dissertation "Good Vibrations: A Microcavity-based Diamond Spin-Photon Interface for Quantum Networking",* 4TU.ResearchData, Dataset (2025).

[83] M. Kasperczyk, J. A. Zuber, A. Barfuss, J. Kölbl, V. Yurgens, S. Flågan, T. Jakubczyk, B. Shields, R. J. Warburton, and P. Maletinsky, *Statistically modeling optical linewidths of nitrogen vacancy centers in microstructures,* Phys. Rev. B **102**, 075312 (2020).

[84] C. Sauerzapf, *Fabrication and characterization of micrometerthin, color center-enriched diamonds for open microcavity quantum network nodes*, Master's thesis, Delft University of Technology (2023).

5

A Low-Temperature Tunable Microcavity featuring High Passive Stability and Microwave Integration

"If you can imagine it, you can build it." - *Hornbach Commercial*

Y. Herrmann*, J. Fischer*, S. Scheijen, C. F. J. Wolfs, J. M. Brevoord, C. Sauerzapf, L. G. C. Wienhoven, L. J. Feije, M. Eschen, M. Ruf, M. J. Weaver and R. Hanson

Open microcavities offer great potential for the exploration and utilization of efficient spin-photon interfaces with Purcell-enhanced quantum emitters, thanks to their large spectral and spatial tunability combined with high versatility of sample integration. However, a major challenge for this platform is the sensitivity to cavity length fluctuations in the cryogenic environment, which leads to cavity resonance frequency variations and thereby a lowered averaged Purcell enhancement. This work presents a closed-cycle cryogenic fiber-based microcavity setup, which is in particular designed for a low passive vibration level, while still providing large tunability and flexibility in fiber and sample integration, and high photon collection efficiency from the cavity mode. At temperatures below 10 *kelvin, a stability level of around* 25 *picometer is reproducibly achieved in different setup configurations, including the extension with microwave control for manipulating the spin of cavity-coupled quantum emitters, enabling a bright photonic interface with optically active qubits.*

*These authors contributed equally to this work.

This chapter has been published in AVS Quantum Science **6**, 041401 (2024) under Ref. [1].

5.1 Microcavities with Single Quantum Emitters

The strength of the light-matter interaction is a key parameter for the realization of efficient interfaces between single quantum emitters and optical photons. Optically active quantum emitters are interesting testbeds for quantum science and are promising candidates for realizing stationary qubits [2–4], but the bare coupling to optical photons in bulk materials is generally weak. This coupling can be greatly improved by integrating the emitter into an optical resonator [5–8]. In the simplest form, two highly reflective mirrors facing each other can be used to realize such a cavity. The cavity can be utilized to efficiently couple quantum emitters to an optical photon mode, thereby selectively enhancing their emission, known as the Purcell effect. When used with solid-state host materials, a hemispherical plano-concave cavity geometry with a low radius of curvature and a micrometer short length can be used to minimize the mode volume. Such open optical microcavities have proven to be a versatile tool in quantum optics, due to their high spectral and spatial tunability and their compatibility with a broad spectrum of quantum systems. The cavity design allows the incorporation of quantum emitters in various ways: quantum dots can be directly grown on top of the mirror [9–12] or emitters in layered materials [13–15] can be bonded onto the mirror surface. Furthermore, the spatial tunability can be used to optimize on localized emitters on the mirror like carbon nanotubes [16, 17], rare-earth ions in nanoparticles [18] or color centers in nanodiamonds [19–22]. And (sub) micrometer thin membranes can integrate color centers in host materials like diamond [23–25], silicon carbide [26, 27], yttrium orthosilicate [28] or organic crystals [29] into the cavity. This approach is especially advantageous for emitters like the nitrogen-vacancy center in diamond, which are notoriously hard to integrate coherently into nanostructures due to the presence of a permanent electric dipole, but maintain good optical properties in micrometer-thin membranes [30].

5

The optical access of the microcavity can conveniently benefit from the realization of the mirrors on the tip of optical fibers [31, 32], enabling direct fiber coupling. Furthermore, high cavity quality factors can be realized by commercially available mirror coatings, including the purposely design of symmetric or single-sided cavities.

The high spectral tunability makes the cavity sensitive to fluctuations in length, leading to variations in the resonance frequency. These perturbations lower the effective coupling of the emitter to the cavity and lead to a reduced averaged Purcell enhancement. This can be expressed with the spectral overlap of the resonance frequency of the emitter and the cavity frequency [33]. Assuming a Gaussian distribution of the varying cavity length [34], we can find a bound for the maximum attainable (effective) Purcell factor

$$F_{P,max} = \frac{3}{4\pi^2}\left(\frac{c}{n\nu}\right)^3 \frac{1}{V}\sqrt{\frac{\pi}{2(s\sigma)^2}}\frac{\nu}{2}, \tag{5.1}$$

which depends on the cavity resonance frequency ν, mode volume V, mode dispersion slope s, and root mean square (RMS) cavity length fluctuations σ with the refractive index in diamond n and the speed of light c. The derivation of equation (5.1) can be found in Appendix 5.8.1. For a hybrid cavity consisting of an air part and a diamond membrane, certain modes of a fixed frequency become more air- or diamond-like [35]. The mode type depends only on the diamond thickness. Due to a smaller slope in the cavity dispersion relation, diamond-like modes are less sensitive to vibrations [33]. Note that for a given

membrane thickness and air length, the cavity mode dispersion slope s can be calculated with an analytic expression [33]. Figure 5.1 (a) shows the maximum attainable Purcell factor depending on the RMS cavity length fluctuations for different cavity parameters realized in other works. To reach a large Purcell enhancement, a vibration level on the order of tens of picometer RMS vibrations is required. This poses a technical challenge, as most quantum systems need to be operated in high vacuum at cryogenic temperatures. For a closed-cycle cryostat configuration, which enables continuous operation and reduced experimental overhead, the vicinity of a running cryostat cold head inevitably introduces vibrations.
Setups with high stability levels have been reported in quiet helium bath cryostats [36] or with limited spatial control in closed-cycle cryostats [28]. Recently, systems with large spatial tunability and passive stability levels at the tens of picometer level have been reported in closed-cycle cryostats [37–40].

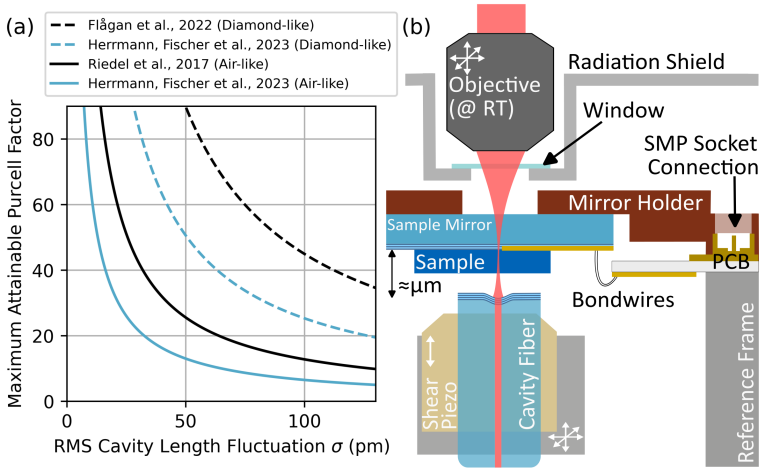

Figure 5.1: (a) Maximum attainable Purcell factor depending on RMS cavity length fluctuations. The black lines show simulations for a microcavity with an around 0.8 µm thin diamond membrane, achieved in Ref. [41] for an air-like mode (mode volume $V = 9\ \lambda^3$, cavity dispersion $s = 139$ MHz/pm for 637 nm) and in Ref. [42] for a diamond-like mode (mode volume $V = 4\ \lambda^3$, cavity dispersion $s = 89$ MHz/pm for 637 nm). The blue lines show simulations for an around 3.7 µm thin diamond membrane, achieved in Ref. [43] for an air-like mode (mode volume $V = 55\ \lambda^3$, cavity dispersion $s = 46$ MHz/pm for 619 nm) and for the diamond-like case (mode volume $V = 31\ \lambda^3$, cavity dispersion $s = 21$ MHz/pm for 619 nm). For a cavity without the diamond membrane, the maximum attainable Purcell factor follows approximately the air-like modes. (b) Sketch of the experimental setup design. The microcavity is composed of a flat sample mirror and a curved microscopic mirror, fabricated on the tip of an optical fiber. Optical access to the sample mirror side of the cavity is provided with a movable objective. The optical cavity axis is changed by moving the cavity fiber and the outcoupling objective over the sample mirror. The objective is kept at room temperature and thermally shielded by an aluminum cone with a thin window for optical access. The sample mirror has embedded gold striplines, which are connected over a support printed circuit board (PCB), to deliver microwaves close to the cavity spot.

In the following, we present a low-temperature fiber-based Fabry-Pérot microcavity setup inside a closed-cycle cryostat, which is designed to maintain a high passive stability level. We present the operation of the cavity together with an analysis of the passive stability. We showcase the functionality of this tunable platform by demonstrating the coupling of two

different diamond color centers, the tin-vacancy center and the nitrogen-vacancy center, to the cavity at temperatures below 10 K. Furthermore, we show that the integration of microwave delivery lines into our system, to address the spin states of cavity-enhanced nitrogen-vacancy centers, does not change the passive stability level.

5.2 Setup Design

A schematic drawing of the cavity geometry and the setup design is shown in Fig. 5.1 (b). The microcavity is mounted in an optical cryostat (Montana Instruments HILA) with an off-table cold head design and a base temperature of 5.6 K. The cold head is a two-stage Gifford-McMahon cryocooler, which is suspended inside a rack-mounted cooling tower assembly, hovering above the optical table. To minimize the vibration transfer, the cold head tower is connected over a loose bellow for vacuum and flexible braiding for cooling to the main chamber (see photograph in Appendix Fig. 5.10).

A computer-aided design (CAD) software drawing of the cryostat baseplate with the microcavity insert is shown in Fig. 5.2 (a) and a photograph in Appendix Fig. 5.9 (a). The baseplate is integrated into an auto-leveling floating stage acting as a low-pass filter for mechanical vibrations with a cutoff frequency of about 1 Hz. The baseplate is separated into three parts: an outer ring, kept at room temperature to mount the objective cone. An intermediate ring, which is connected to stage one of the cold head, reaching about 90 K. This ring is used for connecting the electrical cables and mounting the radiation shield separating microcavity and room temperature objective. The microcavity insert is placed on the central part, connected to stage two of the cold head, reaching the base temperature. The cryostat chamber (photograph shown in Appendix Fig. 5.9 (b)) is constantly pumped to a pressure in the range of 1×10^{-6} mbar, by an integrated turbopump and a differentially pumped outer vacuum.

The flexibility of moving the fiber over a millimeter-large range usually comes with the drawback of lower mechanical resonance frequencies, making the positioning system more susceptible to vibrations [44]. With a microcavity, where the fiber is placed on an orthogonal XYZ nanopositioning stage (JPE CS021), we measure a vibration level of about 0.5 nm directly on the baseplate at room temperature. A possible explanation for this is the low mechanical resonance frequencies of the nanopositioner stack (typically on the order of several 100 Hz), which are less suppressed by the isolation system.

To improve the vibration level, a different positioning system with a high internal resonance frequency is chosen. This is provided by the cryo positioning stage high resonance (JPE CPSHR1-a) placed on a passive vibration isolator (JPE CVIP1). The cross-section through the stage is shown in Fig. 5.2 (b). An optimized stiffness due to parallel kinematics results in a high resonance frequency of about 4 kHz along the cavity axis [45]. Three linear actuators (JPE CLA2201) move the fiber in situ in a tripod configuration over a range of more than 2 mm laterally and 1 mm along the cavity length axis, with a minimum step size of 1 nm at low temperatures. Additionally, each tripod axis is equipped with a fine scanning piezo element, with sub-nanometer resolution. This allows continuous cavity length detuning with frequencies up to 5 kHz over a range of up to 0.5 µm at low temperatures (all specifications of the CPSHR1-a stage can be found online [45]).

We employ two different ways of mounting the fiber, displayed in Fig. 5.2 (d): directly glued on a titanium holder or onto a shear piezo element featuring a high resonance fre-

quency (Noliac CSAP02). The latter enables high-bandwidth fine control of the cavity length, allowing for active cavity length stabilization [46]. In both settings, we use a two-component epoxy (Stycast 2850FT with catalyst LV 24) to glue the fiber. To guide the cavity fiber into the vacuum chamber, we make use of a 1/8 in stainless steel tube fitting (Swagelok male connector) with a custom-made Teflon ferrule. This ferrule has a borehole of 0.17 mm to fit the cavity fiber (Coherent FUD-4519 S630-P single-mode fiber) with a polyimide protection coating. Furthermore, we use a 0.25 mm thin polytetrafluoroethylene (PTFE) film (Reichelt Chemietechnik), cut to pieces of approximately 5 mm width and 25 mm length to further damp the fiber movement. This film connects the fiber mount and the reference frame (not shown in Fig. 5.2, see photograph in Appendix Fig. 5.8 (a)). We see that the additional damping by the film can improve the vibration level.
The sample mirror is mounted on top of the positioning system, separated by > 100 µm to the fiber. To ensure a good thermalization of the sample mirror to the baseplate, three flexible links made out of highly conductive copper (Montana Instruments custom-design) are used (not shown in the drawing, see Appendix Fig. 5.9 (a)). Each link is composed of multiple flat braids to ensure a good thermal connection in combination with a low transfer of vibrations from the baseplate to the cavity. This keeps the temperature difference between the mirror holder and baseplate to about 0.2 K. On the mirror holder, we monitor the temperature with a temperature sensor (Lake Shore Cryotronics Cernox 1050). To further ensure that the sample mirror reaches a low temperature, a 0.2 mm thin window (Edmond Optics Ultra-Thin N-BK7, with anti-reflection coating for 425 nm to 675 nm) glued into the radiation shield is used. This considerably reduces the heat load stemming from the black-body radiation of the room temperature objective that is about 4 mm away. The sample mirror is glued with silver conductive paint to the mirror holder, shown in Fig. 5.2 (c). In a test cooldown, we measure the temperature directly on the center of the sample mirror with a temperature sensor (Lake Shore Cryotronics Cernox Thin Film RTD), glued onto it with GE low-temperature varnish. Without the window, a temperature of around 20 K on the sample mirror is measured, while a temperature of about 8 K is reached with the window. This temperature is consistent with the measured linewidth of cavity-integrated diamond tin-vacancy centers in previous work [43].
To control the spin state of quantum emitters inside the cavity, microwaves are delivered to the cavity spot with gold striplines, embedded into the sample mirror [47]. The striplines are interfaced with 25 µm thin standard wire bonds to a support PCB, glued onto the cryostat insert (see Fig. 5.2 (b),(c) and Appendix Fig. 5.8 (b)). The PCB is connected with flexible coax cables (Montana Instruments LF-5 with SMP female ends) to semi-rigid coax cables (Montana Instruments C-20) on the baseplate, which are interfaced over a vacuum microwave feedthrough.
Optical access to the sample mirror side of the cavity is provided by a standard objective (Zeiss LD EC Epiplan-Neofluar, 100x magnification, 0.75 numerical aperture, 4 mm working distance). The objective can be positioned in a tripod configuration with three linear actuators (Physik Instrumente Q-545), mounted on an encircling stainless steel cone shown in Appendix Fig. 5.9 (b).

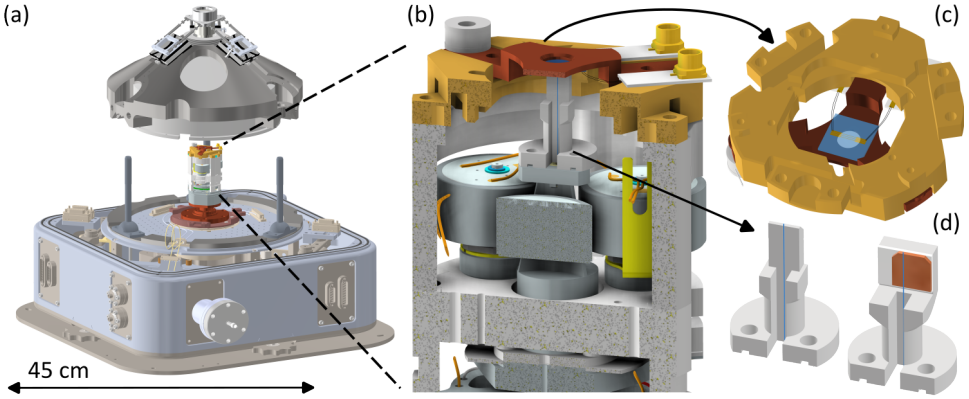

Figure 5.2: CAD drawing of the full setup with detailed individual parts. The drawing of the HILA cryostat in (a) is made by Montana Instruments, and the drawings of the positioner stage in (a) and (b) and the adapter piece in (c) are from JPE, used with permission and available under Ref. [48]. The drawing of the linear actuators in (a) is made by Physik Instrumente, used with permission, and is available under Ref. [49]. The drawing of the temperature sensor in (a) and (b) is made by Lakeshore, used with permission, and is available under Ref. [50]. (a) Floating cryostat baseplate with microcavity insert inside the vacuum chamber. The front part shows the fiber, microwave, and electrical feedthroughs. The insert is mounted on the copper-colored inner part of the baseplate, reaching a base temperature of 5.6 K. Two D-Sub 19 feedthroughs on the baseplate are used to connect the actuators, piezo elements, and temperature sensor to the control and readout electronics. The middle ring of the baseplate mounts the radiation shield (at about 90 K), while the outer part is used for the objective cone (at room temperature). (b) Cross-section of the microcavity insert. The fiber mount is positioned by three linear actuators in a tripod configuration. The sample mirror is glued on a copper holder, which is directly connected with flexible thermal links to the baseplate (not shown here, see photograph of the setup in the Appendix Fig. 5.9 (a)). The sample mirror has a thickness of about 0.5 mm, and is placed at a distance of > 100 µm to the fiber, which can be compensated by the positioning system (a detailed sketch of the full microcavity insert can be found in Appendix Fig. 5.7). Each moving axis has an additional piezo element for fine positioning. We monitor the sample temperature with a sensor mounted on top of the microcavity insert. Furthermore, a support PCB is glued onto the stack to connect the mirror striplines to flexible coax cables. (c) Sample mirror on the copper holder with an adapter piece (JPE I2-CPSHR1) connecting to the reference frame. The gold striplines embedded into the mirror coating are connected with standard wire bonds to the support PCB. (d) Mounting of the cavity fiber: the fiber is glued either directly on a titanium mount (left) or onto a shear piezo element for fast fine control (right). The length of the fiber sticking out is kept as short as possible (between 100 µm and 200 µm) to avoid possible resonances associated with the overhanging fiber tip [46].

5.3 Microcavity Operation

The setup is controlled via a PC and the Python 3 framework QMI [51]. We use a real-time microcontroller (Jäger Computergesteuerte Messtechnik Adwin Pro II) for analog voltage control of the fine piezo element offset. Cavity scans with a frequency of up to 5 kHz are accomplished with a signal generator, connected to the fine piezo via a bias-T. The signal is amplified (JPE Piezo Scanning Module) and filtered afterward with a home-built voltage-controlled, switchable lowpass filter (cutoff frequency in the range of 30 Hz). Without filtering, we see that the noise from the amplifier can excite the resonance frequencies and increase the vibration level by a factor of up to two. The driving voltage of the linear actuators is also filtered and controlled by a high voltage amplifier (JPE Cryo Actuator Driver Module 2).

The microcavity is characterized by linewidth and length (or air length and membrane

thickness). With these parameters, important properties like finesse, quality factor, and mode volume can be calculated, and the sensitivity to vibrations can be determined. To measure the linewidth, we probe the cavity in transmission with two resonant lasers (Newfocus Velocity TLB-6300-LN and Toptica DL Pro), which are frequency-stabilized to a reference wavemeter (High Finesse WS-U). The cavity transmission signal is measured with a free-space photodiode (Thorlabs APD130A2). In Fig. 5.3 (a) we scan the cavity resonance over the two laser frequencies by applying a voltage to one of the fine piezo elements, moving the fiber. The difference in laser frequency is used to transform the scanning voltage into a change in cavity resonance frequency and to fit the two transmission peaks in the frequency domain. The use of two lasers with an arbitrary detuning allows the determination of a narrow, but also broader (> 10 GHz) cavity linewidth. This contrasts the use of a single laser with sidebands imprinted by an electrooptic phase modulator [34], in which case the range is limited by the frequency spacing of sidebands. To determine the cavity length, we probe the cavity in transmission with a supercontinuum white light source (NKT Photonics SC-450-2), filtered to 600 nm to 700 nm, which fully covers the cavity stopband (Fig. 5.3 (b)). The transmission signal is sent to a fiber-coupled spectrometer (Princeton Instruments SP-2500i). The cavity acts as a spectral filter, where fundamental modes appear as bright peaks in transmission. These modes are spaced by the free spectral range, which is directly related to the cavity length.

During cooling to the base temperature, the microcavity insert shrinks in height by about 550 µm (measured by the difference in the focal position of the objective), and the cavity length is reduced by about 50 µm.

Imaging through the objective with an LED and camera provides accurate observation of the cavity fiber position and the sample. The high magnification of the objective makes it possible to move the fiber with micrometer precision laterally over the sample mirror.

The cavity length stability, as a crucial system parameter, needs to be studied for different system configurations. For a given cavity length, the measured spectral cavity linewidth can be translated into a spatial linewidth, which allows direct measurement of the cavity length fluctuations. We use the same method as used in earlier work [34], where the cavity transmission signal is recorded and mapped to a change in cavity lengths (Fig. 5.3 (c)). The length is monitored with the cavity transmission signal, measured on a photodiode (50 MHz bandwidth) over a time of 10 s. This time trace is used to calculate the RMS vibrations, and a Fourier transform gives insights into the corresponding mechanical resonance frequencies. The cavity is operated in the low Finesse regime (1000 to 4000) to make sure that the transmission signal is fully caught on one half of the Lorentzian linewidth. Overshooting would lead to an underestimated cavity vibration level. To avoid this, we make sure that all points of the acquired length displacement trace follow an approximate Gaussian distribution (inset in Fig. 5.3 (c)).

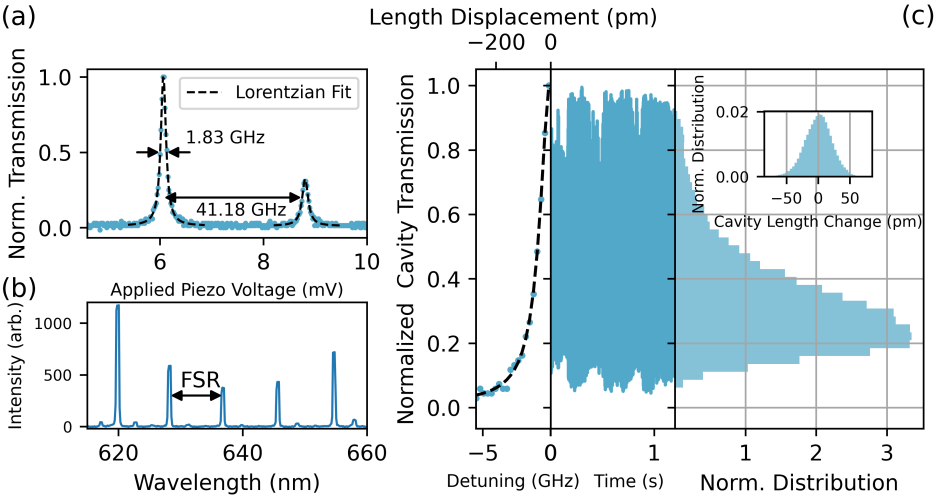

Figure 5.3: Characterizing the microcavity properties and the vibration level. (a) Cavity linewidth measurement with two detuned resonant lasers. The cavity transmission is probed by applying a voltage to one of the fine piezo elements to scan the cavity length (scan frequency of 2.33 kHz). (b) Cavity length measurement by probing the transmission of a broadband supercontinuum white light source. The visible fundamental modes directly determine the free spectral range and the cavity length. (c) Exemplary cavity vibration measurement: the cavity transmission signal (center panel) is mapped on half of the Lorentzian cavity resonance (left panel). The spatial linewidth of the cavity allows for translating the transmission signal into a change in length. The right panel shows a histogram of the transmission for the full measurement (10 s). The insert shows the corresponding distribution of the cavity length values.

5.4 Performance of System at Low Temperatures

At ambient temperature under vacuum of typically 1×10^{-6} mbar, we measure a vibration level less than 4 pm. At low temperatures, we see an increase to about 25 pm. This level is consistently reached for several setup configurations, including different fiber and sample mounting and the integrated electronics for applying microwaves. Figure 5.4 (a) shows the integrated noise spectrum of the measured length fluctuations, and Fig. 5.4 (b) an individual frequency spectrum. The length fluctuations show a small low-frequency contribution, which we attribute to the cold head cycle of the cryostat, running with a speed of about 1.4 Hz (settings: 25 Hz compressor and 70 Hz cold head). For all configurations, the spectrum shows a jump between 2 kHz and 4 kHz, which fits the first resonance of the fiber positioning system along the cavity axis. Most configurations show an almost flat spectrum for frequencies higher than 5 kHz.

Another measure of the vibration level is a resonant laser scan over the cavity transmission, shown in Fig. 5.4 (c). The cavity is probed with a resonant 637 nm laser from the fiber side and the transmission signal is recorded with a fiber-coupled single photon detector (Laser Components COUNT-10C-FC). With the cavity length, we determine a dispersion of 20 MHz/pm. In the previous measurement in Fig. 5.3 (a) the linewidth is measured by scanning the cavity with a high scan speed to 'freeze' the vibrations, revealing the intrinsic cavity linewidth (shown in Fig. 5.3 (a)). In contrast, the cavity is at a fixed length in

Fig. 5.4 (c), but the resonant laser frequency is swept to measure the linewidth. The data is fitted with a Voigt profile with a fixed Lorentzian part set to the intrinsic cavity linewidth. Vibrations lead to a Gaussian broadening, which can be transformed into an RMS vibration level with the dispersion relation. For the scans shown in Fig. 5.4 (c), we measure a vibration level of (25.1 ± 1.1) pm, which is close to the 22 pm measured in Fig. 5.4 (a).
We want to emphasize that the low vibration level is reproducibly reached for different configurations, in which the fiber or sample mounting is changed. Furthermore, it is also independent of the additional integration of microwave cables, a support PCB, and wire bonds to the sample mirror. The microcavity insert was reassembled in between different configurations, and thermally cycled for more than 50 times over two years without a degradation in performance. We do not see a vibration dependence on the exact wiring of cables used to connect the piezo elements or the microwave wires. Moreover, the vibration level did not change after exchanging the cold head.
In addition to vibrations > 1 Hz, the cavity can show drifts on longer timescales. When operated with higher incident laser power (> 1 µW) or microwave power (> 25 dBm measured before the input of the cryostat, see next section for the transmission losses), cavity length drifts of more than one linewidth can be observed. However, after some time (order of minutes), the drifts reduce to a new equilibrium.
The closed-cycle operation of the cryostat allows to operate the cavity at a constant temperature (cryostat temperature stability < 25 mK) and to maintain the exact cavity spot for a longer time. In previous work [43], measurements with the same cavity-coupled diamond tin-vacancy center were conducted for more than two months with preserved cavity parameters.

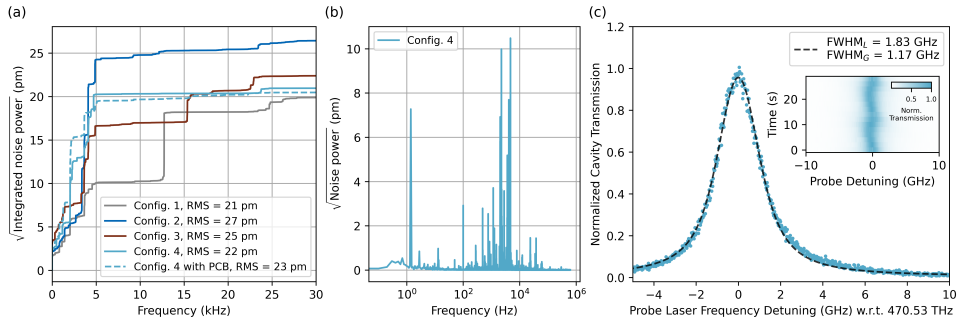

Figure 5.4: System performance at low temperatures for different setup configurations. (a) A comparable vibration level is reached for different settings: for the first three configurations, the fiber is mounted on a shear piezo element (right side of Fig. 2 (d)), while configuration four is without (left side of Fig. 2 (d)). All configurations use different cavity fibers and sample mirrors; configuration two was used in previous work with diamond tin-vacancy centers [43]. The extended PCB for microwave control in configuration four does not influence the vibration level. (b) Resonance spectrum of configuration four, revealing a typical resonance at 1.4 Hz corresponding to the cold head cycle and resonances up to 5 kHz attributed to the fiber positioning system. (c) Resonant cavity transmission scan for configuration four. The cavity is probed with a scan speed of about 10 GHz/s. The data is fitted with a Voigt profile, in which the Lorentzian part is fixed to the cavity linewidth. The Gaussian component can be used to calculate the vibration level. The inset shows 15 consecutive scans.

The same microcavity insert (JPE CVIP 1 with CPSHR1-a) was operated in earlier work [34] in a standard optical cryostation (Montana Instruments C2). Thanks to the similarity in setup design, it is instructive to compare both performances, see Fig. 5.5. The much better vibration isolation of the HILA leads to an almost six times improved RMS vibration level and a much smaller dependence on the cryostat cycle.
There are several further improvements of the vibration level possible: the damping with the PTFE film as explained in Section 5.2 can be optimized. Furthermore, the stability of the system would benefit from an increased mechanical resonance frequency of the positioning system, which can be achieved by further engineering. For example, a higher resonance frequency might be achievable by removing the fine piezo element and losing the ability for precise positioning and scanning of the fiber. Along the cavity axis, this could be compensated by using the shear piezo element with a scanning range of about 300 nm at low temperatures. Another possibility would be to increase the temperature of the positioning system. At room temperature, under vacuum, and with a running cold head, we observe a much better vibration level. An explanation could be that temperature-dependent material properties lead to an increased vibration level at low temperatures. Thus, putting the fiber positioning system at a higher temperature (for example, on stage one of the cold head at 90 K) might further improve the stability.
Furthermore, if it is compatible with the sample, it might be beneficial to operate the fiber in contact with the sample mirror. In a similar setup with a fiber-based microcavity in a closed-cycle cryostat [39], this resulted in a vibration level improved by a factor of six.
So far, we have only discussed the passive stability of the system. Most mechanical resonance frequencies are present below 10 kHz, which makes active length stabilization appealing. The use of a high bandwidth piezo element in a similar system enabled a locking bandwidth of 44 kHz [46], which would be sufficient to compensate for the resonance frequencies present in our system. Active stabilization would require some experimental overhead, like an additional laser and a broad (or second) cavity stopband, to find a cavity resonance that can be used to generate the error signal. This is especially challenging for a short cavity with a large free spectral range. Furthermore, the locking laser could lead to stimulated emission of the cavity-coupled emitters [52]. To avoid this, a second cavity formed by an additional fiber dimple can be utilized for active length stabilization [53].

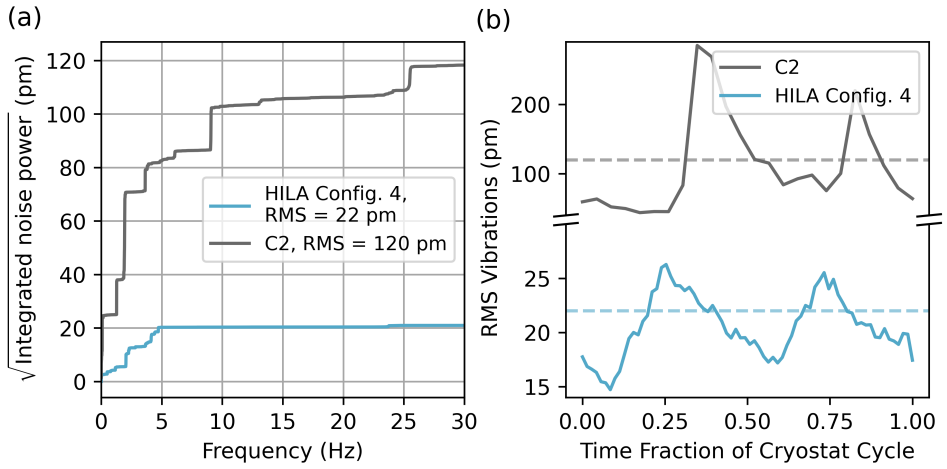

Figure 5.5: Comparison of vibration level achieved in configuration four with the HILA cryostat (light blue) versus the C2 optical cryostation (grey), used in an earlier experiment [34]. (a) Integrated noise spectra show that the mechanical resonance frequencies of the positioning system are excited in both cryostats, although at a much lower level in the HILA. Frequencies larger than 5 kHz are almost completely suppressed in the HILA. (b) RMS vibration level scaled to the time fraction of the cryostat cycle (about 0.7 s for the HILA and 1.2 s for the C2). The HILA shows a much smaller susceptibility to 'kicks' within the cold head cycle.

5.5 Cavity-coupled Diamond Color Centers with Microwave Control

We showcase the versatility of our platform by coupling two types of diamond color centers to the cavity, namely tin-vacancy (SnV) and nitrogen-vacancy (NV) centers, shown in Fig. 5.6 (a) and (b), respectively. The SnV sample is a $70\,\mathrm{x}\,70\,\mu\mathrm{m}^2$ square diamond device with a thickness of about 2.2 µm bonded to the sample mirror via Van der Waals force [41]. SnV centers are created by ion implantation in the range of the first intracavity electric field antinode. The NV sample is a $2\,\mathrm{x}\,2\,\mathrm{mm}^2$ and about 50 µm thick diamond membrane, with a central part thinned down to a thickness of about 5.8 µm, used in earlier work [34]. NV centers are created by electron irradiation and annealing [30]. The cavity spot shown in the inset of Fig. 5.6 (b) is formed in the thinned-down region.

To demonstrate that diamond color centers are coupled to the cavity at low temperature, we use off-resonant 515 nm excitation light (Hübner Photonics Cobolt MLD515) sent into the cavity via the fiber. The detection signal is collected from the sample mirror side by collimating the Gaussian beam leaving the cavity with the objective. The detection is filtered with a 600 nm longpass filter and measured with a spectrometer. The cavity resonance frequency is tuned around the emitter zero-phonon line by scanning the voltage of the three fine piezo elements. Once the cavity becomes resonant with an emitter, enhanced photoluminescence at that frequency is observed. An individual emitter can then be selectively coupled to the cavity by adjusting the fine piezo element voltage to the corresponding resonance frequency.

An essential capability for quantum information applications is qubit control, which can

be efficiently achieved through driving the corresponding spin states with microwaves. To deliver microwaves close to the cavity spot, 65 nm thin gold striplines are partly embedded into the sample mirror with nano-fabrication methods [47]. The striplines are connected as described in Section 5.2. With a vector network analyzer, we measure around 6.5 dB transmission loss including the PCB at a frequency of 2.88 GHz. The total cryostat transmission losses add up to about 25 dB due to several cable connections. To demonstrate the ability to address the spin states of the NV center, we measure an optically detected magnetic resonance (ODMR) spectrum without and with a static magnetic field, shown in Fig. 5.6 (c) and (d). The NV centers are excited with off-resonant green light sent in via the cavity fiber. Cavity-enhanced zero-phonon light is detected from the free space side with a single photon detector. This light is filtered with a 600 nm longpass filter, a (640 ± 5) nm bandpass filter and an angle-tunable etalon filter (LightMachinery custom coating, full width at half maximum ≈ 100 GHz). The cavity is kept on resonance during the ODMR measurement by interleaved probing of the cavity transmission with a reference laser and a voltage feedback on the fine piezo element. An external magnetic field is provided by a neodymium disc magnet (Supermagnete S-70-35-N), which is mounted on top of the cryostat vacuum chamber lid. Microwaves are delivered by a single-sideband modulated vector signal generator (Rohde & Schwarz SMBV100A) with an output power of −5 dBm (−3 dBm for the higher-frequency transition), which is amplified by 35 dB (MiniCiruits ZVE-6W-83+). A reduction in NV photoluminescence is observed when the microwave driving is on resonance with one of the ground-state spin transitions.

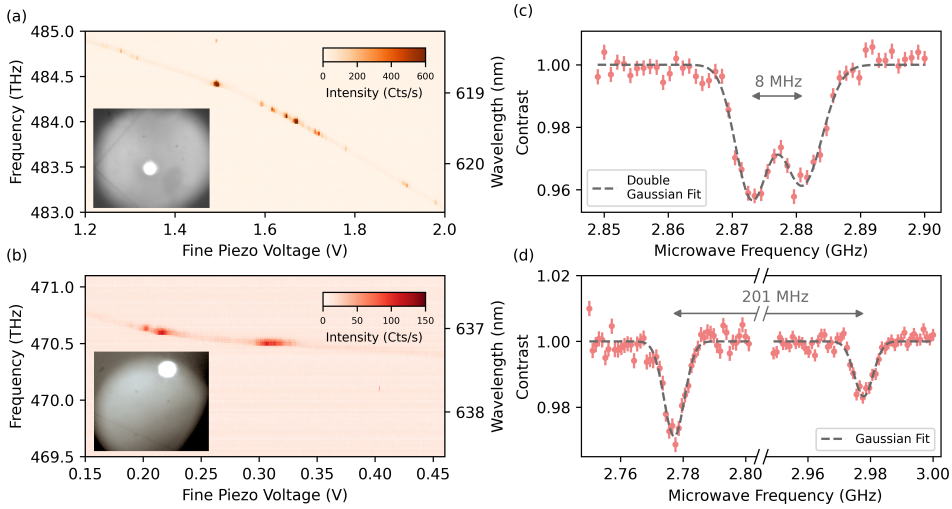

Figure 5.6: Platform versatility and microwave spin addressing. The insets of (a) and (b) show an about $50\,\mathrm{x}\,50\,\mu\mathrm{m}^2$ large section. (a) Cavity-coupled SnV centers under off-resonant excitation. The cavity mode (faint straight line) is scanned over the 619 nm and 620 nm zero-phonon line transitions of several SnV centers within the mode volume, which appear as bright spots. The inset shows the diamond device hosting the color centers bonded to the sample mirror. The position of the cavity on the sample is indicated by the bright laser spot, stemming from a green laser for which the cavity is mostly transparent. (b) Cavity-coupled NV centers. Under green excitation, the NV center is mostly initialized into the spin ground state. When the cavity becomes resonant, it enhances the E_x or E_y zero-phonon line transitions. The inset shows the thinned-down diamond membrane bonded to the sample mirror and the approximately 30 µm distant gold stripline. The nonlinearity in the cavity resonance in (a) and (b) stems from a small cavity length drift during the data acquisition. (c) ODMR measurement of a cavity-coupled NV center without an applied magnetic field. The NV zero field splitting around 2.87 GHz can be observed as a resonance. The splitting of 8 MHz can originate from a residual magnetic field or a strongly coupled carbon nuclear spin in the vicinity of the NV center. (d) ODMR measurement of a cavity-coupled NV center with an external static magnetic field. In the presence of the magnetic field, the two resonances associated with the NV electron spin are separated by the Zeeman splitting $2\gamma_e B_z$, with the NV electron spin gyromagnetic ratio γ_e and the magnetic field B_z. The splitting of 201 MHz corresponds to $B_z \approx 36\,\mathrm{G}$. The lower contrast for the high-frequency transition is caused by increased microwave losses at this frequency. Note that the ODMR measurements were acquired at a cavity spot around 20 µm distant to the stripline, which is a different spot than shown in (b). All measurements are performed at a sample temperature of about 8 K.

5.6 Conclusion

We present the design, assembly, and operation of a fiber-based microcavity platform with high passive stability and demonstrate the cavity coupling of diamond color centers together with the ability to address the spin of cavity-coupled NV centers with microwaves. The key elements for achieving high passive stability are the combination of a low-noise cryostat with incorporated vibration suppression and a positioning system with a high mechanical resonance frequency. The resulting separation of noise frequencies and the positioning system resonance frequencies leads to the high cavity length stability. Our system shows robustness and reproducibility over many thermal cycles with varied setup configurations. Moreover, the passive stability seems to be independent of experimental imperfections such as the exact wiring of cables or the tightness of screws. The vibrations in our system are mainly caused by the cold head, and we do not observe any influences on the vibration level of other external sources, like acoustic noise.
With improvements such as demonstrated by a related system [39] or by active cavity length stabilization [54], it might be possible to further reduce the vibration level. A stability improvement by another order of magnitude would render the effect of the vibrations on the maximum attainable Purcell factor almost negligible.
Notably, all parts for achieving the high passive vibration level, such as the floating baseplate cryostat and the fiber positioning system, are commercial.
For the estimated values for diamond color centers in Fig. 5.1 (a), the achieved passive stability would allow for an air-like Purcell factor up to about 25, with even higher values possible for a diamond-like cavity, in conjunction with good collection efficiency. With the integration of microwaves for full qubit control, this system provides a promising platform for testing and utilizing efficient qubit-photon interfaces.

5.7 Acknowledgement

We thank Arian Stolk and Kai-Niklas Schymik for feedback on the manuscript, Matteo Pasini for helpful discussions, Siebe Visser for technical support, Jason Mensingh and Olaf Benningshof for cryogenic engineering support, Nico Alberts and Tim Hiep for machining the custom parts, Raymond Vermeulen and Raymond Schouten for development of custom electronics, and Henri Ervasti for software development and support.
We thank Robbert Voorhoeve, Tom Duivenvoorde, Teun van den Dool, and Gert Witvoet from TNO for support on the setup design. Furthermore, we thank Hans Spierdijk and Jan de Vreugd from TNO for the design of the objective stage. We acknowledge support on device fabrication from Hans van den Berg, Jasper Flipse, and Nick de Jong from TNO. We thank Bart van Bree and Huub Janssen from JPE for helpful discussions and support on the cryo positioning stage. We thank Matt Ballinger and Alex Crane from Montana Instruments and Robert Janz and David Appel from Quantum Design for helpful discussions and the installation and support of the HILA cryostat.
We acknowledge funding from the Dutch Research Council (NWO) through the Spinoza Prize 2019 (project number SPI 63-264). We further acknowledge financial support from the EU Flagship on Quantum Technologies through the project Quantum Internet Alliance (EU Horizon 2020, grant agreement no. 820445). This research is supported by the Early Research Programme of the Netherlands Organisation for Applied Scientific Research (TNO).

Additional support from the Top Sector High Tech Systems and Materials is highly appreciated.

5.7.1 Author Contributions

Y. H. and J. F. contributed equally to this work. Y. H. and J. F. conducted the experiments and analyzed the data. S. S. characterized the cavity fibers and measured the data for one of the setup configurations. C. W. developed the ODMR measurements. M. R. developed parts of the device fabrication process and designed together with M. J. W., Y. H. and J. F. the setup. Y. H., J. F., L. J. F. and M. J. W. built the setup. J. M. B., C. S. and Y. H. fabricated the tin-vacancy diamond device. L. G. C. W. characterized the tin-vacancy diamond device and cavity fibers in a room-temperature cavity. M. R. fabricated the nitrogen-vacancy diamond device. M. E. fabricated the cavity fibers. Y. H., J. F., and R. H. wrote the manuscript with input from all authors. R. H. supervised the experiments.

5.7.2 Data Availability

The data that support the findings of this study are openly available on 4TU.ResearchData: 'Data underlying the publication "A Low-Temperature Tunable Microcavity featuring', at `https://www.doi.org/10.4121/451152e2-a4d4-4e42-96e0-4147afb1e45c` under reference number [55].

5.8 Appendix

5.8.1 Derivation of the Maximum Attainable Purcell Factor

The Purcell factor is defined as [56]

$$F_P = \frac{3}{4\pi^2}\left(\frac{c}{n\nu}\right)^3 \frac{Q}{V}, \tag{5.2}$$

with the cavity resonance frequency ν, refractive index n, cavity quality factor Q, cavity mode volume V, refractive index of diamond n and the speed of light c.
The spectral overlap of an emitter with a linewidth much smaller than the cavity linewidth is given by [33]

$$\xi_s(\Delta\nu) = \frac{1}{1 + \frac{4Q^2}{\nu^2}\Delta\nu^2}, \tag{5.3}$$

with the cavity resonance frequency ν and the emitter-cavity detuning $\Delta\nu$.
The cavity frequency fluctuations can be modeled by a Gaussian distribution, where the probability density function reads [34]

$$f(\Delta\nu) = \frac{1}{\sqrt{2\pi\sigma_\nu^2}} e^{-\Delta\nu^2/2\sigma_\nu^2}, \tag{5.4}$$

with the RMS value of the cavity frequency fluctuations $\sigma_\nu = s\sigma$, where s is the cavity mode dispersion slope and σ the RMS cavity length fluctuations.

For an emitter on cavity resonance, the effective vibration-averaged Purcell factor can be calculated with

$$F_{P,vib} = F_P \int_{-\infty}^{\infty} d(\Delta\nu)\xi_s(\Delta\nu)f(\Delta\nu). \tag{5.5}$$

For a given cavity geometry, which determines the cavity mode volume V and the cavity mode dispersion slope s, the maximum attainable Purcell factor follows as

$$F_{P,max} = \max_{Q>0} F_{P,vib} = \frac{3}{4\pi^2}\left(\frac{c}{n\nu}\right)^3 \frac{1}{V}\sqrt{\frac{\pi}{2(s\sigma)^2}}\frac{\nu}{2}. \tag{5.6}$$

To obtain equation (5.6) we make use of

$$\int_{-\infty}^{\infty} dx \frac{e^{-x^2/B}}{1+Ax^2} = \frac{\pi e^{1/AB}\mathrm{erfc}\left(1/\sqrt{AB}\right)}{\sqrt{A}}, \tag{5.7}$$

with $A > 0$, $B > 0$ and the complementary error function $\mathrm{erfc}(x) = 1 - \mathrm{erf}(x)$ as well as

$$\max_{x>0}\left(e^{1/x^2}\mathrm{erfc}(1/x)\right) = 1. \tag{5.8}$$

5.8.2 Cavity Fiber Positioning System

Fig. 5.7 shows a sketch of the full microcavity insert, which is presented in the main text as a rendered CAD drawing in Fig. 5.2 (b).

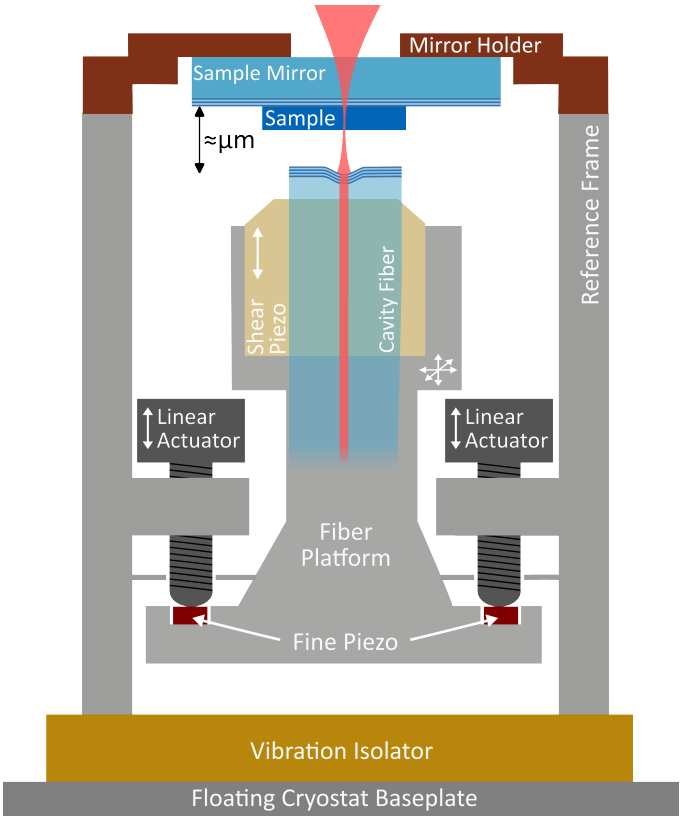

Figure 5.7: Sketch of the microcavity insert. Three linear actuators (JPE CLA2201) position the cavity fiber in front of the sample mirror: moving all three actuators simultaneously changes the cavity length in axial direction, while a single actuator movement changes the lateral position (together with a small change in the fiber angle). Each axis can additionally be controlled with a fine scanning piezo, which is clamped between the fiber platform and the linear actuators. Optionally, the fiber can be glued on a shear piezo for axial cavity length control. A passive vibration isolator (JPE CVIP1) is placed underneath the positioning system (JPE CPSHR1-a).

5.8.3 Photographs of the Setup

Photographs of individual parts of the setup and the cryostat can be found in Fig. 5.8 to Fig. 5.10.

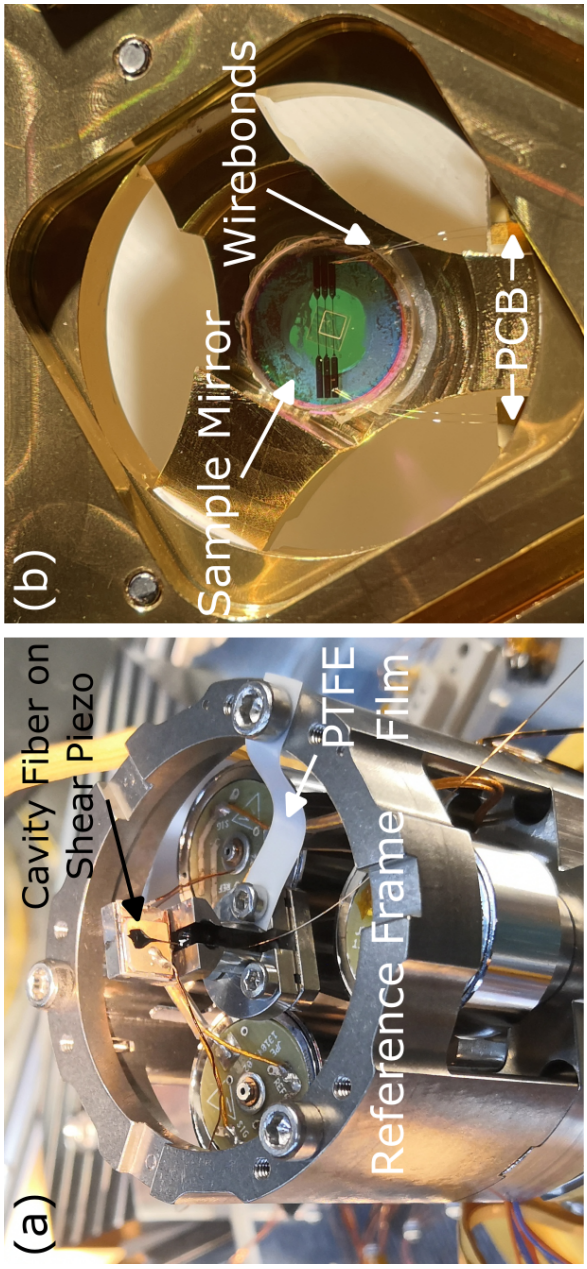

Figure 5.8: Photograph of the fiber and sample mounting. (a) The lower half of the cavity: cavity fiber glued to the shear piezo element for fast cavity length control. A 0.25 mm thin PTFE film is used to introduce additional damping, which can improve the passive stability. The platform with the fiber mount is moved in situ by the positioning system. (b) The upper half of the cavity: the sample mirror with embedded microwave stripline and a partially thinned-down diamond membrane. A support PCB is glued to the mirror holder adapter to connect the microwave lines via wire bonds.

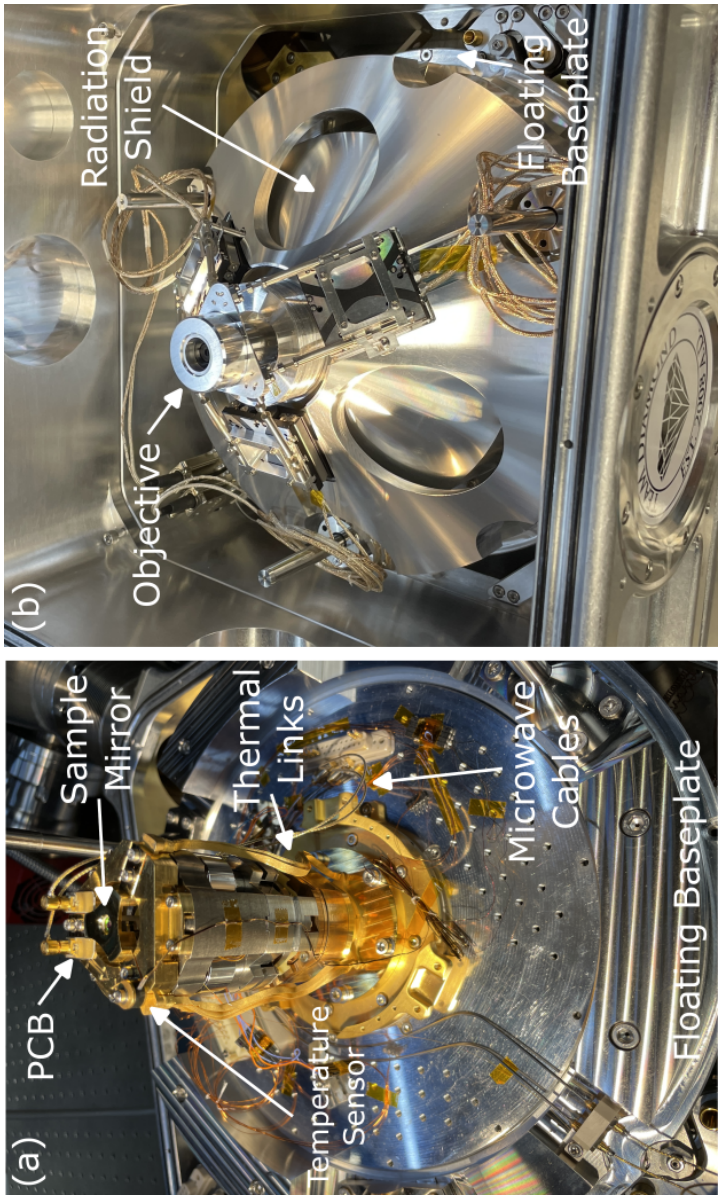

Figure 5.9: Photograph of the microcavity insert and the enclosing objective cone. (a) The insert is placed on the 5.6 K platform of the cryostat baseplate. Three thermal links ensure a good thermalization of the mirror holder to the baseplate. The temperature reached on top of the stack is monitored with a temperature sensor. The microwave lines of the PCB are connected with flexible coax cables to the baseplate to minimize the transfer of vibrations. On the baseplate, microwaves are guided by rigid cables to the vacuum feedthrough. (b) The insert is enclosed by a radiation shield and a stainless steel cone mounting the objective with linear actuators in a tripod setting. The radiation shield is made of a lower cone and an upper cylinder with an opening fitting the objective. The upper part is screwed into the lower part. The cone and objective are at room temperature inside the cryostat vacuum chamber.

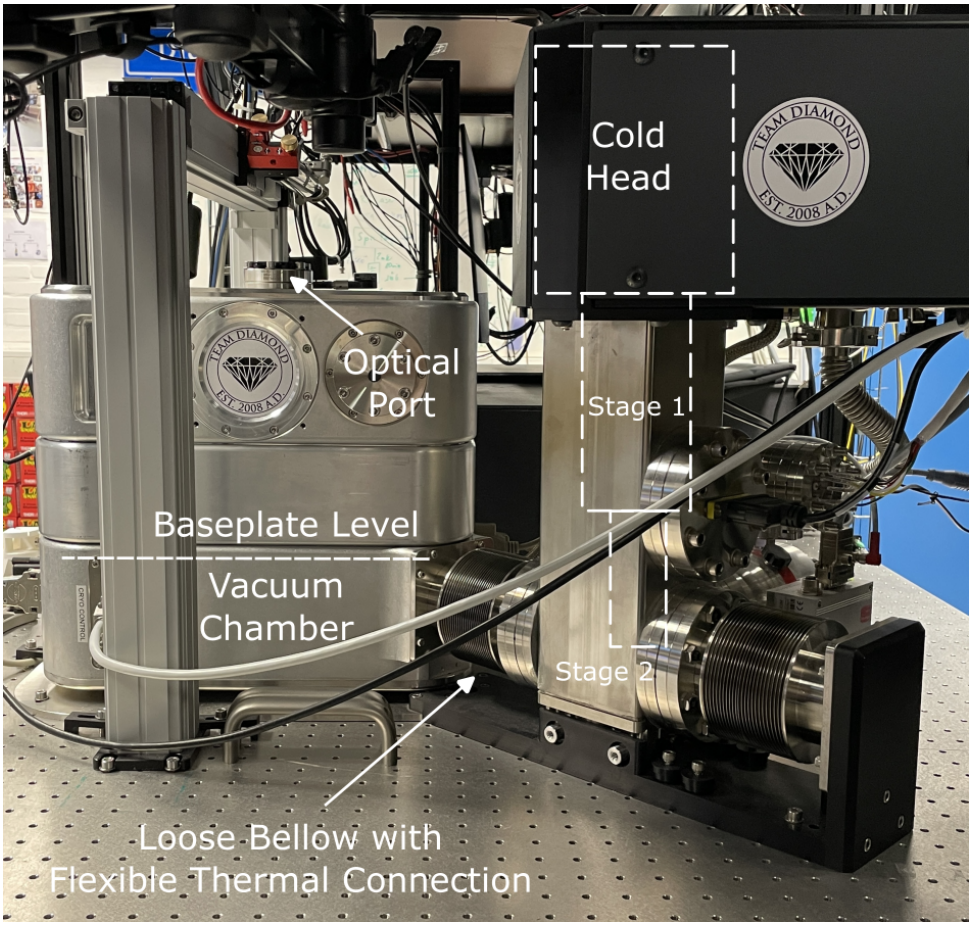

Figure 5.10: Photograph of the HILA cryostat vacuum chamber with the off-table cold head inside the tower assembly, mounted by a rack next to the optical table. Both stages of the cold head are connected over flexible thermal links with the floating baseplate inside the vacuum chamber.

References

[1] Y. Herrmann, J. Fischer, S. Scheijen, C. F. J. Wolfs, J. M. Brevoord, C. Sauerzapf, L. G. C. Wienhoven, L. J. Feije, M. Eschen, M. Ruf, M. J. Weaver, and R. Hanson, *A low-temperature tunable microcavity featuring high passive stability and microwave integration,* AVS Quantum Sci. **6**, 041401 (2024).

[2] D. D. Awschalom, R. Hanson, J. Wrachtrup, and B. B. Zhou, *Quantum technologies with optically interfaced solid-state spins,* Nat. Photonics **12**, 516 (2018).

[3] M. Atatüre, D. Englund, N. Vamivakas, S.-Y. Lee, and J. Wrachtrup, *Material platforms for spin-based photonic quantum technologies,* Nat. Rev. Mater. **3**, 38 (2018).

[4] G. Wolfowicz, F. J. Heremans, C. P. Anderson, S. Kanai, H. Seo, A. Gali, G. Galli, and D. D. Awschalom, *Quantum guidelines for solid-state spin defects,* Nat. Rev. Mater. **6**, 906 (2021).

[5] K. J. Vahala, *Optical microcavities,* Nature **424**, 839 (2003).

[6] A. Reiserer and G. Rempe, *Cavity-based quantum networks with single atoms and optical photons,* Rev. Mod. Phys. **87**, 1379 (2015).

[7] E. Janitz, M. K. Bhaskar, and L. Childress, *Cavity quantum electrodynamics with color centers in diamond,* Optica **7**, 1232 (2020).

[8] M. Ruf, N. H. Wan, H. Choi, D. Englund, and R. Hanson, *Quantum networks based on color centers in diamond,* J. Appl. Phys. **130**, 070901 (2021).

[9] A. Muller, E. B. Flagg, M. Metcalfe, J. Lawall, and G. S. Solomon, *Coupling an epitaxial quantum dot to a fiber-based external-mirror microcavity,* Appl. Phys. Lett. **95**, 173101 (2009).

[10] Z. Di, H. V. Jones, P. R. Dolan, S. M. Fairclough, M. B. Wincott, J. Fill, G. M. Hughes, and J. M. Smith, *Controlling the emission from semiconductor quantum dots using ultrasmall tunable optical microcavities,* New J. Phys. **14**, 103048 (2012).

[11] D. Najer, I. Söllner, P. Sekatski, V. Dolique, M. C. Löbl, D. Riedel, R. Schott, S. Starosielec, S. R. Valentin, A. D. Wieck, N. Sangouard, A. Ludwig, and R. J. Warburton, *A gated quantum dot strongly coupled to an optical microcavity,* Nature **575**, 622 (2019).

[12] N. O. Antoniadis, M. R. Hogg, W. F. Stehl, A. Javadi, N. Tomm, R. Schott, S. R. Valentin, A. D. Wieck, A. Ludwig, and R. J. Warburton, *Cavity-enhanced single-shot readout of a quantum dot spin within 3 nanoseconds,* Nat. Commun. **14**, 3977 (2023).

[13] T. Vogl, R. Lecamwasam, B. C. Buchler, Y. Lu, and P. K. Lam, *Compact Cavity-Enhanced Single-Photon Generation with Hexagonal Boron Nitride,* ACS Photonics **6**, 1955 (2019).

[14] S. Vadia, J. Scherzer, H. Thierschmann, C. Schäfermeier, C. Dal Savio, T. Taniguchi, K. Watanabe, D. Hunger, K. Karraï, and A. Högele, *Open-Cavity in Closed-Cycle Cryostat as a Quantum Optics Platform,* PRX Quantum **2**, 040318 (2021).

[15] L. B. Tan, O. K. Diessel, A. Popert, R. Schmidt, A. Imamoglu, and M. Kroner, *Bose Polaron Interactions in a Cavity-Coupled Monolayer Semiconductor,* Phys. Rev. X **13**, 031036 (2023).

[16] T. Hümmer, J. Noe, M. S. Hofmann, T. W. Hänsch, A. Högele, and D. Hunger, *Cavity-enhanced Raman microscopy of individual carbon nanotubes,* Nat. Commun. **7**, 12155 (2016).

[17] A. Borel, T. Habrant-Claude, F. Rapisarda, J. Reichel, S. K. Doorn, C. Voisin, and Y. Chassagneux, *Telecom Band Single-Photon Source Using a Grafted Carbon Nanotube Coupled to a Fiber Fabry–Perot Cavity in the Purcell Regime,* ACS Photonics **10**, 2839 (2023).

[18] B. Casabone, C. Deshmukh, S. Liu, D. Serrano, A. Ferrier, T. Hümmer, P. Goldner, D. Hunger, and H. De Riedmatten, *Dynamic control of Purcell enhanced emission of erbium ions in nanoparticles,* Nat. Commun. **12**, 3570 (2021).

[19] R. Albrecht, A. Bommer, C. Deutsch, J. Reichel, and C. Becher, *Coupling of a Single Nitrogen-Vacancy Center in Diamond to a Fiber-Based Microcavity,* Phys. Rev. Lett. **110**, 243602 (2013).

[20] S. Johnson, P. R. Dolan, T. Grange, A. A. P. Trichet, G. Hornecker, Y. C. Chen, L. Weng, G. M. Hughes, A. A. R. Watt, A. Auffèves, and J. M. Smith, *Tunable cavity coupling of the zero phonon line of a nitrogen-vacancy defect in diamond,* New J. Phys. **17**, 122003 (2015).

[21] J. Benedikter, H. Kaupp, T. Hümmer, Y. Liang, A. Bommer, C. Becher, A. Krueger, J. M. Smith, T. W. Hänsch, and D. Hunger, *Cavity-Enhanced Single-Photon Source Based on the Silicon-Vacancy Center in Diamond,* Phys. Rev. Applied **7**, 024031 (2017).

[22] G. Bayer, R. Berghaus, S. Sachero, A. B. Filipovski, L. Antoniuk, N. Lettner, R. Waltrich, M. Klotz, P. Maier, V. Agafonov, and A. Kubanek, *Optical driving, spin initialization and readout of single SiV- centers in a Fabry-Perot resonator,* Commun. Phys. **6**, 300 (2023).

[23] V. Yurgens, Y. Fontana, A. Corazza, B. J. Shields, P. Maletinsky, and R. J. Warburton, *Cavity-assisted resonance fluorescence from a nitrogen-vacancy center in diamond,* npj Quantum Inf. **10**, 112 (2024).

[24] R. Berghaus, S. Sachero, G. Bayer, J. Heupel, T. Herzig, F. Feuchtmayr, J. Meijer, C. Popov, and A. Kubanek, *Cavity-enhanced emission and absorption of color centers in a diamond membrane with selectable strain,* Phys. Rev. Applied **23**, 034050 (2025).

[25] R. Zifkin, C. D. Rodríguez Rosenblueth, E. Janitz, Y. Fontana, and L. Childress, *Lifetime Reduction of Single Germanium-Vacancy Centers in Diamond via a Tunable Open Microcavity,* PRX Quantum **5**, 030308 (2024).

[26] D. M. Lukin, M. A. Guidry, and J. Vučković, *Integrated Quantum Photonics with Silicon Carbide: Challenges and Prospects,* PRX Quantum **1**, 020102 (2020).

[27] J. Heiler, J. Körber, E. Hesselmeier, P. Kuna, R. Stöhr, P. Fuchs, M. Ghezellou, J. Ul-Hassan, W. Knolle, C. Becher, F. Kaiser, and J. Wrachtrup, *Spectral stability of V2 centres in sub-micron 4H-SiC membranes,* npj Quantum Mater. **9**, 34 (2024).

[28] B. Merkel, A. Ulanowski, and A. Reiserer, *Coherent and Purcell-Enhanced Emission from Erbium Dopants in a Cryogenic High- Q Resonator,* Phys. Rev. X **10**, 041025 (2020).

[29] D. Wang, H. Kelkar, D. Martin-Cano, D. Rattenbacher, A. Shkarin, T. Utikal, S. Götzinger, and V. Sandoghdar, *Turning a molecule into a coherent two-level quantum system,* Nat. Phys. **15**, 483 (2019).

[30] M. Ruf, M. IJspeert, S. van Dam, N. de Jong, H. van den Berg, G. Evers, and R. Hanson, *Optically Coherent Nitrogen-Vacancy Centers in Micrometer-Thin Etched Diamond Membranes,* Nano Lett. **19**, 3987 (2019).

[31] D. Hunger, T. Steinmetz, Y. Colombe, C. Deutsch, T. W. Hänsch, and J. Reichel, *A fiber Fabry–Perot cavity with high finesse,* New J. Phys. **12**, 065038 (2010).

[32] D. Hunger, C. Deutsch, R. J. Barbour, R. J. Warburton, and J. Reichel, *Laser microfabrication of concave, low-roughness features in silica,* AIP Advances **2**, 012119 (2012).

[33] S. B. van Dam, M. Ruf, and R. Hanson, *Optimal design of diamond-air microcavities for quantum networks using an analytical approach,* New J. Phys. **20**, 115004 (2018).

[34] M. Ruf, M. Weaver, S. van Dam, and R. Hanson, *Resonant Excitation and Purcell Enhancement of Coherent Nitrogen-Vacancy Centers Coupled to a Fabry-Perot Microcavity,* Phys. Rev. Applied **15**, 024049 (2021).

[35] E. Janitz, M. Ruf, M. Dimock, A. Bourassa, J. Sankey, and L. Childress, *Fabry-Perot microcavity for diamond-based photonics,* Phys. Rev. A **92**, 043844 (2015).

[36] L. Greuter, S. Starosielec, D. Najer, A. Ludwig, L. Duempelmann, D. Rohner, and R. J. Warburton, *A small mode volume tunable microcavity: Development and characterization,* Appl. Phys. Lett. **105**, 121105 (2014).

[37] Y. Fontana, R. Zifkin, E. Janitz, C. D. Rodríguez Rosenblueth, and L. Childress, *A mechanically stable and tunable cryogenic Fabry–Pérot microcavity,* Rev. Sci. Instrum. **92**, 053906 (2021).

[38] T. Ruelle, D. Jaeger, F. Fogliano, F. Braakman, and M. Poggio, *A tunable fiber Fabry–Perot cavity for hybrid optomechanics stabilized at 4 K,* Rev. Sci. Instrum. **93**, 095003 (2022).

[39] M. Pallmann, T. Eichhorn, J. Benedikter, B. Casabone, T. Hümmer, and D. Hunger, *A highly stable and fully tunable open microcavity platform at cryogenic temperatures,* APL Photonics **8**, 046107 (2023).

[40] M. Fisicaro, M. Witlox, H. Van Der Meer, and W. Löffler, *Active stabilization of an open-access optical microcavity for low-noise operation in a standard closed-cycle cryostat,* Rev. Sci. Instrum. **95**, 033101 (2024).

[41] D. Riedel, I. Söllner, B. J. Shields, S. Starosielec, P. Appel, E. Neu, P. Maletinsky, and R. J. Warburton, *Deterministic Enhancement of Coherent Photon Generation from a Nitrogen-Vacancy Center in Ultrapure Diamond,* Phys. Rev. X **7**, 031040 (2017).

[42] S. Flågan, D. Riedel, A. Javadi, T. Jakubczyk, P. Maletinsky, and R. J. Warburton, *A diamond-confined open microcavity featuring a high quality-factor and a small mode-volume,* J. Appl. Phys. **131**, 113102 (2022).

[43] Y. Herrmann, J. Fischer, J. M. Brevoord, C. Sauerzapf, L. G. C. Wienhoven, L. J. Feije, M. Pasini, M. Eschen, M. Ruf, M. J. Weaver, and R. Hanson, *Coherent Coupling of a Diamond Tin-Vacancy Center to a Tunable Open Microcavity,* Phys. Rev. X **14**, 041013 (2024).

[44] Y. K. Yong, S. O. R. Moheimani, B. J. Kenton, and K. K. Leang, *Invited Review Article: High-speed flexure-guided nanopositioning: Mechanical design and control issues,* Rev. Sci. Instrum. **83**, 121101 (2012).

[45] JPE, *Cryo Positioning Stage High Resonance CPSHR1 Datasheet,* Company Web Page, available at `https://www.jpe-innovations.com/wp-content/uploads/CPSHR1_Datasheet.pdf` (2024).

[46] E. Janitz, M. Ruf, Y. Fontana, J. Sankey, and L. Childress, *High mechanical bandwidth fiber-coupled Fabry-Perot cavity,* Opt. Express **25**, 20932 (2017).

[47] S. Bogdanović, M. S. Z. Liddy, S. B. van Dam, L. C. Coenen, T. Fink, M. Lončar, and R. Hanson, *Robust nano-fabrication of an integrated platform for spin control in a tunable microcavity,* APL Photonics **2**, 126101 (2017).

[48] JPE, *Cryo Positioning Stage High Resonance CPSHR1,* Company Web Page, available at `https://www.jpe-innovations.com/cryo-uhv-products/cryo-positioning-stage-high-resonance` (2024).

[49] Physik Instrumente (PI), *Linear Stage Q-545,* Company Web Page, available at `https://www.physikinstrumente.com/en/products/linear-stages/miniature-linear-stages/q-545-q-motion-precision-linear-stage-103170` (2024).

[50] Lake Shore Cryotronics, *Cernox Sensors,* Company Web Page, available at `https://www.lakeshore.com/products/categories/downloads/temperature-products/cryogenic-temperature-sensors/cernox` (2024).

[51] I. T. Raa, H. K. Ervasti, P. J. Botma, L. C. Visser, R. Budhrani, J. F. van Rantwijk, S. P. Cadot, J. Vermeltfoort, M. Pompili, A. J. Stolk, M. J. Weaver, K. L. van der Enden, D. de Leeuw Duarte, M. Teng, J. van Zwieten, and F. Grooteman, *QMI - Quantum Measurement Infrastructure, a Python 3 framework for controlling laboratory equipment,* 4TU.ResearchData, Software (2023).

[52] S. Raman Nair, L. J. Rogers, X. Vidal, R. P. Roberts, H. Abe, T. Ohshima, T. Yatsui, A. D. Greentree, J. Jeske, and T. Volz, *Amplification by stimulated emission of nitrogen-vacancy centres in a diamond-loaded fibre cavity,* Nanophotonics **9**, 4505 (2020).

[53] A. Ulanowski, J. Früh, F. Salamon, A. Holzäpfel, and A. Reiserer, *Spectral Multiplexing of Rare-Earth Emitters in a Co-Doped Crystalline Membrane,* Adv. Opt. Mater. **12**, 2302897 (2024).

[54] J. F. S. Brachmann, H. Kaupp, T. W. Hänsch, and D. Hunger, *Photothermal effects in ultra-precisely stabilized tunable microcavities,* Opt. Express **24**, 21205 (2016).

[55] Y. Herrmann, J. Fischer, S. Scheijen, C. F. J. Wolfs, J. M. Brevoord, C. Sauerzapf, L. G. C. Wienhoven, L. J. Feije, M. Eschen, M. Ruf, M. J. Weaver, and R. Hanson, *Data underlying the publication "A Low-Temperature Tunable Microcavity featuring High Passive Stability and Microwave Integration",* 4TU.ResearchData, Dataset (2024).

[56] M. Fox, *Quantum Optics: An Introduction*, Oxford master series in physics No. 15 (Oxford University Press, Oxford; New York, 2006).

6

Coherent Coupling of a Diamond Tin-Vacancy Center to a Tunable Open Microcavity

"Achtung! Now there are only two possible outcomes: Either it works or it doesn't work." - *'Jim Button and Luke the Engine Driver' by Michael Ende*

Y. Herrmann*, J. Fischer*, J. M. Brevoord, C. Sauerzapf, L. G. C. Wienhoven, L. J. Feije, M. Pasini, M. Eschen, M. Ruf, M. J. Weaver and R. Hanson

Efficient coupling of optically active qubits to optical cavities is a key challenge for solid-state-based quantum optics experiments and future quantum technologies. Here we present a quantum photonic interface based on a single tin-vacancy center in a micrometer-thin diamond membrane coupled to a tunable open microcavity. We use the full tunability of the microcavity to selectively address individual tin-vacancy centers within the cavity mode volume. Purcell enhancement of the tin-vacancy center optical transition is evidenced both by optical excited state lifetime reduction and by optical linewidth broadening. As the emitter selectively reflects the single-photon component of the incident light, the coupled emitter-cavity system exhibits strong quantum nonlinear behavior. On resonance, we observe a transmission dip of 50 % for low incident photon number per Purcell-reduced excited state lifetime, while the dip disappears as the emitter is saturated with higher photon number. Moreover, we demonstrate that the emitter strongly modifies the photon statistics of the transmitted light by observing photon bunching. This work establishes a versatile and tunable platform for advanced quantum optics experiments and proof-of-principle demonstrations on quantum networking with solid-state qubits.

*These authors contributed equally to this work.

This chapter has been published in Physical Review X **14**, 041013 (2024) under Ref. [1].

6.1 Introduction

Coherent interactions between photons and two-level matter systems are a central building block in quantum optics and quantum information science, with potential application in future quantum networks for communication and computation [2, 3]. To achieve significant light-matter interaction, optical resonators (cavities) are widely employed [4–7]. In the past years, tunable open microcavities have emerged as a versatile tool to explore and enhance the optical interface for a variety of solid-state emitters like rare-earth ions [8, 9], quantum dots [10–13], two-dimensional materials [14, 15], and dye molecules embedded in organic crystals [16]. These experiments capitalize on the combination of spatial flexibility, large spectral tunability, full optical accessibility, and simple hybrid integration with emitter hosts. Moreover, the mirror parameters can be tailored to a desired application, including native fiber coupling by mirrors fabricated on the tip of optical fibers [17].

Much work with open microcavities has focused on diamond color centers [18–27], which have been the main workhorse for early quantum network nodes [28–30]. The electron spin of those color centers functions as a good communication qubit thanks to the combination of excellent quantum coherence [31] and spin-dependent optical transitions. Furthermore, the center's native nuclear spin [32, 33] as well as surrounding nuclear spins [34] can be utilized as additional qubits, enabling network experiments with multi-qubit nodes [35–37]. Recent experiments on coupling color centers to open microcavities have demonstrated Purcell enhancement [22], resonant excitation and detection [25] and optical addressing of the spin [27]. However, access to the coherent coupling regime, where the color center significantly alters the cavity transmission as well as the photon statistics of the transmitted light, has so far remained elusive.

In this work, we demonstrate the coherent coupling of individual diamond tin-vacancy (SnV) centers to a fiber-based Fabry-Pérot microcavity. We capitalize on the excellent spatial and spectral tunability of the open microcavity to select a well-coupled SnV center, which is characterized through the reduced excited state lifetime and the broadened emitter linewidth. Compared to previous implementations with nitrogen-vacancy centers [22, 25], we achieve an improvement in coherent cooperativity of nearly two orders of magnitude through the combination of SnV centers and a high-quality, stable microcavity. We then exploit the coherent coupling to observe a strong reduction of cavity transmission by the emitter on resonance and study the dependence on detuning and on incident photon number. Finally, we explicitly demonstrate the nonlinearity of the light-emitter interaction by measuring changes in the photon statistics of the transmitted light induced by the emitter.

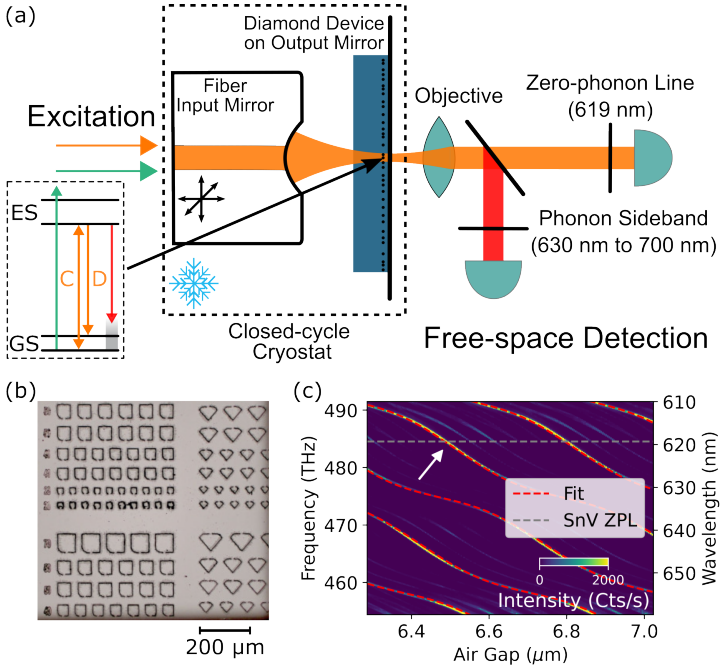

Figure 6.1: Schematical experimental setup, diamond devices, and air-diamond hybrid cavity operation. (a) On- and off-resonant excitation light is sent into the cavity via the fiber input mirror, and the outcoupled Gaussian beam is collimated with an objective, sent to a spectrometer after free-space filtering, or split into zero-phonon line and phonon sideband light and fiber-coupled to single-photon detectors (see Appendix 6.8.1 for details). SnV centers are hosted in the micrometer-thin diamond devices. The inset shows the energy level structure of the negatively charged SnV center in diamond. (b) Light microscope image of the diamond devices in their holding structure. (c) Cavity transmission spectra of a broadband, white light supercontinuum source depending on the cavity air gap, which shows the mode dispersion of the air-diamond hybrid cavity. The dashed red lines display a fit using a one-dimensional hybrid cavity model [38]. The white arrow indicates the operation point of the cavity at an air gap of 6.50 µm and a diamond thickness of 3.72 µm matching the SnV center zero-phonon line wavelength.

6.2 Experimental Setup

We use a fiber-based Fabry-Pérot microcavity, that is schematically depicted in Fig. 6.1 (a). The microcavity is formed by a laser-ablated concave fiber tip input mirror with a radius of curvature of 15.7 µm and a macroscopic flat output mirror [17], where thin diamond samples are bonded via Van der Waals forces. The used diamond device hosts implanted SnV centers and has a thickness of about 3.72 µm in the region of the cavity. SnV centers have recently emerged among solid-state color centers as a promising qubit platform with demonstrations of excellent optical and spin coherence [39–43]. The inset of Fig. 6.1 (a) shows the energy level structure of the negatively charged SnV center in diamond, including the zero-phonon line (ZPL) C and D transition at 619 nm and 620 nm, respectively. These transitions connect the lower branch of the excited states (ES) to the ground states (GS).

The sample fabrication starts with an approximately 50 µm thick and top-facing $\langle 100 \rangle$ ori-

ented diamond membrane, obtained by laser cutting and polishing [44]. In the next step, 25 x 25 µm^2 squares with support bars are patterned into the diamond, followed by tin ion implantation and subsequent annealing at 1200 °C. With the implantation energy of 350 keV (implantation dose of 3×10^{10} ions/cm^2 under an angle of 7°) SnV centers in the range of the first intracavity electric field antinode located about 64 nm away from the output mirror are created. The membranes are further thinned down to a few micrometers using a fused quartz mask and reactive ion etching [44, 45]. Figure 6.1 (b) shows a light microscope image of the membrane after this step. Individual small diamond devices are broken out with a micromanipulator and bonded to the output mirror [22].
The input and output mirror transmittance is specified with 80 ppm and 2000 ppm (diamond termination), respectively. A piezo positioning system moves the fiber across multiple diamond devices and changes cavity position and length in situ. As illustrated in Fig. 6.1 (c) we operate the cavity at an air gap of 6.50 µm (mode number $q = 50$ of the air-diamond hybrid cavity) matching the resonance of the SnV center ZPL wavelength of 619 nm and showing an air-like mode character with a local dispersion slope of 46 MHz/pm. By measuring the cavity mode in transmission with a resonant 619 nm laser a Lorentzian linewidth of (6.86 ± 0.05) GHz is determined (see Appendix 6.8.2, Fig. 6.7), resulting in a cavity quality factor Q of about 7×10^4. Using a transfer matrix model we estimate an effective cavity length $L_{\text{eff}} = 10.8\,\mu\text{m}$ and a beam waist of $\omega_0 = 1.24\,\mu\text{m}$, leading to a mode volume of $V = 55\,\lambda^3$ (see Appendix 6.8.2 for details) [46]. The estimated total cavity losses read 7500 ppm (Finesse $\mathscr{F} = 830$). Comparing with the mirror transmittance values, we find additional losses that we attribute to residual scattering at the refractive index interfaces of our hybrid cavity. With these cavity parameters we calculate a Purcell factor of $F_P = 6.9$ following the definition

$$F_P = \frac{3}{4\pi^2}\left(\frac{\lambda}{n}\right)^3 \frac{Q}{V}, \tag{6.1}$$

with the cavity resonance wavelength λ, the refractive index of diamond n, the cavity quality factor Q and the cavity mode volume V.
The microcavity is cooled by a closed-cycle optical cryostat to a device temperature of about 8 K. We measure cavity length fluctuations of 27 pm over the full cryostat cold head cycle, a five times improvement over our previous work [25] (extended technical details of the cryostat setup can be found in Ref. [47]). For the SnV center measurements, excitation laser light is inserted into the cavity via the fiber input mirror. We use free-space optics to collect the light exiting the cavity through the output mirror for detection (see Fig. 6.1 (a)). In combination with the asymmetric mirror transmittance values, this enables the efficient coupling of the cavity mode signal into a single-mode fiber.
All power and photons per lifetime values stated in this work refer to the values after the output mirror of the microcavity. Moreover, the reported uncertainties correspond to one standard deviation confidence intervals.

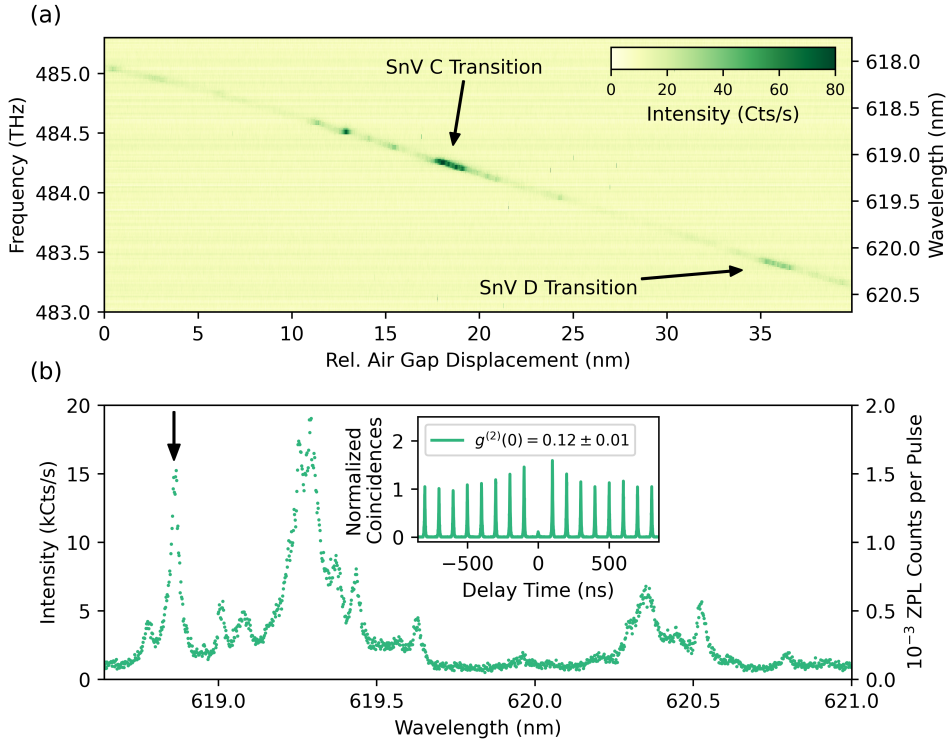

Figure 6.2: Coupling SnV centers to the microcavity under off-resonant excitation. (a) Analyzing the detection with a spectrometer, after filtering out the excitation light with a 600 nm longpass filter. High emission is observed when the cavity mode (straight line) becomes resonant with the C or D transition of a SnV center. (b) The detection path light is sent to a single-photon detector, after filtering with a (620 ± 5) nm bandpass filter and polarization optics. The left and right y-axis show the count rate and the corresponding photon detection probability per pulse (laser repetition rate $f_{\mathrm{rep}} = 10$ MHz), respectively. We tune the cavity to the isolated line, which is marked with an arrow. The inset shows a normalized $g^{(2)}(\tau)$ correlation measurement of the ZPL fluorescence, which is additionally filtered with an etalon (measurement time 20 min, count rate per detector 7 kHz, background count rate 200 Hz).

6.3 Coupling of Individual SnV Centers to the Microcavity

With the cavity resonance set close to the SnV center ZPL we explore the coupling of SnV centers in the diamond device to the optical cavity. We excite the emitters with continuous wave, off-resonant 515 nm excitation through the input mirror and detect the light that is leaving the cavity through the output mirror. The cavity resonance frequency is tuned by applying a voltage to the piezo positioning system, on which the fiber input mirror is mounted. The cavity coating is almost transparent for (525 ± 15) nm light, which renders the emitter excitation independent of the cavity resonance frequency. In this measurement, we directly send the outcoupled light to a spectrometer after filtering out the excitation laser with a 600 nm longpass filter. When the cavity comes in resonance with an emitter, cavity-coupled SnV center light emission is expected to appear. Figure 6.2 (a) shows the resulting spectra as a function of relative cavity air gap displacement. As expected for SnV centers at cryogenic temperatures, two prominent regions of high emission are observed around 619 nm and 620 nm. We attribute these regions to the C and D transition of multiple SnV centers, corresponding to the optical transitions from the lower branch of the excited state to the two ground states (see energy level structure in Fig. 6.1 (a)).

To analyze the emission with the spectral resolution of the cavity (vibration averaged linewidth 8.0 GHz) we scan the cavity mode over the emission lines and measure the intensity in the ZPL detection path with a single-photon detector under pulsed, off-resonant 532 nm excitation (see Fig. 6.2 (b)). The ZPL detection path is equipped with a (620 ± 5) nm bandpass filter and polarization optics, which are already adjusted to the emission line investigated below. In the resulting spectrum, a group of multiple SnV center emission lines around 619 nm and 620 nm is observed together with individual, spectrally isolated emission lines.

In the following, we focus on the isolated 619 nm emission line indicated by the arrow in Fig. 6.2 (b). We additionally filter the ZPL light with an angle-tunable etalon with a full width at half maximum linewidth (FWHM) of ≈ 45 GHz to further reduce background counts. This background emission may originate from parasitic light created by the green excitation laser in the cavity input fiber and in the output mirror substrate. We verify that the selected emission line corresponds to a single SnV center coupled to the cavity by measuring the $g^{(2)}(\tau)$ correlation function of the ZPL light under pulsed, off-resonant 532 nm excitation (inset of Fig. 6.2 (b)). We find $g^{(2)}(0) \ll 0.5$ without background subtraction, showing that indeed this emission is dominated by a single SnV center.

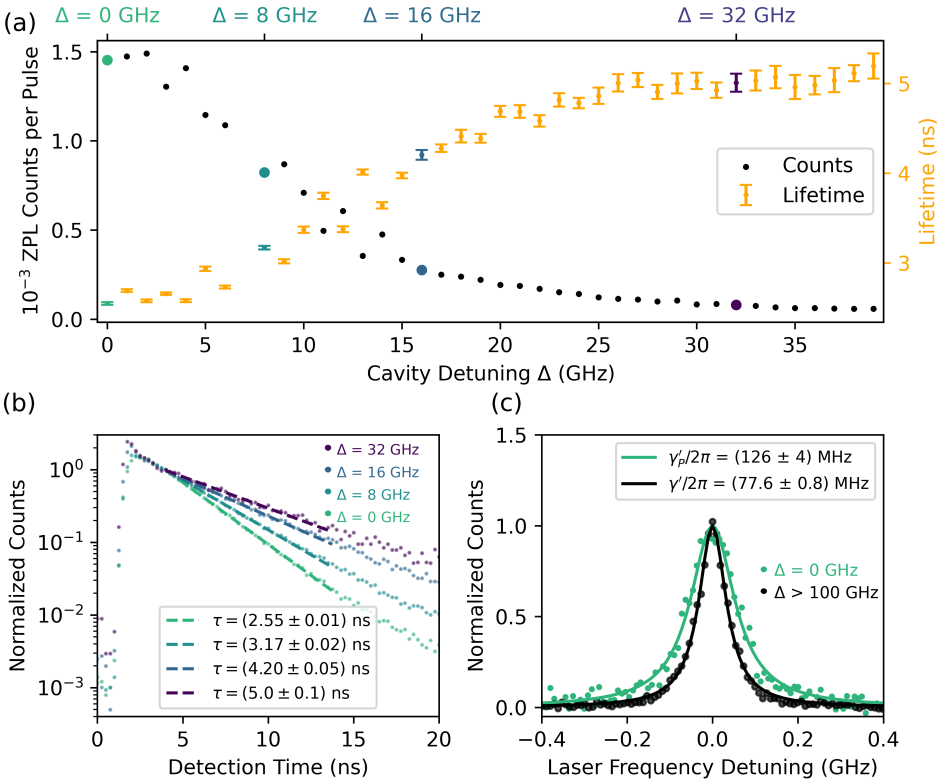

Figure 6.3: Quantifying the emitter-cavity coupling. (a) SnV center fluorescence and excited state lifetime for different cavity detunings with respect to the SnV center. Off-resonant, pulsed excitation ($P \approx 5\,\mathrm{mW}$, $f_{\mathrm{rep}} = 10\,\mathrm{MHz}$) is used to excite the SnV center independently of the cavity resonance. The colored data points indicate the lifetime measurements plotted in (b). The complete dataset is shown in Appendix 6.8.6, Fig. 6.10. The error bars represent one standard deviation confidence intervals of the fit. (b) Individual lifetime measurements (integration time of 30 s) of four different cavity detunings of (a), varying from fully on resonance to off resonance. The dashed lines show the fits to a monoexponential decay in a 10 ns fit window. The lifetime measurements without normalization are shown in Appendix 6.8.6, Fig. 6.11. (c) On and off cavity resonance PLE linewidth measurement of the SnV center. For the off resonance measurement, the cavity is detuned by > 100 GHz with respect to the SnV center.

6.4 Characterization of the Emitter-cavity System

After selecting an isolated SnV center emission line, we quantify the coupling of the SnV center to the cavity. We make use of the tunability of our microcavity, which enables us to switch the coupling on and off by tuning the cavity on and off resonance with the emitter. For emitters with a coupling strength to the cavity field comparable to other decay channels, the emission is significantly altered. In particular, the excited state lifetime is reduced via the Purcell effect. The coupling strength to the cavity can thus be estimated by comparing the excited state lifetimes for the cases where the cavity is on resonance and off resonance with the emitter.

Figure 6.3 (a) shows excited state lifetime measurements of the SnV center at the C transition for different cavity frequency detunings. The emitter is excited by pulsed, off-resonant 532 nm excitation. Each cavity frequency detuning is set by matching the cavity resonance to a frequency-stabilized reference laser before starting the lifetime measurement. When the cavity is fully on resonance with the SnV center, we measure a detector count rate of 15 kHz and a Purcell-reduced excited state lifetime of $\tau_P = (2.55 \pm 0.01)$ ns (see Fig. 6.3 (b)). The emitter's natural lifetime of $\tau = (5.0 \pm 0.1)$ ns (corresponding to a lifetime-limited linewidth of $\gamma = 1/2\pi\tau = 32$ MHz) is determined at large cavity detuning, where the Purcell enhancement is negligible.

As expected qualitatively, the measured emitter count rate in Fig. 6.3 (a) decreases with increasing cavity frequency detuning. However, the range over which the decrease occurs does not quantitatively match the previously characterized cavity linewidth (vibration-averaged 8 GHz). We attribute this to random emission frequency jumps (spectral diffusion) of the SnV center, due to changes in the environment caused by the strong pulsed, off-resonant 532 nm excitation light (see Appendix 6.8.8 for details). The presence of this spectral diffusion in the individual lifetime measurements leads to an averaging of the Purcell enhancement. Thus, the Purcell-reduced excited state lifetime only yields a lower bound on the cooperativity, which we calculate to be $C \geq \tau/\tau_P - 1 = 0.96 \pm 0.05$.

We note that we observe Purcell-reduced lifetimes on several other SnV centers in this device, with the shortest lifetime measured to be (1.78 ± 0.01) ns (see Appendix 6.8.6, Fig. 6.9 and Fig. 6.12). Differences between measured Purcell-reduced lifetimes are likely due to differences in the cavity quality factor at different lateral positions and due to emitters being at different depths in the diamond device, leading to a different overlap with the cavity field.

The Purcell-reduction of the excited state lifetime also reflects in a broadening of the emitter linewidth, which presents an alternative approach to measure the emitter-cavity coupling. Since spectral diffusion is expected to be strongly reduced in linewidth measurements using resonant excitation, the coupling can be more precisely determined. Figure 6.3 (c) shows such photoluminescence excitation (PLE) measurements using phonon sideband (PSB) detection. We define the emitter linewidth for the case that the cavity is on resonance as $\gamma_P'/2\pi$ and for a far-detuned cavity as $\gamma'/2\pi$. On cavity resonance, we measure $\gamma_P'/2\pi = (126 \pm 4)$ MHz, and for a large emitter-cavity detuning of > 100 GHz an emitter linewidth of $\gamma'/2\pi = (77.6 \pm 0.8)$ MHz (see Appendix 6.8.7 for details about the PLE measurements). From these measurements we calculate a cooperativity of $C = 1.7 \pm 0.2$ (see Appendix 6.8.4 for details about the employed vibration correction) and conclude the full set of emitter-cavity parameters $\{g, \kappa, \gamma\}/2\pi = \{0.30, 6.86, 0.032\}$GHz, with the single pho-

ton Rabi frequency g and the total cavity loss rate κ. The determined cooperativity, to our knowledge, the highest reported for color centers in microcavities, puts the emitter-cavity system in the coherent coupling regime in which quantum nonlinear behavior dominates the dynamics.

Since our cavity system is characterized and understood in detail, the measured cooperativity also allows us to draw conclusions about the SnV center properties, when considering the cooperativity definition

$$C = F_P \, \beta_0 \, \eta \, \alpha \, \zeta \, \epsilon, \tag{6.2}$$

with the SnV center Debye-Waller factor β_0, quantum efficiency η, branching ratio between C and D transition α, overlap of cavity polarization with the emitter dipole ζ and the spatial overlap of cavity mode and emitter ϵ. For our implementation $\zeta = \cos^2(35^\circ)$ due to the $\langle 100 \rangle$ diamond crystal orientation. In addition, the SnV center Debye-Waller factor of $\beta_0 = 0.57 \pm 0.01$ [48] is reported. Since the spatial overlap is bounded by unity ($\epsilon \leq 1$) a lower bound for the product of branching ratio and quantum efficiency $\alpha \, \eta \geq 0.64 \pm 0.06$ is calculated. This value represents an important figure of merit to estimate the performance of future SnV-cavity implementations and is consistent with reported estimates $\eta \approx 0.8$ [49] and $\alpha \approx 0.8$ [50].

While the cooperativity quantifies the efficiency of the spin-photon interface, the coherent cooperativity ultimately determines the fidelity of protocols [51]. The investigated emitter exhibits contributions of nonradiative broadening above its lifetime-limited linewidth, likely due to phonon dephasing because of finite temperature effects [52, 53]. Accounting for these contributions a vibration-corrected coherent cooperativity of $C_{\text{coh}} = C\gamma/\gamma' = 0.69 \pm 0.07$ is evaluated.

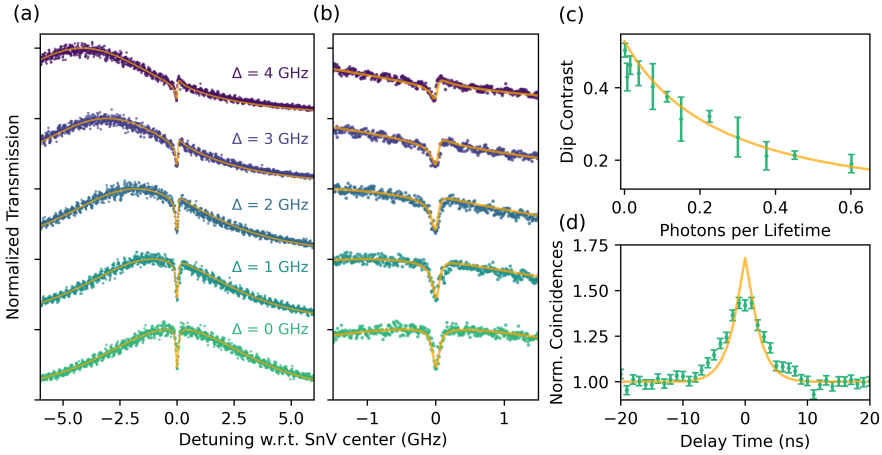

Figure 6.4: Nonlinear quantum effects of the emitter-cavity system. The dots are measured values, while the solid lines are modeled with a Lindblad master equation approach using the previously measured parameters of the emitter-cavity system. (a) Exemplary transmission dip measurements for increasing emitter-cavity detuning in steps of about 1 GHz and weak coherent probe laser power (P = 260 fW). (b) Zoom in on the data and simulated graphs presented in (a). (c) Cavity transmission dip contrast depending on photons per Purcell-reduced excited state lifetime. The evaluation of the transmission dip contrast and error is described in Appendix 6.8.9. (d) Measured $g^{(2)}(\tau)$ correlation function of the transmitted cavity light on emitter resonance, showing photon bunching as a quantum nonlinear effect. For the measured and simulated correlation function, a binning of 1 ns is used. The error bars represent one standard deviation confidence intervals of the data.

6

6.5 Quantum Nonlinear Behavior of the Emitter-cavity System

For an emitter coherently coupled to a cavity, resonant light entering the cavity is significantly modulated by coherent scattering. Due to destructive interference of the incident light with light scattered by the emitter in the forward direction, the transmission through the cavity can be strongly reduced [54]. We probe this effect by scanning the frequency of a weak coherent laser and measuring the cavity transmission with a single-photon detector. Figure 6.4 (a) depicts transmission measurements for different cavity detunings. These measurements exhibit transmission dips at the emitter frequency, with a contrast on resonance reaching 50 %. As the detuning is increased, the transmission dip shape changes from absorptive to dispersive.

We model the emitter-cavity system with a Lindblad master equation approach [55], which allows for quantitative numerical simulations of the cavity transmission as well as photon correlations (see Appendix 6.8.5 for details). All simulation input parameters are determined through independent measurements. The solid lines in Fig. 6.4 (a) and (b) show the predicted, simulated transmission curves, which are in good agreement with the data and confirm our quantitative understanding of the emitter-cavity system.

The coherent scattering observed here is a highly nonlinear quantum effect as it results from the light interacting with a single two-level system. In Fig. 6.4 (c) we plot the transmission dip contrasts for different light intensities, expressed in photons per Purcell-

reduced excited state lifetime measured after the cavity. For the cooperativity $C = 1.7$ of our emitter-cavity system the Purcell-reduced lifetime reads 1.85 ns. For very weak incident light intensity, the emitter acts as an efficient scatterer, whereas the emitter saturates for light intensities on the order of a photon per excited state lifetime.
The nonlinearity of the coherent coupling fundamentally modifies the statistical properties of the transmitted light. To show this quantum nonlinear behavior, we measure the $g^{(2)}(\tau)$ correlation function of the transmitted light when the cavity is on resonance with the SnV center (see Fig. 6.4 (d)). The observed photon bunching $g^{(2)}(0) \approx 1.5$ evidences the modified statistics resulting from the selective reflection of the single-photon component of the incident weak coherent light.
The measured photon bunching time scale, which is related to the Purcell-reduced excited state lifetime, is slightly larger than predicted by our theoretical model (solid line). We attribute this to a residual emitter-cavity detuning during the measurement time, which leads to a slightly longer excited state lifetime (less Purcell-reduction) and thereby to a larger bunching time constant.

6.6 Conclusion and Outlook

Our work establishes a versatile tunable platform for exploring light-matter interactions with individual diamond color centers, showing coherent coupling that modifies the cavity transmission intensity and photon statistics. These results constitute the first demonstration of these quantum nonlinear effects for any color center in a hybrid cavity. Furthermore, the methods used here can be directly extended to other color centers such as diamond nitrogen-vacancy and silicon-vacancy centers as well as color centers in other materials such as silicon carbide [56, 57].
Our results open up near-term opportunities along several directions. First, our cavity performance may be improved by an order of magnitude as finesse values exceeding 10,000 were shown with reduced losses from the diamond sample in comparable systems [24, 58–60]. Furthermore, SnV centers in waveguides and thin membranes have shown near lifetime-limited linewidths at liquid helium temperatures [40, 43], leading to an improved coherent cooperativity.
Moreover, this system can be complemented with the recently established coherent control over the SnV center ground state spin [42, 43]. Striplines to deliver microwaves can be fabricated onto the diamond membrane [43] or embedded into the mirror [61]. Combining the light-matter interface with spin control would enable a versatile spin-photon interface for advanced quantum optics experiments and proof-of-principle demonstrations towards cavity-enhanced quantum networking with solid-state qubits.

6.7 Acknowledgment

We thank Nina Codreanu for help in the cleanroom, Henri Ervasti for software support and Lorenzo De Santis for proofreading the manuscript. We thank Johannes Borregaard, Anders Søndberg Sørensen, Robert Berghaus and Gregor Bayer for helpful discussions.
We acknowledge financial support from the Dutch Research Council (NWO) through the Spinoza prize 2019 (project number SPI 63-264) and from the Dutch Ministry of Economic Affairs and Climate Policy (EZK), as part of the Quantum Delta NL programme. We grate-

fully acknowledge that this work was partially supported by the joint research program "Modular quantum computers" by Fujitsu Limited and Delft University of Technology, co-funded by the Netherlands Enterprise Agency under project number PPS2007.

6.7.1 Author Contributions

Y. H. and J. F. conducted the experiments and analyzed the data. M. R. developed parts of the device fabrication process and designed together with M. J. W., Y. H. and J. F. the setup. Y. H., J. F., L. J. F. and M. J. W. built the setup. J. M. B., C. S. and Y. H. fabricated the diamond devices. M. E. fabricated the cavity fibers. L. G. C. W. characterized the diamond devices and the cavity fiber. J. F. and M. P. developed the simulations. Y. H., J. F. and R. H. wrote the manuscript with input from all authors. R. H. supervised the experiments.

6.7.2 Data Availability

The datasets that support this work are available at 4TU.ResearchData [62].

6.8 Appendix

6.8.1 Experimental Setup

Experimental sequences are orchestrated with a real-time microcontroller (Jäger Adwin Pro II) and time-resolved measurements are recorded with a single photon counting module (Picoquant Hydraharp 400). The setup is controlled and measurements are performed with a PC and the Python 3 framework QMI 0.37 [63]. We use quantify-core [1] for data handling and analysis.

The excitation path consists of a frequency-doubled tunable diode laser (619 nm, Toptica TA-SHG pro), which is frequency stabilized to a wavemeter (High Finesse WS-U) and intensity-controlled with a fiber-based amplitude acousto-optic modulator (Gooch and Housego Fiber-Q 633 nm). After free-space launching, we fix the polarization with a Glan-Thompson polarizer (Thorlabs GTH10M-A), after which half- (HWP) and quarter-wave (QWP) plates are used for polarization control. For off-resonant excitation, a continuous wave laser (515 nm, Hübner Photonics Cobolt MLD515) and a pulsed laser (532 nm, 230 ps pulse duration, (5 – 12) MHz repetition rate, NKT Photonics Katana-05HP) are combined with a 30:70 beam splitter and overlapped with the 619 nm diode laser via a dichroic mirror. The light is coupled into one port of a 4x1 single-mode fiber switch (Agiltron custom version), whose output port is connected to the cavity fiber (single mode, 5 µm mode field diameter, IVG CU600). A different input port of the fiber switch is connected to a white light supercontinuum source (NKT Photonics SC-450-2), which is spectrally filtered for (600 – 700) nm to measure the cavity dispersion.

We use a floating stage helium-free optical cryostat (Montana Instruments HILA) with an off-table cold head design and a base temperature of 6 K. A detailed description of the design and operation of the full setup is presented in Ref. [47]. The fiber can be placed and fine-tuned in situ with a piezo positioning stage (JPE CPSHR1-a), which is mounted on a passive vibration isolator (JPE CVIP1). The output beam of the cavity is collimated with a room temperature objective (100x magnification, 0.75 numerical aperture, 4 mm working

[1] Available under: `https://gitlab.com/quantify-os/quantify-core`

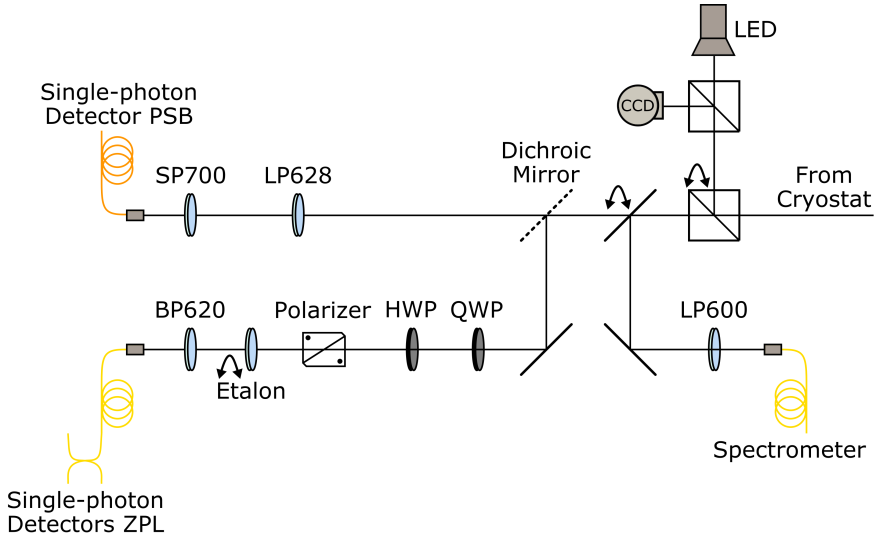

Figure 6.5: Schematic of the detection setup. The collimated cavity beam comes from the right-hand side and is split into ZPL and PSB detection. Alternatively, the cavity light can be sent with a flip mirror to a fiber-coupled spectrometer. Further, a 50:50 pellicle beam splitter can be inserted to image the cavity with an LED and a CCD camera. Spectral filtering is performed with various shortpass (SP), longpass (LP), and bandpass (BP) filters (see main text for details).

distance, Zeiss LD EC Epiplan-Neofluar), which is positioned by three linear piezo stages (Physik Instrumente Q-545) in a tripod configuration.

The collimated cavity beam leaves free-space the cryostat vacuum chamber to the detection path shown in Fig. 6.5. We illuminate and monitor the cavity with an LED lamp and a CCD camera to position the fiber with respect to the sample (see Fig. 6.6 for the exact cavity spot on the diamond device). To measure the cavity dispersion or SnV center fluorescence, the light can be sent to a fiber-coupled spectrometer (Princeton Instruments SP-2500i). For all other measurements, the light is split into the ZPL and PSB path with a longpass filter (Asahi Spectra LP 630 nm). The PSB path is spectrally filtered with two longpass (Semrock VersaChrome Edge TLP01-628) and a shortpass filter (Thorlabs FES700) and fiber-coupled into a multimode fiber (25 µm core size, 0.1 numerical aperture, Thorlabs FG025LJA) with an objective (10x magnification, 0.1 numerical aperture, 10.6 mm working distance, Olympus RMS10X). The PSB light is measured with a single-photon detector (Laser Components COUNT-10C-FC). The ZPL light is filtered for polarization with a quarter- and half-wave plate and a Glan-Thompson polarizer (Thorlabs GTH10M-A) and spectrally with a bandpass filter (Thorlabs FBH620-10). We additionally filter the light for some experiments with an angle-tunable free-space etalon (full width at half maximum ≈ 45 GHz, free spectral range ≈ 2.7 THz, LightMachinery custom coating). The ZPL light is fiber-coupled into a single-mode fiber (3.6 – 5.3 µm mode field diameter, 0.1 – 0.14 numerical aperture, Thorlabs SM600) with an objective (Olympus RMS10X). For the correlation measurements, a 50:50 single-mode fiber beam splitter (Thorlabs TW630R5A2) is used. The ZPL light is measured with a single-photon detector (Picoquant Tau-SPAD-20).

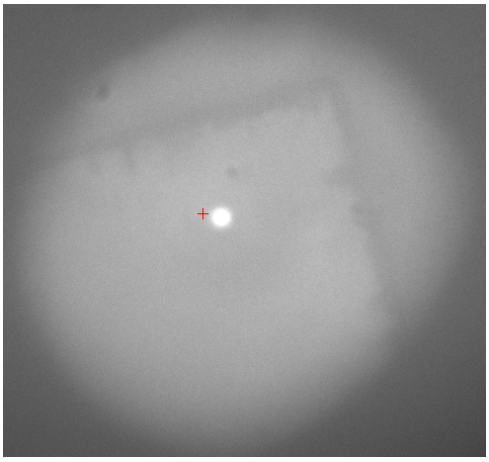

Figure 6.6: Micrograph of the hybrid cavity imaged through the output mirror, showing the diamond device. Off-resonant 515 nm laser light is inserted over the input mirror, illuminating the lateral cavity position used in the experiments.

6.8.2 Hybrid Cavity Characterization and Simulation

Figure 6.7 shows a cavity transmission measurement used to determine the cavity linewidth. In this measurement, a resonant laser is scanned over the cavity resonance, while the transmission is detected with a single-photon detector in the ZPL path. To this transmission signal, a Voigt fit with a fixed Gaussian contribution of 2.92 GHz is applied. This Gaussian contribution accounts for the 27 pm root mean square (RMS) value of cavity length fluctuation. The Voigt fit yields a Lorentzian contribution of (6.86 ± 0.05) GHz, which corresponds to the Lorentzian cavity linewidth.

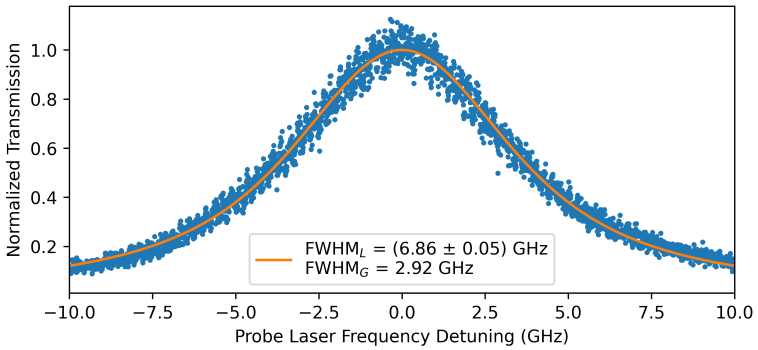

Figure 6.7: Linewidth characterization of the air-diamond hybrid cavity. Extracted from a resonant cavity transmission scan fit, the cavity shows a total Voigt linewidth of 8 GHz, composed of a Lorentzian cavity linewidth of (6.86 ± 0.05) GHz and a Gaussian contribution of 2.92 GHz ($= 27\,\text{pm} \cdot 46\,\text{MHz/pm} \cdot 2\sqrt{2\ln 2}$) accounting for 27 pm RMS cavity length fluctuations.

To calculate the cavity mode volume of our microcavity, the electric field distribution in-

side the cavity is simulated in Fig. 6.8 [46]. The electric field is confined between the dielectric input and output mirrors and spreads over the air and diamond part in between. From simulations, an effective cavity length $L_{\text{eff}} = 10.8\,\mu\text{m}$ is calculated, which leads with the cavity beam waist $\omega_0 = 1.24\,\mu\text{m}$ to a cavity mode volume of 55 λ^3.

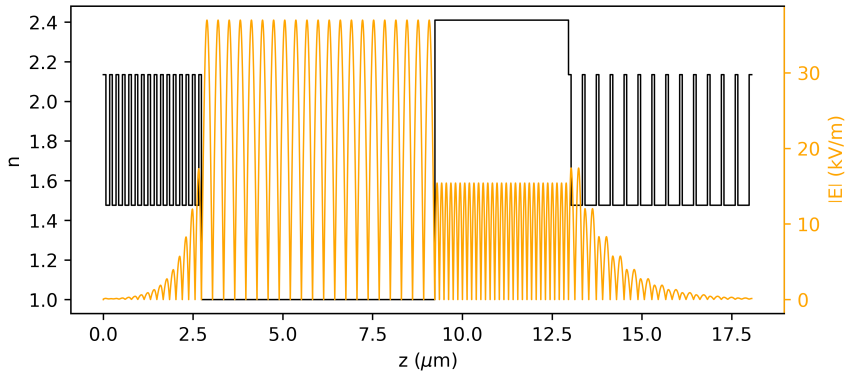

Figure 6.8: Simulation of the electric field distribution inside the microcavity. The solid black line displays the refractive index n over the extent of our microcavity, and the yellow solid line shows the simulated electric field strength $|E|$. The dielectric input and output mirrors are shown on the left and right sides. In between, the air gap of 6.50 µm and the diamond of thickness 3.72 µm are modeled with a refractive index of $n = 1$ and $n = 2.41$, respectively. An effective cavity length of $L_{\text{eff}} = 10.8\,\mu\text{m}$ is numerically calculated.

6.8.3 Vibration Model

The cavity length fluctuations of our microcavity lead to vibration averaging in measurements, which we take into account in simulations and when stating vibration-corrected quantities. We model a Gaussian distribution of cavity length fluctuations that translate over a local linear cavity mode dispersion into cavity frequency detunings $\Delta\nu$. The probability density function is given by [25]

$$f(\Delta\nu) = \frac{1}{\sqrt{2\pi\sigma^2}} e^{-\Delta\nu^2/2\sigma^2}, \tag{6.3}$$

with the RMS value σ of the cavity frequency fluctuations. We perform the vibration averaging by discretizing the probability density function and integrating numerically.

6.8.4 Cooperativity Definitions and Vibration Correction

The efficiency of a spin-photon interface is quantified by the cooperativity [51]

$$C = \frac{4g^2}{\kappa\left(\gamma_{\text{rad}} + \gamma_{\text{nonrad}}\right)}, \tag{6.4}$$

with the single photon Rabi frequency g and the emitter decay rate $\gamma = \gamma_{\text{rad}} + \gamma_{\text{nonrad}}$ with its radiative and nonradiative component. For the SnV center, the radiative component is

composed of a ZPL and a PSB part $\gamma_{\mathrm{rad}} = \gamma_{\mathrm{ZPL}} + \gamma_{\mathrm{PSB}}$. Further, the ZPL component splits up into the SnV center C and D transition $\gamma_{\mathrm{ZPL}} = \gamma_{\mathrm{C}} + \gamma_{\mathrm{D}}$.
In this study, we couple a narrow-linewidth SnV center via its C transition to a spectrally broad cavity ($\kappa \gg \gamma$). The cavity-induced increase in the C transition decay rate with respect to its initial value γ_{C} is determined by the Purcell factor times the spatial ϵ as well as polarization ζ overlap between emitter and cavity mode. Hence, the Purcell-enhanced emitter decay rate reads

$$\gamma_P = F_P \, \epsilon \, \zeta \, \gamma_{\mathrm{C}} + \gamma. \tag{6.5}$$

This Purcell-enhanced decay rate can be expressed as a function of the cooperativity by introducing the branching ratio between C and D transition $\alpha = \gamma_{\mathrm{C}}/\gamma_{\mathrm{ZPL}}$, the Debye-Waller factor $\beta_0 = \gamma_{\mathrm{ZPL}}/\gamma_{\mathrm{rad}}$ and the quantum efficiency $\eta = \gamma_{\mathrm{rad}}/\gamma$. Equation (6.5) transforms to

$$\gamma_P = F_P \, \epsilon \, \zeta \, \alpha \, \beta_0 \, \eta \, \gamma + \gamma = \gamma(C + 1), \tag{6.6}$$

with the cooperativity C as defined in equation (6.2) of the main text.
Following equation (6.6) the cooperativity

$$C = (\gamma_P - \gamma)/\gamma = \tau/\tau_P - 1, \tag{6.7}$$

can be determined by measuring the Purcell-reduced excited state lifetime τ_P and the natural excited state lifetime τ. In the case of a linewidth-broadened emitter $\gamma' = \gamma + \gamma_{\mathrm{dp}}$ with pure dephasing rate γ_{dp} the cooperativity

$$C = (\gamma_P' - \gamma')/\gamma, \tag{6.8}$$

can be calculated by measuring the emitter linewidth γ' and the Purcell-enhanced linewidth γ_P' together with the lifetime-limited linewidth $\gamma = 1/2\pi\tau$ deduced from a lifetime measurement.
The coherent cooperativity that takes emitter coherence into account reads [51]

$$C_{\mathrm{coh}} = C\frac{\gamma}{\gamma'} = \frac{\gamma_P'}{\gamma'} - 1, \tag{6.9}$$

and hence can be determined by measuring the emitter linewidth and the Purcell-enhanced linewidth only.
Moreover, the emitter-cavity coupling, described by the cooperativity C, depends on the spectral overlap between emitter and cavity. In the regime where the emitter linewidth is much smaller than the cavity linewidth, the cooperativity is given by [46]

$$C_{\mathrm{overlap}}(\nu_e, \nu_c) = \frac{C}{1 + 4Q^2(\nu_e/\nu_c - 1)^2}, \tag{6.10}$$

with the maximal cooperativity C on emitter-cavity resonance, the cavity quality factor Q, the cavity resonance frequency ν_c and the emitter transition frequency ν_e. Note that this dependency needs to be generally considered for emitter-cavity detunings and also vibration averaging. Using equation (6.10) and (6.3), a ratio of 0.90 between measured (vibration averaged) and maximal cooperativity on emitter-cavity resonance is calculated for our RMS vibration level of 27 pm. We take this factor into account when stating vibration-corrected cooperativity values.

6.8.5 Modeling SnV Centers in Optical Cavities

The investigated emitter-cavity system under resonant excitation is described by an atomic system and a driven optical cavity, modeling the SnV center and the probed microcavity, respectively. For sample temperatures of about 8 K, the SnV center in diamond is well approximated by a two-level atomic system, considering only the lower branches of the excited and ground states that are linked via the SnV center C transition.

The population in the upper branch states of the ground state can be calculated by the ratio of the fast electron-phonon transition rates between the ground state branches γ_+ and γ_- [52]. The ratio γ_+/γ_- is determined by the thermal population of the corresponding phonon mode, which for the SnV center ground state splitting of ≈ 850 GHz and temperature of 8 K is well approximated by the Maxwell-Boltzmann distribution. In this regime, the population of the upper branch states follows the Maxwell-Boltzmann distribution as well and is with $< 1\,\%$ very low, allowing to disregard this state. Note that the SnV center Debye-Waller factor, quantum efficiency, and branching ratio are included in the cooperativity of the emitter-cavity system.

The dynamics of the emitter-cavity system are modeled with a Lindblad master equation approach, where the Hamiltonian of the system in the rotating frame of the probe frequency reads [55]

$$\hat{H} = \Delta_e \left|e\right\rangle\!\left\langle e\right| + \Delta_c \hat{a}^\dagger \hat{a} + i\xi\left(\hat{a}^\dagger - \hat{a}\right) + ig\left(\hat{a}\left|e\right\rangle\!\left\langle g\right| - \hat{a}^\dagger \left|g\right\rangle\!\left\langle e\right|\right) \tag{6.11}$$

with $\Delta_e/2\pi = \nu_e - \nu_p$, $\Delta_c/2\pi = \nu_c - \nu_p$, where ν_e is the emitter transition frequency between excited state $\left|e\right\rangle$ and ground state $\left|g\right\rangle$ and ν_c the resonance frequency of the cavity. The cavity field is described by the bosonic photon annihilation operator $\hat{a}$. The single photon Rabi frequency g determines the coupling strength between the two atomic levels and the cavity field via the Jaynes-Cummings interaction. The weak coherent probe laser field at frequency ν_p has a photon flux amplitude of $\xi/\sqrt{\kappa_{in}}$ at the cavity input mirror. The Lindblad operators of the system are

$$\begin{aligned} \hat{L}_1 &= \sqrt{\gamma}\left|g\right\rangle\!\left\langle e\right|, \\ \hat{L}_2 &= \sqrt{\gamma_{\mathrm{dp}}}\left|e\right\rangle\!\left\langle e\right|, \\ \hat{L}_3 &= \sqrt{\kappa}\hat{a}, \end{aligned} \tag{6.12}$$

with the decay rate γ from the state $\left|e\right\rangle$ to $\left|g\right\rangle$, the dephasing rate γ_{dp} and the total cavity loss rate κ. The Linblad master equation for the system density matrix ρ reads

$$\dot{\rho} = -\left[\hat{H}, \rho\right] + \sum_{x=1}^{3} \hat{L}_x \rho \hat{L}_x^\dagger - \frac{1}{2}\left(\hat{L}_x^\dagger \hat{L}_x \rho + \rho \hat{L}_x^\dagger \hat{L}_x\right). \tag{6.13}$$

In the weak driving regime ($\xi \ll \kappa$), the Hilbert space can be truncated, and we assume at most two excitations in our system, which results in the basis

$$\left\{\left|0,g\right\rangle, \left|0,e\right\rangle, \left|1,g\right\rangle, \left|1,e\right\rangle, \left|2,g\right\rangle\right\}. \tag{6.14}$$

To calculate the cavity transmission and intensity correlation function of the transmitted light, the steady state of the system is considered. The cavity transmission is given by

$$T = \frac{\kappa_{out}\left\langle \hat{a}^\dagger \hat{a} \middle| \hat{a}^\dagger \hat{a} \right\rangle}{\left\langle \hat{a}_{in}^\dagger \hat{a}_{in} \middle| \hat{a}_{in}^\dagger \hat{a}_{in} \right\rangle} = \frac{\kappa_{out}\kappa_{in}}{\xi^2}\left\langle \hat{a}^\dagger \hat{a} \middle| \hat{a}^\dagger \hat{a} \right\rangle, \tag{6.15}$$

with the loss rate of the output mirror κ_{out} and the input photon flux $\left\langle \hat{a}_{in}^\dagger \hat{a}_{in} \middle| \hat{a}_{in}^\dagger \hat{a}_{in} \right\rangle = \xi^2/\kappa_{in}$. The normalized intensity correlation function of the transmitted light is given by

$$g_T^{(2)}(\tau) = \frac{\left\langle \hat{a}^\dagger(0)\hat{a}^\dagger(\tau)\hat{a}(\tau)\hat{a}(0) \middle| \hat{a}^\dagger(0)\hat{a}^\dagger(\tau)\hat{a}(\tau)\hat{a}(0) \right\rangle}{\left\langle \hat{a}^\dagger \hat{a} \middle| \hat{a}^\dagger \hat{a} \right\rangle^2}, \tag{6.16}$$

with the correlation time delay τ.
We use the Python toolbox qutip [64] to solve for the operator expectation values. To calculate the photon field expectation values of the correlation functions, we increase the photon Hilbert space to eight excitations for numerical stability.

6.8.6 Further Data on SnV-Cavity Coupling

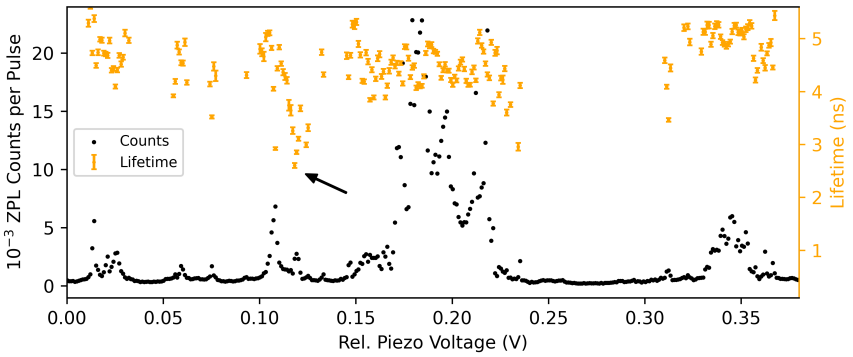

Figure 6.9: Detuning of the cavity resonance from about 617 nm to 621 nm with a lifetime measurement triggered on a predefined count rate threshold of 7 kCts (background of 2 kCts). The ZPL path is filtered with a (620 ± 5) nm bandpass filter only. We attribute the clustered peaks around 0.2 V and 0.35 V to the C and D transition of multiple SnV centers. The SnV center used in this study is indicated by the black arrow with a Purcell-reduced excited state lifetime of about 2.5 ns. The error bars represent one standard deviation confidence intervals of the fit.

To identify SnV centers exhibiting large cavity coupling strengths within the cavity mode volume, we tune the cavity resonance over a large range by sweeping the piezo voltage of the fiber positioning system. We simultaneously excite with a pulsed, off-resonant 532 nm laser and monitor the counts in the ZPL detection. Once a certain count rate is exceeded, the sweep is paused and a lifetime measurement (usually 10 s to 60 s integration time) is performed to extract the excited state lifetime. The measurement and analysis are fully automated, and the best coupled SnV centers are found efficiently. For the cavity used in

this work, an exemplary sweep is shown in Fig. 6.9, where the SnV center used in this study is located at a piezo voltage of 0.12 V with a Purcell-reduced excited state lifetime of about 2.5 ns as indicated by the black arrow.

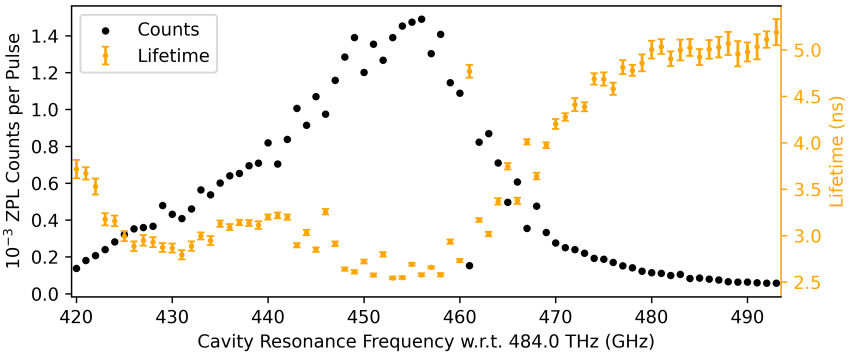

Figure 6.10: Full dataset of the cavity detuning measurement presented in Fig. 6.3 (a). The cavity frequency, which is matched to a frequency-stabilized reference laser, is stated in absolute values. Note that in the lifetime measurement of frequency 461 GHz, the cavity is not set to the correct resonance frequency, which leads to a wrong lifetime value. The error bars represent one standard deviation confidence intervals of the fit.

After finding a SnV center with a good coupling strength to the cavity, an etalon filter (full width at half maximum ≈ 45 GHz) is added to the ZPL path to further reduce the background and the polarization detection is optimized on the emitter counts under pulsed, off-resonant 532 nm excitation. The coupling is then quantified via cavity detuning-dependent lifetime measurements as reported in Fig. 6.3 (a) and (b). Figure 6.10 depicts the full dataset, which is used in Fig. 6.3 (a). The investigated emission line is located at around 455 GHz (with respect to 484 THz), whereas at around 430 GHz another weaker coupled emission line is present. We choose to analyze the data for frequencies ≥ 455 GHz only, where leakage of the 430 GHz emission line is very small. Note that these measurements under pulsed, off-resonant 532 nm excitation were performed last and caused the emitter frequency to jump from the initial 484.558 THz to 484.455 THz. We attribute this jump to the extensive irradiation of the diamond device with high power (≈ 5 mW) pulsed 532 nm light.
The lifetime measurements of Fig. 6.3 (b) are shown without normalization in Fig. 6.11 together with the monoexponential fits, which are used to extract the lifetime.
The lifetime measurement of a different SnV center with a larger lifetime reduction is shown in Fig. 6.12. Note that this is measured at a different lateral cavity position with a better cavity quality factor.

6.8.7 PLE Measurements of SnV Centers with the Microcavity

The investigated SnV center shows spectral diffusion and emitter ionization. In the PLE measurements, a conditional off-resonant 515 nm laser pulse is applied before scanning the resonant laser over the emission line. This sequence measures the emitter linewidth without contributions of spectral diffusion, and the SnV center is likely found in its negative charge state. The usage of the 515 nm pulse is conditioned on the detected emitter counts of the previous scan. If a specified peak contrast is not reached, the emitter is likely

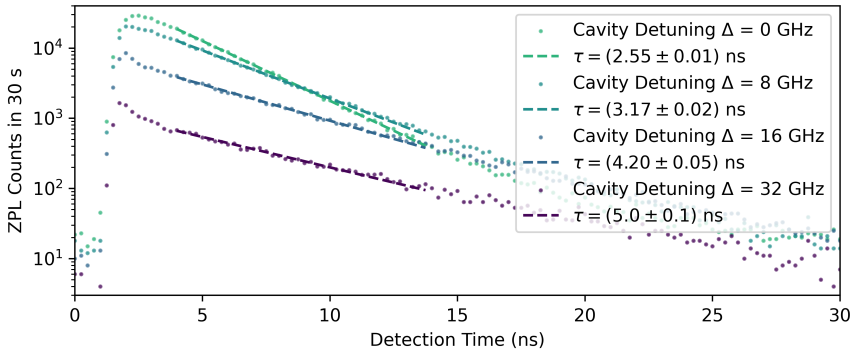

Figure 6.11: Lifetime measurements and fits (dashed lines) of the data presented in Fig. 6.3 (b) without normalization. The signal of the SnV center is reduced for larger cavity detuning. Here, an additional fast-decaying signal can be observed for short detection times. We attribute this to background fluorescence, which could stem from the cavity fiber, the mirror coating, or the output mirror substrate. The fit window is chosen to exclude this fast decay. A binning of 0.25 ns is used.

ionized, and a 10 µW 515 nm laser pulse is applied for 50 ms to repump the charge state. The resonant laser is scanned with about 180 MHz/s, while we integrate the emitter counts for 50 ms at each frequency step. Phonon sideband detection is utilized to filter out residual resonant excitation laser after the microcavity. The microcavity itself strongly filters the PSB emission of the emitter, resulting in a low PSB photon collection rate. Therefore, individual PLE scans are postselected and averaged to get a good estimate of the emitter linewidth.

Cavity On Resonance PLE Measurement Analysis

For the cavity on resonance, PLE scans a low excitation power corresponding to 260 fW is used. This enables the acquisition of the ZPL counts next to the PSB counts with single-photon detectors in the detection. These ZPL count traces are equivalent to transmission dip measurements, which show a significantly better signal-to-noise than the PSB count traces. We use the transmission dips for postselecting PLE measurements. First, we only consider measurements that exhibit a transmission dip and where the cavity mode is resonant with the laser scan range. Next, each transmission dip is fitted with a Lorentzian function, and further postselection is performed on the resulting fit parameters. The transmission dip, and therewith the emission frequency, has to be in the range (558 – 559) GHz in the center of the laser scan. In addition, a Lorentzian width > 100 MHz and a dip contrast > 50 % are required, which sorts out scans where emitter ionization occurred. The selected PLE scans are centered using the Lorentzian fit center frequencies and finally averaged. For the data presented in Fig. 6.3 (c), where the cavity is on resonance with the emitter, the average is performed with 170 individual scans.

Cavity Off Resonance PLE Measurement Analysis

For cavity off resonance PLE scans, the propagation of the scanned resonant laser light into the cavity is highly suppressed. To achieve similar PSB emitter count rates, the excitation

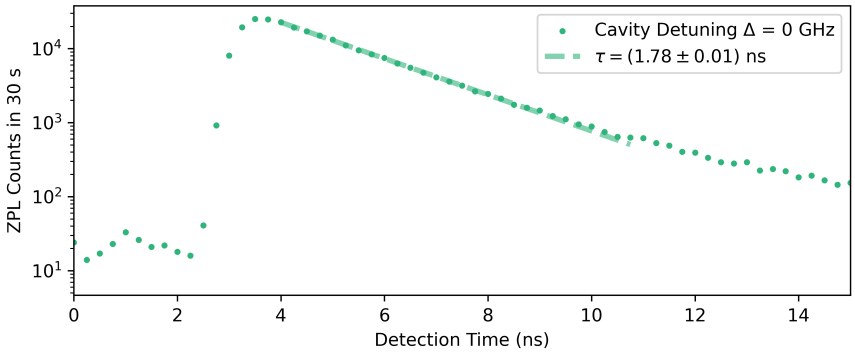

Figure 6.12: Lifetime measurement of the SnV center, which shows the largest lifetime reduction. This is measured at a different lateral position on the diamond device with a better cavity quality factor of about 8×10^4 and a comparable mode volume. Note that, in this measurement, the ZPL signal is filtered in a 10 nm window. The change in the exponential slope for longer detection times could stem from weaker coupled SnV centers or not filtered slow-decaying background fluorescence. A binning of 0.25 ns is used.

laser power is increased by a factor of 400. In postselection, we use the knowledge if a conditional repump is applied to select scans where no ionization occurred and additionally require a certain emission peak contrast. Then, each PLE scan is fitted with a Lorentzian peak, and further postselection is performed based on the resulting fitting parameters. A Lorentzian center frequency in the range of (558 – 559) GHz and the linewidth in the range of (30 – 500) MHz is required. Moreover, we select on the Lorentzian peak amplitude as a criterion for a successful fit. The selected PLE scans are centered using the Lorentzian fit center frequencies and finally averaged. For the data presented in Fig. 6.3 (c), where the cavity is off resonance with the emitter, the average is performed with 307 individual scans.

6.8.8 Cavity Transmission Dip Measurements

The cavity transmission dip measurements are performed by scanning a weak coherent laser over the cavity resonance and detecting the transmitted laser signal with a single-photon detector in the ZPL path. These transmission scans exhibit a good signal-to-noise ratio, allowing to scan the laser faster than in the PLE measurements, which is beneficial to lower the chance of emitter ionization. The measurements depicted in Fig. 6.4 (a) and (b) were conducted with a laser power of 260 fW, a laser scan speed of about 350 MHz/s and an integration time of 20 ms for each frequency step. A 50 uW off-resonant 515 nm laser pulse is applied for 50 ms before each scan. Figure 6.13 depicts successively acquired cavity transmission dip measurements. These reveal the effect of spectral diffusion of the investigated SnV center. In individual measurements, the SnV center exhibits its narrow emitter linewidth, whereas between measurements, spectral diffusion on the order of GHz is observed. We attribute these frequency jumps to changes in the SnV center environment due to the application of the off-resonant 515 nm laser before each measurement. Without the application of the off-resonant 515 nm laser, the frequency jumps between successive measurements are on the order of the emitter linewidth.

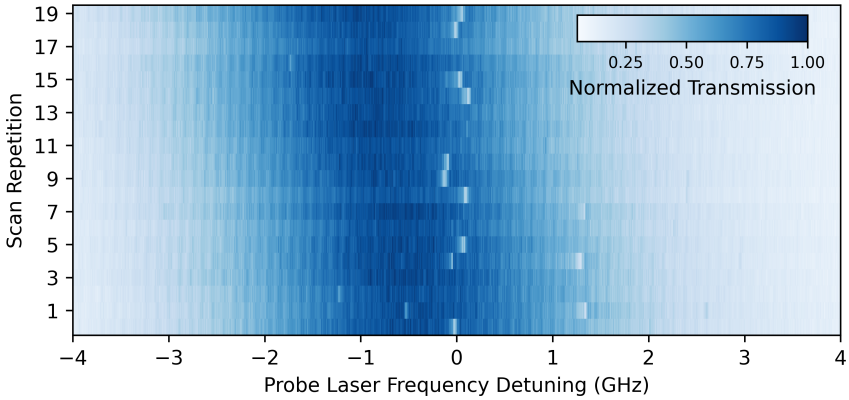

Figure 6.13: Successively acquired cavity transmission dip measurements. The cavity resonance is not actively controlled during these measurements.

6.8.9 Transmission Dip Contrast Measurements

The transmission dip contrasts, depending on photons per Purcell-reduced excited state lifetime, are determined by performing transmission dip measurements with different laser powers. In all of these measurements, we use a scan range of 1.8 GHz and apply an off-resonant 515 nm laser pulse before each scan. The laser scan speed and the frequency step integration time are adjusted for each laser power to acquire transmission dips before they vanish due to emitter ionization. An exemplary transmission dip contrast analysis is shown in Fig. 6.14. For each power value, we analyze four scans and take the mean contrast value with standard deviation as the dip contrast displayed in Fig. 6.4 (c).
The experimental data of Fig. 6.4 (c) is fit to the simulations by scaling the used excitation powers to the simulated photons per lifetime, which maps the experimentally set laser power to the actual laser power leaving the cavity. A set laser power of 1.0 nW measured in our excitation setup corresponds to 0.015 photons per lifetime and a power of 2.6 pW after the cavity. This power ratio originates from an initial free space to fiber coupling efficiency, fiber and fiber splice losses, fiber mode to cavity mode matching efficiency, and cavity transmission. The cavity transmission is calculated to be 2.4 %, and an achievable fiber mode to cavity mode efficiency of 47 % is calculated for the used cavity geometry. The determined power ratio is used to state the resonant laser power values. By comparing the detector count rate with the expected photons per lifetime after the cavity, we estimate a cavity mode collection efficiency of about 12 %. An independent measurement of the collection efficiency confirms this value.

6.8.10 Photon Statistics Measurement of the Cavity Transmission on Emitter Resonance

The measurement, depicted in Fig. 6.4 (d), shows the photon statistics of the light that is transmitted through the cavity on emitter resonance. The transmitted light is collected by a single-mode fiber in the ZPL path and guided by a 50:50 fiber beam splitter to two single-photon detectors, which are connected to time-tagging electronics. In this mea-

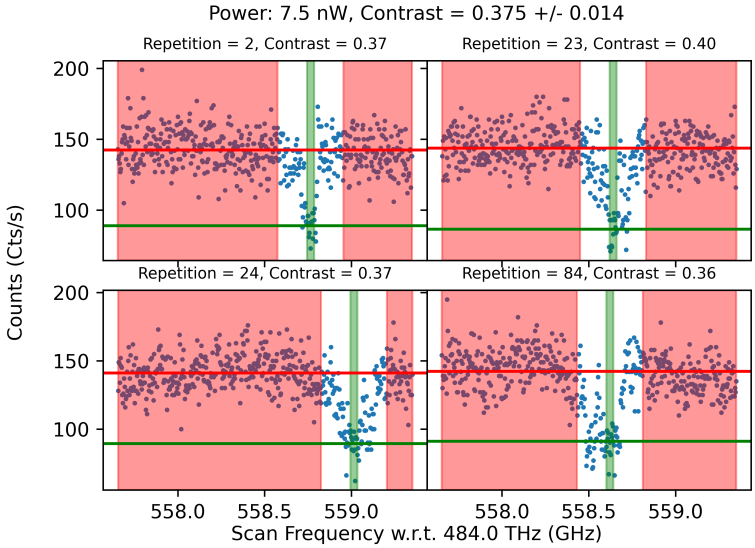

Figure 6.14: Exemplary analysis of the cavity transmission dip contrasts shown in Fig. 6.4 (c) for a set laser power of 7.5 nW, corresponding to about 0.1 photons per lifetime. Four individual scans of the resonant cavity transmission measurements, where a clear dip is visible, are selected. We use a running average of the count rate to automatically identify the position of the dip. 12 data points inside the dip are taken as an average to define the dip depth (green area). Excluding 50 data points to both sides of the dip, the remaining points are averaged to calculate the cavity transmission peak height (red area).

surement, a probe laser power of 2.6 pW, a scan speed of about 1.8 GHz/s, and a frequency step integration time of 5 ms is used. To exclusively acquire data on emitter resonance, we only trigger the time tagging electronics to record for the next 5 ms if the transmission dip contrast is > 35 % in the previous frequency step. Before each scan a 10 uW off-resonant 515 nm laser pulse is applied for 50 ms. In the simulated graph of Fig. 6.4 (d), the detunings between emitter and probe laser due to the transmission dip trigger threshold of 35 % are taken into account. Emitter-cavity detunings due to spectral diffusion and small cavity drift during the course of the experiment are not captured by the measurement routine nor by the simulations.

6.8.11 Summary of System Parameters

An overview of measured, estimated, and simulated values of this work is summarized in Tab. 6.1.

Table 6.1: Overview of system parameters.

Parameter	Value
Input mirror radius of curvature	15.7 µm
Cavity air gap	6.50 µm
Diamond thickness	3.72 µm
Hybrid cavity mode number q	50
Effective cavity length L_{eff} [46]	10.8 µm
Estimated cavity beam waist ω_0 [46]	1.24 µm
Estimated cavity mode volume V [46]	55 λ^3
Cavity Lorentzian linewidth $\kappa/2\pi$	(6.86 ± 0.05) GHz
Root mean square cavity length fluctuations	27 pm
Cavity mode dispersion slope	46 MHz/pm
Cavity quality factor Q	7×10^4
Cavity finesse $\mathscr{F}$	830
Calculated Purcell factor F_P [46]	6.9
Calculated cavity transmission	2.4 %
SnV center natural lifetime τ	(5.0 ± 0.1) ns
SnV center lifetime-limited linewidth $\gamma/2\pi$	32 MHz
SnV center linewidth $\gamma'/2\pi$	(77.6 ± 0.8) MHz
Purcell-enhanced emitter linewidth $\gamma'_P/2\pi$	(126 ± 4) MHz
Vibration-corrected cooperativity C	1.7 ± 0.2
Vibration-corrected coherent cooperativity C_{coh}	0.69 ± 0.07
Single photon Rabi frequency g	(300 ± 20) MHz

References

[1] Y. Herrmann, J. Fischer, J. M. Brevoord, C. Sauerzapf, L. G. C. Wienhoven, L. J. Feije, M. Pasini, M. Eschen, M. Ruf, M. J. Weaver, and R. Hanson, *Coherent Coupling of a Diamond Tin-Vacancy Center to a Tunable Open Microcavity,* Phys. Rev. X **14**, 041013 (2024).

[2] H. J. Kimble, *The quantum internet,* Nature **453**, 1023 (2008).

[3] S. Wehner, D. Elkouss, and R. Hanson, *Quantum internet: A vision for the road ahead,* Science **362** (2018).

[4] K. J. Vahala, *Optical microcavities,* Nature **424**, 839 (2003).

[5] A. Reiserer and G. Rempe, *Cavity-based quantum networks with single atoms and optical photons,* Rev. Mod. Phys. **87**, 1379 (2015).

[6] E. Janitz, M. K. Bhaskar, and L. Childress, *Cavity quantum electrodynamics with color centers in diamond,* Optica **7**, 1232 (2020).

[7] M. Ruf, N. H. Wan, H. Choi, D. Englund, and R. Hanson, *Quantum networks based on color centers in diamond,* J. Appl. Phys. **130**, 070901 (2021).

[8] B. Merkel, A. Ulanowski, and A. Reiserer, *Coherent and Purcell-Enhanced Emission from Erbium Dopants in a Cryogenic High- Q Resonator,* Phys. Rev. X **10**, 041025 (2020).

[9] B. Casabone, C. Deshmukh, S. Liu, D. Serrano, A. Ferrier, T. Hümmer, P. Goldner, D. Hunger, and H. De Riedmatten, *Dynamic control of Purcell enhanced emission of erbium ions in nanoparticles,* Nat. Commun. **12**, 3570 (2021).

[10] A. Muller, E. B. Flagg, M. Metcalfe, J. Lawall, and G. S. Solomon, *Coupling an epitaxial quantum dot to a fiber-based external-mirror microcavity,* Appl. Phys. Lett. **95**, 173101 (2009).

[11] T. Herzog, M. Sartison, S. Kolatschek, S. Hepp, A. Bommer, C. Pauly, F. Mücklich, C. Becher, M. Jetter, S. L. Portalupi, and P. Michler, *Pure single-photon emission from In(Ga)As QDs in a tunable fiber-based external mirror microcavity,* Quantum Sci. Technol. **3**, 034009 (2018).

[12] D. Najer, I. Söllner, P. Sekatski, V. Dolique, M. C. Löbl, D. Riedel, R. Schott, S. Starosielec, S. R. Valentin, A. D. Wieck, N. Sangouard, A. Ludwig, and R. J. Warburton, *A gated quantum dot strongly coupled to an optical microcavity,* Nature **575**, 622 (2019).

[13] N. Tomm, A. Javadi, N. O. Antoniadis, D. Najer, M. C. Löbl, A. R. Korsch, R. Schott, S. R. Valentin, A. D. Wieck, A. Ludwig, and R. J. Warburton, *A bright and fast source of coherent single photons,* Nat. Nanotechnol. **16**, 399 (2021).

[14] S. Häußler, G. Bayer, R. Waltrich, N. Mendelson, C. Li, D. Hunger, I. Aharonovich, and A. Kubanek, *Tunable Fiber-Cavity Enhanced Photon Emission from Defect Centers in hBN,* Adv. Opt. Mater. **9**, 2002218 (2021).

[15] S. Vadia, J. Scherzer, H. Thierschmann, C. Schäfermeier, C. Dal Savio, T. Taniguchi, K. Watanabe, D. Hunger, K. Karraï, and A. Högele, *Open-Cavity in Closed-Cycle Cryostat as a Quantum Optics Platform,* PRX Quantum **2**, 040318 (2021).

[16] D. Wang, H. Kelkar, D. Martin-Cano, T. Utikal, S. Götzinger, and V. Sandoghdar, *Coherent Coupling of a Single Molecule to a Scanning Fabry-Perot Microcavity,* Phys. Rev. X **7**, 021014 (2017).

[17] D. Hunger, T. Steinmetz, Y. Colombe, C. Deutsch, T. W. Hänsch, and J. Reichel, *A fiber Fabry–Perot cavity with high finesse,* New J. Phys. **12**, 065038 (2010).

[18] R. Albrecht, A. Bommer, C. Deutsch, J. Reichel, and C. Becher, *Coupling of a Single Nitrogen-Vacancy Center in Diamond to a Fiber-Based Microcavity,* Phys. Rev. Lett. **110**, 243602 (2013).

[19] S. Johnson, P. R. Dolan, T. Grange, A. A. P. Trichet, G. Hornecker, Y. C. Chen, L. Weng, G. M. Hughes, A. A. R. Watt, A. Auffèves, and J. M. Smith, *Tunable cavity coupling of the zero phonon line of a nitrogen-vacancy defect in diamond,* New J. Phys. **17**, 122003 (2015).

[20] H. Kaupp, T. Hümmer, M. Mader, B. Schlederer, J. Benedikter, P. Haeusser, H.-C. Chang, H. Fedder, T. W. Hänsch, and D. Hunger, *Purcell-Enhanced Single-Photon Emission from Nitrogen-Vacancy Centers Coupled to a Tunable Microcavity,* Phys. Rev. Applied **6**, 054010 (2016).

[21] J. Benedikter, H. Kaupp, T. Hümmer, Y. Liang, A. Bommer, C. Becher, A. Krueger, J. M. Smith, T. W. Hänsch, and D. Hunger, *Cavity-Enhanced Single-Photon Source Based on the Silicon-Vacancy Center in Diamond,* Phys. Rev. Applied **7**, 024031 (2017).

[22] D. Riedel, I. Söllner, B. J. Shields, S. Starosielec, P. Appel, E. Neu, P. Maletinsky, and R. J. Warburton, *Deterministic Enhancement of Coherent Photon Generation from a Nitrogen-Vacancy Center in Ultrapure Diamond,* Phys. Rev. X **7**, 031040 (2017).

[23] M. Salz, Y. Herrmann, A. Nadarajah, A. Stahl, M. Hettrich, A. Stacey, S. Prawer, D. Hunger, and F. Schmidt-Kaler, *Cryogenic platform for coupling color centers in diamond membranes to a fiber-based microcavity,* Appl. Phys. B **126**, 131 (2020).

[24] R. Høy Jensen, E. Janitz, Y. Fontana, Y. He, O. Gobron, I. P. Radko, M. Bhaskar, R. Evans, C. D. Rodríguez Rosenblueth, L. Childress, A. Huck, and U. Lund Andersen, *Cavity-Enhanced Photon Emission from a Single Germanium-Vacancy Center in a Diamond Membrane,* Phys. Rev. Applied **13**, 064016 (2020).

[25] M. Ruf, M. Weaver, S. van Dam, and R. Hanson, *Resonant Excitation and Purcell Enhancement of Coherent Nitrogen-Vacancy Centers Coupled to a Fabry-Perot Microcavity,* Phys. Rev. Applied **15**, 024049 (2021).

[26] F. Feuchtmayr, R. Berghaus, S. Sachero, G. Bayer, N. Lettner, R. Waltrich, P. Maier, V. Agafonov, and A. Kubanek, *Enhanced spectral density of a single germanium vacancy center in a nanodiamond by cavity integration,* Appl. Phys. Lett. **123**, 024001 (2023).

[27] G. Bayer, R. Berghaus, S. Sachero, A. B. Filipovski, L. Antoniuk, N. Lettner, R. Waltrich, M. Klotz, P. Maier, V. Agafonov, and A. Kubanek, *Optical driving, spin initialization and readout of single SiV- centers in a Fabry-Perot resonator,* Commun. Phys. **6**, 300 (2023).

[28] H. Bernien, B. Hensen, W. Pfaff, G. Koolstra, M. S. Blok, L. Robledo, T. H. Taminiau, M. Markham, D. J. Twitchen, L. Childress, and R. Hanson, *Heralded entanglement between solid-state qubits separated by three metres,* Nature **497**, 86 (2013).

[29] P. C. Humphreys, N. Kalb, J. P. J. Morits, R. N. Schouten, R. F. L. Vermeulen, D. J. Twitchen, M. Markham, and R. Hanson, *Deterministic delivery of remote entanglement on a quantum network,* Nature **558**, 268 (2018).

[30] M. K. Bhaskar, R. Riedinger, B. Machielse, D. S. Levonian, C. T. Nguyen, E. N. Knall, H. Park, D. Englund, M. Lončar, D. D. Sukachev, and M. D. Lukin, *Experimental demonstration of memory-enhanced quantum communication,* Nature **580**, 60 (2020).

[31] M. H. Abobeih, J. Cramer, M. A. Bakker, N. Kalb, M. Markham, D. J. Twitchen, and T. H. Taminiau, *One-second coherence for a single electron spin coupled to a multi-qubit nuclear-spin environment,* Nat. Commun. **9**, 2552 (2018).

[32] T. Van Der Sar, Z. H. Wang, M. S. Blok, H. Bernien, T. H. Taminiau, D. M. Toyli, D. A. Lidar, D. D. Awschalom, R. Hanson, and V. V. Dobrovitski, *Decoherence-protected quantum gates for a hybrid solid-state spin register,* Nature **484**, 82 (2012).

[33] P.-J. Stas, Y. Q. Huan, B. Machielse, E. N. Knall, A. Suleymanzade, B. Pingault, M. Sutula, S. W. Ding, C. M. Knaut, D. R. Assumpcao, Y.-C. Wei, M. K. Bhaskar, R. Riedinger, D. D. Sukachev, H. Park, M. Lončar, D. S. Levonian, and M. D. Lukin, *Robust multi-qubit quantum network node with integrated error detection,* Science **378**, 557 (2022).

[34] C. E. Bradley, J. Randall, M. H. Abobeih, R. C. Berrevoets, M. J. Degen, M. A. Bakker, M. Markham, D. J. Twitchen, and T. H. Taminiau, *A Ten-Qubit Solid-State Spin Register with Quantum Memory up to One Minute,* Phys. Rev. X **9**, 031045 (2019).

[35] N. Kalb, A. A. Reiserer, P. C. Humphreys, J. J. W. Bakermans, S. J. Kamerling, N. H. Nickerson, S. C. Benjamin, D. J. Twitchen, M. Markham, and R. Hanson, *Entanglement distillation between solid-state quantum network nodes,* Science **356**, 928 (2017).

[36] S. L. N. Hermans, M. Pompili, H. K. C. Beukers, S. Baier, J. Borregaard, and R. Hanson, *Qubit teleportation between non-neighbouring nodes in a quantum network,* Nature **605**, 663 (2022).

[37] C. M. Knaut, A. Suleymanzade, Y.-C. Wei, D. R. Assumpcao, P.-J. Stas, Y. Q. Huan, B. Machielse, E. N. Knall, M. Sutula, G. Baranes, N. Sinclair, C. De-Eknamkul, D. S. Levonian, M. K. Bhaskar, H. Park, M. Lončar, and M. D. Lukin, *Entanglement of nanophotonic quantum memory nodes in a telecom network,* Nature **629**, 573 (2024).

[38] E. Janitz, M. Ruf, M. Dimock, A. Bourassa, J. Sankey, and L. Childress, *Fabry-Perot microcavity for diamond-based photonics,* Phys. Rev. A **92**, 043844 (2015).

[39] M. E. Trusheim, B. Pingault, N. H. Wan, M. Gündoğan, L. De Santis, R. Debroux, D. Gangloff, C. Purser, K. C. Chen, M. Walsh, J. J. Rose, J. N. Becker, B. Lienhard, E. Bersin, I. Paradeisanos, G. Wang, D. Lyzwa, A. R.-P. Montblanch, G. Malladi, H. Bakhru, A. C. Ferrari, I. A. Walmsley, M. Atatüre, and D. Englund, *Transform-Limited Photons From a Coherent Tin-Vacancy Spin in Diamond,* Phys. Rev. Lett. **124**, 023602 (2020).

[40] A. E. Rugar, C. Dory, S. Aghaeimeibodi, H. Lu, S. Sun, S. D. Mishra, Z.-X. Shen, N. A. Melosh, and J. Vučković, *Narrow-Linewidth Tin-Vacancy Centers in a Diamond Waveguide,* ACS Photonics **7**, 2356 (2020).

[41] J. Arjona Martínez, R. A. Parker, K. C. Chen, C. M. Purser, L. Li, C. P. Michaels, A. M. Stramma, R. Debroux, I. B. Harris, M. Hayhurst Appel, E. C. Nichols, M. E. Trusheim, D. A. Gangloff, D. Englund, and M. Atatüre, *Photonic Indistinguishability of the Tin-Vacancy Center in Nanostructured Diamond,* Phys. Rev. Lett. **129**, 173603 (2022).

[42] E. I. Rosenthal, C. P. Anderson, H. C. Kleidermacher, A. J. Stein, H. Lee, J. Grzesik, G. Scuri, A. E. Rugar, D. Riedel, S. Aghaeimeibodi, G. H. Ahn, K. Van Gasse, and J. Vučković, *Microwave Spin Control of a Tin-Vacancy Qubit in Diamond,* Phys. Rev. X **13**, 031022 (2023).

[43] X. Guo, A. M. Stramma, Z. Li, W. G. Roth, B. Huang, Y. Jin, R. A. Parker, J. Arjona Martínez, N. Shofer, C. P. Michaels, C. P. Purser, M. H. Appel, E. M. Alexeev, T. Liu, A. C. Ferrari, D. D. Awschalom, N. Delegan, B. Pingault, G. Galli, F. J. Heremans, M. Atatüre, and A. A. High, *Microwave-Based Quantum Control and Coherence Protection of Tin-Vacancy Spin Qubits in a Strain-Tuned Diamond-Membrane Heterostructure,* Phys. Rev. X **13**, 041037 (2023).

[44] M. Ruf, M. IJspeert, S. van Dam, N. de Jong, H. van den Berg, G. Evers, and R. Hanson, *Optically Coherent Nitrogen-Vacancy Centers in Micrometer-Thin Etched Diamond Membranes,* Nano Lett. **19**, 3987 (2019).

[45] P. Appel, E. Neu, M. Ganzhorn, A. Barfuss, M. Batzer, M. Gratz, A. Tschöpe, and P. Maletinsky, *Fabrication of all diamond scanning probes for nanoscale magnetometry,* Rev. Sci. Instrum. **87**, 063703 (2016).

[46] S. B. van Dam, M. Ruf, and R. Hanson, *Optimal design of diamond-air microcavities for quantum networks using an analytical approach,* New J. Phys. **20**, 115004 (2018).

[47] Y. Herrmann, J. Fischer, S. Scheijen, C. F. J. Wolfs, J. M. Brevoord, C. Sauerzapf, L. G. C. Wienhoven, L. J. Feije, M. Eschen, M. Ruf, M. J. Weaver, and R. Hanson, *A low-temperature tunable microcavity featuring high passive stability and microwave integration,* AVS Quantum Sci. **6**, 041401 (2024).

[48] J. Görlitz, D. Herrmann, G. Thiering, P. Fuchs, M. Gandil, T. Iwasaki, T. Taniguchi, M. Kieschnick, J. Meijer, M. Hatano, A. Gali, and C. Becher, *Spectroscopic investigations of negatively charged tin-vacancy centres in diamond,* New J. Phys. **22**, 013048 (2020).

[49] T. Iwasaki, Y. Miyamoto, T. Taniguchi, P. Siyushev, M. H. Metsch, F. Jelezko, and M. Hatano, *Tin-Vacancy Quantum Emitters in Diamond,* Phys. Rev. Lett. **119**, 253601 (2017).

[50] A. E. Rugar, S. Aghaeimeibodi, D. Riedel, C. Dory, H. Lu, P. J. McQuade, Z.-X. Shen, N. A. Melosh, and J. Vučković, *Quantum Photonic Interface for Tin-Vacancy Centers in Diamond,* Phys. Rev. X **11**, 031021 (2021).

[51] J. Borregaard, A. S. Sørensen, and P. Lodahl, *Quantum Networks with Deterministic Spin–Photon Interfaces,* Adv. Quantum Technol. **2**, 1800091 (2019).

[52] K. D. Jahnke, A. Sipahigil, J. M. Binder, M. W. Doherty, M. Metsch, L. J. Rogers, N. B. Manson, M. D. Lukin, and F. Jelezko, *Electron–phonon processes of the silicon-vacancy centre in diamond,* New J. Phys. **17**, 043011 (2015).

[53] P. Wang, L. Kazak, K. Senkalla, P. Siyushev, R. Abe, T. Taniguchi, S. Onoda, H. Kato, T. Makino, M. Hatano, F. Jelezko, and T. Iwasaki, *Transform-Limited Photon Emission from a Lead-Vacancy Center in Diamond above 10 K,* Phys. Rev. Lett. **132**, 073601 (2024).

[54] R. J. Thompson, G. Rempe, and H. J. Kimble, *Observation of normal-mode splitting for an atom in an optical cavity,* Phys. Rev. Lett. **68**, 1132 (1992).

[55] A. Sipahigil, R. E. Evans, D. D. Sukachev, M. J. Burek, J. Borregaard, M. K. Bhaskar, C. T. Nguyen, J. L. Pacheco, H. A. Atikian, C. Meuwly, R. M. Camacho, F. Jelezko, E. Bielejec, H. Park, M. Lončar, and M. D. Lukin, *An integrated diamond nanophotonics platform for quantum-optical networks,* Science **354**, 847 (2016).

[56] D. M. Lukin, M. A. Guidry, and J. Vučković, *Integrated Quantum Photonics with Silicon Carbide: Challenges and Prospects,* PRX Quantum **1**, 020102 (2020).

[57] J. Heiler, J. Körber, E. Hesselmeier, P. Kuna, R. Stöhr, P. Fuchs, M. Ghezellou, J. Ul-Hassan, W. Knolle, C. Becher, F. Kaiser, and J. Wrachtrup, *Spectral stability of V2 centres in sub-micron 4H-SiC membranes,* npj Quantum Mater. **9**, 34 (2024).

[58] S. Bogdanović, S. B. van Dam, C. Bonato, L. C. Coenen, A.-M. J. Zwerver, B. Hensen, M. S. Z. Liddy, T. Fink, A. Reiserer, M. Lončar, and R. Hanson, *Design and low-temperature characterization of a tunable microcavity for diamond-based quantum networks,* Appl. Phys. Lett. **110**, 171103 (2017).

[59] S. Flågan, D. Riedel, A. Javadi, T. Jakubczyk, P. Maletinsky, and R. J. Warburton, *A diamond-confined open microcavity featuring a high quality-factor and a small mode-volume,* J. Appl. Phys. **131**, 113102 (2022).

[60] J. Körber, M. Pallmann, J. Heupel, R. Stöhr, E. Vasilenko, T. Hümmer, L. Kohler, C. Popov, and D. Hunger, *Scanning Cavity Microscopy of a Single-Crystal Diamond Membrane,* Phys. Rev. Applied **19**, 064057 (2023).

[61] S. Bogdanović, M. S. Z. Liddy, S. B. van Dam, L. C. Coenen, T. Fink, M. Lončar, and R. Hanson, *Robust nano-fabrication of an integrated platform for spin control in a tunable microcavity,* APL Photonics **2**, 126101 (2017).

[62] Y. Herrmann, J. Fischer, J. M. Brevoord, C. Sauerzapf, L. G. C. Wienhoven, L. J. Feije, M. Pasini, M. Eschen, M. Ruf, M. J. Weaver, and R. Hanson, *Data underlying the publication "Coherent Coupling of a Diamond Tin-Vacancy Center to a Tunable Open Microcavity",* 4TU.ResearchData, Dataset (2023).

[63] I. T. Raa, H. K. Ervasti, P. J. Botma, L. C. Visser, R. Budhrani, J. F. van Rantwijk, S. P. Cadot, J. Vermeltfoort, M. Pompili, A. J. Stolk, M. J. Weaver, K. L. van der Enden, D. de Leeuw Duarte, M. Teng, J. van Zwieten, and F. Grooteman, *QMI - Quantum Measurement Infrastructure, a Python 3 framework for controlling laboratory equipment,* 4TU.ResearchData, Software (2023).

[64] J. Johansson, P. Nation, and F. Nori, *QuTiP: An open-source Python framework for the dynamics of open quantum systems,* Comput. Phys. Commun. **183**, 1760 (2012).

7

Spin-Photon Correlations from a Purcell-enhanced Diamond Nitrogen-Vacancy Center Coupled to an Open Microcavity

"If you want to find the secrets of the universe, think in terms of energy, frequency, and vibration." - *Nikola Tesla*

J. Fischer*, Y. Herrmann*, C. F. J. Wolfs, S. Scheijen, M. Ruf and R. Hanson

An efficient interface between a spin qubit and single photons is a key enabling system for quantum science and technology. We report on a coherently controlled diamond nitrogen-vacancy center electron spin qubit that is optically interfaced with an open microcavity. Through Purcell enhancement and an asymmetric cavity design, we achieve efficient collection of resonant photons, while on-chip microwave lines allow for spin qubit control at a 10 MHz *Rabi frequency. With the microcavity tuned to resonance with the nitrogen-vacancy center's optical transition, we use excited state lifetime measurements to determine a Purcell factor of* 7.3 ± 1.6*. Upon pulsed resonant excitation, we find a coherent photon detection probability of* 0.5 % *per pulse. Although this result is limited by the finite excitation probability, it already presents an order of magnitude improvement over the solid immersion lens devices used in previous quantum network demonstrations. Furthermore, we use resonant optical pulses to initialize and read out the electron spin. By combining the efficient interface with spin qubit control, we generate two-qubit and three-qubit spin-photon states and measure heralded Z-basis correlations between the photonic time-bin qubits and the spin qubit.*

*These authors contributed equally to this work.

The results of this chapter are under peer review and available as preprint under Ref. [1].

7.1 Introduction

Optically active solid-state qubits are promising physical systems for quantum networking [2–5]. Among several candidates [6–9], the nitrogen-vacancy (NV) center in diamond is one of the most-studied, with the realization of qubit teleportation [10] across a multi-node quantum network [11] and metropolitan-scale heralded entanglement [12]. Furthermore, efficient quantum frequency conversion to telecom wavelength [13, 14] and hybrid entanglement of photons and nuclear spins [15, 16] have been demonstrated. The NV center offers excellent spin qubit properties [17] and the nitrogen nuclear spin [18] together with nearby carbon-13 spins [19] can function as a multi-qubit register [20, 21] to store [22–24] and process [25–27] quantum states with high fidelities [28]. The main challenges for the generation of spin-photon states with the NV center are the relatively low zero-phonon line (ZPL) emission of ~ 3 % [29] and the reduced optical coherence in the presence of charge noise hindering integration into nanophotonic devices [30–33]. State-of-the-art quantum network nodes [10] are thus realized with solid immersion lenses (SIL) [34], in which the NV center retains lifetime-limited optical linewidth [35]. In practice, such systems have shown ZPL detector click probabilities around 5×10^{-4} upon pulsed resonant excitation [10, 11, 36, 37].

In this work, we realize the integration of a NV center into a fiber-based Fabry-Pérot microcavity [38, 39] in combination with coherent microwave spin control, enabling the generation of spin-photon states. This platform features bulk-like optical coherence of the NV center by incorporating a micrometer-thin diamond membrane into the cavity [40, 41] and a Purcell-enhanced emission into the ZPL combined with an efficient photon extraction. We quantify the coupling of the NV center's readout transition to the cavity modes with the Purcell factor by measuring the reduction of the excited state lifetime. Further, we investigate the cavity-coupled readout transition with a photoluminescence excitation (PLE) measurement to determine the optical linewidth, a Hanbury Brown and Twiss (HBT) experiment to verify single-photon emission, and a saturation measurement, which reveals a ZPL detector click probability that is an order of magnitude higher compared to standard solid immersion lens systems. Moreover, we demonstrate coherent control of the NV center's electron spin and characterize its coherence properties in a Ramsey and a Hahn-Echo measurement. Finally, we use our platform to generate spin-photon states of the electron spin qubit with one and two time-bin encoded ZPL photon qubits. We herald on the photon detection in their time-bin states and observe the correlation with the corresponding spin qubit readout.

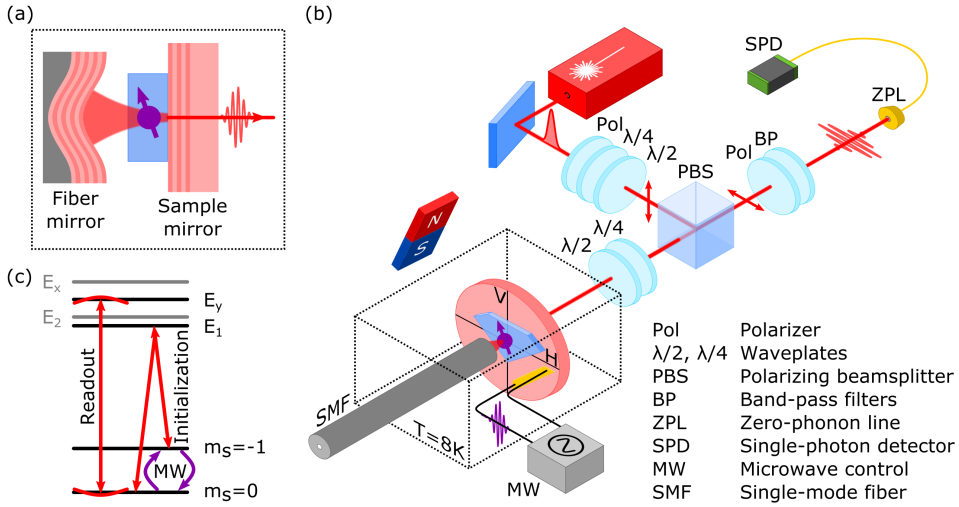

Figure 7.1: (a) Schematic of the fiber-based Fabry-Pérot microcavity. The NV center is hosted in a diamond membrane bonded to a planar sample mirror that faces a spherical mirror on the tip of an optical fiber, forming the cavity. The cavity mirrors are dielectric Bragg mirrors. (b) Schematic experimental setup to efficiently interface a NV center qubit with an optical microcavity. The cavity-coupled NV center spin qubit is controlled with microwave signals, which are delivered via a gold stripline that is embedded into the sample mirror. Outside the cryostat, a permanent magnet is mounted to apply a static magnetic field to the qubit. The optical readout of the cavity-coupled NV center is achieved using free-space cross-polarized resonant excitation and detection via the sample mirror side. Additional lasers for charge repump, spin initialization, and cavity locking are deployed in fiber via the fiber mirror side. (c) Energy diagram showing the investigated levels of the cavity-coupled NV center. The microwave qubit control, as well as the optical interface for readout and spin initialization, is depicted. The cavity is on resonance with the NV center E_y transition for readout.

7.2 Interfacing Diamond Nitrogen-Vacancy Center Spin Qubits with an Optical Microcavity

In this section, we conceptually outline the optical interfacing of NV centers which are coupled to a fiber-based Fabry-Pérot microcavity as schematically depicted in Fig. 7.1(a). At its heart, a sample mirror with a bonded diamond membrane faces a laser-ablated spherical mirror on the tip of an optical fiber forming the microcavity [39]. Using the experimental setup presented in Fig. 7.1(b), the cavity-coupled NV centers are optically addressed via the microcavity, which is mounted inside a closed-cycle optical cryostat. Details about the low-vibration cryogenic microcavity setup can be found in Ref. [42], and the fabrication of the thinned-down diamond membrane, which is also used in earlier work [41], is reported in Ref. [40].

For the experiments in this study, the two orthogonal, linear polarization modes of the microcavity must be considered. Due to birefringence in the diamond membrane, the frequency degeneracy of these cavity modes is lifted, which is identified as a polarization mode splitting in the optical cavity response. In our lab frame, the low frequency (LF) and high frequency (HF) cavity mode is referred to as horizontal and vertical polarization cavity modes, respectively. The NV center's optical dipole of the readout transition around

637 nm couples to both polarization cavity modes, enabling resonant excitation and detection in a cross-polarized fashion [43]. Nanosecond optical excitation pulses are coupled into the vertical polarization cavity mode through the sample mirror via the reflection of a polarizing beamsplitter. Upon excitation, the NV center ZPL emission into the horizontal polarization cavity mode is coupled out through the sample mirror and detected by a fiber-coupled single-photon detector in transmission of the polarizing beamsplitter. This cross-polarization filtering reaches high suppression values of the excitation laser and is actively optimized during the experiments via piezo rotation mounted waveplates. In addition, a cavity lock laser at 637 nm is launched over the optical fiber mirror into the horizontal polarization cavity mode and is detected in cavity transmission by the same single-photon detector. This signal is used in the experiments to run a side-of-fringe lock that feeds back on the piezo that is controlling the fiber mirror position to maintain a constant cavity length. More details about the experimental setup and the methods to maintain a high excitation laser suppression and to lock the cavity are described in Appendix 7.8.1.

To prepare the NV center in its negatively charged state an off-resonant 515 nm charge repump laser is deployed over the fiber mirror next to a second, 637 nm laser to initialize the NV center in its $m_s = 0$ spin ground state via the E_1 transition (see Fig. 7.1(c)). A permanent magnet outside the cryostat creates a static magnetic field at the position of the NV center, which Zeeman-splits the NV center's $m_s = \pm 1$ spin states, allowing us to define a qubit subspace consisting of the $m_s = 0$ and $m_s = -1$ states. Microwave pulses for qubit control are delivered via a gold stripline, which is embedded into the sample mirror [44].

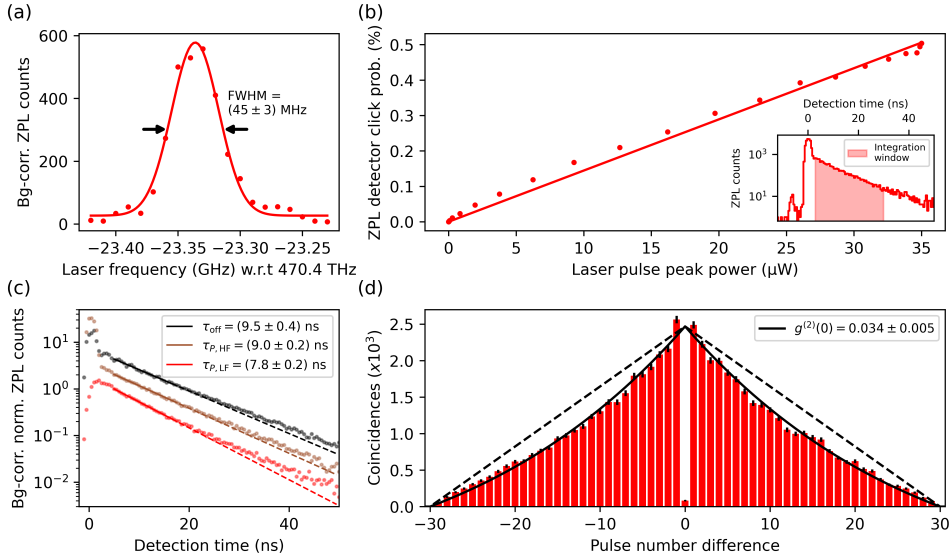

Figure 7.2: Characterization of the optical interface of the cavity-coupled NV center. (a) PLE measurement of the NV center's E_y transition (readout transition) in the LF cavity mode with a Gaussian fit (solid line). Details about the PLE measurement sequence and the applied background correction are presented in Appendix 7.8.3. (b) Pulsed resonant saturation measurement of the readout transition in the LF cavity mode, together with a linear fit as a guide for the eye. The inset shows the time-resolved detector counts for a laser pulse peak power of 35 μW measured free-space before the objective and the used integration window from 3 ns to 30 ns with respect to the excitation pulse center. The small peak at a detection time of about −5 ns is light of the excitation pulse that is backscattered into the free-space detection before reaching the cryostat. (c) Lifetime measurements of the NV center's E_y excited state on cavity resonance in the LF and HF cavity modes, as well as off resonance in the LF mode. Details about the applied background correction are outlined in Appendix 7.8.5. The fit windows of 5 ns to 18 ns are represented by the length of the solid lines of the monoexponential fits. The data is offset for visual clarity. (d) Second-order correlation measurement of the readout transition in the LF cavity mode for a pulse train of 30 consecutive short resonant excitation pulses. In this measurement, the integration window of (b) is used. The triangular function capturing the finite pulse train (black dashed line) is shown next to the fit function that also includes the spin flipping process (black solid line).

7.3 Coupling a Single Nitrogen-Vacancy Center to the Microcavity

With the full spatial and spectral tunability of the microcavity [45], we select a position on the diamond membrane that is close to the mirror-embedded gold stripline, exhibits a high cavity quality factor, and a well-coupled NV center. At the selected position, a frequency splitting between the horizontal and vertical polarization cavity mode of (9.56 ± 0.02) GHz is observed, which we attribute to birefringence due to the presence of strain in the diamond membrane. The individual cavity polarization mode shows a linewidth of (1.69 ± 0.02) GHz, which corresponds to a quality factor of 280×10^3. With the determined cavity geometry, a cavity mode volume of 86 λ^3 is simulated. Accounting for our residual cavity vibration level of 22 pm, this results in a maximal vibration-averaged Purcell factor of 12 for a NV center that is perfectly coupled to a single cavity mode [46]. In addition,

a cavity mode outcoupling efficiency through the sample mirror of 39 % is calculated by taking the mirror coating transmission losses into account (see Appendix 7.8.2 for the cavity characterization details).

For the investigated cavity, we find a NV center that is coupled with its E_y transition (readout transition) at a frequency of 470.377 THz (−23.34 GHz with respect to 470.4 THz). Figure 7.2(a) shows a PLE measurement of this transition in the LF cavity mode, resulting in a linewidth of (45 ± 3) MHz determined by a Gaussian fit. We attribute the additional broadening above the expected linewidth of $1/2\pi\tau_{P,\mathrm{LF}} \approx 20$ MHz for the Purcell-reduced lifetime $\tau_{P,\mathrm{LF}}$ in the LF cavity mode as stated below to spectral diffusion. The determined transition linewidth is typical for NV centers with bulk-like optical properties and the used experimental PLE sequence involving 515 nm repump laser pulses [40]. Furthermore, we find the NV center's E_x transition at a frequency of 10 GHz. This corresponds to a lateral strain with E_x - E_y excited state splitting of ~ 33 GHz, which is larger compared to typical bulk samples. We note that we also find NV centers with less strain in the diamond membrane. Next to these NV center transitions associated with the $m_s = 0$ spin state, we find emission lines at −26.0 GHz as well as −24.5 GHz that are associated with the $m_s = \pm 1$ spin states. We attribute these to the NV center's E_1 and E_2 transitions, where we use the former as our spin initialization transition. In all measurements, a static magnetic field of about 37.5 G is present along the NV center crystal axis. See Appendix 7.8.3 and 7.8.10 for the PLE measurements of the other transitions and details about the used sequences of the here studied and another cavity-coupled NV center.

In the sequences of all following measurements, we start by applying a 515 nm charge repump laser pulse to prepare the NV center with high probability in its negatively charged state, and a spin initialization laser pulse to initialize the NV center in its $m_s = 0$ spin state (see Appendix 7.8.7 for details). Figure 7.2(c) shows lifetime measurements of the NV center's E_y excited state using 2 ns short resonant excitation pulses (see Appendix 7.8.4 for details about the excitation pulse). The Purcell-reduced lifetime is measured in the LF and HF cavity modes with the cavity being on resonance with the readout transition. An off resonance lifetime is determined in the LF mode by detuning the cavity from the readout transition by −4 GHz. The lifetime measurement data is fitted with monoexponential curves. We observe that the data start to deviate from a monoexponential behavior for detection times $\gtrsim 20$ ns. We attribute this to the detected fluorescence of other (weaker coupled) NV centers and therefore restrict the fit window size. Details about the applied background subtraction and the influence of the fit window are further outlined in Appendix 7.8.5. From the monoexponential fit, we determine an off resonance lifetime of $\tau_{\mathrm{off}} = (9.5 \pm 0.4)$ ns and a Purcell-reduced lifetime of $\tau_{P,\mathrm{LF}} = (7.8 \pm 0.2)$ ns and $\tau_{P,\mathrm{HF}} = (9.0 \pm 0.2)$ ns for the LF and HF cavity mode, respectively. The off resonance lifetime differs from the expected excited state lifetime of 12.4 ns for low-strained NV centers [35]. We attribute this to strain-induced mixing in excited states [47, 48]. In Appendix 7.8.5 we show a complementary investigation of this mechanism with time-resolved detection during continuous wave resonant excitation. The determined lifetimes allow to calculate the Purcell factor

$$F_P = \frac{1}{\beta_0}\left(\frac{\tau_{\mathrm{off}}}{\tau_P} - 1\right), \tag{7.1}$$

with the NV center Debye-Waller factor $\beta_0 = 0.03$ [29]. The Purcell factors for the LF and HF cavity mode are $F_{P,\mathrm{LF}} = 7.3 \pm 1.6$ and $F_{P,\mathrm{HF}} = 2.0 \pm 1.4$. In all the following measurements, we use the stronger coupling to the LF cavity mode to enhance the NV center emission and the HF cavity mode for excitation. Based on the determined Purcell factor the NV center coherently emits $\beta_{\mathrm{LF}} = \beta_0 F_{P,\mathrm{LF}}/(\beta_0 F_{P,\mathrm{LF}} + 1) \approx 18\,\%$ into the LF cavity mode, which corresponds to a cavity outcoupled ZPL emission of about 7 % and a maximal detector click probability of about 1.4 % per excitation pulse for our setup efficiency and detection time window (see Appendix 7.8.11 for details).

In Figure 7.2(b), the saturation behavior of the NV center readout transition is studied. For that, the peak power of the short excitation pulse is varied, and the ZPL detector click probability after the first excitation pulse is measured. A ZPL detector click probability of 0.5 % per pulse is determined for the highest power applied, which outperforms the standard NV center quantum network node setups based on solid immersion lenses by an order of magnitude [10, 11, 36, 37]. In addition, the detector click probability still increases linearly for the investigated laser power regime showing that higher detector click probabilities can be reached if more laser power is applied. In the experiments, we are limited to the here investigated laser power regime due to the efficiency of our short optical pulse generation setup.

Furthermore, we confirm single-photon emission by performing a pulsed resonant HBT experiment on the readout transition. In the experiment, we perform in total 55×10^6 measurement sequence repetitions in which we apply a train of short excitation pulses with a consecutive time separation of 126 ns. Figure 7.2(d) shows the second-order correlation function for 30 consecutive excitation pulses. The second-order correlation function exhibits clear antibunching at zero pulse number difference. Further, it shows two bunching-like features, which we attribute to the spin flipping probability into the $m_s = \pm 1$ states for larger pulse number differences and the probability to decay back into the $m_s = 0$ state from the intersystem crossing singlet state for small pulse number differences. We fit the data with a triangular function as expected for the finite pulse train multiplied by a monoexponential function capturing the spin flipping process (see Appendix 7.8.6 for details)). The exponential decay for small pulse number differences is not included, since the amount of affected data points is insufficient for a reliable fit. We quantify an antibunching value of $g^{(2)}(0) = 0.034 \pm 0.005$ by the ratio of measured coincidences in the zero bin to the triangular fit amplitude.

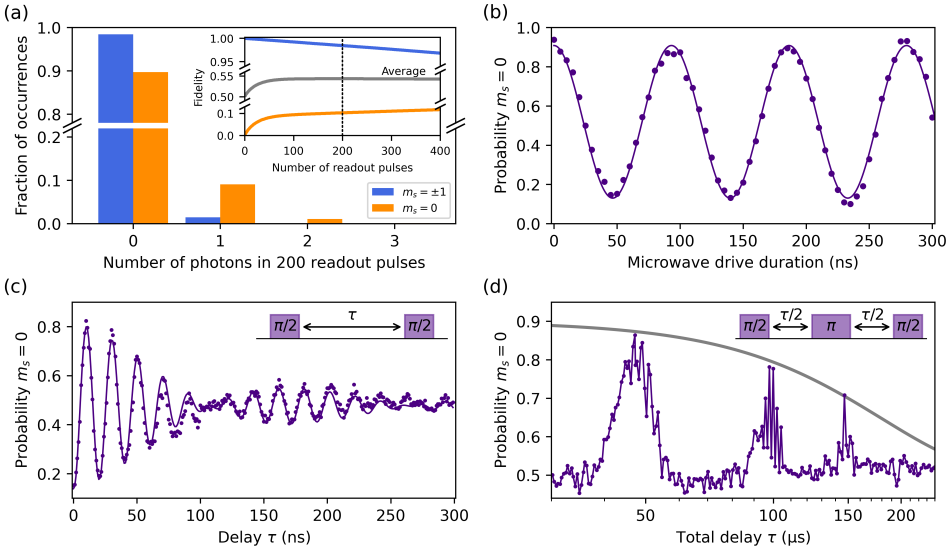

Figure 7.3: Characterization of the NV center electron spin qubit. (a) Statistics of detected photons for our spin qubit readout after spin initialization in the $m_s = \pm 1$ or $m_s = 0$ state. The inset presents the corresponding readout fidelities depending on the number of used short excitation pulses. For the experiments 200 short readout pulses are used, which leads to fidelities of $F_{\pm 1} = 98.4\,\%$, $F_0 = 10.3\,\%$ and $F_{\text{avg}} = 54.4\,\%$ for the shown calibration. (b) Coherent Rabi oscillations with a fit (solid line) showing a Rabi frequency of $\Omega = (10.73 \pm 0.02)\,\text{MHz}$. The error bars are within the dot size. (c) Ramsey measurement with an artificial detuning of 50 MHz. The inset shows the used microwave pulse sequence, where a delay time-dependent phase is applied to the second pulse to generate the artificial detuning. The fit (solid line) captures a beating signature of $(2.68 \pm 0.05)\,\text{MHz}$ which is attributed to the coupled nitrogen nuclear spin and the free-induction decay of $T_2^* = (170 \pm 20)\,\text{ns}$ with an exponent of $n = 1.0 \pm 0.2$. The error bars are within the dot size. (d) Hahn-Echo measurement with its microwave pulse sequence in the inset. The grey solid line is a guide for the eye of a Gaussian decay curve with an amplitude of 0.9 and a decay time of 180 µs. The error bars are within the dot size.

7.4 Coherent Microwave Control of the Nitrogen-Vacancy Center Spin Qubit

The NV center electron spin is coherently manipulated with microwave pulses, that are delivered via an about 10 µm distant gold stripline. Before microwave spin manipulation a 515 nm charge repump laser pulse prepares the NV center with high probability in its negatively charged state and the spin is optically initialized in its $m_s = 0$ ground state with a spin initialization laser pulse and a fidelity of $(93.5 \pm 0.9)\,\%$ (see Appendix 7.8.7 for details about the initialization and qubit readout analysis). The applied magnetic field along the NV center crystal axis splits the $m_s = \pm 1$ states by about 210 MHz, enabling selective driving of the $m_s = 0$ and $m_s = -1$ qubit subsystem. After spin manipulation, the qubit is read out via the readout transition using the short excitation pulses and the same integration window as introduced in Fig. 7.2(b). Figure 7.3(a) shows the statistics of detected photons for our spin qubit readout after spin initialization in the $m_s = \pm 1$ or $m_s = 0$ state. This measurement is used as a readout fidelity calibration, and its dependency on the number of used short readout pulses is presented in the inset. The average fidelity F_{avg} of the $m_s = \pm 1$

readout fidelity $F_{\pm1}$ and the $m_s = 0$ readout fidelity F_0 plateaus for larger readout pulse numbers and is optimal around 200 pulses, which is used in the following experiments. These readout fidelities are used for qubit readout correction, where the finite spin state initialization fidelity is also taken into account. We note that the average readout fidelity is not limited by laser power, but rather the average number of emitted photons before the studied NV center spin flips. The outcoupled ZPL emission of about 7 % for our system is comparable to the collected non-coherent phonon sideband (PSB) emission used for readout in a SIL setup, rendering high-fidelity qubit readout possible [49].

In Figure 7.3(b), coherent Rabi oscillations with a Rabi frequency of $\Omega = (10.73 \pm 0.02)$ MHz are shown for our spin qubit at a microwave frequency of 2.773 GHz. Based on the fitted contrast of the Rabi oscillations and correcting for the finite spin state initialization fidelity, a microwave π pulse fidelity of (83 ± 9) % is extracted.

For the next experiments, a π pulse and a $\pi/2$ pulse are calibrated by varying the amplitude of five consecutively applied π pulses that minimize the probability to readout $m_s = 0$. The π pulse duration is fixed to 64 ns, and half of that duration is used for the $\pi/2$ pulse. As depicted in Fig. 7.3(c), the qubit coherence is probed in a Ramsey experiment with an artificial detuning of 50 MHz by applying a delay time-dependent phase shift to the second $\pi/2$ pulse. The observed beating signature is attributed to the hyperfine coupling of the nitrogen nuclear spin, which is included in the fit model (see Appendix 7.8.8 for details). By fitting the measurement data, a free-induction decay time of $T_2^* = (170 \pm 20)$ ns is determined, which is short compared to typical T_2^* times for these diamond membranes (see Appendix 7.8.10 for additional data).

Using a Hahn-Echo experiment as presented in Fig. 7.3(d), the qubit coherence can be largely recovered by choosing an appropriate total delay time τ, which mitigates quasi-static magnetic field fluctuations. In this measurement, three revivals are observed and a Gaussian decay curve with a time constant of 180 µs is displayed as a guide for the eye in Fig. 7.3(d). The revivals occur around decoupling interpulse delay times $\tau/2$ that correspond to integer multiples of the bare Larmor period of the carbon-13 nuclear spin bath of about 25 µs ($\gamma_{C13} = 1.0705$ kHz/G and $B = 37.5$ G) [50].

7.5 Generation of Spin-Photon States

In this section, we use our system to generate two-qubit and three-qubit spin-photon states and measure heralded correlations between the photonic and spin states. Figure 7.4(a) depicts the used pulse sequence, which combines spin qubit microwave control with the short resonant excitation pulses to generate spin-dependent photonic time-bin qubits. After optical initialization, the spin qubit is brought into equal superposition with a $\pi/2$ microwave pulse, followed by two resonant excitation pulses with an intermediate microwave π pulse. This generates the Bell state $\left|\text{NV spin, photon}\right\rangle = (\left|1,\text{E}\right\rangle + \left|0,\text{L}\right\rangle)/\sqrt{2}$ between the spin qubit states $m_s = 0$ ($\left|0\right\rangle$) and $m_s = -1$ ($\left|1\right\rangle$) and the photonic qubit in the time-bin basis of early ($\left|\text{E}\right\rangle$) and late ($\left|\text{L}\right\rangle$) as used for remote entanglement generation in quantum network demonstrations [6, 36, 51]. The generated photon is measured by a single-photon detector, which heralds an early or late detection event. The spin qubit is optically read out in its Z-basis by 200 short readout pulses. The qubit readout probabilities conditioned on a photon heralding event in the early or late time-bin are shown in

Fig. 7.4(b) (see Appendix 7.8.7 for details about the applied qubit readout correction and Appendix 7.8.9 for an X-basis spin qubit readout). A photon detection event in the late time-bin heralds the qubit in its expected $|0\rangle$ state. For an early time-bin photon detection event, the spin is read out with a probability of 82 % in its expected $|1\rangle$ state. We attribute the lower readout probability of the $|1\rangle$ state to our limited microwave π pulse fidelity and an imperfect pulse calibration. In the Bell state correlation measurement, we record 27143 photon heralding events in 5×10^6 attempts, which corresponds to a probability of 0.54 % per attempt.

Furthermore, the Greenberger–Horne–Zeilinger (GHZ) state $|\text{NV spin, photon, photon}\rangle = (|0,\text{E},\text{L}\rangle + |1,\text{L},\text{E}\rangle)/\sqrt{2}$ can be generated by repeating the center sequence with the two short resonant excitation pulses before readout (see case $N = 2$ in Fig. 7.4(a)). The correlations after a successful double photon heralding event are displayed in Fig. 7.4(c). After heralding a correct two-photon state, the expected spin state is read out with similar probabilities as in the Bell state measurement. In total, we measure 5242 two-photon heralding events in 220×10^6 attempts, which corresponds to a probability of 2.4×10^{-5} per attempt.

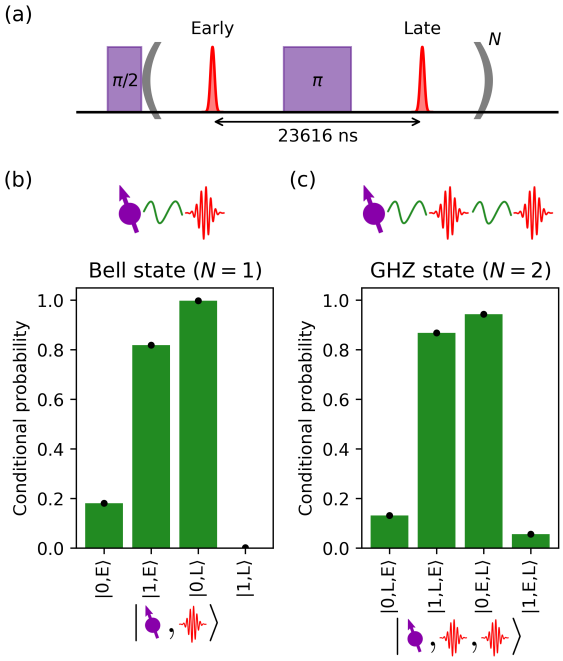

Figure 7.4: Spin-photon correlation measurements. (a) Pulse sequence to generate spin-photon states involving microwave pulses (in purple) for qubit control and short excitation pulses (in red) to generate spin-dependent time-bin photons. In the experiments, a microwave decoupling interpulse delay time of $\tau/2 = 23568$ ns is used. (b) Conditional probabilities of the spin qubit readout in the Z-basis after successful heralding an early ($|\text{E}\rangle$) or late ($|\text{L}\rangle$) photon of the spin-photon Bell state. The error bars are within the black dot size. (c) Conditional probabilities of the spin qubit readout in the Z-basis after a successful double heralding event of the photonic state $|\text{L},\text{E}\rangle$ or $|\text{E},\text{L}\rangle$ of the spin-photon GHZ state. The error bars are within the black dot size.

7.6 Discussion

We have equipped a coherent NV center spin qubit with an efficient spin-photon interface by coupling it to an open microcavity. Coherent qubit control is realized with microwave pulses, and qubit initialization as well as qubit readout are achieved with optical pulses in a cross-polarized resonant excitation and detection scheme. Moreover, we have demonstrated the quantum networking capabilities of our system by generating two-qubit and three-qubit spin-photon states and measuring heralded correlations between the photonic time-bin and the spin qubit states.
For the presented system, we project a saturation ZPL detector click probability of 1.4 % per pulse, by improving the excitation efficiency without modifying the microcavity. Furthermore, improving the device quality to eliminate additional cavity losses suggests a ZPL detector click probability of about 5 %, which corresponds to a cavity outcoupled ZPL emission of 26 %. Moreover, the system can be further optimized by implementing a charge-resonant check procedure of the optical transitions to mitigate spectral diffusion, improving charge state and qubit initialization fidelities [52], as well as microwave pulse shaping for high-fidelity qubit control [28].
Our work opens up opportunities to explore quantum networking with Purcell-enhanced NV centers, promising remote entanglement generation with higher rates and fidelities. Furthermore, we expect that the here developed methods provide guidance for other solid-state qubits to realize efficient spin-photon interfaces based on microcavities for quantum network applications [46, 53–56].

7.7 Acknowledgment

We thank Raymond Vermeulen for designing and building the standalone pulse generator used to modulate the electro-optical amplitude modulator. We thank Martin Eschen for laser-ablating the fiber mirror. We thank Jiwon Yun, Kai-Niklas Schymik, Conor Bradley, Alexander Stramma, and Mariagrazia Iuliano for helpful discussions. We thank Alexander Stramma for feedback on the manuscript.

We acknowledge financial support from the Dutch Research Council (NWO) through the Spinoza prize 2019 (project number SPI 63-264) and from the EU Flagship on Quantum Technologies through the project Quantum Internet Alliance (EU Horizon 2020, grant agreement no. 820445).

7.7.1 Author Contributions

J. F. and Y. H. contributed equally to this work. J. F. and Y. H. conducted the experiments and analyzed the data. J. F., Y. H., and S. S. developed and built the cross-polarization filtering setup. J. F. developed the cavity lock and the polarization suppression control. J. F., Y. H., and C. F. J. W. developed and built the short optical laser pulse generation setup. J. F. and C. F. J. W. developed the microwave qubit control. S. S. characterized the cavity fiber. M. R. fabricated the diamond membrane. J. F., Y. H., and R. H. wrote the manuscript with input from all authors. R. H. supervised the experiments.

7.7.2 Data Availability

The datasets that support this manuscript are available at 4TU.ResearchData [57].

7.8 Appendix

7.8.1 Experimental Setup

We use a floating stage closed-cycle optical cryostat (Montana Instruments HILA) with a base temperature of about 6 K and a sample mirror holder temperature of about 8 K. The spherical fiber mirror, that faces the sample mirror, is made out of a single-mode optical fiber with a pure silica core and a polyimide protection coating (Coherent FUD-4519, S630-P) and is mounted on a cryo-compatible positioning stage (JPE CPSHR1-a). A room temperature objective (Zeiss LD EC Epiplan-Neofluar), which is thermally shielded, is used to optically interface the sample mirror side of the cavity. The objective is positioned with three linear nanopositioning stages (Physik Instrumente Q-545) in a tripod configuration. A permanent neodymium disc magnet (Supermagnete S-70-35-N), which is mounted on the lid of the cryostat, is used to create a static magnetic field at the position of the sample mirror. Further details about the cryogenic setup can be found in Ref. [42].
The setup is operated with a computer and the Python-based software QMI, in the version 0.44 [58]. The data is stored and analyzed with the Python framework quantify-core. The actual measurement sequences are timed and executed by an interplay between a microcontroller (Jäger Computergesteuerte Messtechnik Adwin Pro II) and an arbitrary waveform generator (Tektronix AWG5014C). Microwave pulses are generated with a single sideband modulated vector signal generator (Rohde & Schwarz SMBV100A), amplified by a microwave amplifier (Mini-Circuits ZHL-50W-63+) and delivered to the cryostat via a home-built microwave switch. At the qubit frequency of 2.773 GHz we measure about 26 dB transmission loss through the cryostat. Further details about the microwave wiring and a picture of the sample mirror with mirror-embedded gold striplines can be found in Ref. [42].

Laser Pulse Generation and Delivery

We use one 637 nm continuous wave diode laser each for cavity locking (Newport Newfocus Velocity TLB-6300-LN) and spin initialization (Toptica DL Pro 637 nm). To modulate the laser intensity and generate microsecond-long optical pulses with high on/off ratios, two cascaded in-fiber acousto-optic modulators (AOM, Gooch and Housego Fiber-Q 633 nm) are used. Both lasers are combined free-space by a 50:50 non-polarizing beamsplitter (Thorlabs BS016). Then, a Glan-Taylor polarizer (Thorlabs GT10-A) and a half-wave and quarter-wave plate (Thorlabs WPH05M-633 and WPQ05M-633) are used to set and control the polarization. Finally, the 637 nm lasers are overlapped with the 515 nm repump laser (Hübner Photonics Cobolt 06-MLD) by a dichroic mirror (Semrock Di01-R532) and coupled into a single-mode fiber, which is connected to the cavity fiber.
A frequency-doubled, high-power tunable diode laser (Toptica TA-SHG Pro 637 nm) is used for readout as well as for cross-polarization control. For that, the laser is split by a 50:50 fiber beamsplitter (Thorlabs PN635R5A2) into two in-fiber paths. In the path for cross-polarization control, two in-fiber AOMs are used for modulation, whereas in the readout laser path, a temperature-stabilized electro-optical amplitude modulator (EOM, Jenoptik AM635) is deployed additionally. This allows for faster intensity modulation and

the generation of nanosecond-short resonant excitation pulses. The EOM is DC biased by a programmable bench power supply (Tenma 72-13360) using a bias-tee (Mini-Circuits ZX85-12G-S+) and a DC block (Mini-Circuits BLK-89-S+) to control a constant transmission level. In addition, fast electrical pulses are generated with a home-built standalone pulse generator [59] and applied to the EOM via the RF input of the bias-tee to generate nanosecond-short excitation pulses (see Appendix 7.8.4 for their characterization). Finally, both in-fiber paths are combined with a 75:25 fiber beamsplitter (Thorlabs PN635R3A2) whose 75 % output is connected to a polarization-maintaining fiber (Thorlabs P3-630PM-FC-2) before free-space launching. The 25 % output is connected to a power meter (Thorlabs PM100USB with head S130VC) for laser power monitoring. To preserve a high polarization extinction ratio in both paths, in-line fiber polarizers (Thorlabs ILP630PM-APC) are used.
All 637 nm lasers are stabilized on a wave meter (HighFinesse WS-U).

Free-space Cross-polarization Optics
The cavity is interfaced from the sample mirror side with free-space cross-polarization optics as depicted in Fig. 7.1(b). The collimated beam leaving the cryostat chamber is guided by broadband dielectric mirrors (Thorlabs BB03-E03) on the optical table and is reflected off a dichroic mirror (Semrock Di02-R635) before reaching the polarization optics. Next, the beam passes through half-wave and quarter-wave plates (Thorlabs WPH05M-633 and WPQ05M-633), which are mounted in piezo rotation stages (Newport AG-PR100 controlled by Newport AG-UC8). These wave plates map the excitation and detection polarization of the polarizing beamsplitter cube (PBS, Thorlabs PBS202) to the cavity polarization modes.
In the excitation path of the PBS the readout laser is launched from the polarization-maintaining fiber into free-space (Thorlabs KT120 with objective RMS10X) and passes a Glan-Thompson polarizer (Thorlabs GTH10M-A), followed by a quarter-wave and half-wave plate, which are mounted in piezo rotation stages as well.
In the detection path of the PBS, the light is filtered by a Glan-Thompson polarizer (Thorlabs GTH10M-A), an angle-tunable etalon (Light Machinery custom coating, ≈ 100 GHz full width at half maximum (FWHM) at 637 nm), and a bandpass filter (Thorlabs FBH640-10). Finally, the light is coupled (Thorlabs KT120 with objective RMS10X) into a single-mode fiber (Thorlabs P3-630A-FC-2) and detected by a single-photon detector (Picoquant Tau-SPAD-20). For the HBT experiment shown in Fig. 7.2(d), a 50:50 fiber beamsplitter (Thorlabs TW630R5A2) is added, and a second single-photon detector (Laser Components Count-10C-FC) is used. The detectors are connected to a single-photon counting module (Picoquant Hydraharp 400) and the counter module of the microcontroller. The gating of the single-photon detectors is used to protect them against blinding during the application of the spin initialization laser.

Microcavity Operation
For the resonant cross-polarization excitation and detection scheme used in this work, it is essential to keep the cavity on resonance with the NV center and to maintain a high excitation laser suppression during the measurements. To ensure these operational conditions, we probe the cavity resonance as well as the excitation laser suppression interleaved

with the experimental sequences and stream the data to a computer in real-time to run an optimization routine next to the measurement. In both cases, the probe laser light is detected with the ZPL single-photon detector and recorded with the counter module of the microcontroller. This technique allows for live feedback on the order of Hertz, which is sufficient to compensate for drifts of the cavity resonance and the cross-polarization filtering. With the methods outlined in the following, it is possible to run measurements remotely for days.

To keep the cavity on resonance with the readout transition of the NV center, a side-of-fringe lock is deployed. For that, the cavity lock laser is frequency-tuned to the fringe of the cavity mode, and the single-photon detector counts are recorded during interleaved 100 µs long probe laser pulses. The recorded counts are streamed to a computer that uses a proportional control loop programmed in Python to optimize on a specified set value. The proportional control loop feeds back on the piezo that is controlling the fiber mirror position and, by that, locks the cavity on resonance. The cavity lock laser power is adjusted such that a count rate of about 700 kHz is measured when the cavity is on resonance with the cavity lock laser. For every specified set value, the cavity lock laser frequency can be slightly adjusted to fine-tune the cavity resonance on the NV center.

For the cross-polarization filtering, interleaved 10 nW probe pulses of the cross-polarization control laser are applied for 400 µs while recording the single-photon detector counts. These counts represent the current excitation laser suppression and are streamed to a computer that runs a hill-climbing type algorithm programmed in Python. The algorithm makes iterative changes to the four piezo rotation-mounted wave plates as introduced in Fig. 7.1(b) to minimize the recorded counts. With this polarization suppression control loop, typical long-term count rates are < 2 kHz for 10 nW probe pulses, which corresponds to excitation laser suppression values > 60 dB.

7.8.2 Hybrid Cavity Characterization

All measurements presented in the main text are performed at the same cavity length and lateral cavity position. By measuring the cavity mode dispersion as shown in Fig. 7.5, we extract an air gap of 6.39 µm and a diamond thickness of 6.20 µm, which corresponds to an air-like cavity mode [60] with hybrid cavity mode number 67. Due to a non-uniform bond, there might be a bond gap between the sample mirror and the diamond membrane. Further, a cavity mode dispersion slope of 34 MHz/pm and an effective cavity length of 13.2 µm is estimated [61]. Together with the 21.4 µm radius of curvature of the fiber mirror, a cavity beam waist of 1.46 µm and a cavity mode volume of 86 λ^3 is calculated.

To determine the FWHM Lorentzian linewidth of the cavity mode, we scan a laser over the cavity resonance as shown in Fig. 7.6. In this measurement, the linewidth of the cavity is broadened due to cavity length fluctuations. An independent measurement (as described in Ref. [42]) yields a vibration level of 22 pm root mean square of the cavity length fluctuations. Modeling these vibrations with a Gaussian distribution results in a Gaussian contribution of $\mathrm{FWHM_G} = 22\,\mathrm{pm} \times 34\,\mathrm{MHz/pm} \times 2\sqrt{2\ln 2}$ next to the Lorentzian cavity linewidth. By fitting a Voigt function with the determined Gaussian contribution, an intrinsic cavity linewidth of $\mathrm{FWHM_L} = (1.69 \pm 0.02)\,\mathrm{GHz}$ is obtained. This corresponds to a cavity quality factor of 280×10^3 and, for our cavity geometry, to a cavity finesse of 2800.

The cavity mirrors are both coated with dielectric Bragg mirrors (Laseroptik), that are

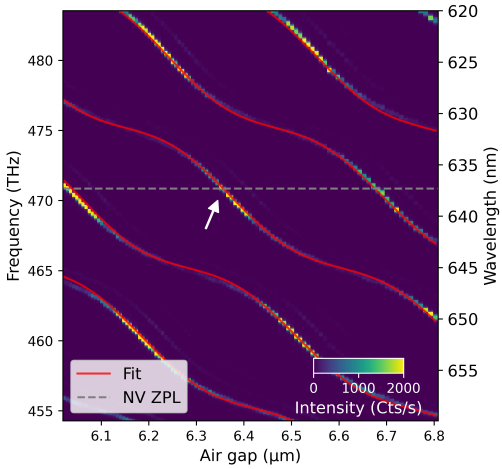

Figure 7.5: Cavity mode dispersion measurement of the hybrid air-diamond cavity. The cavity transmission of a broadband white light source spanning from 600 nm to 700 nm is measured on a spectrometer depending on the air gap. The bright fundamental modes are extracted and fitted by an analytical equation [60] to determine the air gap and the diamond thickness. In all measurements, the cavity is operated in the air-like mode at 637 nm as indicated by the white arrow.

optimized for maximum reflectivity at 637 nm. At this wavelength, the fiber mirror (sample mirror) exhibits a transmission value of 50 ppm (875 ppm) for air (diamond) termination. With the determined finesse, total cavity losses of 2260 ppm are calculated, which reveal additional losses of 1260 ppm. We attribute these additional losses to residual scattering at the interface of different refractive indices in the microcavity. Considering these losses, an outcoupling efficiency through the sample mirror of about 39 % is estimated, which reflects our asymmetric cavity design.
The inset of Fig. 7.6 shows another resonant laser scan, which is used to determine the frequency splitting between the LF and the HF cavity mode of (9.56 ± 0.02) GHz. For the used spherical fiber mirror, we do not observe a significant mode splitting on the bare mirror and hence attribute it mainly to the birefringence of the diamond membrane.

7.8.3 NV Center PLE measurements

The power values of the lasers that are deployed via the cavity fiber mirror are stated as measured in transmission after the cavity (on cavity resonance), whereas the power values of the lasers deployed via the sample mirror side are measured free-space before entering the cryostat.
All PLE measurements of the NV center are performed by repetitively running a certain PLE sequence for every swept excitation laser frequency. The number of repetitions and the exact PLE sequences for the different PLE measurements are outlined in the following subsections. All PLE sequences start with a 515 nm repump pulse, that prepares the NV center with high probability in its negatively charged state and predominantly in its $m_s = 0$ spin ground state. This pulse consists of a 50 µs long and 60 µW strong 515 nm repump laser pulse followed by a 5 µs wait time.

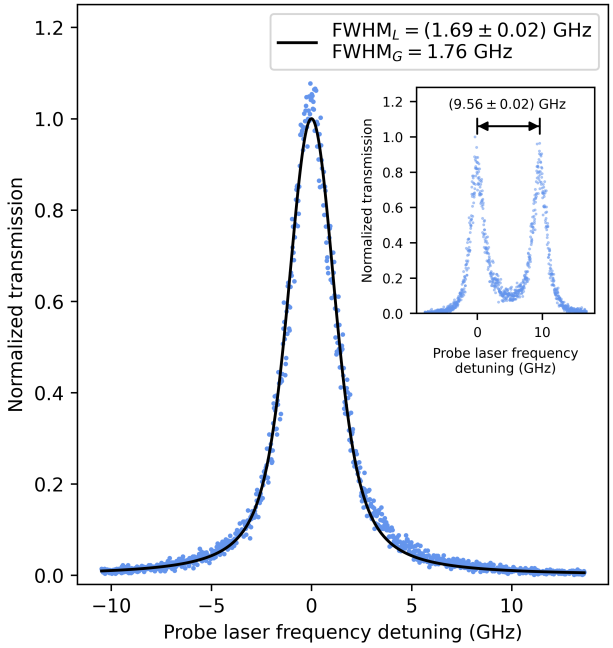

Figure 7.6: Resonant laser frequency scan over the cavity resonance to determine the cavity linewidth. The polarization of the laser is aligned to the LF cavity mode. The cavity transmission is measured on the ZPL single-photon detector. A Voigt function with a fixed Gaussian FWHM$_G$ contribution, set by the vibration level, is used to fit the data (see text). The fit yields the cavity linewidth FWHM$_L$ as the Lorentzian contribution. The inset shows a laser frequency scan, where a laser polarization is used that illuminates both cavity modes. This measurement reveals a frequency splitting between the LF and HF cavity mode of (9.56 ± 0.02) GHz.

7

PLE Sequence of the NV Center E_y Transition

In the PLE measurement of the NV center E_y transition, shown in Fig. 7.2(a), the following PLE sequence is applied 200×10^3 times per excitation laser frequency. The sequence starts with the above-described repump pulse followed by a 100 µs long 0.2 nW spin initialization laser pulse on the E_1 transition to initialize the NV center in the $m_s = 0$ spin ground state. Then a free-space 1 nW excitation laser pulse is applied for 200 µs, while simultaneously measuring the ZPL signal of the NV center in the cross-polarized detection. The ZPL counts are acquired time-resolved, which results in an exponential decaying signal as can be seen exemplarily in Fig. 7.11(a) after averaging the repetitions for each excitation laser frequency. For the used excitation laser power of 1 nW, the decay is described well by a monoexponential fit on top of a constant offset level, which is determined by excitation laser leakage into the cross-polarized detection. Thus, the monoexponential fit amplitudes resemble a background-corrected measure of the ZPL counts, which are plotted in Fig. 7.2(a). In this measurement, the NV center is excited via the HF cavity mode, and fluorescence is detected in the LF cavity mode. In addition, the LF mode is kept on resonance with the excitation laser frequency by the cavity lock.

PLE Sequence of the NV Center E_1 and E_2 Transition

In the PLE measurement of the NV center E_1 and E_2 transition, shown in Fig. 7.7(a), the following PLE sequence is applied 100×10^3 times per excitation laser frequency. The sequence starts with the above-described repump pulse followed by 300 short excitation pulses on the NV center E_y transition to prepare the NV center in the $m_s = \pm 1$ spin ground states (see Fig. 7.12(a)). Then a 0.01 nW excitation laser pulse is applied for 100 µs via the cavity fiber, followed by 30 short excitation pulses to read out the NV center $m_s = 0$ spin state (as used in the main text). If the excitation laser is resonant with a transition associated with the $m_s = \pm 1$ spin states, some population is optically pumped back into the $m_s = 0$ spin ground state, and the ZPL signal is detected by the readout as shown in Fig. 7.7(a). This technique is used since the direct ZPL signal acquisition of the weaker coupled NV transitions in cross-polarized resonant excitation and detection is inefficient. In this measurement, the LF cavity mode is used for readout and kept on resonance with the NV center E_y transition by the cavity lock.

In the acquired PLE measurement shown in Fig. 7.7(a), two additional peaks with a splitting of about 200 MHz that overlap with the E_1 transition are observed. We attribute these peaks to the transitions between the Zeeman-split $m_s = \pm 1$ ground states and the excited E_y state. This observation reveals a finite strength of these transitions for the investigated NV center.

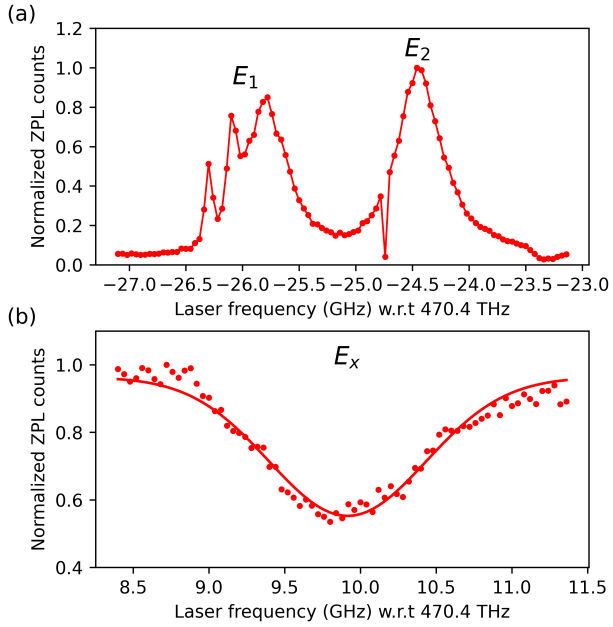

Figure 7.7: Further PLE measurements of the NV center used in the main text. (a) NV center E_1 and E_2 transition. For the laser frequency of −24.74 GHz, we suspect that our spin initialization laser did not switch on, resulting in ZPL counts on the background level. (b) NV center E_x transition with a Gaussian fit as a guide for the eye.

PLE Sequence of the NV Center E_x Transition

In the PLE measurement of the NV center E_x transition, shown in Fig. 7.7(b), the following PLE sequence is applied 100×10^3 times per excitation laser frequency. The sequence starts with the above-described repump pulse. Then a 200 µs long 50 nW excitation laser pulse is applied via the cavity fiber, followed by 30 short excitation pulses to read out the NV center $m_s = 0$ spin state. If the excitation laser is resonant with a transition associated with the $m_s = 0$ spin state, some population is optically pumped into the $m_s = \pm 1$ spin ground states, and a reduction of ZPL signal is detected by the readout as shown in Fig. 7.7(b). This technique is used since the direct ZPL acquisition of the weaker coupled NV transitions in cross-polarized resonant excitation and detection is inefficient. In this measurement, the LF cavity mode is used for readout and kept on resonance with the NV center E_y transition by the cavity lock.

7.8.4 Pulsed Resonant Excitation

Figure 7.8(a) shows the temporal shape of the short excitation pulse used throughout the study.

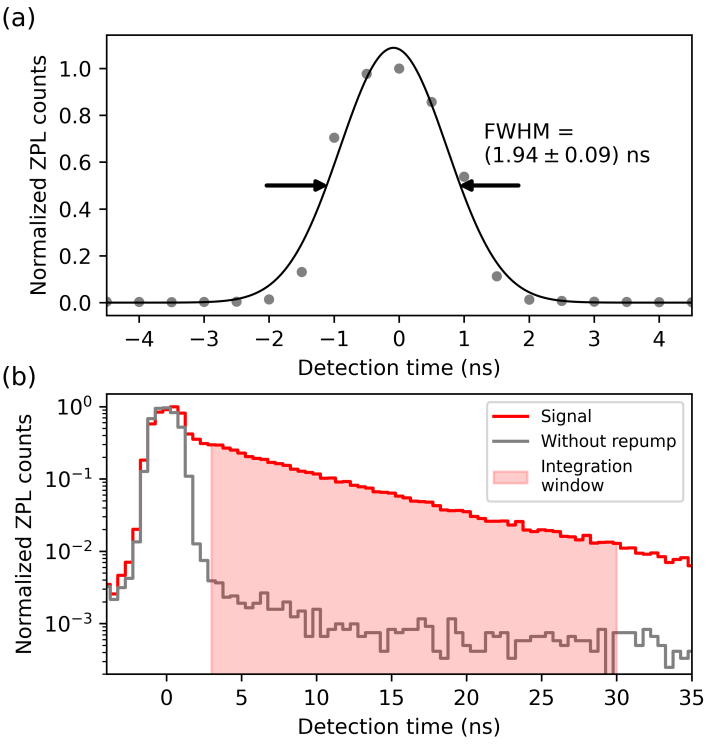

Figure 7.8: (a) Temporal shape of the short excitation pulse used in this study. (b) Short excitation pulse next to a time-resolved NV center readout signal. For the short excitation pulse measurement, the NV center is 'switched off' by not applying the charge repump pulse at the start of the measurement sequence.

A FWHM value of (1.94 ± 0.09) ns is determined by a Gaussian fit. In addition, Fig. 7.8(b) shows the same short excitation pulse next to a time-resolved pulsed readout measurement of the NV center E_y transition. The short excitation pulse is declined before the integration window, from 3 ns to 30 ns with respect to the excitation pulse center, starts. The integration window includes about 75 % of the studied Purcell-enhanced NV center emission, assuming the NV center population inversion is completed 1 ns after the excitation pulse center.

7.8.5 NV Center Excited State Lifetime Measurements

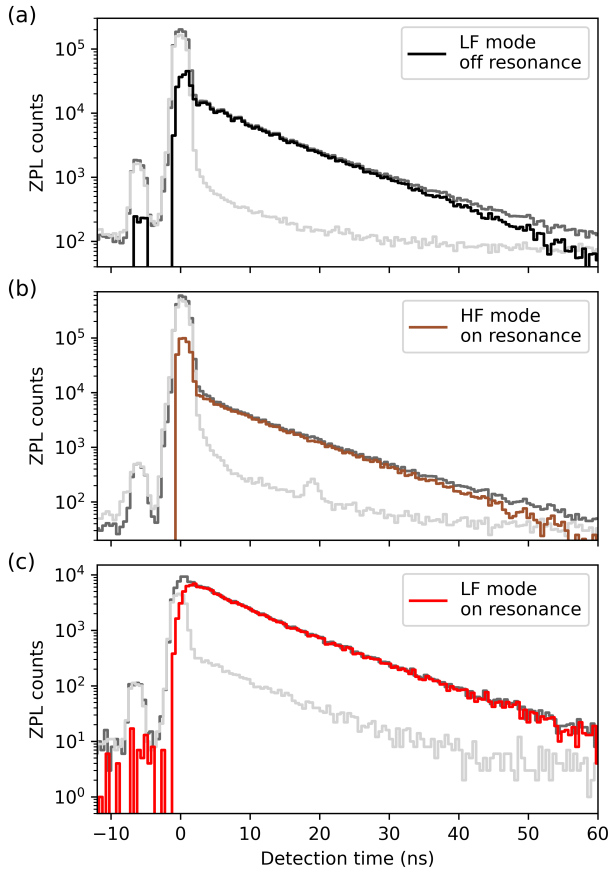

Figure 7.9: Background correction of the NV center E_y excited state lifetime measurement. Data in dark (light) gray shows the ZPL signal of the first (last) 5 short excitation pulses of the in total applied 100 pulses. The small peak at a detection time of about −5 ns is light of the excitation pulse that is backscattered into the free-space detection before reaching the cryostat. (a) Background correction of the lifetime measurement in the LF mode with a cavity detuning of −4 GHz from the E_y transition. (b) Background correction of the lifetime measurement in the HF mode and the cavity on resonance with the E_y transition. (c) Background correction of the lifetime measurement in the LF mode and the cavity on resonance with the E_y transition.

The NV center excited state lifetime measurement sequences used in Fig. 7.2(c) start with a 515 nm repump pulse, that prepares the NV center with high probability in its negatively charged state. This pulse consist of a 50 µs long and 60 µW strong 515 nm repump laser pulse followed by a 5 µs wait time. Subsequently, a 0.2 nW spin initialization laser pulse is applied for 100 µs (20 µs) on the E_1 transition to initialize the NV center in the LF (HF) cavity mode in its $m_s = 0$ spin ground state. Then 100 short excitation pulses are used in the sequence to excite the NV center, followed by time-resolved detection of the ZPL signal. To correct for background, we make use of the pumping into the NV center $m_s = \pm 1$ spin ground states with more applied short excitation pulses (see Fig. 7.12(a)). This allows to take the high signal-to-noise part of the first 5 short excitation pulses and subtract the last 5, which corrects for constant background contributions. The data underlying the background subtraction is shown in Fig. 7.9 and leads to the lifetime measurement data used in the main text Fig. 7.2(c).
Despite the background subtraction, we see that the data deviates from a monoexponential behavior with increasing detection time, which is also observed in the extracted lifetimes for different fit windows shown in Fig. 7.10. This hints towards a time-dependent background contribution of fluorescence that might stem from other weaker coupled NV centers in the diamond membrane or the cavity mirror materials.

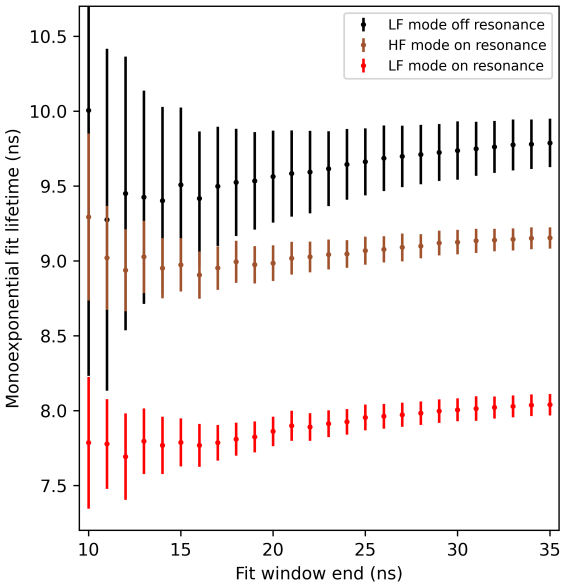

Figure 7.10: Extracted excited state lifetime from a monoexponential fit on the lifetime measurement data of main text Fig. 7.2(c). The fit window start is set to 5 ns while the fit window end is varied.

Furthermore, an off resonance lifetime of $\tau_{\text{off}} = (9.5 \pm 0.4)$ ns is measured for the NV center E_y excited state in the main text, which deviates from the expected about 12.4 ns lifetime in bulk samples [35]. This reveals a larger excited state decay rate of the studied NV center, which we attribute to strain-induced mixing in the excited states [47, 48]. In Fig. 7.11(b),

we conduct a continuous wave saturation measurement of the NV center E_y transition using 32 µs long resonant pulses and detect the ZPL signal time-resolved as shown in Fig. 7.11(a). The ZPL signal fits well to a double exponential fit with a constant offset accounting for excitation laser leakage into the cross-polarized detection. The summed amplitudes resemble a measure for the saturating ZPL counts, while the exponential time constants give insights into the decay dynamics of the studied NV center. We attribute the fast decay time constant to additional decay from the excited state, next to the decay into the $m_s = 0$ spin ground state. Assuming that saturating the NV center with high excitation power leads to an average excited state population of 50 %, half of the fitted fast decay time constant 110 ns/2 (see Fig. 7.11(b)) determines the additional decay rate. With that additional decay, the predicted lifetime of the excited state is about 10 ns, which matches with the value of the off resonance lifetime measurement.

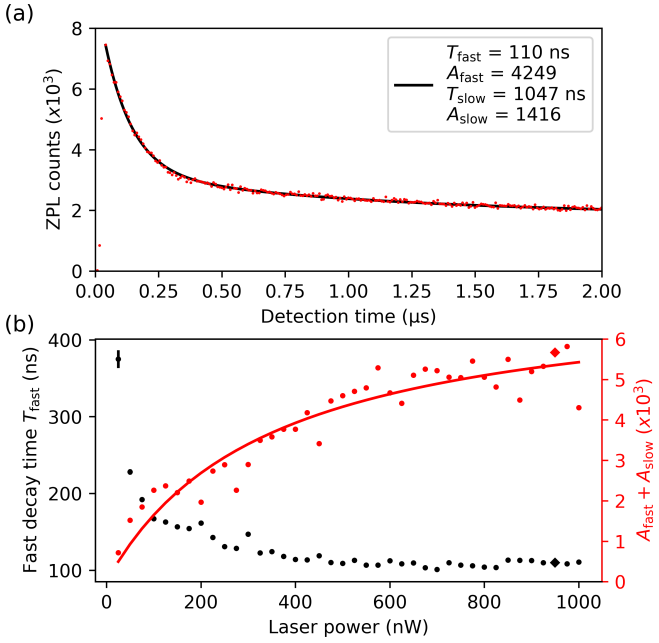

Figure 7.11: (a) Exemplary time-resolved ZPL signal of the NV center E_y transition saturation measurement. In this measurement, a resonant laser power of 950 nW is used, and the black solid line is a double exponential fit with offset to the data. The fast decay for short detection times is described with the time constant T_{fast} while the slow decay is captured by T_{slow}. (b) NV center E_y transition saturation measurement with extracted fit parameters. The total fit amplitude $A_{fast} + A_{slow}$ resembles the saturating ZPL counts, and T_{fast} is the fast exponential decay time constant. The total fit amplitudes that depend on the laser power P are fitted to a function proportional to $P/(P + 2P_{sat})$ as a guide for the eye. The individual measurement shown in (a) is indicated by the diamond-shaped data point.

7.8.6 NV Center Second-order Correlation Measurement

The second-order correlation measurement of the E_y transition (readout transition) in Fig. 7.2(d) is fitted by the following function

$$g^{(2)}(n) = A\left|1 - \frac{|n|}{N}\right|\exp\left(-\frac{|n|}{B}\right) \quad \forall \quad 0 < |n| < N, \tag{7.2}$$

with the amplitude A, the spin flipping constant B and the number of consecutive short resonant excitation pulses N. In our experiments, the parameter B takes the spin flipping process into the $m_s = \pm 1$ states into account, where $1 - \exp\{(-1/B)\}$ is the probability per excitation pulse to spin flip. The consequence of a spin flip is that the NV center stops emitting photons with excitation pulses addressing the readout transition.

7.8.7 NV Center Spin Initialization and Readout

All measurement sequences used in Fig. 7.3 and Fig. 7.4 start with a 515 nm repump pulse, which prepares the NV center with high probability in its negatively charged state. This pulse consist of a 50 µs long and 60 µW strong 515 nm repump laser pulse followed by a 5 µs wait time. Subsequently, and if not stated otherwise, a 100 µs long 0.2 nW spin initialization laser pulse on the E_1 transition is applied to initialize the NV center in its $m_s = 0$ spin ground state. Then the actual measurement sequence, composed of microwave (and individual short resonant excitation) pulses, is played, followed by a series of short excitation pulses to read out the NV center qubit state. If at least one photon is detected during the readout, the $m_s = 0$ qubit state is measured; otherwise, the $m_s = -1$ qubit state is assigned. Since these outcomes are subject to measurement errors like photon loss as well as dark or background photon detection events, a readout correction is used to recover the measurement statistics. For this purpose, the initialization fidelity in the $m_s = 0$, as well as $m_s = \pm 1$ spin state and their corresponding readout fidelities, are determined, and the correction formalism as outlined in Ref. [62] is used.

The initialization in the $m_s = \pm 1$ spin states is performed using the short excitation pulses that are resonant with the NV center readout transition. The detected ZPL counts in the integration window of 3 ns to 30 ns after each short excitation pulse are shown in Fig. 7.12(a). The ZPL counts, depending on the pulse number, follow a double exponential behavior similar to the second-order correlation measurement in Fig. 7.2(d). The measurement shows that after about 200 short excitation pulses, a constant ZPL count level is reached. Comparing the total ZPL count amplitude with the offset determined by fitting an initialization fidelity of $(98.15 \pm 0.04)\,\%$ is determined.

The initialization in the $m_s = 0$ spin state is performed by optical pumping on the NV center E_1 transition. To investigate the spin initialization behavior, the NV center is first prepared in the $m_s = \pm 1$ spin states by 600 short excitation pulses, and then a 0.2 nW spin initialization laser pulse is applied for different durations, followed by 5 short excitation pulses for readout. The measured readout ZPL counts depending on the spin initialization pulse duration are shown in Fig. 7.12(b). For longer spin initialization pulse durations, the detected ZPL counts increase until they settle exponentially. From a double exponential fit, a slow decay time constant of $(9.1 \pm 0.7)\,\mu s$ is determined. This indirect spin initialization measurement via the NV center readout transition gives insights about the required spin initialization pulse durations for the used laser power, but does not allow us to deter-

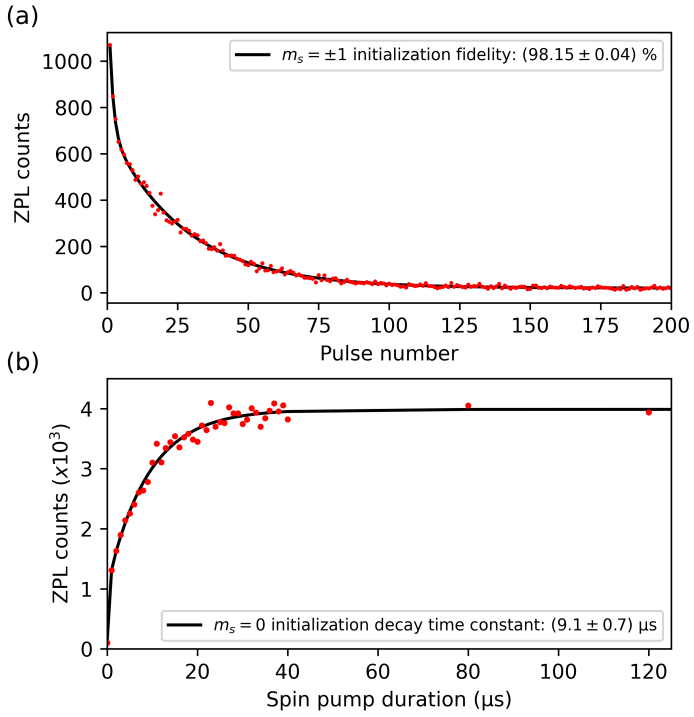

Figure 7.12: (a) Spin initialization measurement in the $m_s = \pm 1$ spin states by optical pumping with short excitation pulses on the NV center E_y transition. Before the short excitation pulses are applied, a 0.2 nW spin initialization pulse is applied for 120 µs on the E_1 transition. (b) Indirect spin initialization measurement in the $m_s = 0$ spin state by optical pumping on the NV center E_1 transition and readout by 5 short excitation pulses. In this measurement, a spin initialization pulse power of 0.2 nW is used, while the spin initialization pulse duration is varied.

mine an initialization fidelity in the $m_s = 0$ spin state.
To estimate the $m_s = 0$ initialization fidelity, the NV center $m_s = 0$ spin state is first heralded by measuring a photon after a single short excitation pulse and then read out with 200 short excitation pulses. This results in the maximal readout probability, since the $m_s = 0$ spin state is heralded just before the readout. After this first readout, further short excitation pulses are used to initialize the NV center in the $m_s = \pm 1$ states followed by a 0.2 nW spin initialization laser pulse on the E_1 transition for 100 µs and another readout with 200 short excitation pulses. This results in a second readout probability, which is set by the optical pumping performance of the initialization laser pulse. Comparing the second to the first readout yields an initialization fidelity in the $m_s = 0$ spin state of $(93.5 \pm 0.9)\,\%$. To exclude NV center ionization, a third iteration is performed, leading to the same result as the second readout.
Moreover, this experiment reveals the combined probability that the initial repump and spin initialization pulse prepares the NV center in its negatively charged and $m_s = 0$ state by comparing the probability of the first readout with and without the described herald-

ing. From this, a probability of $(72.8 \pm 0.6)\,\%$ is found, which is considered in the readout of the heralded measurements in Fig. 7.4. Further, we note that an initialization laser pulse duration of 20 µs instead of 100 µs is used in the GHZ state measurement of Fig. 7.4(c).

7.8.8 NV Center Ramsey Measurement

The Ramsey fringes measured in Fig. 7.3(c) are determined by the hyperfine coupling of the nitrogen-14 nuclear spin ω_{hf}, the free-induction decay time T_2^*, and the used artificial detuning Δ. The artificial detuning is implemented by applying a phase of $\tau\Delta$ to the second $\pi/2$ pulse in the Ramsey sequence. The data is well fitted by the following function

$$P_{m_s=0}(\tau) = c - \exp\left(-\left(\frac{\tau}{T_2^*}\right)^n\right) \cdot \sum_{k=-1,0,+1} P_k \cos\left((\Delta + k\omega_{\mathrm{hf}})\tau + \phi\right), \tag{7.3}$$

with the offset c, the decay exponent n, the nitrogen nuclear spin amplitudes P_k and a common phase ϕ. The amplitudes P_k take partial polarization of the nitrogen nuclear spin into account, and the common phase ϕ accounts for a phase offset between the two applied $\pi/2$ pulses.

7.8.9 Bell State Spin-photon Correlations with Spin Qubit Readout in X-Basis

In addition to the Bell state spin-photon correlation measurement of Fig. 7.4(b), where the spin qubit is read out in its Z-basis, we perform an X-basis spin qubit readout in Fig. 7.13(b). The used pulse sequence is depicted in Fig. 7.13(a), which exhibits another $\pi/2$ pulse after the Bell state generation to perform the qubit readout in the X-basis. As in the main text, 200 short excitation pulses are used for readout.

In the X-basis measurement, the spin is measured with equal probability in one of the qubit states. In total we record 24456 photon heralding events in 5×10^6 attempts, which corresponds to a probability of 0.49 % per attempt.

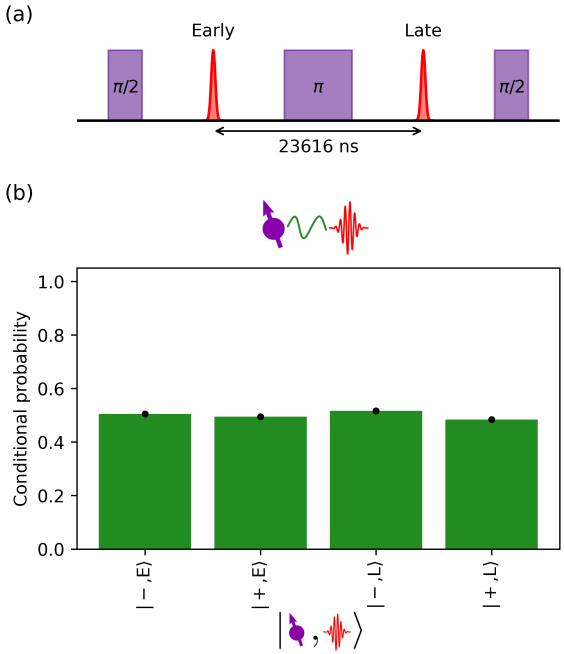

Figure 7.13: (a) Pulse sequence to generate a spin-photon Bell state and a spin qubit readout in the X-basis. In the experiment, a microwave decoupling interpulse delay time of $\tau/2$ = 23568 ns is used. (b) Conditional probabilities of the spin qubit readout in the X-basis after successful heralding an early ($|E\rangle$) or late ($|L\rangle$) photon of the spin-photon Bell state. The error bars are within the black dot size.

7.8.10 Additional Data of a Second Cavity-coupled NV Center

At a different lateral position on the diamond membrane, a second NV center coupled to the cavity is investigated. For this cavity position a frequency splitting of the two polarization cavity modes of about 10.7 GHz is observed and a NV center coupled with its E_y transition at a frequency of about 36.8 GHz (with respect to 470.4 THz) is found. The frequency splitting of the polarization cavity modes ~ 10 GHz is observed for all cavity spots in the investigated range of ~ 100 µm along the gold stripline. The E_x transition of the NV center is identified with a frequency of about 48.8 GHz, resulting in a lower lateral strain with E_x - E_y excited state splitting of ~ 12 GHz compared to the NV center studied in the main text. The corresponding PLE measurements are shown in Fig. 7.14. The absolute transition frequencies as well as the lateral strain level are comparable to NV centers in solid immersion lens devices, which have also been used to demonstrate high-fidelity readout [49]. This shows that low-strained NV centers, similar to solid immersion lens devices, are found in the diamond membrane.

In addition, the spin coherence of this NV center is measured in a Ramsey experiment as shown in Fig. 7.15(b). Compared to the Ramsey experiment shown in Fig. 7.3(c) of the main text, only the m_I = 0 spin resonance of the coupled nitrogen nuclear spin is driven. This transition is identified beforehand in an electron spin resonance measurement as shown

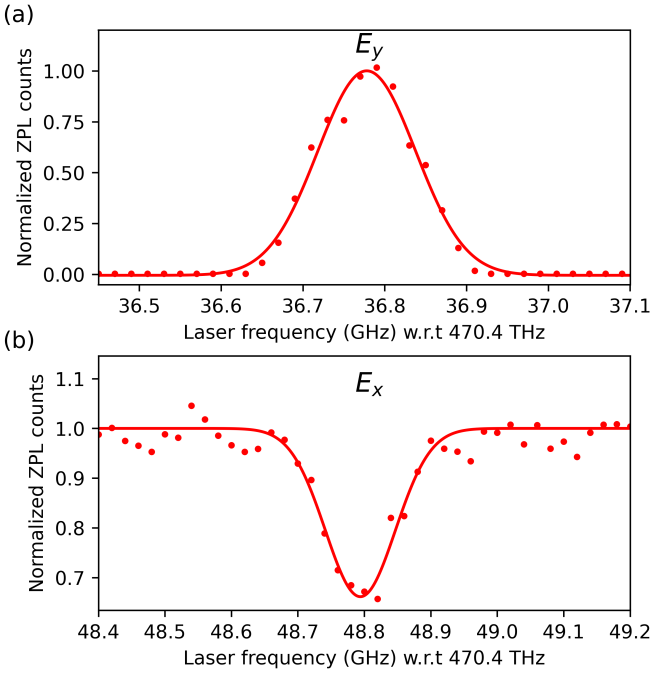

Figure 7.14: PLE measurements of a second cavity-coupled NV center at a different lateral position on the diamond membrane. (a) NV center E_y transition. (b) NV center E_x transition. For both measurements, 200 short readout pulses are used.

in Fig. 7.15(a). The resulting Ramsey fringes are well fitted by the function

$$P_{m_s=0}(\tau) = c - A \exp\left(-\left(\frac{\tau}{T_2^*}\right)^n\right) \cdot \sum_{k=-1,+1} \cos\left((\Delta + k\omega_c/2)\tau + \phi\right), \tag{7.4}$$

with the amplitude A and the carbon-13 nuclear spin coupling frequency ω_c. Fitting the Ramsey experiment yields a free-induction decay time of $T_2^* = (3.7 \pm 0.4)\,\mu s$ with a decay exponent of $n = 1.1 \pm 0.3$ and a beating with a frequency of $(218 \pm 4)\,kHz$, which we attribute to the coupling of a carbon-13 nuclear spin. To summarize, NV centers with electron spin coherence times similar to diamond bulk samples can be observed [6].

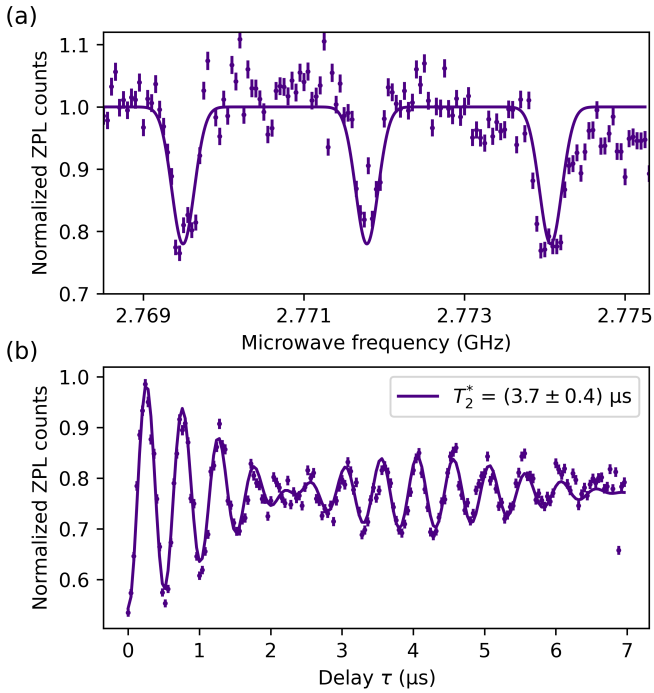

Figure 7.15: (a) Electron spin resonance measurement. The NV center is initialized in its $m_s = 0$ state, then a microwave pulse of 10 µs is applied, and finally the NV center $m_s = 0$ state is read out with 50 short excitation pulses. The microwave frequency is swept over the $m_s = -1$ electron spin state, and for each nitrogen nuclear spin resonance ($m_I = -1, 0, +1$), a decrease in ZPL counts is observed. The fit with three Gaussian dips is a guide for the eye. (b) Ramsey experiment at the $m_I = 0$ nitrogen nuclear spin resonance frequency with an artificial detuning of 2 MHz. In this measurement, a microwave $\pi/2$ pulse duration of 350 ns is used.

7.8.11 Summary of System Parameters

Next to the parameters of the emitter-cavity system, the efficiency of the free-space cross-polarization setup determines the total efficiency of the short excitation pulse excitation and detection scheme. The photon collection efficiency into the ZPL single-mode fiber comprising all the optics after the microcavity amounts to about 39 %, and the used single-photon detectors are specified with 70 %. Including the integration time window used for short excitation pulse readout with a collected fraction of about 75 %, the total ZPL setup efficiency is estimated to be about 20 %. Considering the ZPL emission into the LF mode of about 18 % together with the cavity outcoupling efficiency of 39 %, a detector click probability of about 1.4 % per pulse is estimated upon NV center excitation as stated in the main text.
An overview of measured, estimated, and simulated values of this work is summarized in Table 7.1.

Table 7.1: Overview of system parameters.

Parameter	Value
Fiber mirror radius of curvature	21.4 µm
Cavity air gap	6.39 µm
Diamond thickness	6.20 µm
Hybrid cavity mode number q	67
Effective cavity length L_{eff} [61]	13.2 µm
Estimated cavity beam waist ω_0 [61]	1.46 µm
Estimated cavity mode volume V [61]	86 λ^3
Cavity Lorentzian linewidth $\kappa/2\pi$	(1.69 ± 0.02) GHz
Root mean square cavity length fluctuations	22 pm
Cavity mode dispersion slope	34 MHz/pm
Cavity quality factor Q	280×10^3
Cavity finesse $\mathscr{F}$	2800
Cavity outcoupling efficiency	39 %
Calculated cavity transmission	8 %
Calculated vibration-averaged Purcell factor [46]	12
NV center Debye-Waller factor β_0	0.03 [29]
Measured Purcell factor LF mode $F_{P,\text{LF}}$	7.3 ± 1.6
Measured Purcell factor HF mode $F_{P,\text{HF}}$	2.0 ± 1.4
Measured cooperativity LF mode $\beta_0 F_{P,\text{LF}}$	0.22 ± 0.05
Measured cooperativity HF mode $\beta_0 F_{P,\text{HF}}$	0.06 ± 0.04
ZPL emission into LF mode β_{LF}	18 %
Cavity outcoupled ZPL emission LF mode	7 %
ZPL detector click probability per pulse LF mode (end-to-end efficiency at saturation)	1.4 %

References

[1] J. Fischer, Y. Herrmann, C. F. J. Wolfs, S. Scheijen, M. Ruf, and R. Hanson, *Spin-Photon Correlations from a Purcell-enhanced Diamond Nitrogen-Vacancy Center Coupled to an Open Microcavity,* arXiv:2506.20722 (2025).

[2] H. J. Kimble, *The quantum internet,* Nature **453**, 1023 (2008).

[3] S. Wehner, D. Elkouss, and R. Hanson, *Quantum internet: A vision for the road ahead,* Science **362** (2018).

[4] M. Ruf, N. H. Wan, H. Choi, D. Englund, and R. Hanson, *Quantum networks based on color centers in diamond,* J. Appl. Phys. **130**, 070901 (2021).

[5] E. Janitz, M. K. Bhaskar, and L. Childress, *Cavity quantum electrodynamics with color centers in diamond,* Optica **7**, 1232 (2020).

[6] H. Bernien, B. Hensen, W. Pfaff, G. Koolstra, M. S. Blok, L. Robledo, T. H. Taminiau, M. Markham, D. J. Twitchen, L. Childress, and R. Hanson, *Heralded entanglement between solid-state qubits separated by three metres,* Nature **497**, 86 (2013).

[7] C. M. Knaut, A. Suleymanzade, Y.-C. Wei, D. R. Assumpcao, P.-J. Stas, Y. Q. Huan, B. Machielse, E. N. Knall, M. Sutula, G. Baranes, N. Sinclair, C. De-Eknamkul, D. S. Levonian, M. K. Bhaskar, H. Park, M. Lončar, and M. D. Lukin, *Entanglement of nanophotonic quantum memory nodes in a telecom network,* Nature **629**, 573 (2024).

[8] A. Ruskuc, C.-J. Wu, E. Green, S. L. N. Hermans, W. Pajak, J. Choi, and A. Faraon, *Multiplexed entanglement of multi-emitter quantum network nodes,* Nature **639**, 54 (2025).

[9] F. Afzal, S. J. Beale, O. Bedroya, K. Bell, L. Bergeron, K. Bonsma-Fisher, P. Bychkova, Z. M. E. Chaisson, C. Chartrand, C. Clear, A. Darcie, A. DeAbreu, C. DeLisle, L. A. Duncan, C. D. Smith, J. Dunn, A. Ebrahimi, N. Evetts, D. F. Pinheiro, P. Fuentes, T. Georgiou, B. Guha, R. Haenel, D. Higginbottom, D. M. Jackson, N. Jahed, A. Khorshidahmad, P. K. Shandilya, A. T. K. Kurkjian, N. Lauk, N. R. Lee-Hone, E. Lin, R. Litynskyy, D. Lock, L. Ma, I. MacGilp, E. R. MacQuarrie, A. Mar, A. M. Khah, A. Matiash, E. Meyer-Scott, C. P. Michaels, J. Motira, N. K. Noori, E. Ospadov, E. Patel, A. Patscheider, D. Paulson, A. Petruk, A. L. Ravindranath, B. Reznychenko, M. Ruether, J. Ruscica, K. Saxena, Z. Schaller, A. Seidlitz, J. Senger, Y. S. Lee, O. Sevoyan, S. Simmons, O. Soykal, L. Stott, Q. Tran, S. Tserkis, A. Ulhaq, W. Vine, R. Weeks, G. Wolfowicz, and I. Yoneda, *Distributed Quantum Computing in Silicon,* arXiv:2406.01704 (2024).

[10] S. L. N. Hermans, M. Pompili, H. K. C. Beukers, S. Baier, J. Borregaard, and R. Hanson, *Qubit teleportation between non-neighbouring nodes in a quantum network,* Nature **605**, 663 (2022).

[11] M. Pompili, S. L. N. Hermans, S. Baier, H. K. C. Beukers, P. C. Humphreys, R. N. Schouten, R. F. L. Vermeulen, M. J. Tiggelman, L. dos Santos Martins, B. Dirkse, S. Wehner, and R. Hanson, *Realization of a multinode quantum network of remote solid-state qubits,* Science **372**, 259 (2021).

[12] A. J. Stolk, K. L. Van Der Enden, M.-C. Slater, I. Te Raa-Derckx, P. Botma, J. Van Rantwijk, J. J. B. Biemond, R. A. J. Hagen, R. W. Herfst, W. D. Koek, A. J. H. Meskers, R. Vollmer, E. J. Van Zwet, M. Markham, A. M. Edmonds, J. F. Geus, F. Elsen, B. Jungbluth, C. Haefner, C. Tresp, J. Stuhler, S. Ritter, and R. Hanson, *Metropolitan-scale heralded entanglement of solid-state qubits,* Sci. Adv. **10**, eadp6442 (2024).

[13] A. Tchebotareva, S. L. N. Hermans, P. C. Humphreys, D. Voigt, P. J. Harmsma, L. K. Cheng, A. L. Verlaan, N. Dijkhuizen, W. de Jong, A. Dréau, and R. Hanson, *Entanglement between a Diamond Spin Qubit and a Photonic Time-Bin Qubit at Telecom Wavelength,* Phys. Rev. Lett. **123**, 063601 (2019).

[14] J. F. Geus, F. Elsen, S. Nyga, A. J. Stolk, K. L. Van Der Enden, E. J. Van Zwet, C. Haefner, R. Hanson, and B. Jungbluth, *Low-noise short-wavelength pumped frequency downconversion for quantum frequency converters,* Opt. Quantum **2**, 189 (2024).

[15] J. Javadzade, M. Zahedian, F. Kaiser, V. Vorobyov, and J. Wrachtrup, *Efficient nuclear spin–photon entanglement with optical routing,* Phys. Rev. Applied **24**, 024059 (2025).

[16] X.-Y. Chang, P.-Y. Hou, W.-G. Zhang, X.-Q. Meng, Y.-F. Yu, Y.-N. Lu, Y.-Q. Liu, B.-X. Qi, D.-L. Deng, and L.-M. Duan, *Hybrid entanglement and bit-flip error correction in a scalable quantum network node,* Nat. Phys. **21**, 583 (2025).

[17] M. H. Abobeih, J. Cramer, M. A. Bakker, N. Kalb, M. Markham, D. J. Twitchen, and T. H. Taminiau, *One-second coherence for a single electron spin coupled to a multi-qubit nuclear-spin environment,* Nat. Commun. **9**, 2552 (2018).

[18] T. Van Der Sar, Z. H. Wang, M. S. Blok, H. Bernien, T. H. Taminiau, D. M. Toyli, D. A. Lidar, D. D. Awschalom, R. Hanson, and V. V. Dobrovitski, *Decoherence-protected quantum gates for a hybrid solid-state spin register,* Nature **484**, 82 (2012).

[19] L. Childress, M. V. Gurudev Dutt, J. M. Taylor, A. S. Zibrov, F. Jelezko, J. Wrachtrup, P. R. Hemmer, and M. D. Lukin, *Coherent Dynamics of Coupled Electron and Nuclear Spin Qubits in Diamond,* Science **314**, 281 (2006).

[20] C. E. Bradley, J. Randall, M. H. Abobeih, R. C. Berrevoets, M. J. Degen, M. A. Bakker, M. Markham, D. J. Twitchen, and T. H. Taminiau, *A Ten-Qubit Solid-State Spin Register with Quantum Memory up to One Minute,* Phys. Rev. X **9**, 031045 (2019).

[21] G. L. Van De Stolpe, D. P. Kwiatkowski, C. E. Bradley, J. Randall, M. H. Abobeih, S. A. Breitweiser, L. C. Bassett, M. Markham, D. J. Twitchen, and T. H. Taminiau, *Mapping a 50-spin-qubit network through correlated sensing,* Nat. Commun. **15**, 2006 (2024).

[22] A. Reiserer, N. Kalb, M. S. Blok, K. J. M. Van Bemmelen, T. H. Taminiau, R. Hanson, D. J. Twitchen, and M. Markham, *Robust Quantum-Network Memory Using Decoherence-Protected Subspaces of Nuclear Spins,* Phys. Rev. X **6**, 021040 (2016).

[23] C. E. Bradley, S. W. De Bone, P. F. W. Möller, S. Baier, M. J. Degen, S. J. H. Loenen, H. P. Bartling, M. Markham, D. J. Twitchen, R. Hanson, D. Elkouss, and T. H. Taminiau, *Robust quantum-network memory based on spin qubits in isotopically engineered diamond,* npj Quantum Inf. **8**, 122 (2022).

[24] H. P. Bartling, M. H. Abobeih, B. Pingault, M. J. Degen, S. J. H. Loenen, C. E. Bradley, J. Randall, M. Markham, D. J. Twitchen, and T. H. Taminiau, *Entanglement of Spin-Pair Qubits with Intrinsic Dephasing Times Exceeding a Minute,* Phys. Rev. X **12**, 011048 (2022).

[25] T. H. Taminiau, J. Cramer, T. van der Sar, V. V. Dobrovitski, and R. Hanson, *Universal control and error correction in multi-qubit spin registers in diamond,* Nat. Nanotechnol. **9**, 171 (2014).

[26] N. Kalb, A. A. Reiserer, P. C. Humphreys, J. J. W. Bakermans, S. J. Kamerling, N. H. Nickerson, S. C. Benjamin, D. J. Twitchen, M. Markham, and R. Hanson, *Entanglement distillation between solid-state quantum network nodes,* Science **356**, 928 (2017).

[27] M. H. Abobeih, Y. Wang, J. Randall, S. J. H. Loenen, C. E. Bradley, M. Markham, D. J. Twitchen, B. M. Terhal, and T. H. Taminiau, *Fault-tolerant operation of a logical qubit in a diamond quantum processor,* Nature **606**, 884 (2022).

[28] H. Bartling, J. Yun, K. Schymik, M. Van Riggelen, L. Enthoven, H. Van Ommen, M. Babaie, F. Sebastiano, M. Markham, D. Twitchen, and T. Taminiau, *Universal high-fidelity quantum gates for spin qubits in diamond,* Phys. Rev. Applied **23**, 034052 (2025).

[29] D. Riedel, I. Söllner, B. J. Shields, S. Starosielec, P. Appel, E. Neu, P. Maletinsky, and R. J. Warburton, *Deterministic Enhancement of Coherent Photon Generation from a Nitrogen-Vacancy Center in Ultrapure Diamond,* Phys. Rev. X **7**, 031040 (2017).

[30] A. Faraon, C. Santori, Z. Huang, V. M. Acosta, and R. G. Beausoleil, *Coupling of Nitrogen-Vacancy Centers to Photonic Crystal Cavities in Monocrystalline Diamond,* Phys. Rev. Lett. **109**, 033604 (2012).

[31] T. Ishikawa, K.-M. C. Fu, C. Santori, V. M. Acosta, R. G. Beausoleil, H. Watanabe, S. Shikata, and K. M. Itoh, *Optical and Spin Coherence Properties of Nitrogen-Vacancy Centers Placed in a 100 nm Thick Isotopically Purified Diamond Layer,* Nano Lett. **12**, 2083 (2012).

[32] I. Lekavicius, T. Oo, and H. Wang, *Diamond Lamb wave spin-mechanical resonators with optically coherent nitrogen vacancy centers,* J. Appl. Phys. **126**, 214301 (2019).

[33] T. Jung, J. Görlitz, B. Kambs, C. Pauly, N. Raatz, R. Nelz, E. Neu, A. M. Edmonds, M. Markham, F. Mücklich, J. Meijer, and C. Becher, *Spin measurements of NV centers coupled to a photonic crystal cavity,* APL Photonics **4**, 120803 (2019).

[34] J. P. Hadden, J. P. Harrison, A. C. Stanley-Clarke, L. Marseglia, Y.-L. D. Ho, B. R. Patton, J. L. O'Brien, and J. G. Rarity, *Strongly enhanced photon collection from diamond defect centers under microfabricated integrated solid immersion lenses,* Appl. Phys. Lett. **97**, 241901 (2010).

[35] S. L. N. Hermans, M. Pompili, L. D. Santos Martins, A. R-P Montblanch, H. K. C. Beukers, S. Baier, J. Borregaard, and R. Hanson, *Entangling remote qubits using the*

single-photon protocol: an in-depth theoretical and experimental study, New J. Phys. **25**, 013011 (2023).

[36] B. Hensen, H. Bernien, A. E. Dréau, A. Reiserer, N. Kalb, M. S. Blok, J. Ruitenberg, R. F. L. Vermeulen, R. N. Schouten, C. Abellán, W. Amaya, V. Pruneri, M. W. Mitchell, M. Markham, D. J. Twitchen, D. Elkouss, S. Wehner, T. H. Taminiau, and R. Hanson, *Loophole-free Bell inequality violation using electron spins separated by 1.3 kilometres,* Nature **526**, 682 (2015).

[37] P. C. Humphreys, N. Kalb, J. P. J. Morits, R. N. Schouten, R. F. L. Vermeulen, D. J. Twitchen, M. Markham, and R. Hanson, *Deterministic delivery of remote entanglement on a quantum network,* Nature **558**, 268 (2018).

[38] K. J. Vahala, *Optical microcavities,* Nature **424**, 839 (2003).

[39] D. Hunger, T. Steinmetz, Y. Colombe, C. Deutsch, T. W. Hänsch, and J. Reichel, *A fiber Fabry–Perot cavity with high finesse,* New J. Phys. **12**, 065038 (2010).

[40] M. Ruf, M. IJspeert, S. van Dam, N. de Jong, H. van den Berg, G. Evers, and R. Hanson, *Optically Coherent Nitrogen-Vacancy Centers in Micrometer-Thin Etched Diamond Membranes,* Nano Lett. **19**, 3987 (2019).

[41] M. Ruf, M. Weaver, S. van Dam, and R. Hanson, *Resonant Excitation and Purcell Enhancement of Coherent Nitrogen-Vacancy Centers Coupled to a Fabry-Perot Microcavity,* Phys. Rev. Applied **15**, 024049 (2021).

[42] Y. Herrmann, J. Fischer, S. Scheijen, C. F. J. Wolfs, J. M. Brevoord, C. Sauerzapf, L. G. C. Wienhoven, L. J. Feije, M. Eschen, M. Ruf, M. J. Weaver, and R. Hanson, *A low-temperature tunable microcavity featuring high passive stability and microwave integration,* AVS Quantum Sci. **6**, 041401 (2024).

[43] V. Yurgens, Y. Fontana, A. Corazza, B. J. Shields, P. Maletinsky, and R. J. Warburton, *Cavity-assisted resonance fluorescence from a nitrogen-vacancy center in diamond,* npj Quantum Inf. **10**, 112 (2024).

[44] S. Bogdanović, M. S. Z. Liddy, S. B. van Dam, L. C. Coenen, T. Fink, M. Lončar, and R. Hanson, *Robust nano-fabrication of an integrated platform for spin control in a tunable microcavity,* APL Photonics **2**, 126101 (2017).

[45] S. Bogdanović, S. B. van Dam, C. Bonato, L. C. Coenen, A.-M. J. Zwerver, B. Hensen, M. S. Z. Liddy, T. Fink, A. Reiserer, M. Lončar, and R. Hanson, *Design and low-temperature characterization of a tunable microcavity for diamond-based quantum networks,* Appl. Phys. Lett. **110**, 171103 (2017).

[46] Y. Herrmann, J. Fischer, J. M. Brevoord, C. Sauerzapf, L. G. C. Wienhoven, L. J. Feije, M. Pasini, M. Eschen, M. Ruf, M. J. Weaver, and R. Hanson, *Coherent Coupling of a Diamond Tin-Vacancy Center to a Tunable Open Microcavity,* Phys. Rev. X **14**, 041013 (2024).

[47] N. B. Manson, J. P. Harrison, and M. J. Sellars, *Nitrogen-vacancy center in diamond: Model of the electronic structure and associated dynamics,* Phys. Rev. B **74**, 104303 (2006).

[48] M. L. Goldman, M. W. Doherty, A. Sipahigil, N. Y. Yao, S. D. Bennett, N. B. Manson, A. Kubanek, and M. D. Lukin, *State-selective intersystem crossing in nitrogen-vacancy centers,* Phys. Rev. B **91**, 165201 (2015).

[49] L. Robledo, L. Childress, H. Bernien, B. Hensen, P. F. A. Alkemade, and R. Hanson, *High-fidelity projective read-out of a solid-state spin quantum register,* Nature **477**, 574 (2011).

[50] C. A. Ryan, J. S. Hodges, and D. G. Cory, *Robust Decoupling Techniques to Extend Quantum Coherence in Diamond,* Phys. Rev. Lett. **105**, 200402 (2010).

[51] W. Pfaff, B. J. Hensen, H. Bernien, S. B. van Dam, M. S. Blok, T. H. Taminiau, M. J. Tiggelman, R. N. Schouten, M. Markham, D. J. Twitchen, and R. Hanson, *Unconditional quantum teleportation between distant solid-state quantum bits,* Science **345**, 532 (2014).

[52] J. M. Brevoord, L. De Santis, T. Yamamoto, M. Pasini, N. Codreanu, T. Turan, H. K. Beukers, C. Waas, and R. Hanson, *Heralded initialization of charge state and optical-transition frequency of diamond tin-vacancy centers,* Phys. Rev. Applied **21**, 054047 (2024).

[53] G. Bayer, R. Berghaus, S. Sachero, A. B. Filipovski, L. Antoniuk, N. Lettner, R. Waltrich, M. Klotz, P. Maier, V. Agafonov, and A. Kubanek, *Optical driving, spin initialization and readout of single SiV- centers in a Fabry-Perot resonator,* Commun. Phys. **6**, 300 (2023).

[54] R. Zifkin, C. D. Rodríguez Rosenblueth, E. Janitz, Y. Fontana, and L. Childress, *Lifetime Reduction of Single Germanium-Vacancy Centers in Diamond via a Tunable Open Microcavity,* PRX Quantum **5**, 030308 (2024).

[55] J. Hessenauer, J. Körber, M. Ghezellou, J. Ul-Hassan, G. V. Astakhov, W. Knolle, J. Wrachtrup, and D. Hunger, *Cavity enhancement of V2 centers in 4H-SiC with a fiber-based Fabry–Perot microcavity,* Opt. Quantum **3**, 175 (2025).

[56] A. Ulanowski, J. Früh, F. Salamon, A. Holzäpfel, and A. Reiserer, *Spectral Multiplexing of Rare-Earth Emitters in a Co-Doped Crystalline Membrane,* Adv. Opt. Mater. **12**, 2302897 (2024).

[57] J. Fischer, Y. Herrmann, C. F. J. Wolfs, S. Scheijen, M. Ruf, and R. Hanson, *Data underlying the publication "Spin-Photon Correlations from a Purcell-enhanced Diamond Nitrogen-Vacancy Center Coupled to an Open Microcavity",* 4TU.ResearchData, Dataset (2025).

[58] I. T. Raa, H. K. Ervasti, P. J. Botma, L. C. Visser, R. Budhrani, J. F. van Rantwijk, S. P. Cadot, J. Vermeltfoort, M. Pompili, A. J. Stolk, M. J. Weaver, K. L. van der Enden,

D. de Leeuw Duarte, M. Teng, J. van Zwieten, and F. Grooteman, *QMI - Quantum Measurement Infrastructure, a Python 3 framework for controlling laboratory equipment,* 4TU.ResearchData, Software (2023).

[59] R. F. L. Vermeulen, *Pulse generator and method for generating pulses,* Patent, IPC No. H03K, H04L, Priority date 23 Jun 2022, Priority No. WO2022/131924 (2020).

[60] E. Janitz, M. Ruf, M. Dimock, A. Bourassa, J. Sankey, and L. Childress, *Fabry-Perot microcavity for diamond-based photonics,* Phys. Rev. A **92**, 043844 (2015).

[61] S. B. van Dam, M. Ruf, and R. Hanson, *Optimal design of diamond-air microcavities for quantum networks using an analytical approach,* New J. Phys. **20**, 115004 (2018).

[62] M. Pompili, *Multi-Node Quantum Networks with Diamond Qubits*, Ph.D. thesis, Delft University of Technology (2021).

8

Conclusions and Outlook

”It is difficult to make predictions, especially about the future.”
- Niels Bohr

This chapter summarizes the experimental results of the thesis. Improvements for the microcavity diamond system are presented, which promise a resonant photon extraction efficiency of 10 % for nitrogen-vacancy (NV) centers and a coherent cooperativity of ten for tin-vacancy (SnV) centers. Furthermore, near-future experimental implementations and measurements are summarized, which are a direct follow-up on the cavity quantum optics experiments of Chapters 6 and 7. This includes the extension of the NV center measurements with an imbalanced interferometer, enabling the verification of cavity-enhanced spin-photon entanglement. Afterwards, we provide an outlook on generating microcavity-enhanced remote entanglement with NV centers in emission-based protocols and SnV centers in reflection-based protocols. Finally, we discuss the exploration of novel solid-state quantum emitters with the microcavity platform and consider the prospects of photonic integration.

8.1 Summary of Results

This thesis demonstrates the Purcell enhancement of single diamond color centers with a hybrid open microcavity and their potential as next-generation nodes for quantum networks. The thesis can be summarized and concluded as follows:

- **Chapters 4 and 6:** Laser-cutting in combination with reactive ion etching is a convenient and less expensive method to fabricate millimeter-sized diamond membranes into micrometer-sized structures. Microdevices with lateral dimensions of tens to hundreds of micrometers maintain a good surface quality, resulting in a high cavity finesse. NV and SnV centers maintain bulk-like optical properties in these devices, making them suited for quantum networking experiments and enabling the demonstration of coherent coupling with the microcavity.

- **Chapters 5, 6 and 7:** Open microcavities can be operated for months in a closed-cycle cryostat while maintaining the same experimental conditions. This includes a constant temperature below 10 K on the sample mirror, a passive stability around 25 pm, and addressing the same color center with the cavity. These conditions can be obtained reproducibly. Furthermore, experiments can be run remotely for days with an excitation laser suppression ratio of 60 dB and keeping the cavity on resonance with a specific frequency. This is also required for advanced quantum networking experiments.

- **Chapter 6:** A single SnV center is coupled to an open microcavity, and a coherent cooperativity of 0.7 is reached experimentally, allowing the observation of nonlinear quantum effects at the single-photon level. This regime has remained elusive for diamond color centers in hybrid cavities.

- **Chapter 6:** The microcavity experiments can be used to determine the combined product of quantum efficiency, Debye-Waller factor, and branching ratio for a SnV center of 0.36 . This number contributes to the efficiency of the SnV center's optical interface for quantum networking and is consistent with previous works.

- **Chapters 6 and 7:** Open microcavities are used to gain a significant improvement in the extraction of zero-phonon line (ZPL) photons from diamond color centers compared to conventional setups using confocal microscopy and non-resonant photonic structures like a solid-immersion lens (SIL). For NV centers, the extraction of ZPL photons is an order of magnitude higher than in SILs.

- **Chapter 7:** Full quantum control (qubit initialization, manipulation, and readout) of the NV center's electron spin qubit can be obtained inside the microcavity. This is enabled by mapping out optical transitions of a cavity-coupled NV center. Furthermore, the control can be utilized to generate spin-photon correlated states, which is a similar experimental sequence as used in the generation of remote entanglement. The microwave spin control via an on-chip stripline can also be used with other quantum emitters coupled to microcavities, such as diamond silicon-vacancy (SiV) centers or rare-earth ion emitters.

8.2 Improvements and Near Future Experiments

This section discusses possible improvements to the diamond samples and cavity parameters, which enable a stronger cavity enhancement. Furthermore, an overview of near-future experimental implementations is provided.

8.2.1 Fabrication of Diamond Samples

As summarized in Section 4.1, several fabrication methods can be found in the literature to obtain micrometer-thin diamond samples, with millimeter- to micrometer-sized lateral dimensions. The laser-cut microdevices presented in Chapter 4 enable Purcell factors up to 43 (see Tab. 8.1) combined with a large cavity outcoupling of about 50 % in the diamond-like modes.

To reach a higher finesse, the diamond samples can be improved with a lower surface roughness. Values around 0.2 nm have been demonstrated by employing a cyclic reactive ion etching recipe to smooth the diamond surface [1, 2]. To obtain a smooth surface on both sides of the microdevices, this method can also be adapted for the strain relief and release etch of the laser-cut fabrication (see Tab. 4.1). The release (deep) etching method [3, 4] has also been shown to produce microdevices with cavity finesse values up to 11000 in a diamond-like microcavity mode combined with an outcoupling efficiency of 67 % by Flågan et al. [5]. Furthermore, by replacing the quartz mask with a thinner silicon oxide hard mask with outward-slanted sidewalls, more homogeneously thin devices (< 0.35 nm/µm) in combination with a smooth surface (< 0.2 nm) have been demonstrated recently by Corazza et al. [6]. This allows for maintaining the same mode character (air-like or diamond-like) over larger areas, such as a full diamond microdevice. Furthermore, the laser-cut fabrication method can be improved by using a novel polishing method for the diamond membrane used as starting material (offered by the same company as used for the samples in Chapter 4, Almax easyLab). Also studied by Corazza et al., this method results in low waviness and exceptional surface smoothness.

Next to the release etching method of tens of micrometer-thin diamond membranes, the recently established diamond-on-insulator (DOI) platform based on the smart cut in combination with diamond overgrowth [7, 8] presents an alternative for producing diamond samples with a high surface quality. This fabrication method can be used especially to produce samples with a very low thickness around one hundred nanometers [9], that can host SnV centers showing good optical properties in nanostructures [10–12]. Furthermore, membranes fabricated by this method have been successfully transferred and bonded on different materials, including a distributed Bragg cavity mirror [13].

8.2.2 Microcavity Improvements

As shown in equation (3.23), the Purcell factor of open microcavities depends on the cavity finesse and the cavity beam waist. While the finesse can be increased with a different mirror coating and a high-quality diamond sample, the cavity beam waist depends mostly on the radius of curvature (ROC) of the spherical (fiber) mirror (equation (3.21)). Throughout this thesis, fibers with ROCs in the range of 15 µm to 25 µm are used, which are produced by laser ablation [14]. ROCs around 10 µm have been demonstrated by laser ablation on fused-silica substrates [15, 16] and with focused ion beam (FIB) milling on fibers [17]. FIB milling has resulted in mirrors with even smaller ROCs in the range of a few micrometers

in glass or silicon substrates [18–20]. Such small ROCs are especially appealing with SnV centers and very thin (hundreds of nanometers or lower) diamond membranes [21].
Table 8.1 summarizes improvements of the microcavity in terms of finesse and ROCs, determining the (vibration-averaged) Purcell factor. For an air-like mode, a vibration-averaged Purcell factor of 57 is possible with realistic cavity parameters. Going beyond this will require using diamond-like modes due to their lower sensitivity to cavity length fluctuations [22], which have not yet been experimentally used. A Purcell factor above 33 would lead to a coherent cooperativity approaching one for an optimally coupled, transform-limited NV center. This would enable the first demonstration of coherent coupling of an NV center to an optical cavity, a regime that remained elusive with any cavity approach. Note that for this demonstration, microwave driving might also be required to keep the NV center in the bright state, resonant with the cavity.

Radius of curvature ROC	Finesse	Cavity mode character	Cavity mode dispersion slope s	Projected Purcell factor F_P	Projected vib.-avg. Purcell factor $F_{P,avg}$
15 µm (Chapter 6)	3700 (Chapter 4)	Air-like	52 MHz/pm	33	23
15 µm	4800 (Chapter 4)	Diamond-like	17 MHz/pm	43	38
15 µm	≈11000 (Flågan et al. [5])	Diamond-like	17 MHz/pm	98	70
10 µm (Wang et al. [17])	≈12000 (Bogdanović et al. [23])	Air-like	52 MHz/pm	168	57
10 µm	≈11000	Diamond-like	17 MHz/pm	152	108

Table 8.1: Improvements of the microcavity diamond system to increase the Purcell factor by a higher cavity finesse and by reducing the cavity beam waist with a lower radius of curvature of the spherical mirror. A typical cavity air length around $t_a = 5\,\mu m$ and a diamond thickness of about $t_d = 3.5\,\mu m$ is assumed, which results in a fundamental mode number of $q = 43$ [22]. The beam waist is calculated by equation (3.29), which is then used to determine the Purcell factor by equation (3.23). The dispersion slope is calculated by equation (3.32), and the averaged Purcell factor for a cavity length fluctuation level of 25 pm is determined by equation (3.35). Furthermore, a cavity and emitter resonance wavelength of 637 nm is assumed; the determined values do not change significantly for 620 nm. Note that the finesse of the cavity is given in the frequency regime [22].

8.2.3 Next Experimental Steps

Experimentally, the following direct implementations and measurements can be made:

- **Charge-resonance (CR)** checks can be implemented in real-time to ensure that the color center is in the right charge state and at a specific frequency, on resonance with the excitation lasers [24]. Such a deterministic preparation improves the ZPL photon generation due to the otherwise probabilistic preparation (in Chapter 7, the NV center is prepared with a 72 % probability into the bright state). CR checks have been used with several solid state systems, including diamond NV centers [25], SnV centers [26], and V2 centers in silicon carbide (SIC) [27].

- **Improve ZPL excitation and detection efficiency.** Note that an improved detection would also improve the qubit readout fidelity. The following steps can be done:

  - Efficient excitation can be achieved with a reduced polarization frequency splitting (such as shown for the microdevices in Chapter 4). By reducing the polarization splitting of the NV center measurements in Chapter 7 from 9.6 GHz to 3 GHz, a factor of ten more excitation light would enter the cavity (for a cavity linewidth of 1.7 GHz). This would facilitate saturating the excitation power and increase the ZPL photon collection by a factor of three.
  - The detection efficiency can be improved by adapting the optical setup (excitation laser light suppression, filtering, and single-mode fiber coupling), which has an efficiency of about 39 % (subsection 7.8.11). This could be further improved to 69 % as shown with a quantum dot microcavity setup [16]. Furthermore, detector efficiencies above 95 % can be realized by using superconducting nanowire single photon detectors [28].
  - A NV center with less strain typically has a much higher cyclicity of around 250 [29]. With the ZPL detection efficiency in the range of a few percent, more than one photon is detected on average for the bright state. This would enable qubit readout with a much higher fidelity than in Chapter 7.
    For the SnV center, the high cyclicity (up to 2500 [11]) in combination with the efficient resonant photon extraction enables high-fidelity qubit readout.

- **Photon indistinguishability** can be demonstrated with the cavity-coupled color center by characterizing the ZPL emission with a Hong-Ou-Mandel interferometer setup and a two-photon quantum interference (TPQI) measurement [30]. The setup of the NV center measurements from Chapter 7 can be extended by connecting a fiber-based interferometer to the ZPL path after the filtering stage.

- **Emission-frequency tuning** of a cavity-coupled color center utilizing the Stark effect can be achieved by a static DC bias voltage applied to the on-chip stripline. This can be employed to overlap the emission frequency with a second, remote color center, as the indistinguishability of both emitters is required for generating entanglement. For the NV center, Stark tuning has been demonstrated with low voltages [28, 31]. This can be implemented with the cavity by DC-biasing the stripline, which is used for microwave control.
  In contrast, due to the first-order insensitivity, the Stark tuning of the SnV center is more challenging. However, Stark tuning has been shown with micrometer-sized inter-electrode spacing and high voltages [32, 33]. Such electrodes can be embedded into the cavity mirror to minimize the distance to the bonded diamond sample [34].

- **Improve microwave control** of the NV center's electron spin by using Hermite pulse envelopes to minimize the effects of detuning due to the different nitrogen spin states [35]. These pulses can be realized by reducing the microwave transmission losses through the cryostat [36] or with a stronger microwave amplifier. This may enable single-and two-qubit gates with fidelities exceeding 99.99 % [37, 38].

For the SnV center, the sample temperature of about 8 K of the cryostat (Chapter 5) is becoming the main limitation for spin measurements. However, this is more a technical issue, as other works have shown stable microcavities at 4 K [39–41], which can be used with highly-strained SnV centers [11], and 1.7 K [42], which not requires high strain [43].

- **Extension with nuclear spins** forming a qubit register [44]. For the NV center, the nitrogen spin [45] and surrounding carbon-13 spins [46] can be used as memory and data processing qubits [47, 48]. This would require high-fidelity microwave qubit control and a higher magnetic field strength, usually in the range of hundreds of Gauss [44, 49]. In the current setup (Chapter 5), this can be attained by placing the permanent magnet on a positioning system inside the cryostat chamber to reduce the distance to the sample.

Extending the NV center measurements of Chapter 7 with an imbalanced, phase-stabilized interferometer enables the verification of spin-photon entanglement [50]. This could be a step toward demonstrating spin-spin entanglement with a remote color center, which is discussed in the next sections.

8.3 Outlook

The microcavity combined with microwave spin qubit control can be used as a quantum network node. For the generation of entanglement with a remote color center, we can distinguish between emission-based and reflection-based protocols discussed in the following section [51]. Emission-based protocols have been implemented with NV centers in SILs [47, 52], while reflection-based protocols have been used recently with SiV centers in nanophotonic cavities [53]. We focus the discussion on NV centers and emission-based protocols, as well as SnV centers with reflection-based protocols, due to the higher attainable cooperativity of SnV centers.

In quantum networking experiments, the fast tunability of the cavity resonance frequency of open microcavities (tens of kilohertz [54]) can also be utilized for spectral multiplexing between different cavity-coupled color centers or optical transitions. The dynamic tuning can be used to switch the cavity resonance within one experimental sequence. This has been recently harnessed with rubidium atoms in a fiber-fiber microcavity to address different hyperfine transitions [55].

8.3.1 Emission-based Entanglement Protocols

The extraction of resonant photons of the quantum emitter into a single-mode fiber connected to the heralding station is the figure of merit for the entanglement generation efficiency of emission-based protocols. As summarized in Figure 8.1, the microcavity-enhanced NV center is at a comparable level to other solid-state quantum emitters, used for quantum networking, such as ytterbium rare earth ions in a nanocavity [56]. With a vibration-averaged Purcell factor of 40 in the diamond-like mode (Tab. 8.1), combined with the 50 % outcoupling efficiency and assuming an improved total ZPL setup efficiency of 40 % (see Section 8.2.3), a resonant photon extraction of ten percent with the NV center is

within reach. Using microcavity-enhanced NV centers with this ZPL extraction would improve the success rate of single- (double-) click protocols (see Sections 2.5 and 2.6) by a factor of one hundred (ten thousand) compared to SIL-based quantum network nodes [57, 58]. Especially with the double-click (Barett-Kok [59]) protocol (shown in Fig. 2.8), this improvement would enable high-fidelity entanglement, without requiring path length stabilization.
Furthermore, the NV center with higher strain from Chapter 7 exhibits a lower excited state lifetime. After being further reduced by the Purcell effect of the cavity (in the experiment in Chapter 7, the Purcell reduced lifetime is 7.8 ns), the cavity on resonance lifetime is approaching the value of a SnV center, for example, hosted inside bulk diamond [60] or a waveguide [12, 30] for efficient photon extraction. The indistinguishability in temporal shape of the emitted photon wave packets can be used, after down-conversion of both ZPL signals to telecom wavelength [61, 62], to entangle the cavity-coupled NV center with a remote SnV center. A future large-scale quantum network might contain quantum network nodes based on different quantum systems, requiring such cross-platform remote entanglement.

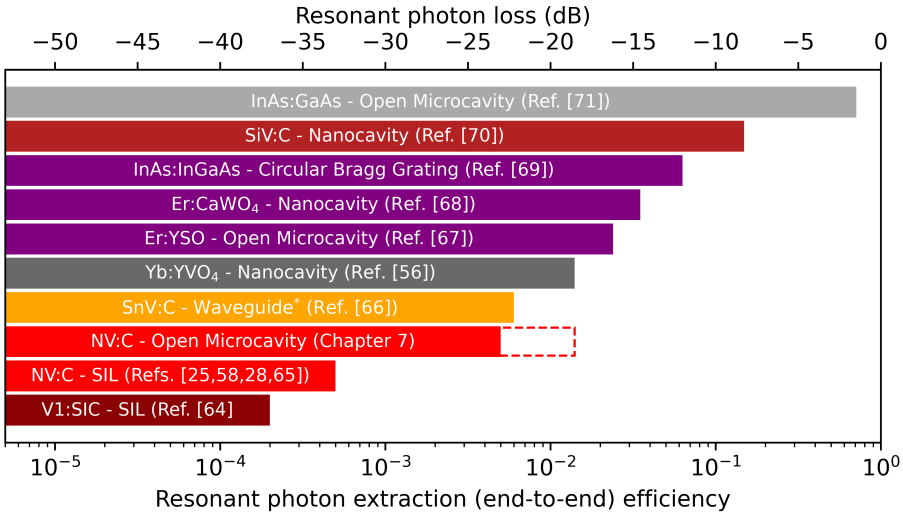

Figure 8.1: Resonant end-to-end efficiencies of different state-of-the-art realizations with solid-state quantum emitters. All stated numbers are measured, often directly by (resonant) excitation and detection, and after coupling into a single-mode fiber connecting the detector. Some efficiencies can include the detection efficiency of the single photon detectors, which is typically above 70 %. The nanocavities are all monolithic, one-dimensional photonic crystal cavities, milled into the host crystals (stated after the colon). The dashed box of the NV microcavity indicates the anticipated performance in saturation of the laser excitation power (Chapter 7). Naming scheme adapted from Reiserer [63]. Abbreviations: SIC - silicon carbide, SIL - solid immersion lens, C - carbon (diamond), Yb - ytterbium, YVO_4 - yttrium orthovanadate, Er - erbium, YSO - yttrium orthosilicate, $CaWO_4$ - calcium tungstate (scheelite), InAs - indium arsenide, (In)GaAs - (indium) gallium arsenide. References: Fang et al. [64], Hensen et al. [25], Humphreys et al. [58], Pompili et al. [28], Hermans et al. [65], * value calculated from Parker et al. [66] with a ratio of 0.36 to 0.57 of C-transition ZPL ratio and the Debye-Waller factor, respectively (see also Section 2.3.1), Ruskuc et al. [56], Ulanowski et al. [67], Ourari et al. [68], Nawrath et al. [69], Knall et al. [70] and Ding et al. [71]. The plot script can be found under Ref. [72].

8.3.2 Reflection-based Entanglement Protocols

The figure of merit for reflection-based entanglement protocols is the coherent cooperativity, which translates directly to the entanglement rate and fidelity [51, 73]. As shown in Figure 8.2, many diamond color centers have been successfully coupled to open microcavities, while maintaining good optical properties and coherent cooperativities improved over the last years by almost two orders of magnitude. Currently, microcavities with SiV centers [74], NV centers [75], and SnV centers (Chapter 6) are close to a coherent cooperativity of one. A Purcell factor above 28 allows reaching a cooperativity of more than ten for an optimally coupled SnV center. This regime is comparable to the SiV nanophotonic devices used for reflection-based entanglement by Knaut et al. [53].
Furthermore, a cavity outcoupling efficiency of (above) 50 % leads to a symmetric (overcoupled) cavity. This could be achieved in the diamond-like modes with the laser-cut diamond samples from Chapter 4. An overcoupled cavity is beneficial for a high contrast in the reflection signal of the different spin states [53].

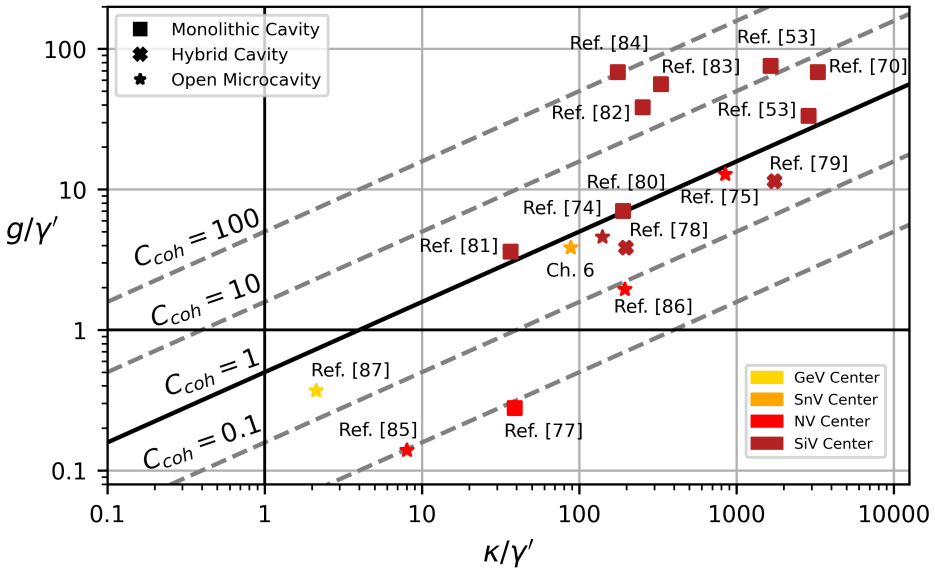

Figure 8.2: Coherent cooperativities achieved with diamond color centers and different cavity approaches. Plot inspired by Pfeifer et al. [76]. References are grouped depending on the cavity QED parameters $\{g,\kappa,\gamma'\}/2\pi$ = {cavity coupling strength, cavity linewidth, emitter linewidth}, leading to the coherent cooperativity of equation (3.10). The emitter linewidth $\gamma' = \gamma + \gamma_d$ also captures additional dephasing γ_d, which broadens the transform-limited linewidth γ. Note that all shown diamond cavity experiments are operated in the bad-cavity regime $\kappa > (\gamma, \gamma')$ (section 3.1.2). All monolithic cavities are diamond-based one-dimensional photonic crystal cavities (PCC), except the two-dimensional PCC in Ref. [77]. Hybrid cavities are realized by one-dimensional PCCs in an external material such as gallium phosphide [78] and silicon nitride [79]. References, monolithic cavities: Faraon et al. [77], Sipahigil et al. [80], Zhang et al. [81], Evans et al. [82], Nguyen et al. [83], Bhaskar et al. [84], Knall et al. [70], Knaut et al. [53]; hybrid cavities: Chakravarthi et al. [78] and Antoniuk et al. [79]; open microcavities: Riedel et al. [85], Ruf et al. [86], Bayer et al. [74], Zifkin et al. [87] and Yurgens et al. [75]. The plot script can be found under Ref. [72].

Due to the high SnV center density in the microdevices (see Fig. 6.2 (b) and 6.9), it might also be possible to find two (or more) emitters with the same emission frequency at one cavity spot. This could enable studying collective multi-emitter cavity effects [88], by probing the cavity spectrum with resonant laser light in transmission or reflection [82]. Similar experiments have been recently reported with several optically active molecules coupled to a microcavity [89].

Single Photon Source for Reflection-based Protocols
For efficient entanglement generation, reflection-based protocols require a single photon to mediate entanglement between the remote nodes [53, 90]. A cavity-coupled SnV center could be used as a highly efficient single-photon source. The shown cooperativity of 1.7 in Chapter 6 can be combined with a 50 % cavity outcoupling efficiency. With an improved total ZPL setup efficiency of 65 %, a resonant, fiber-coupled photon could be generated with a probability around 20 %. These single photons can be used to mediate entanglement of two remote SnV centers through a reflection-based protocol [51]. The SnV centers can be hosted inside a photonic crystal cavity, which can enable high cooperativities at sufficiently low temperatures, as shown with SiV centers [84]. In the demonstration of Knaut et al. [53], a weak coherent pulse is used, limiting the overall efficiency to about 2 %. Thus, the entanglement generation success chance could be improved by the microcavity-enhanced SnV center by a factor of ten. The high SnV center density in the microdevices can be used to find a SnV center in the required frequency range. Additional fine-tuning of the emission frequency could be achieved with the Stark effect and on-chip gold electrodes [32, 33] or by shifting the emitted photon frequency by electro-optic modulators [91].

8.3.3 Exploration of Novel Quantum Emitters

Due to the versatile and direct sample integration, open microcavities can be used with a broad range of optically active solid-state quantum emitters (or defects) [92–94]. These can be incorporated into the cavity hosted in different structures, such as nanoparticles or nanotubes, two-dimensional materials, membranes, or even directly grown into or on the mirror material (see Section 5.1 for an overview). The cavity-enhanced sensitivity might even enable working with single molecules placed on the cavity mirror [95–97]. Patterning the cavity sample mirror prior with striplines can further be used to deliver static electric, radio-frequency, or microwave fields to the quantum emitters. With the spatial tunability of about 2 mm laterally on the mirror, many samples could be placed or bonded and characterized with a high throughput. Furthermore, the sample mirror can be studied in different setups, such as with a confocal (cryogenic) microscope, which can be used to determine emitter parameters in the absence of the cavity. This also allows for screening samples on their performance (emitter properties and quality of the host material) before they are used in the low-temperature microcavity experiments.
The stopband of the cavity mirror coating can be tailored to the specific emission wavelength and can also be adapted to support a broadband spectral range (hundreds of nanometers) or multiple, separate central wavelengths, including demonstrations at telecom wavelength [98]. This enables the exploration and characterization of novel quantum emitters [99], for example, in layered materials [100] like hexagonal boron nitride (hBN) [101], or in host crystals like silicon [102, 103]. The cavity enhancement can especially help for very dim emitters. Moreover, as demonstrated with the SnV center in Chapter 6, the cavity

experiments can also be utilized to directly determine optical properties of novel quantum emitters. With the on-chip striplines, the potential spin properties of emitters can also be directly probed [104].

8.3.4 Photonic Integration

In a larger quantum network, multiple communication qubits coupled to cavities might be required per node. To scale the platform to several microcavities per cryogenic system, a smaller footprint of the microcavity and its interfacing optics is beneficial. A convenient size would be to make the platform compatible with a standard 19-inch server rack, which can be placed and operated remotely in a data center. For continuous operation and to avoid a liquid helium infrastructure, a closed-cycle cryostat is also needed. The rack integration has been, for example, demonstrated with trapped ions [105] or optical semiconductor quantum dots [106].

There are several ways to reduce the system's footprint. These approaches usually necessitate a reduced sample space, which might require a high density of color centers to have a good chance of finding a well-coupled emitter. As shown in the SnV center experiments in Chapter 6 (Fig. 6.9), the spectral tunability of the cavity can then be used to select a well-coupled emitter. One approach is a microcavity constructed by two fibers, which enables direct optical access to the cavity without bulk optics. This can also be integrated into a cryogenic system without optical free-space access. Such a microcavity has been demonstrated with a NV center in a nanodiamond at room temperature by Albrecht et al. [107], shown in Fig. 8.3 (a). As an alternative to the nanodiamond, a diamond microdevice could be bonded or placed on the (flat) output cavity fiber. Moreover, to make it possible to probe several cavity spots on the device in transmission, a multi-mode fiber with a larger core can be used, and the spherical (excitation) fiber can be positioned by short-range nanopositioners to change the lateral position. Piezo with a travel range of around ten micrometers and a mechanical resonance frequency of tens of kilohertz are commercially available, which lowers the sensitivity to vibrations [108]. Furthermore, microwaves can be delivered via electrodes on the fiber tip [109] (see also Fig. 3.6 (b)) or via a bondwire or loop antenna close to or around the fiber end facet.

A way to combine a fiber array with open microcavities is proposed by Derntl et al. [110]. As shown in Fig. 8.3 (b), an array of spherical micro-mirrors is fabricated into silicon, which can be individually tuned by a micro-electro-mechanical system (MEMS)-based actuator. The cavity is closed from the top by approaching with an array of cavity fibers. The actuator allows for tuning or stabilizing the cavity resonance frequency by changing the length. Diamond microdevices could be incorporated into the cavity placed on the flat fiber tips. As an alternative, the spherical mirrors can be fabricated into the fiber array, and the chip mirror can be flat with a bonded microdevice.

Next to fiber-based approaches, there are also proposals to interface wafer-scale [111], chip-based microcavities with photonic integrated circuits (PICs) [97, 112, 113], which can also be packaged into one device [114]. This approach is sketched in Fig. 8.3 (c). The programmability and many spatial modes combined with low-loss on-chip components, such as waveguides, switches, or filters, make PICs essential in the scaling of quantum network nodes [115–118]. Further, PICs can be produced on a foundry scale, CMOS (complementary metal–oxide–semiconductor) compatible, and also enable on-chip frequency

conversion [119] and the detection of single photons [120–122], which can be used to herald the generation of on-chip entanglement between cavity-coupled color centers.

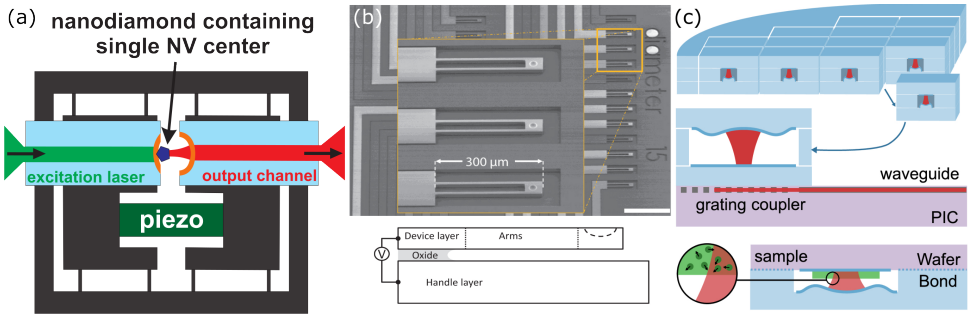

Figure 8.3: Photonic integration of open microcavities. (a) An all-fiber-based microcavity with a single NV center hosted inside a nanodiamond. The cavity resonance frequency is tuned via the cavity length with a piezo clamped between the fiber mounts. The optical access via both fibers can be used to split excitation and detection. Furthermore, the detection output fiber has a high-reflectivity coating for the green excitation light for direct filtering. Adapted from Albrecht et al. [107], with the permission of AIP Publishing. (b) Scanning electron microscope image of an array of micrometer-sized silicon mirrors on cantilevers. The schematic below shows the individual actuation of the micro-mirrors (not to scale). The microcavity array is approached from above with a mirror-coated fiber array. Adapted with permission from Derntl et al. [110] © Optical Society of America. (c) Integration of silicon-chip microcavities with a photonic integrated circuit (PIC). Miniaturized open microcavities are segmented after wave-scale fabrication and placed on a PIC. A grating coupler is used to guide the mode leaving the cavity into an on-chip waveguide (upper part). A membrane hosting solid-state quantum emitters is incorporated into the microcavity (lower part). Figure adapted from Jin et al. [112] under the Optica Publishing Group Open Access Publishing Agreement.

8.4 The End

Open microcavities provide an efficient platform for resonantly brightening solid-state quantum emitters in a variety of host materials. Combined with micrometer-thin membranes, they enable the gentle, bulk-like cavity integration of quantum emitters, especially of candidates that are notoriously hard to incorporate with coherent optical properties into nanophotonic structures, such as NV centers in diamond [123], rare-earth erbium ions in YSO [42], or divacancy centers in SIC [124]. The platform has also been commercialized by several companies[1].

Realistic improvements promise that resonant photon extraction (end-to-end) efficiencies of more than ten percent and coherent cooperativities above ten can be reached soon with microcavity-coupled diamond color centers. Proposals and first realizations show that photonic integration can be further developed for multiplexing to several microcavities per cryostat as a more scalable quantum network node. Open microcavities have reached the maturity needed for quantum networking and can be optimized for specific entanglement protocols, unlocking the possibility of next-generation cavity-enhanced quantum networking.

[1]With companies such as Qlibri in Munich, Mirega in Grenoble, Mode Labs in Oxfordshire, or Nu Quantum in Cambridge (UK).

References

[1] R. Høy Jensen, E. Janitz, Y. Fontana, Y. He, O. Gobron, I. P. Radko, M. Bhaskar, R. Evans, C. D. Rodríguez Rosenblueth, L. Childress, A. Huck, and U. Lund Andersen, *Cavity-Enhanced Photon Emission from a Single Germanium-Vacancy Center in a Diamond Membrane,* Phys. Rev. Applied **13**, 064016 (2020).

[2] J. Heupel, M. Pallmann, J. Körber, D. Hunger, J. P. Reithmaier, and C. Popov, *Fabrication of High-Quality Thin Single-Crystal Diamond Membranes with Low Surface Roughness,* Phys. Status Solidi (a) **220**, 2200465 (2023).

[3] P. Maletinsky, S. Hong, M. S. Grinolds, B. Hausmann, M. D. Lukin, R. L. Walsworth, M. Lončar, and A. Yacoby, *A robust scanning diamond sensor for nanoscale imaging with single nitrogen-vacancy centres,* Nat. Nanotechnol. **7**, 320 (2012).

[4] P. Appel, E. Neu, M. Ganzhorn, A. Barfuss, M. Batzer, M. Gratz, A. Tschöpe, and P. Maletinsky, *Fabrication of all diamond scanning probes for nanoscale magnetometry,* Rev. Sci. Instrum. **87**, 063703 (2016).

[5] S. Flågan, D. Riedel, A. Javadi, T. Jakubczyk, P. Maletinsky, and R. J. Warburton, *A diamond-confined open microcavity featuring a high quality-factor and a small mode-volume,* J. Appl. Phys. **131**, 113102 (2022).

[6] A. Corazza, S. Ruffieux, Y. Zhu, C. A. Jaramillo Concha, Y. Fontana, C. Galland, R. J. Warburton, and P. Maletinsky, *Homogeneous Free-Standing Nanostructures from Bulk Diamond over Millimeter Scales for Quantum Technologies,* Nano Lett. **25**, 14526 (2025).

[7] A. P. Magyar, J. C. Lee, A. M. Limarga, I. Aharonovich, F. Rol, D. R. Clarke, M. Huang, and E. L. Hu, *Fabrication of thin, luminescent, single-crystal diamond membranes,* Appl. Phys. Lett. **99**, 081913 (2011).

[8] I. Aharonovich, J. C. Lee, A. P. Magyar, B. B. Buckley, C. G. Yale, D. D. Awschalom, and E. L. Hu, *Homoepitaxial Growth of Single Crystal Diamond Membranes for Quantum Information Processing,* Adv. Mater. **24** (2012).

[9] X. Guo, N. Delegan, J. C. Karsch, Z. Li, T. Liu, R. Shreiner, A. Butcher, D. D. Awschalom, F. J. Heremans, and A. A. High, *Tunable and Transferable Diamond Membranes for Integrated Quantum Technologies,* Nano Lett. **21**, 10392 (2021).

[10] A. E. Rugar, C. Dory, S. Aghaeimeibodi, H. Lu, S. Sun, S. D. Mishra, Z.-X. Shen, N. A. Melosh, and J. Vučković, *Narrow-Linewidth Tin-Vacancy Centers in a Diamond Waveguide,* ACS Photonics **7**, 2356 (2020).

[11] X. Guo, A. M. Stramma, Z. Li, W. G. Roth, B. Huang, Y. Jin, R. A. Parker, J. Arjona Martínez, N. Shofer, C. P. Michaels, C. P. Purser, M. H. Appel, E. M. Alexeev, T. Liu, A. C. Ferrari, D. D. Awschalom, N. Delegan, B. Pingault, G. Galli, F. J. Heremans, M. Atatüre, and A. A. High, *Microwave-Based Quantum Control and Coherence Protection of Tin-Vacancy Spin Qubits in a Strain-Tuned Diamond-Membrane Heterostructure,* Phys. Rev. X **13**, 041037 (2023).

[12] M. Pasini, N. Codreanu, T. Turan, A. Riera Moral, C. F. Primavera, L. De Santis, H. K. C. Beukers, J. M. Brevoord, C. Waas, J. Borregaard, and R. Hanson, *Nonlinear Quantum Photonics with a Tin-Vacancy Center Coupled to a One-Dimensional Diamond Waveguide,* Phys. Rev. Lett. **133**, 023603 (2024).

[13] X. Guo, M. Xie, A. Addhya, A. Linder, U. Zvi, S. Wang, X. Yu, T. D. Deshmukh, Y. Liu, I. N. Hammock, Z. Li, C. T. DeVault, A. Butcher, A. P. Esser-Kahn, D. D. Awschalom, N. Delegan, P. C. Maurer, F. J. Heremans, and A. A. High, *Direct-bonded diamond membranes for heterogeneous quantum and electronic technologies,* Nat. Commun. **15**, 8788 (2024).

[14] D. Hunger, T. Steinmetz, Y. Colombe, C. Deutsch, T. W. Hänsch, and J. Reichel, *A fiber Fabry–Perot cavity with high finesse,* New J. Phys. **12**, 065038 (2010).

[15] D. Najer, I. Söllner, P. Sekatski, V. Dolique, M. C. Löbl, D. Riedel, R. Schott, S. Starosielec, S. R. Valentin, A. D. Wieck, N. Sangouard, A. Ludwig, and R. J. Warburton, *A gated quantum dot strongly coupled to an optical microcavity,* Nature **575**, 622 (2019).

[16] N. Tomm, A. Javadi, N. O. Antoniadis, D. Najer, M. C. Löbl, A. R. Korsch, R. Schott, S. R. Valentin, A. D. Wieck, A. Ludwig, and R. J. Warburton, *A bright and fast source of coherent single photons,* Nat. Nanotechnol. **16**, 399 (2021).

[17] D. Wang, H. Kelkar, D. Martin-Cano, D. Rattenbacher, A. Shkarin, T. Utikal, S. Götzinger, and V. Sandoghdar, *Turning a molecule into a coherent two-level quantum system,* Nat. Phys. **15**, 483 (2019).

[18] A. A. P. Trichet, P. R. Dolan, D. M. Coles, G. M. Hughes, and J. M. Smith, *Topographic control of open-access microcavities at the nanometer scale,* Opt. Express **23**, 17205 (2015).

[19] L. C. Flatten, L. Weng, A. Branny, S. Johnson, P. R. Dolan, A. A. P. Trichet, B. D. Gerardot, and J. M. Smith, *Microcavity enhanced single photon emission from two-dimensional WSe2,* Appl. Phys. Lett. **112**, 191105 (2018).

[20] T. Vogl, R. Lecamwasam, B. C. Buchler, Y. Lu, and P. K. Lam, *Compact Cavity-Enhanced Single-Photon Generation with Hexagonal Boron Nitride,* ACS Photonics **6**, 1955 (2019).

[21] S. Häußler, J. Benedikter, K. Bray, B. Regan, A. Dietrich, J. Twamley, I. Aharonovich, D. Hunger, and A. Kubanek, *Diamond photonics platform based on silicon vacancy centers in a single-crystal diamond membrane and a fiber cavity,* Phys. Rev. B **99**, 165310 (2019).

[22] S. B. van Dam, M. Ruf, and R. Hanson, *Optimal design of diamond-air microcavities for quantum networks using an analytical approach,* New J. Phys. **20**, 115004 (2018).

[23] S. Bogdanović, S. B. van Dam, C. Bonato, L. C. Coenen, A.-M. J. Zwerver, B. Hensen, M. S. Z. Liddy, T. Fink, A. Reiserer, M. Lončar, and R. Hanson, *Design and low-temperature characterization of a tunable microcavity for diamond-based quantum networks,* Appl. Phys. Lett. **110**, 171103 (2017).

[24] S. Hermans, *Quantum Networks using Spins in Diamond*, Ph.D. thesis, Delft University of Technology (2022).

[25] B. Hensen, H. Bernien, A. E. Dréau, A. Reiserer, N. Kalb, M. S. Blok, J. Ruitenberg, R. F. L. Vermeulen, R. N. Schouten, C. Abellán, W. Amaya, V. Pruneri, M. W. Mitchell, M. Markham, D. J. Twitchen, D. Elkouss, S. Wehner, T. H. Taminiau, and R. Hanson, *Loophole-free Bell inequality violation using electron spins separated by 1.3 kilometres,* Nature **526**, 682 (2015).

[26] J. M. Brevoord, L. De Santis, T. Yamamoto, M. Pasini, N. Codreanu, T. Turan, H. K. Beukers, C. Waas, and R. Hanson, *Heralded initialization of charge state and optical-transition frequency of diamond tin-vacancy centers,* Phys. Rev. Applied **21**, 054047 (2024).

[27] G. L. Van De Stolpe, L. J. Feije, S. J. H. Loenen, A. Das, G. M. Timmer, T. W. De Jong, and T. H. Taminiau, *Check-probe spectroscopy of lifetime-limited emitters in bulk-grown silicon carbide,* npj Quantum Inf. **11**, 31 (2025).

[28] M. Pompili, S. L. N. Hermans, S. Baier, H. K. C. Beukers, P. C. Humphreys, R. N. Schouten, R. F. L. Vermeulen, M. J. Tiggelman, L. dos Santos Martins, B. Dirkse, S. Wehner, and R. Hanson, *Realization of a multinode quantum network of remote solid-state qubits,* Science **372**, 259 (2021).

[29] O. S. M. Ubbens, *A Unified Model to Predict Excited State Cyclicity of Nitrogen Vacancy Centres in Diamond*, Master's thesis, Delft University of Technology (2022).

[30] J. Arjona Martínez, R. A. Parker, K. C. Chen, C. M. Purser, L. Li, C. P. Michaels, A. M. Stramma, R. Debroux, I. B. Harris, M. Hayhurst Appel, E. C. Nichols, M. E. Trusheim, D. A. Gangloff, D. Englund, and M. Atatüre, *Photonic Indistinguishability of the Tin-Vacancy Center in Nanostructured Diamond,* Phys. Rev. Lett. **129**, 173603 (2022).

[31] P. Tamarat, T. Gaebel, J. R. Rabeau, M. Khan, A. D. Greentree, H. Wilson, L. C. L. Hollenberg, S. Prawer, P. Hemmer, F. Jelezko, and J. Wrachtrup, *Stark Shift Control of Single Optical Centers in Diamond,* Phys. Rev. Lett. **97**, 083002 (2006).

[32] L. De Santis, M. Trusheim, K. Chen, and D. Englund, *Investigation of the Stark Effect on a Centrosymmetric Quantum Emitter in Diamond,* Phys. Rev. Lett. **127**, 147402 (2021).

[33] V. Bushmakin, O. v. Berg, C. Sauerzapf, S. Jayaram, A. Denisenko, V. Vorobyov, I. Gerhardt, D. Liu, and J. Wrachtrup, *Two-Photon Interference of Photons from Remote Tin-Vacancy Centers in Diamond,* arXiv:2412.17539 (2024).

[34] S. Bogdanović, M. S. Z. Liddy, S. B. van Dam, L. C. Coenen, T. Fink, M. Lončar, and R. Hanson, *Robust nano-fabrication of an integrated platform for spin control in a tunable microcavity,* APL Photonics **2**, 126101 (2017).

[35] M. H. Abobeih, J. Cramer, M. A. Bakker, N. Kalb, M. Markham, D. J. Twitchen, and T. H. Taminiau, *One-second coherence for a single electron spin coupled to a multi-qubit nuclear-spin environment,* Nat. Commun. **9**, 2552 (2018).

[36] I. Karapatzakis, J. Resch, M. Schrodin, P. Fuchs, M. Kieschnick, J. Heupel, L. Kussi, C. Sürgers, C. Popov, J. Meijer, C. Becher, W. Wernsdorfer, and D. Hunger, *Microwave Control of the Tin-Vacancy Spin Qubit in Diamond with a Superconducting Waveguide,* Phys. Rev. X **14**, 031036 (2024).

[37] X. Rong, J. Geng, F. Shi, Y. Liu, K. Xu, W. Ma, F. Kong, Z. Jiang, Y. Wu, and J. Du, *Experimental fault-tolerant universal quantum gates with solid-state spins under ambient conditions,* Nat. Commun. **6**, 8748 (2015).

[38] H. Bartling, J. Yun, K. Schymik, M. Van Riggelen, L. Enthoven, H. Van Ommen, M. Babaie, F. Sebastiano, M. Markham, D. Twitchen, and T. Taminiau, *Universal high-fidelity quantum gates for spin qubits in diamond,* Phys. Rev. Applied **23**, 034052 (2025).

[39] T. Ruelle, D. Jaeger, F. Fogliano, F. Braakman, and M. Poggio, *A tunable fiber Fabry–Perot cavity for hybrid optomechanics stabilized at 4 K,* Rev. Sci. Instrum. **93**, 095003 (2022).

[40] M. Pallmann, T. Eichhorn, J. Benedikter, B. Casabone, T. Hümmer, and D. Hunger, *A highly stable and fully tunable open microcavity platform at cryogenic temperatures,* APL Photonics **8**, 046107 (2023).

[41] M. Fisicaro, M. Witlox, H. Van Der Meer, and W. Löffler, *Active stabilization of an open-access optical microcavity for low-noise operation in a standard closed-cycle cryostat,* Rev. Sci. Instrum. **95**, 033101 (2024).

[42] B. Merkel, A. Ulanowski, and A. Reiserer, *Coherent and Purcell-Enhanced Emission from Erbium Dopants in a Cryogenic High- Q Resonator,* Phys. Rev. X **10**, 041025 (2020).

[43] E. I. Rosenthal, C. P. Anderson, H. C. Kleidermacher, A. J. Stein, H. Lee, J. Grzesik, G. Scuri, A. E. Rugar, D. Riedel, S. Aghaeimeibodi, G. H. Ahn, K. Van Gasse, and J. Vučković, *Microwave Spin Control of a Tin-Vacancy Qubit in Diamond,* Phys. Rev. X **13**, 031022 (2023).

[44] C. E. Bradley, J. Randall, M. H. Abobeih, R. C. Berrevoets, M. J. Degen, M. A. Bakker, M. Markham, D. J. Twitchen, and T. H. Taminiau, *A Ten-Qubit Solid-State Spin Register with Quantum Memory up to One Minute,* Phys. Rev. X **9**, 031045 (2019).

[45] T. Van Der Sar, Z. H. Wang, M. S. Blok, H. Bernien, T. H. Taminiau, D. M. Toyli, D. A. Lidar, D. D. Awschalom, R. Hanson, and V. V. Dobrovitski, *Decoherence-protected quantum gates for a hybrid solid-state spin register,* Nature **484**, 82 (2012).

[46] T. H. Taminiau, J. Cramer, T. van der Sar, V. V. Dobrovitski, and R. Hanson, *Universal control and error correction in multi-qubit spin registers in diamond,* Nat. Nanotechnol. **9**, 171 (2014).

[47] N. Kalb, A. A. Reiserer, P. C. Humphreys, J. J. W. Bakermans, S. J. Kamerling, N. H. Nickerson, S. C. Benjamin, D. J. Twitchen, M. Markham, and R. Hanson, *Entanglement distillation between solid-state quantum network nodes,* Science **356**, 928 (2017).

[48] M. H. Abobeih, Y. Wang, J. Randall, S. J. H. Loenen, C. E. Bradley, M. Markham, D. J. Twitchen, B. M. Terhal, and T. H. Taminiau, *Fault-tolerant operation of a logical qubit in a diamond quantum processor,* Nature **606**, 884 (2022).

[49] G. L. Van De Stolpe, D. P. Kwiatkowski, C. E. Bradley, J. Randall, M. H. Abobeih, S. A. Breitweiser, L. C. Bassett, M. Markham, D. J. Twitchen, and T. H. Taminiau, *Mapping a 50-spin-qubit network through correlated sensing,* Nat. Commun. **15**, 2006 (2024).

[50] A. Tchebotareva, S. L. N. Hermans, P. C. Humphreys, D. Voigt, P. J. Harmsma, L. K. Cheng, A. L. Verlaan, N. Dijkhuizen, W. de Jong, A. Dréau, and R. Hanson, *Entanglement between a Diamond Spin Qubit and a Photonic Time-Bin Qubit at Telecom Wavelength,* Phys. Rev. Lett. **123**, 063601 (2019).

[51] H. K. Beukers, M. Pasini, H. Choi, D. Englund, R. Hanson, and J. Borregaard, *Remote-Entanglement Protocols for Stationary Qubits with Photonic Interfaces,* PRX Quantum **5**, 010202 (2024).

[52] H. Bernien, B. Hensen, W. Pfaff, G. Koolstra, M. S. Blok, L. Robledo, T. H. Taminiau, M. Markham, D. J. Twitchen, L. Childress, and R. Hanson, *Heralded entanglement between solid-state qubits separated by three metres,* Nature **497**, 86 (2013).

[53] C. M. Knaut, A. Suleymanzade, Y.-C. Wei, D. R. Assumpcao, P.-J. Stas, Y. Q. Huan, B. Machielse, E. N. Knall, M. Sutula, G. Baranes, N. Sinclair, C. De-Eknamkul, D. S. Levonian, M. K. Bhaskar, H. Park, M. Lončar, and M. D. Lukin, *Entanglement of nanophotonic quantum memory nodes in a telecom network,* Nature **629**, 573 (2024).

[54] E. Janitz, M. Ruf, Y. Fontana, J. Sankey, and L. Childress, *High mechanical bandwidth fiber-coupled Fabry-Perot cavity,* Opt. Express **25**, 20932 (2017).

[55] B. Grinkemeyer, E. Guardado-Sanchez, I. Dimitrova, D. Shchepanovich, G. E. Mandopoulou, J. Borregaard, V. Vuletić, and M. D. Lukin, *Error-detected quantum operations with neutral atoms mediated by an optical cavity,* Science **387**, 1301 (2025).

[56] A. Ruskuc, C.-J. Wu, E. Green, S. L. N. Hermans, W. Pajak, J. Choi, and A. Faraon, *Multiplexed entanglement of multi-emitter quantum network nodes,* Nature **639**, 54 (2025).

[57] W. Pfaff, B. J. Hensen, H. Bernien, S. B. van Dam, M. S. Blok, T. H. Taminiau, M. J. Tiggelman, R. N. Schouten, M. Markham, D. J. Twitchen, and R. Hanson, *Unconditional quantum teleportation between distant solid-state quantum bits,* Science **345**, 532 (2014).

[58] P. C. Humphreys, N. Kalb, J. P. J. Morits, R. N. Schouten, R. F. L. Vermeulen, D. J. Twitchen, M. Markham, and R. Hanson, *Deterministic delivery of remote entanglement on a quantum network,* Nature **558**, 268 (2018).

[59] S. D. Barrett and P. Kok, *Efficient high-fidelity quantum computation using matter qubits and linear optics,* Phys. Rev. A **71**, 060310 (2005).

[60] J. Görlitz, D. Herrmann, G. Thiering, P. Fuchs, M. Gandil, T. Iwasaki, T. Taniguchi, M. Kieschnick, J. Meijer, M. Hatano, A. Gali, and C. Becher, *Spectroscopic investigations of negatively charged tin-vacancy centres in diamond,* New J. Phys. **22**, 013048 (2020).

[61] J. F. Geus, F. Elsen, S. Nyga, A. J. Stolk, K. L. Van Der Enden, E. J. Van Zwet, C. Haefner, R. Hanson, and B. Jungbluth, *Low-noise short-wavelength pumped frequency downconversion for quantum frequency converters,* Opt. Quantum **2**, 189 (2024).

[62] J. M. Brevoord, J. F. Geus, T. Turan, M. G. Romero, D. B. Rodríguez, N. Codreanu, A. M. Stramma, R. Hanson, F. Elsen, and B. Jungbluth, *Quantum Frequency Conversion of Single Photons from a Tin-Vacancy Center in Diamond,* arXiv:2509.01661 (2025).

[63] A. Reiserer, *Colloquium : Cavity-enhanced quantum network nodes,* Rev. Mod. Phys. **94**, 041003 (2022).

[64] R.-Z. Fang, X.-Y. Lai, T. Li, R.-Z. Su, B.-W. Lu, C.-W. Yang, R.-Z. Liu, Y.-K. Qiao, C. Li, Z.-G. He, J. Huang, H. Li, L.-X. You, Y.-H. Huo, X.-H. Bao, and J.-W. Pan, *Experimental Generation of Spin-Photon Entanglement in Silicon Carbide,* Phys. Rev. Lett. **132**, 160801 (2024).

[65] S. L. N. Hermans, M. Pompili, H. K. C. Beukers, S. Baier, J. Borregaard, and R. Hanson, *Qubit teleportation between non-neighbouring nodes in a quantum network,* Nature **605**, 663 (2022).

[66] R. A. Parker, J. Arjona Martínez, K. C. Chen, A. M. Stramma, I. B. Harris, C. P. Michaels, M. E. Trusheim, M. Hayhurst Appel, C. M. Purser, W. G. Roth, D. Englund, and M. Atatüre, *A diamond nanophotonic interface with an optically accessible deterministic electronuclear spin register,* Nat. Photon. **18**, 156 (2024).

[67] A. Ulanowski, B. Merkel, and A. Reiserer, *Spectral multiplexing of telecom emitters with stable transition frequency,* Sci. Adv. **8**, eabo4538 (2022).

[68] S. Ourari, Ł. Dusanowski, S. P. Horvath, M. T. Uysal, C. M. Phenicie, P. Stevenson, M. Raha, S. Chen, R. J. Cava, N. P. De Leon, and J. D. Thompson, *Indistinguishable telecom band photons from a single Er ion in the solid state,* Nature **620**, 977 (2023).

[69] C. Nawrath, R. Joos, S. Kolatschek, S. Bauer, P. Pruy, F. Hornung, J. Fischer, J. Huang, P. Vijayan, R. Sittig, M. Jetter, S. L. Portalupi, and P. Michler, *Bright Source of Purcell-Enhanced, Triggered, Single Photons in the Telecom C-Band,* Adv. Quantum Tech. **6**, 2300111 (2023).

[70] E. N. Knall, C. M. Knaut, R. Bekenstein, D. R. Assumpcao, P. L. Stroganov, W. Gong, Y. Q. Huan, P.-J. Stas, B. Machielse, M. Chalupnik, D. Levonian, A. Suleymanzade,

R. Riedinger, H. Park, M. Lončar, M. K. Bhaskar, and M. D. Lukin, *Efficient Source of Shaped Single Photons Based on an Integrated Diamond Nanophotonic System,* Phys. Rev. Lett. **129**, 053603 (2022).

[71] X. Ding, Y.-P. Guo, M.-C. Xu, R.-Z. Liu, G.-Y. Zou, J.-Y. Zhao, Z.-X. Ge, Q.-H. Zhang, H.-L. Liu, L.-J. Wang, M.-C. Chen, H. Wang, Y.-M. He, Y.-H. Huo, C.-Y. Lu, and J.-W. Pan, *High-efficiency single-photon source above the loss-tolerant threshold for efficient linear optical quantum computing,* Nat. Photon. **19**, 387 (2025).

[72] Y. Herrmann, *Data underlying the dissertation "Good Vibrations: A Microcavity-based Diamond Spin-Photon Interface for Quantum Networking",* 4TU.ResearchData, Dataset (2025).

[73] J. Borregaard, A. S. Sørensen, and P. Lodahl, *Quantum Networks with Deterministic Spin–Photon Interfaces,* Adv. Quantum Technol. **2**, 1800091 (2019).

[74] G. Bayer, R. Berghaus, S. Sachero, A. B. Filipovski, L. Antoniuk, N. Lettner, R. Waltrich, M. Klotz, P. Maier, V. Agafonov, and A. Kubanek, *Optical driving, spin initialization and readout of single SiV- centers in a Fabry-Perot resonator,* Commun. Phys. **6**, 300 (2023).

[75] V. Yurgens, Y. Fontana, A. Corazza, B. J. Shields, P. Maletinsky, and R. J. Warburton, *Cavity-assisted resonance fluorescence from a nitrogen-vacancy center in diamond,* npj Quantum Inf. **10**, 112 (2024).

[76] H. Pfeifer, L. Ratschbacher, J. Gallego, C. Saavedra, A. Faßbender, A. Von Haaren, W. Alt, S. Hofferberth, M. Köhl, S. Linden, and D. Meschede, *Achievements and perspectives of optical fiber Fabry–Perot cavities,* Appl. Phys. B **128**, 29 (2022).

[77] A. Faraon, C. Santori, Z. Huang, V. M. Acosta, and R. G. Beausoleil, *Coupling of Nitrogen-Vacancy Centers to Photonic Crystal Cavities in Monocrystalline Diamond,* Phys. Rev. Lett. **109**, 033604 (2012).

[78] S. Chakravarthi, N. S. Yama, A. Abulnaga, D. Huang, C. Pederson, K. Hestroffer, F. Hatami, N. P. De Leon, and K.-M. C. Fu, *Hybrid Integration of GaP Photonic Crystal Cavities with Silicon-Vacancy Centers in Diamond by Stamp-Transfer,* Nano Lett. **23**, 3708 (2023).

[79] L. Antoniuk, N. Lettner, A. P. Ovvyan, S. Haugg, M. Klotz, H. Gehring, D. Wendland, V. N. Agafonov, W. H. Pernice, and A. Kubanek, *All-optical spin access via a cavity-broadened optical transition in on-chip hybrid quantum photonics,* Phys. Rev. Applied **21**, 054032 (2024).

[80] A. Sipahigil, R. E. Evans, D. D. Sukachev, M. J. Burek, J. Borregaard, M. K. Bhaskar, C. T. Nguyen, J. L. Pacheco, H. A. Atikian, C. Meuwly, R. M. Camacho, F. Jelezko, E. Bielejec, H. Park, M. Lončar, and M. D. Lukin, *An integrated diamond nanophotonics platform for quantum-optical networks,* Science **354**, 847 (2016).

[81] J. L. Zhang, S. Sun, M. J. Burek, C. Dory, Y.-K. Tzeng, K. A. Fischer, Y. Kelaita, K. G. Lagoudakis, M. Radulaski, Z.-X. Shen, N. A. Melosh, S. Chu, M. Lončar, and J. Vučković, *Strongly Cavity-Enhanced Spontaneous Emission from Silicon-Vacancy Centers in Diamond,* Nano Lett. **18**, 1360 (2018).

[82] R. E. Evans, M. K. Bhaskar, D. D. Sukachev, C. T. Nguyen, A. Sipahigil, M. J. Burek, B. Machielse, G. H. Zhang, A. S. Zibrov, E. Bielejec, H. Park, M. Lončar, and M. D. Lukin, *Photon-mediated interactions between quantum emitters in a diamond nanocavity,* Science **362**, 662 (2018).

[83] C. T. Nguyen, D. D. Sukachev, M. K. Bhaskar, B. Machielse, D. S. Levonian, E. N. Knall, P. Stroganov, R. Riedinger, H. Park, M. Lončar, and M. D. Lukin, *Quantum Network Nodes Based on Diamond Qubits with an Efficient Nanophotonic Interface,* Phys. Rev. Lett. **123**, 183602 (2019).

[84] M. K. Bhaskar, R. Riedinger, B. Machielse, D. S. Levonian, C. T. Nguyen, E. N. Knall, H. Park, D. Englund, M. Lončar, D. D. Sukachev, and M. D. Lukin, *Experimental demonstration of memory-enhanced quantum communication,* Nature **580**, 60 (2020).

[85] D. Riedel, I. Söllner, B. J. Shields, S. Starosielec, P. Appel, E. Neu, P. Maletinsky, and R. J. Warburton, *Deterministic Enhancement of Coherent Photon Generation from a Nitrogen-Vacancy Center in Ultrapure Diamond,* Phys. Rev. X **7**, 031040 (2017).

[86] M. Ruf, M. Weaver, S. van Dam, and R. Hanson, *Resonant Excitation and Purcell Enhancement of Coherent Nitrogen-Vacancy Centers Coupled to a Fabry-Perot Microcavity,* Phys. Rev. Applied **15**, 024049 (2021).

[87] R. Zifkin, C. D. Rodríguez Rosenblueth, E. Janitz, Y. Fontana, and L. Childress, *Lifetime Reduction of Single Germanium-Vacancy Centers in Diamond via a Tunable Open Microcavity,* PRX Quantum **5**, 030308 (2024).

[88] A. González-Tudela, A. Reiserer, J. J. García-Ripoll, and F. J. García-Vidal, *Light–matter interactions in quantum nanophotonic devices,* Nat. Rev. Phys. **6**, 166 (2024).

[89] J. Nobakht, A. Pscherer, J. Renger, S. Götzinger, and V. Sandoghdar, *Hybridization of molecules via a common photonic mode,* Proc. Natl. Acad. Sci. U.S.A. **122**, e2505161122 (2025).

[90] S. Daiss, S. Langenfeld, S. Welte, E. Distante, P. Thomas, L. Hartung, O. Morin, and G. Rempe, *A quantum-logic gate between distant quantum-network modules,* Science **371**, 614 (2021).

[91] D. S. Levonian, R. Riedinger, B. Machielse, E. N. Knall, M. K. Bhaskar, C. M. Knaut, R. Bekenstein, H. Park, M. Lončar, and M. D. Lukin, *Optical Entanglement of Distinguishable Quantum Emitters,* Phys. Rev. Lett. **128**, 213602 (2022).

[92] D. D. Awschalom, R. Hanson, J. Wrachtrup, and B. B. Zhou, *Quantum technologies with optically interfaced solid-state spins,* Nat. Photonics **12**, 516 (2018).

[93] M. Atatüre, D. Englund, N. Vamivakas, S.-Y. Lee, and J. Wrachtrup, *Material platforms for spin-based photonic quantum technologies,* Nat. Rev. Mater. **3**, 38 (2018).

[94] L. C. Bassett, A. Alkauskas, A. L. Exarhos, and K.-M. C. Fu, *Quantum defects by design,* Nanophotonics **8**, 1867 (2019).

[95] A. A. P. Trichet, J. Foster, N. E. Omori, D. James, P. R. Dolan, G. M. Hughes, C. Vallance, and J. M. Smith, *Open-access optical microcavities for lab-on-a-chip refractive index sensing,* Lab Chip **14**, 4244 (2014).

[96] M. Mader, J. Reichel, T. W. Hänsch, and D. Hunger, *A scanning cavity microscope,* Nat. Commun. **6**, 7249 (2015).

[97] M. Bitarafan and R. DeCorby, *On-Chip High-Finesse Fabry-Perot Microcavities for Optical Sensing and Quantum Information,* Sensors **17**, 1748 (2017).

[98] J. Fait, S. Putz, G. Wachter, J. Schalko, U. Schmid, M. Arndt, and M. Trupke, *High finesse microcavities in the optical telecom O-band,* Appl. Phys. Lett. **119** (2021).

[99] G. Wolfowicz, F. J. Heremans, C. P. Anderson, S. Kanai, H. Seo, A. Gali, G. Galli, and D. D. Awschalom, *Quantum guidelines for solid-state spin defects,* Nat. Rev. Mater. **6**, 906 (2021).

[100] A. R.-P. Montblanch, M. Barbone, I. Aharonovich, M. Atatüre, and A. C. Ferrari, *Layered materials as a platform for quantum technologies,* Nat. Nanotechnol. **18**, 555 (2023).

[101] S. Häußler, G. Bayer, R. Waltrich, N. Mendelson, C. Li, D. Hunger, I. Aharonovich, and A. Kubanek, *Tunable Fiber-Cavity Enhanced Photon Emission from Defect Centers in hBN,* Adv. Opt. Mater. **9**, 2002218 (2021).

[102] A. Durand, Y. Baron, W. Redjem, T. Herzig, A. Benali, S. Pezzagna, J. Meijer, A. Y. Kuznetsov, J.-M. Gérard, I. Robert-Philip, M. Abbarchi, V. Jacques, G. Cassabois, and A. Dréau, *Broad Diversity of Near-Infrared Single-Photon Emitters in Silicon,* Phys. Rev. Lett. **126**, 083602 (2021).

[103] Y. Xiong, C. Bourgois, N. Sheremetyeva, W. Chen, D. Dahliah, H. Song, J. Zheng, S. M. Griffin, A. Sipahigil, and G. Hautier, *High-throughput identification of spin-photon interfaces in silicon,* Sci. Adv. **9**, eadh8617 (2023).

[104] H. L. Stern, C. M. Gilardoni, Q. Gu, S. Eizagirre Barker, O. F. J. Powell, X. Deng, S. A. Fraser, L. Follet, C. Li, A. J. Ramsay, H. H. Tan, I. Aharonovich, and M. Atatüre, *A quantum coherent spin in hexagonal boron nitride at ambient conditions,* Nat. Mater. **23**, 1379 (2024).

[105] I. Pogorelov, T. Feldker, C. D. Marciniak, L. Postler, G. Jacob, O. Krieglsteiner, V. Podlesnic, M. Meth, V. Negnevitsky, M. Stadler, B. Höfer, C. Wächter, K. Lakhmanskiy, R. Blatt, P. Schindler, and T. Monz, *Compact Ion-Trap Quantum Computing Demonstrator,* PRX Quantum **2** (2021).

[106] N. Maring, A. Fyrillas, M. Pont, E. Ivanov, E. Bertasi, M. Valdivia, and J. Senellart, *One Nine Availability of a Photonic Quantum Computer on the Cloud Toward HPC Integration,* in *2023 IEEE International Conference on Quantum Computing and Engineering (QCE)*, Vol. 15 (IEEE, Bellevue, WA, USA, 2023) pp. 112–116.

[107] R. Albrecht, A. Bommer, C. Pauly, F. Mücklich, A. W. Schell, P. Engel, T. Schröder, O. Benson, J. Reichel, and C. Becher, *Narrow-band single photon emission at room temperature based on a single nitrogen-vacancy center coupled to an all-fiber-cavity,* Appl. Phys. Lett. **105**, 073113 (2014).

[108] Y. K. Yong, S. O. R. Moheimani, B. J. Kenton, and K. K. Leang, *Invited Review Article: High-speed flexure-guided nanopositioning: Mechanical design and control issues,* Rev. Sci. Instrum. **83**, 121101 (2012).

[109] A. Faßbender, *Adding New Functionalities to Optical Fiber Cavities by Direct Laser Writing*, Ph.D. thesis, Rheinische Friedrich-Wilhelms-Universität Bonn (2023).

[110] C. Derntl, M. Schneider, J. Schalko, A. Bittner, J. Schmiedmayer, U. Schmid, and M. Trupke, *Arrays of open, independently tunable microcavities,* Opt. Express **22**, 22111 (2014).

[111] G. Wachter, S. Kuhn, S. Minniberger, C. Salter, P. Asenbaum, J. Millen, M. Schneider, J. Schalko, U. Schmid, A. Felgner, D. Hüser, M. Arndt, and M. Trupke, *Silicon microcavity arrays with open access and a finesse of half a million,* Light. Sci. Appl. **8**, 37 (2019).

[112] N. Jin, C. A. McLemore, D. Mason, J. P. Hendrie, Y. Luo, M. L. Kelleher, P. Kharel, F. Quinlan, S. A. Diddams, and P. T. Rakich, *Micro-fabricated mirrors with finesse exceeding one million,* Optica **9**, 965 (2022).

[113] H. Cheng, C. Xiang, N. Jin, I. Kudelin, J. Guo, M. Heyrich, Y. Liu, J. Peters, Q.-X. Ji, Y. Zhou, K. J. Vahala, F. Quinlan, S. A. Diddams, J. E. Bowers, and P. T. Rakich, *Harnessing micro-Fabry–Pérot reference cavities in photonic integrated circuits,* Nat. Photon. **19**, 992 (2025).

[114] H. Cheng, N. Jin, Z. Dai, C. Xiang, J. Guo, Y. Zhou, S. A. Diddams, F. Quinlan, J. Bowers, O. Miller, and P. Rakich, *A novel approach to interface high-Q Fabry–Pérot resonators with photonic circuits,* APL Photonics **8** (2023).

[115] W. Bogaerts, D. Pérez, J. Capmany, D. A. B. Miller, J. Poon, D. Englund, F. Morichetti, and A. Melloni, *Programmable photonic circuits,* Nature **586**, 207 (2020).

[116] A. W. Elshaari, W. Pernice, K. Srinivasan, O. Benson, and V. Zwiller, *Hybrid integrated quantum photonic circuits,* Nat. Photonics **14**, 285 (2020).

[117] E. Pelucchi, G. Fagas, I. Aharonovich, D. Englund, E. Figueroa, Q. Gong, H. Hannes, J. Liu, C.-Y. Lu, N. Matsuda, J.-W. Pan, F. Schreck, F. Sciarrino, C. Silberhorn, J. Wang, and K. D. Jöns, *The potential and global outlook of integrated photonics for quantum technologies,* Nat. Rev. Phys. **4**, 194 (2022).

[118] S. Shekhar, W. Bogaerts, L. Chrostowski, J. E. Bowers, M. Hochberg, R. Soref, and B. J. Shastri, *Roadmapping the next generation of silicon photonics,* Nat. Commun. **15**, 751 (2024).

[119] X. Guo, C.-L. Zou, H. Jung, and H. X. Tang, *On-Chip Strong Coupling and Efficient Frequency Conversion between Telecom and Visible Optical Modes,* Phys. Rev. Lett. **117** (2016).

[120] S. Ferrari, C. Schuck, and W. Pernice, *Waveguide-integrated superconducting nanowire single-photon detectors,* Nanophotonics **7**, 1725 (2018).

[121] M. Schwartz, E. Schmidt, U. Rengstl, F. Hornung, S. Hepp, and S. L. Portalupi, *Fully On-Chip Single-Photon Hanbury-Brown and Twiss Experiment on a Monolithic Semiconductor–Superconductor Platform,* Nano Lett. (2018).

[122] S. Gyger, J. Zichi, L. Schweickert, A. W. Elshaari, S. Steinhauer, S. F. Covre Da Silva, A. Rastelli, V. Zwiller, K. D. Jöns, and C. Errando-Herranz, *Reconfigurable photonics with on-chip single-photon detectors,* Nat. Commun. **12** (2021).

[123] M. Ruf, M. IJspeert, S. van Dam, N. de Jong, H. van den Berg, G. Evers, and R. Hanson, *Optically Coherent Nitrogen-Vacancy Centers in Micrometer-Thin Etched Diamond Membranes,* Nano Lett. **19**, 3987 (2019).

[124] A. L. Crook, C. P. Anderson, K. C. Miao, A. Bourassa, H. Lee, S. L. Bayliss, D. O. Bracher, X. Zhang, H. Abe, T. Ohshima, E. L. Hu, and D. D. Awschalom, *Purcell Enhancement of a Single Silicon Carbide Color Center with Coherent Spin Control,* Nano Lett. **20**, 3427 (2020).

Acknowledgments

"Mille Grazie!" - *Roy Bianco & Die Abbrunzati Boys*

Many people have directly or indirectly contributed to the work presented in this thesis, and I hope to have included them all in the following.
Ronald, thank you very much for offering me a PhD position, for your supervision and trust, and for giving me so many opportunities to grow as a researcher. You are showing us every day that it is possible to be an excellent scientist while also maintaining a fun and healthy environment, combined with a great team spirit! Open microcavities might be the longest project running in your group, and it took quite a long breath to bring it all together and to a good end! Thank you for your strong vision and for providing the best environment and infrastructure one could imagine for its realization. I am looking forward to seeing the next scientific and commercial developments from you, operating at the cutting edge of quantum science!
Stephanie, thank you for being my second promoter and for always having time for a more zoomed-out meeting. The Körber price is already quite impressive, but being live interviewed in the *Tagesthemen* is even more!
I also want to thank the committee members of my PhD defense: **David Hunger**, we have already worked together during the time of my master's project in Mainz. Thank you for all the open and helpful discussions since then. It is great to see the versatility of open microcavities fully in use by your group. **Martin van Exter**, thank you for your compliments on our setup and for all the nice discussions during conferences and meetings. **Erika Janitz**, you are one of the pioneers of the diamond microcavity platform, and I am looking forward to meeting you. Since I started working with microcavities, there was always the *"The Janitz Paper"*. **Shima Rajabali**, thank you for showing us around in Harvard, and it is great that you decided to start your own group in Delft. Good luck with this adventure. **Toeno van der Saar**, you have worked as well with NV centers in cavities in your PhD, and you have also been in my Go-No-Go meeting. It is nice to close these circles with the defense. Thank you all for your feedback on the thesis and for taking the extra time!
Since 2008, **Team Diamond** has been part of TU Delft. It is an honor and a lot of fun to be part of such a special group. Over the years, the group developed a solid foundation in diamond fabrication, optics, electronics, and software, which is extremely useful for building on. I am glad that I had the chance to meet many former group members, also during visits and conferences. Thank you all for the great scientific and team environment that you have created!
Julius and **Julia**, who are standing (or sitting) next to me during the defence, have also accompanied me during the time of my PhD. Thank you both for this great time, all the

nice (road) trips to Chicago & New York, Darmstadt, Fryslân, Freiburg (aka tropical Germany), sweet home Alabama & the Smokies, and Cologne, as well as for sharing a lot of enthusiasm for *RB & DAB*.

Julius, you were my partner in crime on the cavity project. Soon after teaming up, we became the infamous *"The Cavity Boys"*, and I think we pushed the microcavity platform to the next level. I enjoyed working with you every day, and I admire your perfection, which you can apply to everything from quantum simulations, over hands-on building of optical setups (or gluing temperature sensors), to planning and organizing events. I leave the question of why we work so well together to the sociologists, but I guess our shared Hessian-Siberian background might be one reason. I will for sure miss our coffee break and the *hot chocolate booster* in the afternoon!

Julia, you are opposite to me on the communication styles chart, but despite this (or maybe because of this), we worked pretty well together. I would have been lost without you in the cleanroom, and I'm very thankful that you spent time on the device fabrication despite it not being your main project. It is great that we could put this together into the microdevice paper, and it was very helpful to work on the thesis with you in parallel. It is good to see that you succeeded in making the tins more equal in your PhD! I will miss working with you a lot!

Over the past five years, many students have done their thesis projects in our group, and I am proud to have supervised four of them. **Laurens**, you were the first student to bring life into the new lab. Setting up a new experimental setup is very challenging and hard to plan, but you managed to do it twice in your master's and PhD! It is great to see the results coming in on the SIC project. All the best with finishing up your PhD, and I am looking forward to the four generations picture! **Leo** (formerly known as the "Lab Benjamin"), you built the room temperature microcavity setup, which was essential for characterizing cavity fibers and diamond samples. It is great that you are now doing your PhD in our group, and I am looking forward to all the new diamond nanodevices. Good luck also with your goal of becoming the longest member of Team Diamond (after Ronald). **Boris**, you built the student practicum setup, which is successfully running now and hopefully luring in some future students. Good luck with your PhD in GLab! **Stijn** (aka *"The Fiber Whisperer"*), you truly earned that name during the time of your project. It's great that you found an exciting PhD project in TU/e, of course, involving fibers! I hope that you enjoy Rosmalen and that you can make it to Okinawa during your PhD! Next to the students supervised by me, more were working on the HILA project. **Colin**, you got diamonds on the sole of your shoe, and you also fabricated excellent devices, which made it into three papers and one patent. Good luck with your PhD in Stuttgart, and I'm looking forward to *Herrn Dr. Sauerzapf, MdL*! **Yuran**, you recorded the first finesse maps, which enabled the beautiful measurements of the device paper. Good luck with your master's studies in Delft! **Cees**, you built the laser excitation and the microwave control setups. Although the measurement results were not so pretty during the time of your project, these were the crucial parts for the NV paper!

Nina (aka *"The Queen of the Cleanroom"*), it was great to do the PhD adventure together with you. Thank you for always having time to talk and for the memorable road trips! And congrats on writing the new *fab bible*! **Max**, you were the first person I've talked with from Delft. Thank you for welcoming and introducing me to the lab and the clean-

room. **Matthew**, it was very helpful to have you as a Postdoc at the beginning of my PhD. I think that QPhoX was the perfect match for you afterwards, lots of success there! **Max and Matthew**, thank you also for planning and organizing the new lab and the HILA setup. Starting the PhD in a freshly renovated lab with a just-delivered setup was perfect and saved a lot of time! **MG**, you ensured that the networks project was finished with grace and dignity, both scientifically and culturally. Thank you for establishing the *Sinterklaas* tradition. Learning German can also be enhanced by listening to the *right* band! **Chris**, your motivation and dedication are important for our group, both in the lab and on the sports field. Thanks for the nice trip to Switzerland and Bella Italia, and for sharing the lab & office! **Hans**, you can easily fetch enthusiasm for every topic. Thank you for organising an awesome sailing trip to Terschelling and enjoy Züri together with **Sophie** and **Hannah**. Finally, **Hans and Chris**, also thank you for borrowing the 619 nm laser for the microcavity SnV experiments! **Tim**, your calmness and your fiber handling skills are very impressive. Both have helped a lot in getting these 15-meter fibers into the fridge *in one piece*. **Dani**, your energy is unmatched. Thank you for the nice conference week in Bonn! **Tim and Dani**, it was also a great time to work with you together on *Macaroni*. Good luck with the first measurements, and please keep the lab clean and organized! **Arian**, the central pillar of Team Diamond. I took some inspiration from your thesis. Enjoy Singapore together with **Vincy**! **Kian**, your enthusiasm for Team Diamond (including merch) is unsurpassed. Thank you very much for inventing the team diamond stickers! You played QuTech fully through. Enjoy Canada! **Christian**, you are always open to discussions about the Roman Empire, Dutch politics, and (drinking) culture. You started a completely new solid-state host in Delft, and it feels like it is already established. **Matteo P. Jr.**, it was nice to do almost the same experiments at the same time, although in a very different system. Thank you for helping to put *the street sign* in its right location, and enjoy Barcelona! **Lorenzo**, you were always ready for all SnV-related questions. Enjoy the Alps! **Niv**, it is very helpful to have you always around for all theory-related questions. Great to see you so enthusiastic about doing your first beam walk, and I hope that you keep walking into the lab! **Marta**, good luck with finding a PhD project! **MC**, thank you for inviting us to your wedding in Vienna. I hope that you enjoy being back in Austria! **Alex**, you have already become a stable member of Team Diamond. Thank you also for your feedback on the device paper and my conclusion chapter! **Alejandro**, our leading Postdoc! It was an honor to share the hotel room with you in Vegas. **Timo**, it is great that you are back from Chicago, and I think that you are already fully re-integrated in the lab. Enjoy the PhD! **Matteo P. Sn.**, your coding skills are unrivaled. This is probably best reflected by the code you developed, e.g., for Grafana, which is still in heavy use.
It is great to have a partner group in QuTech, working on very similar topics, the **TimTams**. **Sjoerd**, it was great that you also had the vision of a sports tournament, and that you got the funding for it with your talk in the Theater de Veste! **Guido**, mapping out a 50-spin network is very impressive. Enjoy Stanford! **Sjoerd and Guido**, thank you both also for the amazing hike through the Grand Canyon! **Jiwon**, thank you for always being helpful on all sorts of questions related to nuclear spin control and for the great road trip through California! **Christina**, thank you for sharing the office! It's good to see that your experiments on such a complicated system are working. **Nic**, thank you for always having time for a small chat on the floor. Good luck with the last part of your

PhD. **Hans Bartling**, your skills in nuclear spin control and ball-throwing are unbeatable. **Dan**, thank you for your feedback on my introduction chapter! **Margriet**, thank you for the nice time during the NNV AMO meeting in Egmond aan Zee, and also for sharing the office! **Ben**, you are always a great help with software, code, and Grafana! Also you good luck with finishing up. **Gerben**, I am sure that you will tame that zoo of photonic crystal cavities! **Conor**, it is great that you came back to Delft. Good luck with your commercial endeavor. **Damian**, thank you for starting together in Delft! **Tobi**, good luck with building up M5! **Kilian**, great that you keep the Stuttgart-Delft connection running. All the best with finishing your master's project and finding a PhD! **Madhu**, I am looking forward to the quantum simulations. Enjoy your PhD! **Jasper**, congrats on getting the 'GO'! **Anta**, thanks for being a very reliable part of QuTech. Enjoy ICFO with Matteo! **Tim Taminiau**, your experiments are amazing. It is very helpful and always fun to have this close connection between the groups.
Jan Riegelmeister, you did a great job with setting up new labs and multiple setups, and you might also become the new record holder in supervising students. Thank you for organizing the great hike through the Eifel and for taking over the NV practicum and making it ready for the students. **Elena**, it is always nice to have a chat with you. Much success with your PhD! **Matteo P. III**, thanks for taking over, both the practicum and the organization of social activities. I am looking forward to the silicon devices! **Lin**, it is always interesting to talk with you about nanophotonics and the Chinese or German research landscape! Enjoy your Postdoc in Delft!
The cavity project is probably the longest project of Team Diamond. The results of this thesis would not have been possible without the work of people before me. Thank you, **Stefan**, **Suzanne**, and **Max**, including all students and Postdocs who have worked on the project, for laying the foundations!
Over the past years, there have also been many students doing projects in our group. Thank you for all the insights and fun, **Chris van Egmond**, **Annick**, **Kamiel**, **Lisa**, **Caroline**, **Sezer**, **Sarel**, **Adrià**, **Zarije**, **Otmar**, **Elvis**, **Pepijn**, **Joan**, **Constantijn**, **Alexandre**, **Miguel**, **Noé**, **Mark**, **Bram**, and **Leanne**.
Sjoerd, **Julius**, **Guido**, **Gerben**, **Jan**, and **Matteo P. III**, thank you for all the fun during organizing the *Diamond Cup™*. I am wondering if, after all these years dominated by the Hanson Lab, finally a different team will win it for the first time. It is also great that Carlos Lab, Hermans Lab, and Delft Networks are joining. And maybe at some point, there will also be a *QuTech Cup* in Delft, sponsored by all the spin-offs!
Next to the *Diamond Cup™*, the Quantum Internet Division's Beach Day has become an important annual event. It was a great opportunity to share a relaxed day with the whole division, and I enjoyed organizing it over the years together with **Shannon**, **Julius**, **Maurice**, **Jan**, **Sara**, **Christina**, **Vicky**, **Sjoerd**, **Francisco**, **Matteo P. III**, **Thomas**, **Niv** and **Tim**. Thank you!
People say that it takes a village to raise a PhD Student. **QuTech** is a great village that provides awesome and very helpful support for researchers in many aspects. Looking at other institutions, this support is very unique in the world, and I am grateful to all of these kind people who contributed to making the experiments possible. Many custom parts need to be machined for the HILA microcavity setup. An excellent job was done by **Nico Alberts**, **Tim Hiep**, **Femke Jansen**, and **Ronald Bode** from the machine shop. On

the technical side, **Siebe Visser**, **Vinod Narain**, **Anh Tran**, **Roy Schoonenboom**, **Jelle Haanstra**, **Mark Ammerlaan**, and **Remco Roeleveld** provided great support for everything needed around the lab. For the smooth running of all cryostats, we can trust in **Olaf Benningshof**, **Jason Mensingh**, **Tom Orton**, and **Erik van der Wiel**. On the electronic side, there is legendary support by *"The Raymonds"*, composed of **Raymond Schouten** and **Raymond Vermeulen**, **Roy Birnholtz**, and **Berend Otto**. **DEMO**, in particular, **Kees Esser**, provided a lot of help for making all kinds of custom PCBs. **Takashi Yamamoto**, thank you for all the grown diamonds. The codebase of Team Diamond (aka *Diamondos*) comprises more than a hundred branches and is used to run more than ten different setups. It is great that this is managed and supported by a professional software team, who are also always helpful in developing code for new instruments. This team includes **Henri Ervasti**, **Pieter Botma**, **Ravi Budhrani**, and **Ingmar te Raa-Derckx**. **Mayank Singh** was an important help in routing through the process of making a patent. **Hitham Mahmoud Amin** and **Régis Méjard** are always available for all questions about general and laser safety. **Régis**, thank you also for taking over the fiber dimple fabrication setup and for producing new cavity fibers! QuTech could not run for a single day without the great work of the managing team. In particular, I would like to thank **Sara Bedin**, **Esther Kruithof**, **Chantal Smith**, **Shannon de Groot-Finch**, **Eva Kaul**, **Rebecca Mayrhofer**, **Arthur Newton**, **Erik van den Biggelaar**, and **Milan Verbrugge**. **Sophie**, **Carlos** and **Francisco**, good luck with your own research groups. I am sure that your groups will contribute to keeping Delft high up on the quantum map in the future! **Sophie**, thank you for your hospitality when we visited Pasadena.

Next to QuTech, I thank the excellent **Kavli** NanoLab Cleanroom staff, in particular **Marc Zuiddam**, **Charles "Chuck" de Boer**, **Eugene Straver**, **Anja van Langen**, **Lodi Schriek**, **Pauline Stevic**, **Hozanna Miro**, and **Brian van den Bulk**, for their help and for keeping the cleanroom up and running. Without your work, no diamond samples could have been fabricated!

Over the time of my PhD, some projects were done in collaboration with **TNO**. Thank you, **Martin Eschen**, for building up the fiber dimple fabrication setup and for producing many cavity fibers. The experiments would not have been possible without these! Thank you, **Nick de Jong**, for the work on the diamond microdevices and the patent coming out of it. Also, thanks to **Zahra Sadre Momtaz** for making new fancy devices and combining this with a perfectly aligned microwave stripline. Furthermore, I thank **Robbert Voorhoeve**, **Tom Duivenvoorde**, **Teun van den Dool**, **Gert Witvoet**, **Hans Spierdijk**, and **Jan de Vreugd** for support on the setup design.

My academic path would not have led me to Delft if I hadn't worked in the lab of **Ferdinand Schmidt-Kaler** in Mainz. Thank you for your enthusiasm about quantum optics and for giving me a lot of freedom and possibilities (even as a master's student), and especially for enabling a research internship in Jerusalem! For their hospitality in Israel, I would like to thank **Nir Bar-Gill** and **Demitry Farfurnik**. **Dima**, all the best with your research group in North Carolina! Thank you to **Max** and **Alex** for taking me under your wings and for teaching me all the basics and daily practices in a research lab. Thank you **Marcel** for being a fantastic supervisor, for teaching me everything about fibercavities and for the great time during QlinkX meetings and in Japan!

I would also like to acknowledge the microcavity research community for their openness,

insights, and helpful discussions. This includes **David Hunger**, **Timon Eichhorn**, **Maximilian Pallmann**, **Jonathan Körber**, **András Laukó**, **Jannis Hessenauer**, **Kerim Köster**, **Michael Förg**, **Alexander Kubanek**, **Robert Berghaus**, **Gregor Bayer**, **Selene Sachero**, **Patrick Maier**, **Florian Feuchtmayr**, **Patrick Maletinsky**, **Yannik Fontana**, **Sigurd Flågan**, **Nadia Antoniadis**, **Daniel Riedel**, **Martin van Exter**, **Corné Koks**, **Jonah Post**, **Wolfgang Löffler**, **Matteo Fisicaro**, **Mio Poortvliet**, **Thomas Steenbergen**, **Andreas Reiserer** and **Alexander Ulanowski**.

Experimental realizations like those presented in this thesis are heavily dependent on complicated and advanced research instruments. Key parts of the setup are made by JPE and Montana Instruments, who have always been helpful and supportive in solving all kinds of problems. From JPE, I would like to thank **Bart van Bree** and **Huub Janssen**. For the installation and the support of the HILA cryostat, I would like to thank **Matt Ballinger**, **Alex Crane**, and **Christoph Karl** from Montana Instruments and **Robert Janz** and **David Appel** from Quantum Design. Finally, I would also like to thank the kind man who pulled our car out of the snow in the lovely town of Panguitch (Utah), you saved part of Team Diamond!

Pavlo, thanks for renting out the most beautiful apartment in Delft. Thank you also for the fun time, and all the best with your own research group in Eindhoven!

I want to thank all my friends back home and in Mainz for all the fun and support. For the great time during studying, this goes to **David**, **Rebecca**, **Leonard**, **Noel**, **Oli**, **Christoph**, **Fabian**, **Jessy**, **Simon**, **Manu**, **Larissa**, **Jana**, **Laura**, **Julia**, **Dette**, **Bruno**, **Hannah**, **Kiki**, **Claas**, **Nadya**, **Nadège**, and **Annette**. This would not have been such a fantastic and memorable time without you!

A stable, yearly event is a great hike through eastern Hessia together with **Christoph**, **Max**, **Constantin**, and **Maxi**. Thank you for this! Furthermore, another annual event is the primary school meeting, enhanced by some Glühwein. For this, I want to thank **Mareike**, **Johannes**, **Isabell**, **Florian**, **Johanna**, **Rebekka**, and **Marius**. It is great that we keep connected, although primary school is already some time ago. And last but not least, thanks to my good old friends **Maxi**, with **Luba**, and **Florian**, with **Laura**!

Thanks to my whole family, which extends over the names of **Knobel**, **Eisenblätter**, **Höra** and **Herrmann**. In particular, I thank **Christian**, **Christa**, **Michael**, and **Lina**. I thank my grandparents, **Gudrun** & **Adolf**, and **Rosel** & **Franz** for their love and support. Finally, I thank my sister **Theresa**, and my mother **Birgit**, with **Horst**, and my father **Dietmar**, with **Andrea**, for supporting me along every step. This would not have been possible without you!

Yanik Herrmann
Delft, November 2025

List of Publications

Journal Articles

5. J. Fischer*, **Y. Herrmann***, C. F. J. Wolfs, S. Scheijen, M. Ruf, and R. Hanson, *Spin-Photon Correlations from a Purcell-enhanced Diamond Nitrogen-Vacancy Center Coupled to an Open Microcavity*, arXiv:2506.20722 (2025)

4. **Y. Herrmann***, J. M. Brevoord*, J. Fischer*, S. Scheijen, C. Sauerzapf, N. Codreanu, L. G. C. Wienhoven, Y. M. Q. van der Graaf, C. F. J. Wolfs, R. Méjard, M. Ruf, N. de Jong, and R. Hanson, *Laser-cut Patterned, Micrometer-thin Diamond Membranes with Coherent Color Centers for Open Microcavities*, Mater. Quantum. Technol. **5**, 035001 (2025)

3. **Y. Herrmann***, J. Fischer*, S. Scheijen, C. F. J. Wolfs, J. M. Brevoord, C. Sauerzapf, L. G. C. Wienhoven, L. J. Feije, M. Eschen, M. Ruf, M. J. Weaver, and R. Hanson, *A Low-temperature Tunable Microcavity featuring High Passive Stability and Microwave Integration*, AVS Quantum Sci. **6**, 041401 (2024)

2. **Y. Herrmann***, J. Fischer*, J. M. Brevoord, C. Sauerzapf, L. G. C. Wienhoven, L. J. Feije, M. Pasini, M. Eschen, M. Ruf, M. J. Weaver, and R. Hanson, *Coherent Coupling of a Diamond Tin-Vacancy Center to a Tunable Open Microcavity*, Phys. Rev. X **14**, 041013 (2024)

1. M. Salz, **Y. Herrmann**, A. Nadarajah, A. Stahl, M. Hettrich, A. Stacey, S. Prawer, D. Hunger, and F. Schmidt-Kaler, *Cryogenic Platform for Coupling Color Centers in Diamond Membranes to a Fiber-based Microcavity*, Appl. Phys. B **126**, 131 (2020)

Patents

1. **Y. Herrmann**, N. de Jong, J. M. Brevoord, C. Sauerzapf, M. Ruf, J. Fischer, and R. Hanson, *A Hybrid Methodology to Produce Diamond Membranes, using a Combination of Reactive Ion Etching and Laser Engraving* (2024)

Included in this thesis.
* Equally contributing authors.

Curriculum Vitæ

Yanik Stefan Herrmann
October 19th 1994, Fulda, Germany

2020-2025 **Ph.D. in Experimental Physics**
QuTech and Kavli Institute of Nanoscience, Delft University of Technology, Delft, The Netherlands. Thesis: *"Good Vibrations: A Microcavity-based Diamond Spin-Photon Interface for Quantum Networking"*. Promotors: Prof. dr. ir. Ronald Hanson and Prof. dr. Stephanie Wehner.

2017-2019 **Master of Science in Physics**
Johannes Gutenberg University, Mainz, Germany. Thesis: *"Silicon Vacancy Centers in Diamond Coupled to a Fiber-based Microcavity at Cryogenic Temperatures"*. Supervisors: Marcel Salz and Prof. dr. Ferdinand Schmidt-Kaler.

Spring 2018 **Research Internship**
The Racah Institute of Physics, The Hebrew University of Jerusalem, Israel. Project: Cryogenic nitrogen-vacancy centers and coplanar waveguides. Supervisors: Dr. Demitry Farfurnik and Prof. dr. Nir Bar-Gill.

2017-2018 **Research Assistant**
PRISMA Detector Lab and Institute of Physics, Johannes Gutenberg University, Mainz, Germany. Project: Assembly of Micromegas detectors for detecting muons in the ATLAS particle detector at the Large Hadron Collider of the European Organization for Nuclear Research (CERN). Supervisors: Dr. Tai-Hua Lin, Dr. Andreas Düdder and Prof. dr. Matthias Schott.

2013-2017 **Bachelor of Science in Physics**
Johannes Gutenberg University, Mainz, Germany. Thesis: *"Frequency Stabilization of a Laser at 737 nm for Measurements with Silicon Vacancy Centers"*. Supervisors: Dr. Max Hettrich and Prof. dr. Ferdinand Schmidt-Kaler.

2010-2013 **Secondary School**
Ferdinand-Braun-School, Fulda, Germany.

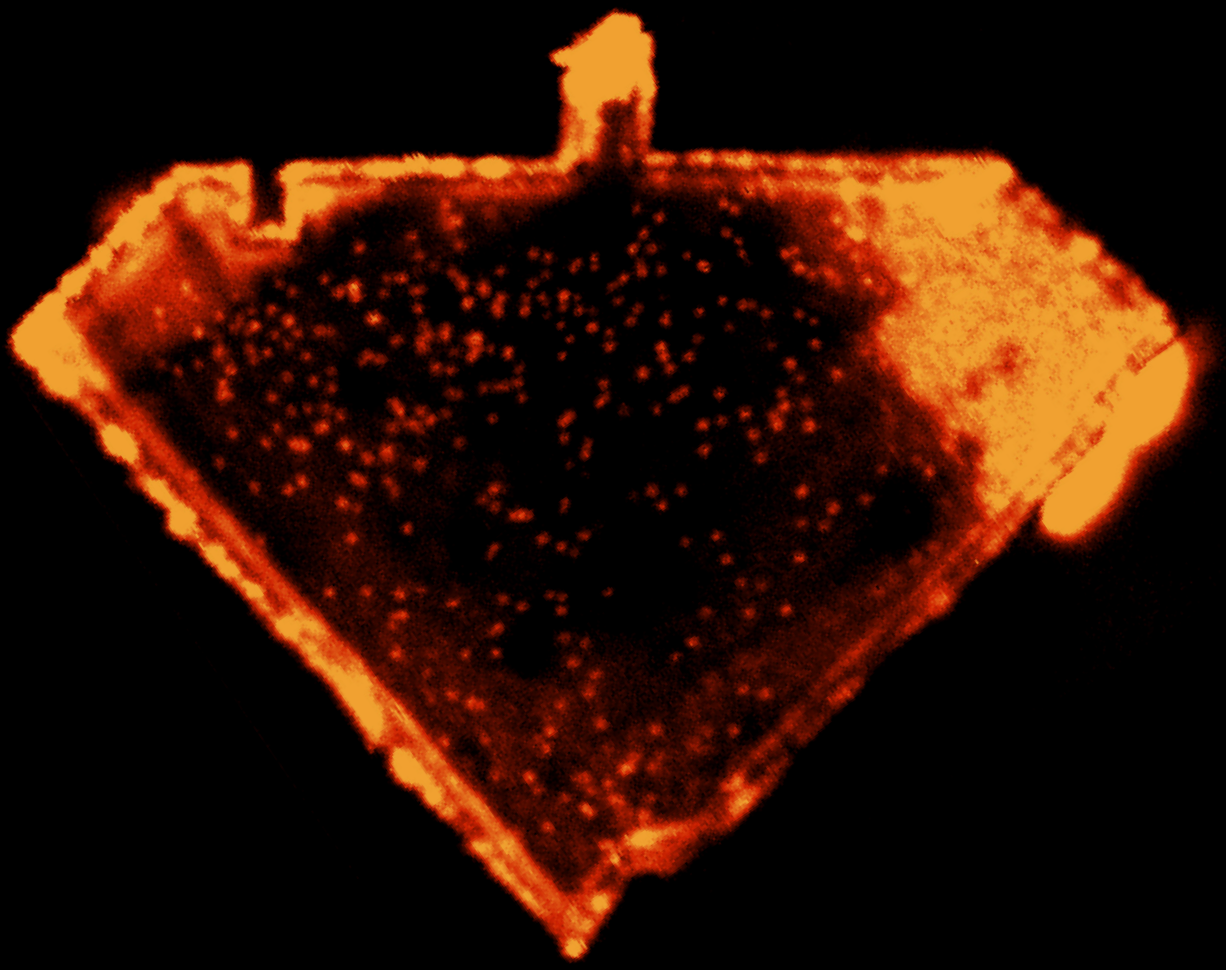

TU Delft

QuTech

TEAM DIAMOND EST. 2008 A.D.

ISBN: 978-94-6518-180-6